Title	Nanocomposite and Microcomposite Materials for Power Electronics Interconnections
Author(s)	巽, 裕章
Citation	大阪大学, 2020, 博士論文
Version Type	VoR
URL	https://doi.org/10.18910/77491
rights	
Note	

Doctoral Dissertation

Nanocomposite and Microcomposite Materials for Power Electronics Interconnections

微細複合材料を用いたパワー半導体向け接合技術に関する研究

Hiroaki Tatsumi
巽　裕章

June 2020

Division of Materials and Manufacturing Science,
Graduate School of Engineering,
Osaka University

Abstract

Nanocomposite (NC) and microcomposite (MC) materials are broad categories of composite materials consisting of two or more constituent materials characterized at nanoscale or microscale with significantly different physical or chemical properties. These materials are expected to enhance the properties of the individual ingredients. Monolithic solder alloys have been conventionally used for electronics interconnections. However, these alloys cannot meet all the requirements for state-of-the-art power electronics applications; these requirements include higher complexity, system integration, product miniaturization, higher power density, and reliability enhancement. In this dissertation, the concept of hybridization of different materials tailored to various requirements for power electronics interconnections is verified through experimental and computational investigations.

In Chapter 1, the fundamentals of interconnections and assembly in power electronics are described. Subsequently, a wide variety of NC and MC interconnection materials are reviewed based on our morphological classification (i.e., matrix-dilute inclusion composites and bicontinuous composites).

The effects of the combination and geometrical arrangements of various constituents on their composite properties are comprehensively discussed through finite element (FE) simulations using simplified representative volume element (RVE) models from a macroscopic perspective in Chapter 2. The calculations of equivalent Young's modulus and thermal conductivity of the RVE models, representing the matrix-dilute inclusion and bicontinuous composites, reveal that the bicontinuous morphology further enhances these equivalent properties. Based on the FE simulations, three distinctive NC and MC candidates, promising the favorable material properties—low Young's modulus, high thermal conductivity and strength, and high-temperature tolerance—are proposed as follows: porous Ag material, Cu-embedded solder composite, and Cu (and/or Cu_6Sn_5)-embedded polymer composite.

An approach utilizing a sintered closed-porous Ag material is discussed in Chapter 3. The closed-porous morphology is successfully realized by a pressure-assisted sintering process at 260 °C by employing a Ag nanoparticle paste. Metallurgical observations highlight the nanocrystalline closed-porous microstructure at the as-sintered state. Further, tensile tests of the sintered Ag films reveal their low ductility, temperature-dependent characteristics, and lower stiffness than that estimated from the porosity. A thermal cycling test performed on die-attached specimens at a peak

temperature of 250 °C shows their applicability to SiC high-temperature interconnections.

An approach utilizing a metallic mesh-embedded solder composite is described in Chapter 4. The composite consists of a Sn-based solder matrix and thin Cu or Ni meshes, which are expected to stabilize the solder matrix against mechanical and thermomechanical loadings and enhance the thermal conductivity of the composite. Microstructural observation and shear strength tests verify good structural integrity of such metallic mesh-embedded solder composite joints. Additionally, thermal and mechanical FE simulations provide an understanding of their thermal- and mechanical-reinforced joint characteristics, which suggests superiority of the Cu mesh inlet over that of Ni. Furthermore, thermal and thermomechanical resistances of the metallic mesh-embedded solder composite joints to elevated and/or cyclic temperatures are clarified and benchmarked with solder reference joints. These results verify that the metallic mesh-embedded solder composite joint, especially the Cu mesh inlet, is an attractive cost-effective joining solution for power modules at a maximum temperature below 200 °C.

An approach utilizing a Cu-intermetallic compound (IMC)-embedded polymer composite is detailed in Chapter 5. In this approach, a skeleton-shaped microstructure consisting of Cu particles connected with Cu–Sn IMC bridges embedded in a polyimide resin matrix is successfully fabricated by a pressureless transient liquid-phase sintering (TLPS) process using a Cu-solder-resin composite paste at 250 °C. Microstructural evaluation, joint strength tests, and thermal conductivity measurements verify the superior performance of this approach. Furthermore, mechanical FE simulations based on three-dimensional (3D) image reconstruction to elucidate its macro- and micro-deformation properties reveal its mechanical characteristics of small elongation and significantly low stiffness. The implementation of the obtained composite joints for the die-attachments of power modules is validated through thermal aging at 200 °C and thermal cycling tests of the die-attached specimens at a temperature range in the range of -55 to 175 °C. This stiffness-reduction approach has a significant potential to be applied in TLPS techniques under strain-dominated loading conditions; thin-chip die-attachments of power modules can be expected to be achieved.

The concept of NC and MC materials tailored to various requirements for electronics interconnections is comprehensively verified by the prediction of equivalent characteristics, and the experimental and computational evaluations of three specific NC and MC interconnection materials. Furthermore, the concept of NC and MC interconnection may still have a tremendous potential by employing various constituents and morphologies. This dissertation is expected to contribute to the further development of material-hybridization methods in electronics interconnections.

Table of Contents

Chapter 1. Introduction

1.1. Brief introduction of nanocomposite (NC) and microcomposite (MC) materials

Simple monolithic materials have limitations for modern engineering applications, requiring multifunctional properties such as light weight, high strength, and high conductivity; therefore, researchers have recently focused on hybrid materials, which consist of materials with complementary and synergistic properties. The simple approach of materials hybridization leads to the tremendous potential of material development, where the materials, size, geometry, and ingredient arrangement combinations can be chosen. These hybrid materials, known as composite materials, are recognized in various material systems, e.g., polymer-matrix composites (PMCs), metal-matrix composites (MMCs), and ceramic-matrix composites (CMCs) [1]. Moreover, composite materials are evolving into more highly controlled and designed structures at the nano or microscale level, labeled “architectured materials”, composed of building blocks of well-defined shape and size, arranged in two or three dimensions, such as periodic cellular, lattice, and porous materials [2]–[4].

Nanocomposite (NC) and microcomposite (MC) materials are a broad category of composite materials consisting of two or more constituent materials characterized at the nanoscale or microscale level with significantly different physical or chemical properties, which can extend the range of properties and therefore, applications of the individual ingredients. These NC and MC materials have recently been utilized for electronic interconnection applications. Solder materials, generally treated as monolithic materials, have conventionally been used for electronic interconnections. Higher complexity, system integration, product miniaturization, higher power density, and reliability enhancement are emerging electronic component requirements; that cannot be fulfilled by traditional simple homogeneous materials. For example, high strength, low stiffness, high thermal conductivity, and high melting point are important representative factors for electronic interconnections, that homogeneous materials do not offer. A wide variety of NC and MC materials have been reported as interconnection materials, e.g., conductive adhesives composed of polymers and metal fillers, porous sintered materials consisting of metal regions and pores, and solders reinforced by nanoparticles. These NC and MC interconnection materials commonly have a microstructure composed of highly conductive and space-filling materials. There are common morphological characteristics found in these various NC and MC interconnection materials; however, a comprehensive classification and discussion of NC and MC interconnection materials has not been adequately conducted. Furthermore, the methodology to computationally predict structural-property relationships in NC and MC materials is desired.

This chapter discusses the favorable attributes of NC and MC materials that make them promising interconnection materials for electronics applications, especially power electronics. First, the fundamentals of interconnections and assembly of power modules are discussed to clarify modern power electronics interconnection requirements. Second, recent interconnection materials and technologies, especially in power electronics fields, are reviewed. Third, the classification of NC and MC interconnection materials is performed based on their morphological features.

1.2. Fundamentals of interconnections and assembly in power electronics

1.2.1. Overview of power modules

Electronic systems are composed of multiple interconnected devices and components to realize their wide functional variety, including information processing, telecommunication, power transmission, and conversion. In particular, power electronic systems are used in numerous fields related to the creation, transmission, storage, and use of electricity for various applications, including home appliances, automobiles, industrial machines, and railway vehicles, among others. [5]. Power modules, key devices of power electronics, are needed to achieve power loss reduction, increased switching frequency, higher voltage capability, reliability enhancement in harsh environments, and system miniaturization. In addition, a wide variety of modules are offered for various power-related electronic applications [6].

Si-based insulated gate bipolar transistors (IGBT) and diodes have been utilized as power semiconductor chips. Refinements of power chips have been driven by precision processing technology enhancement, device architecture structural optimization, and wafer-thickness reduction to meet market demands for decades [7]–[9]. Recently, power semiconductor chips made of silicon carbide (SiC), a wide-bandgap semiconductor material, has been actively developed. Excellent physical and electrical SiC characteristics allow increased power conversion capability and power loss reduction, far exceeding conventional Si-based power chip capabilities. Compared to Si power chips, SiC chips have lower intrinsic carrier concentration (10–35 orders of magnitude), larger saturated electron drift velocity (2–2.5 times), higher electrical breakdown field (4–20 times), and higher thermal conductivity (3–13 times) [10], which enable higher voltage-capable, lower power-loss, higher frequency-band power modules [11]. Additionally, higher current density and miniaturization of cooling systems are also expected because of the heat tolerance property of SiC chips, leading to miniaturization of total power systems [12]–[14]. For the utilization of these outstanding benefits, interconnections have limitations for next-generation applications.

Graphical representations of a conventional power module are shown in Fig. 1.1. Power chips are interconnected (die-attached) on a substrate where conductive layers are bonded to both sides of a ceramic insulation layer, and the chips and substrate are connected to external terminals via wirebonds. The Al_2O_3, AlN, or Si_3N_4 plates are usually applied as the ceramic insulation layer, which is sandwiched between Cu or Al films as the conductive layers. This substrate is bonded (base-attached) onto a base plate and encapsulated with polymer materials in an insulating case. In some instances, Cu or Al is used as a base plate, while silicone gel or epoxy-potting resin is used as the encapsulation material. This assembled component is placed on an Al or Cu heatsink by grease or thermal interface material (TIM). Moreover, other power module types, utilizing various materials and components, e.g., a polymer sheet as an insulation layer, transfer-molded epoxy encapsulation, or heatsink-integrated substrate, have emerged to meet various industrial requirements [10], [15]–[18].

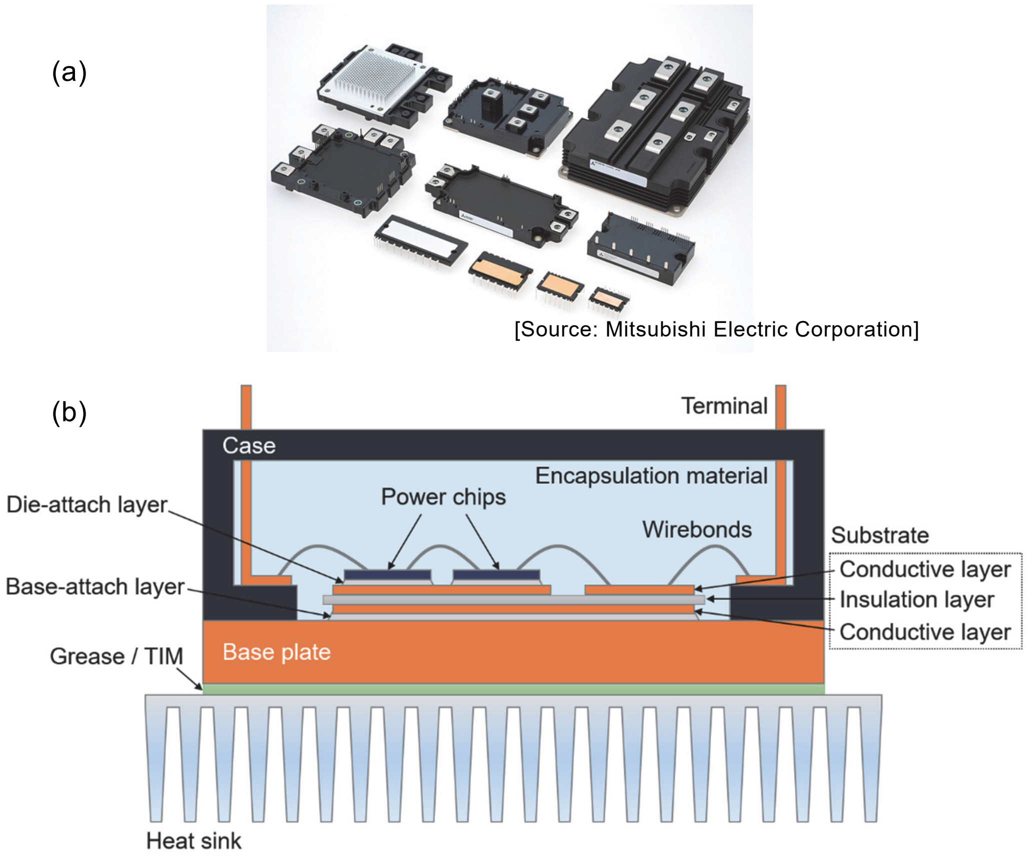

[Source: Mitsubishi Electric Corporation]

Fig. 1.1. (a) Representative power modules and (b) graphical representation of a power module.

Power modules are required to have various characteristics tailored to their applications. Some examples are described, as follows.

- Railway power modules: Extremely high reliability and heat dissipation performance are required. In contrast, production volume is generally small; therefore, moderate mass production capability is satisfactory. The railway power modules would be positioned at high-end.

- Automotive power modules: High reliability and heat dissipation performance are strongly desired because power density is one of the most important requirements. Additionally, mass production capability is desirable because production volume is generally large. The automotive power modules would be positioned as mid-range.
- Industry- and home-appliance-use power modules: Cost-effective mass production capability is demanded because of their large production volumes. Recently, power-chip-thickness reduction is actively promoted for power loss reduction. These power modules would be positioned as volume-zone products.

1.2.2. Requirements for interconnection materials

Enhancement of interconnection reliability against repetitive thermal stress caused by changes in electrical loading or ambient temperature is one of the most challenging power electronics issues. Here, we discuss the interconnection material requirements, especially die-attach materials for power modules. The maximum junction temperature ($T_{\mathrm{j,max}}$) of Si power chips has recently approached the range of 150 to 175 °C. In contrast, the $T_{\mathrm{j,max}}$ of SiC is expected to reach 200 °C or higher in the near future. Therefore, leading-edge die-attachment materials are urgently required for future applications.

Die-attached power electronics interconnections have three main requirements: (a) Heat dissipation performance, (b) joint reliability, and (c) stress-reduction for bonded components, especially power chips.

(a) Heat dissipation performance

Efficient heat dissipation from power chips (heat source) toward the heatsink is required for the operation of power modules, which leads to elevation reduction of T_{j}. Fig. 1.2 shows a schematic of a heat-dissipation path from a power chip to a heatsink. Thermal resistance between a power chip and a base plate ($R_{\mathrm{th(j\text{-}c)}}$), junction temperature (T_{j}), and case temperature (T_{c}) are described as follows:

$$T_{\mathrm{j}} = P \times R_{\mathrm{th(j-c)}} + T_{\mathrm{c}}, \qquad (1.1)$$

$$R_{\mathrm{th(j-c)}} = R_{\mathrm{th(j)}} + R_{\mathrm{th(i)}} + R_{\mathrm{th(c)}}, \tag{1.2}$$

where Q is a power loss, and $R_{\mathrm{th(j)}}$, $R_{\mathrm{th(i)}}$, and $R_{\mathrm{th(c)}}$ is the thermal resistance of the chip, interconnection layer, and case, respectively. T_{c} is usually decided by the cooling condition. $R_{\mathrm{th(i)}}$ is described as follows:

$$R_{\mathrm{th(i)}} = R_{\mathrm{th(bulk)}} + R_{\mathrm{th(interface)}} = \left(\frac{t}{\lambda} + \frac{1}{h}\right) \cdot \frac{1}{A}, \tag{1.3}$$

where t and λ is the thickness and thermal conductivity of the die-attach layer, respectively. h is the interfacial heat transfer coefficient, and A is the area of the die-attach layer. $R_{\mathrm{th(bulk)}}$ and $R_{\mathrm{th(interface)}}$ is the thermal resistance at bulk (sometimes homogenized) interconnection material and interface, respectively. When $R_{\mathrm{th(j)}}$, $R_{\mathrm{th(c)}}$ and Q, which depend on power module structure and chip-characteristics being constant, the following equation is given:

$$(T_{\mathrm{j}} - T_{\mathrm{c}}) \cdot A = Q \cdot \left(\frac{t}{\lambda} + \frac{1}{h}\right) + \mathrm{C}, \tag{1.4}$$

where C is a constant. Eq. 1.4 shows that the decreased thickness of die-attach layer t, or the increased thermal conductivity λ, or interfacial heat transfer coefficient h can reduce the junction temperature T_{j} and chip area A. Therefore, thermal performance enhancement of interconnection materials contributes to power chip shrinkage or miniaturization of the entire power system.

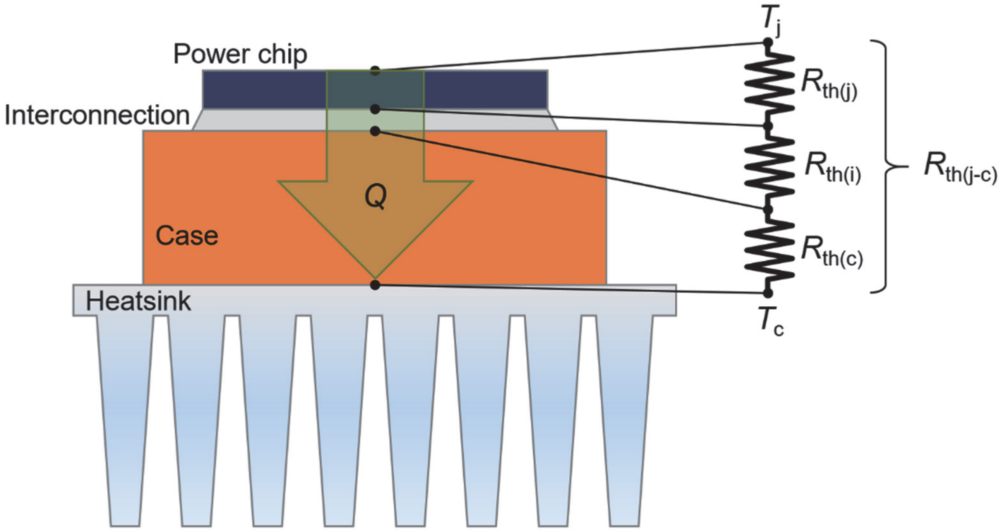

Fig. 1.2. Schematic of the heat-dissipation path of a power module.

(b) Interconnection reliability

Based on Eq. 1.4, the elevation of T_j enables the reduction of area A, i.e., miniaturization of power modules; therefore, a high-temperature-tolerant interconnection technology is required. Sn-based lead-free solders are conventionally used as interconnection materials. These solders, having a melting point of approximately 220 °C, have limitations for use at T_j of 200 °C or higher. Furthermore, the swing of junction temperature ΔT_j increases repetitive thermal strain at interconnection materials because of the coefficient of thermal expansion (CTE) mismatch between assembled components. For example, the CTE of Si, Si_3N_4 ceramic, Cu, and Al is 2.6, 3.0, 16.7, and 23.0×10^{-6}/K, respectively, where severe thermal strain occurs. Besides, the recent utilization of SiC power chips increases the thermal stress in the interconnection layer due to four times higher Young's modulus of SiC than that of Si [19]. Thus, resistant properties of interconnection materials against thermal stress caused by temperature swing are in high demand.

The thermal stress at a die-attach layer between a chip and substrate can be roughly calculated, as shown below; assuming linear-elastic material properties, the maximum shear stress amplitude $\Delta\tau$ on the die-attach layer when the temperature changes between the minimum temperature $T_{\min}$ and maximum temperature $T_{\max}$ is,

$$\Delta\tau = \frac{E}{1+\nu}\left(\alpha_{\text{chip}} - \alpha_{\text{substrate}}\right) \cdot \left(T_{\max} - T_{\min}\right), \tag{1.5}$$

where E is Young's modulus, ν is Poisson's ratio, and $\alpha_{\text{chip,substrate}}$ is the coefficient of thermal expansion of the chip and substrate [20]. Eq. 1.5 shows that the maximum shear stress amplitude $\Delta\tau$ is proportional to Young's modulus E. This understanding is also supported by analytical calculations of thermal stress within multi-layered structure, described in Appendix A and B. Although the nonlinear properties of the complicated system must be considered for detailed assessment, both of the estimation suggest that joint stiffness reduction is an approach to improve joint reliability because of the stress relaxation. Moreover, the strengthening of the interconnection layer is another approach to improve joint reliability.

(c) Stress-relaxation for power chips

The other problem is a mechanical or electrical failure of power chips constrained by a die-attach layer against thermal stress. Large CTE mismatch between a power chip, die-attach layer, and substrate is seen in most power modules, which enhance the power chip failure risk during temperature changes. Semiconductor chips tend to show brittle fracture behavior against stress because of their brittle nature. Bohm et al. [21] reported that the strengths of the Si-wafer by a three-point bending test, which are approximately 200 MPa in 1%-probability, were determined by the Weibull-statistical approach. Furthermore, mechanical stress affects electrical characteristics of power chips, such as IGBT. Usui et al. [22] showed the stress-dependency of trench IGBT by experimental and numerical approaches, as shown in Fig. 1.3, where, e.g., a change of on-stage voltage within a few percent occurred by applying mechanical stress of 200 MPa.

These risks are enhanced by the recent progress of power chips, i.e., a decrease in the power chip thickness and utilization of SiC as an alternative for Si. Power chips with less thickness, e.g., 100 μm or less, have recently emerged to reduce power loss. The Young's modulus of SiC is four times higher than Si, which leads to an increase in thermal stress with power chips. Thermal stress within power chips can be analytically calculated based on linear-elastic properties, as described in Appendix A and B, indicating the effectiveness of Young's modulus reduction of interconnection. For these reasons, the die-attach layer is required to act as a stress-relaxation layer for power chips.

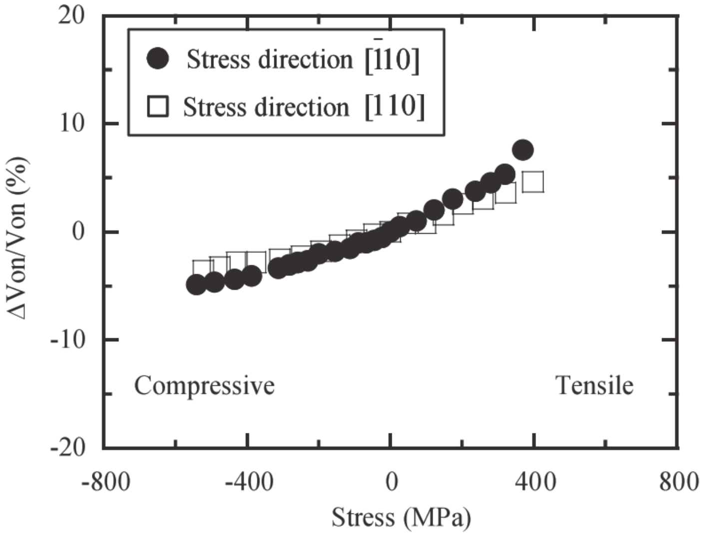

Fig. 1.3. Mechanical-stress-dependent characteristics of the on-stage voltage of trench IGBT: Experimental results with stress direction along [110] and [$\bar{1}$10] direction of Si wafer [22].

1.3. Interconnection materials and technologies overview

Here, we discuss the NC and MC materials and technologies for electronics interconnections, especially die-attach materials and technologies for power modules. The composite material characteristics depend on microstructural features: (a) Constituent characteristics, (b) constituent geometrical arrangements, and (c) interface properties between the constituents. Here, we discuss electronics interconnection materials based on the first and second features.

The constituent characteristics significantly affect various composite material properties. For electronics interconnection materials, various favorable characteristics, e.g., high electrical and thermal conductivity, sufficiently high melting point, low modulus, and high strength, among others, are required. For example, the melting point, Young's modulus, thermal conductivity, and tensile strength of commonly used materials as the constituents of die-attach materials are shown in Table 1.1. The durable temperature was defined as temperature characteristics as follows: Melting point for pure metals, alloys, and ceramics; phase transformation temperature for IMCs; and decomposition temperature for polymers. Generally, Young's modulus, thermal conductivity, and tensile strength have a positive correlation with material durable temperature, as shown in Fig. 1.4. Furthermore, the relationships between thermal conductivity and Young's modulus of these materials, as shown in Fig. 1.5, similarly shows a positive correlation with these properties, where no candidates can be found in the region showing both of high thermal conductivity and low Young's modulus. Low Young's modulus, high thermal conductivity, and high tensile strength are required for die-attachment of power modules, as described in Section 1.2.2. Additionally, a lower bonding temperature is favorable to industrial uses. However, a simple monolithic material that can meet all these requirements is not available. Thus, NC and MC interconnection materials have a tremendous potential for meeting the requirements of die-attachment for state-of-the-art power modules.

Table 1.1. Representative monolithic material properties for die-attach [20], [23]–[42].

Category	Materials	Durable temperature* [°C]	Young's modulus [GPa]	Thermal conductivity [W/m·K]	Tensile strength [MPa]
Pure metal	Cu	1085	100	401	213
	Ag	962	83	429	124
	Al	660	70	237	47
	Zn	420	108	116	118
	Bi	272	32	8	12
	Sn	232	50	67	17
Alloy (solder)	Pb-5Sn	310	35	23	18
	Au-20Sn	280	68	57	275
	Sn-3Ag-0.5Cu	218	31	55	52
	Sn-37Pb	183	27	50	56
	Sn-57Bi-1Ag	138	24	21	42
IMC	Ni_3Sn_4	795	125	20	--**
	Cu_3Sn	676	120	60	2150
	Ag_3Sn	480	80	76	--**
	Cu_6Sn_5	415	102	45	1130
Ceramic***	Al_2O_3	2072	370	30	260
	TiO_2	1825	283	5	--**
Polymer***	Polyimide	410	3–7	0.2	350
	Epoxy	250	2–5	0.3	50

* Melting point for pure metals, alloys, and ceramics; phase transformation temperature for IMCs; decomposition temperature for polymers.

** Unidentified.

*** The listed values of ceramics and polymers are examples within their wide variation range.

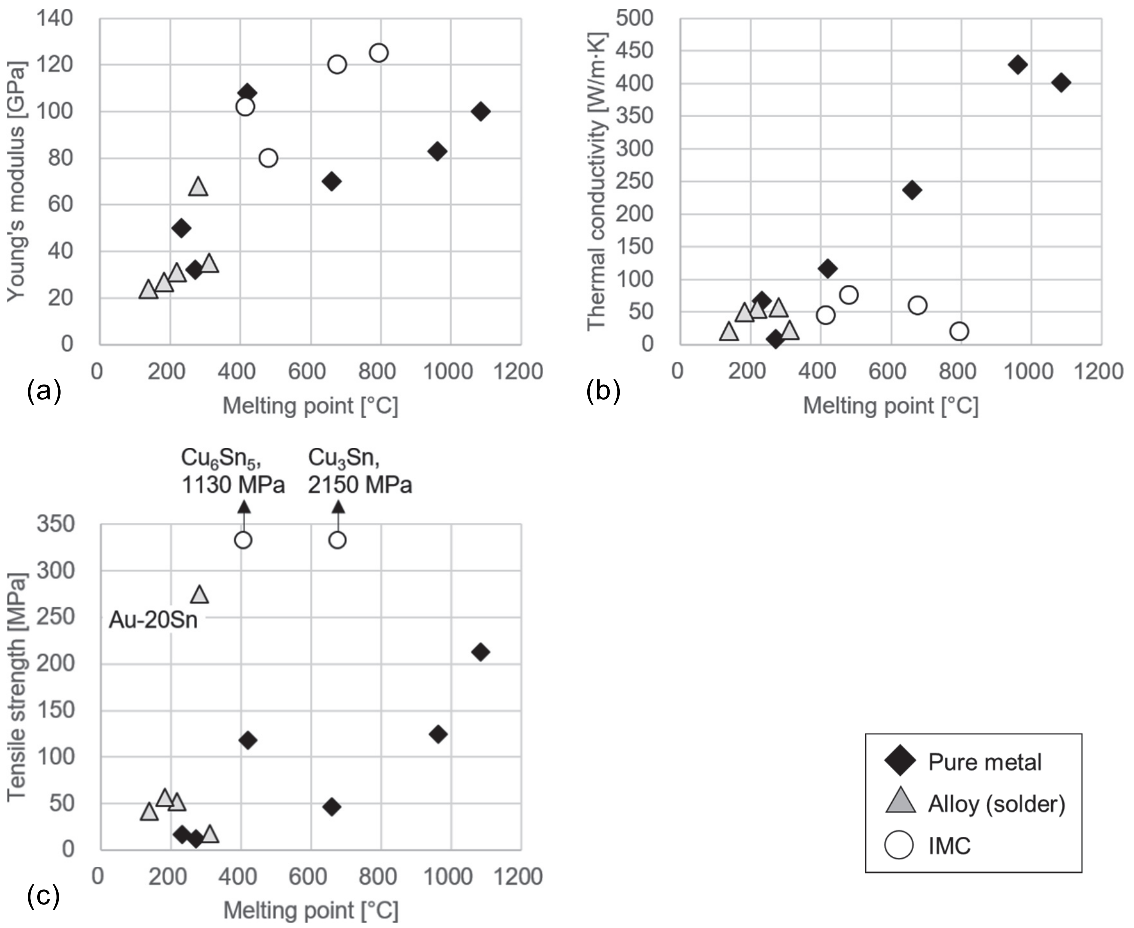

Fig. 1.4. Relationships between the melting point of the die-attaching material constituents and (a) Young's modulus, (b) thermal conductivity, and (c) tensile strength.

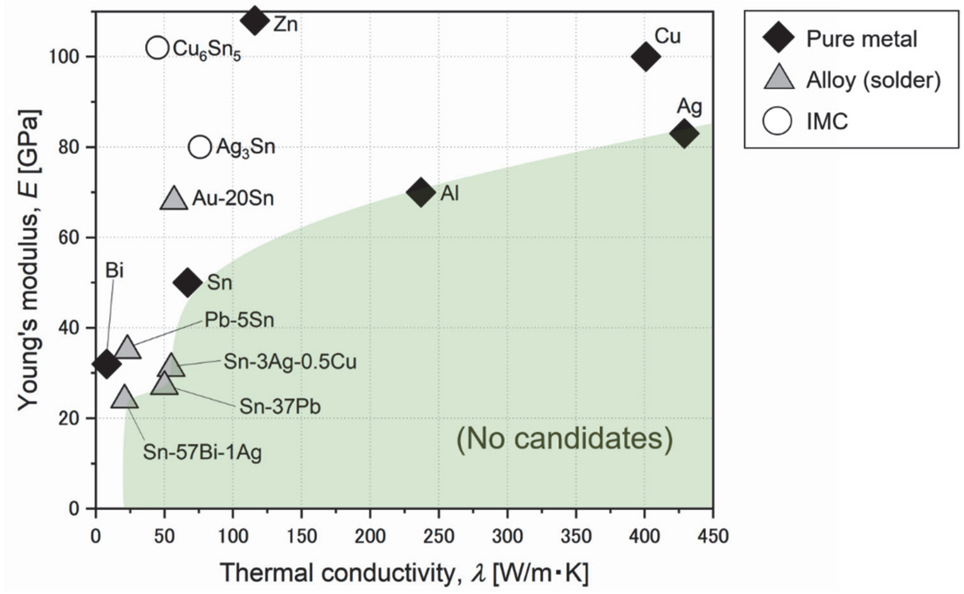

Fig. 1.5. Relationships between thermal conductivity and Young's modulus of the die-attaching material constituents.

The geometrical arrangements of the constituents also affect the mechanical and conductive characteristics of the composite materials. Bargmann et al. [43] proposed the systematic classification considering a wide range of heterogeneous materials, which are divided into porous and non-porous materials by assuming the "space-filling property" of the material domain as the basis. In their work, non-porous materials are further subdivided into non-matrix materials, bicontinuous, and matrix-reinforced composites. In contrast, porous materials are further subdivided into fabrics, agglomerates, and aggregates, where a wide range of heterogeneous materials are treated by discussing the methods of computational modeling of representative volume elements (RVE) of these materials. However, for a comprehensive understanding of interconnection materials, the geometrical arrangements of the composite constituents have to be further discussed by assuming the electrical- and thermal-conductive properties of the materials as the basis.

The NC and MC electronics interconnection materials consist of conductive constituents and space-filling constituents. The characteristics of the NC and MC interconnection materials dominantly depend on the geometrical arrangements of the conductive constituents. Additionally, the space-filling constituents can often be selected for two targets: Reinforcement or stiffness reduction. Thus, based on the morphology of the conductive constituents and the target of the space-filling constituents, we categorized electronics interconnection materials into monolithic, and two categories of composite materials: *Matrix-dilute inclusion composites* and *bicontinuous composites*, as shown in Table 1.2. The category of the matrix-dilute inclusion composites is further divided into *matrix-particle composites* and *closed-porous materials*. The bicontinuous composites category is also subdivided into *matrix-skeleton composites* and *open-porous materials*. In Table 1.2, we show representative die-attach materials and bonding processes with examples and references, considering the combination of the primary and secondary constituents following these categories. In the following, we provide a state-of-the-art overview of various die-attach materials separately for each microstructure class by regarding them as NC and MC materials.

Table 1.2. Classification of electronics interconnection materials into monolithic materials, matrix-dilute inclusion composites, and bicontinuous composites. These categories are subdivided based on the morphological features and combination of the first and second materials, where the primary material is defined as the main electrical- and thermal-conductive part within the composite structure.

Category	Subcategory	Constituents		Typical materials	Example of materials and references
		Primary	Secondary		
Monolithic materials		Metal	--	Solders	Solders based on Sn [44]–[46], Au [47]–[50], Zn [51]–[56], Bi [57]–[60]
		IMC	--	IMCs by TLPB	Cu-Sn [61]–[67], Ag-Sn [68], Ag-In [68]–[70], Ni-Sn [71], Au-In [70]
Matrix-dilute inclusion composites	Matrix-particle composites	Metal	Ceramic	Inclusion-reinforced solders	Solder with microparticles of Ni, Cu, Ag [72], [73], nanoparticles of Al_2O_3 [74]–[77], TiO_2 [77]–[79], Fe_2O_3[80], SiC[81]
		IMC	Metal	IMC and metal particles by TLPS	Cu-Sn IMCs with Cu particles [82]–[87], Ni-Sn IMC with Ni particles [88]
	Closed-porous materials	Metal	Air	Sintered closed-porous materials	Ag [89]–[99], Cu [100]–[102], Ag or Cu composites [103]–[106]
Bicontinuous composites	Matrix-skeleton composites	Metal	Polymer	Sintered conductive adhesives	Ag nanoparticle-epoxy adhesives [107]–[109]
	Open-porous materials	Metal	Air	Sintered open-porous materials Nanoporous films	Sintered Ag [110]–[114], Cu [115], Nanoporous films of Ag [116]–[118], Au [119], and Cu [120]

1.3.1. Monolithic materials

A monolithic material is a material composed of a single solid part showing both a conductive and space-filling property for interconnections. Here, solders are categorized as the most common monolithic interconnection materials, where they are regarded as a single solid layer except in grain boundaries, minute precipitates, or interfacial IMCs. Furthermore, monolithic IMC layers are also utilized as an interconnection layer derived by transient liquid phase bonding (TLPB). In the following, we discuss monolithic interconnection materials of solders and IMCs.

Sn-based lead-free solders have been used as a conventional die-attach solution for power modules. Sn-Ag and Sn-Cu are the representative compositions, with a melting point around 220 °C [44], [45]. Recently, Sn-Sb solders have emerged for targeting the increased melting point and solid-solution strengthening, and have a melting point around 240 °C [46]. As a rule of thumb, solder materials can be reliably used when the homologous temperature: T_{h}, as shown in T/T_{m}, is below 80% [121]. Considering the Sn-based solder melting points, ranging from 220 to 240 °C as described above, these solder materials have many problems for use at temperatures higher than 200 °C.

Au-based solders, especially Au-Sn solder, with a melting point of 278 °C, are primarily used for die-attach of optical or high-frequency precision devices [47]. Lee et al. [48] demonstrated that the growth rate of IMCs on Cu or Ni interfaces of Au-Sn solder was less than that of Sn-Ag-Cu solder, which is one of the most common Sn-based solder compositions. However, Arabi et al. [49] reported that the crack propagation within the Au-Sn solder layer of power modules was observed while operating at 175 °C. Lang et al. [50] clarified the favorable temperature tolerance property of Au-Ge solder, which has a melting point of 360 °C, on Ni-metallized chips by utilizing the W interlayer as a diffusion barrier, which reduced the IMC interface thickness. However, the use of the Au-based solders as a die-attach solution for power modules is limited because of their high cost.

Pure Zn solder [51] and Zn-xSn (x = 20, 30, 40 wt%) solders [52] have been proposed as candidates of Zn-based solders. A common problem with Zn-based solders is the IMC brittleness between the solders and commonly used electrode materials: Ni or Cu. Suganuma et al. [51] demonstrated that the utilization of the TiN interlayer in a chip-metallization as a barrier layer improved the joint reliability of the pure Zn solder. Takaku et al. [53], [54] reported that a Zn-Al solder showed a relatively low growth rate of interfacial IMC on a Ni electrode because Al-Ni IMC preferentially grew. Yamaguchi et al. [55], [56] developed a multi-layered solder material, which consists of a Zn film sandwiched between Al and/or Cu films to achieve good Zn-based solder wettability, which usually show poor wettability because of the stable oxidized surface of Zn. The pure Zn, Zn-Sn, or Zn-Al solders have a liquidus temperature of approximately 365–400 °C; therefore, the high-temperature-tolerant property is expected compared to conventional Sn-based solders. However, the use of the Zn-based solders as a die-attach solution for power modules is limited because of their high melting point.

Bi-based solders, Bi-Ag, Bi-Sn, and Bi-Zn have been proposed. Bi-Ag [57], [58] and Bi-Zn [59] solders, with eutectic points of 263 and 255 °C, respectively, were attempted for power module applications. Bi-Sn solder, which includes several percent of Sn, is proposed for operation at 250 °C or higher [60]. Well-known problems of the Bi-based solders include brittleness and low Bi thermal conductivity, along with a brittle IMC on the Ni-metallization layer: $BiNi_3$. Wang et al. [60] reported that a 5%-or-higher addition of Sn enabled the priority growth of Ni_3Sn_4 instead of the $BiNi_3$, enhancing the high-temperature reliability. Iseki et al. [59] demonstrated that improvement of mechanical properties could be achieved by utilizing Bi-2.6Zn solder because of the lower $BiNi_3$ growth rate compared to the pure Bi solder. However, low joint reliability on Ni metallization, brittle mechanical properties, and low thermal conductivity disturb power module applications.

Transient liquid phase bonding (TLPB) [122], which utilizes IMCs as a bonding layer, has been developed. The bonding layer is obtained through the isothermal layered sheet solidification, with the first material being a low-melting-point metal (e.g., In, Sn), and the second material, a high-melting-point-metal (e.g., Cu, Ag, Ni, Au), at a temperature above the liquidus temperature of the first material under static bonding pressure for intimate contact. The remelting point of the bonding layer rises from the first material melting point to the IMCs. Lee et al. [61] demonstrated joints with a remelting point of 713 °C bonded at 280 °C by the TLPB process of the Cu-Sn system. Bosco et al. showed the heating rate impacts during the bonding process on the IMC-grain growth behavior, and the guideline of bonding layer thickness and temperature profiles for void formation reduction [62], and excellent joint strength [63]. Guth et al. utilized the Cu-Sn TLPB into power module die-attachment [64] and demonstrated the excellent joint reliability [65]. Fukumoto et al. [66] presented the rapid isothermal solidification by increasing the area of Cu-Sn interfacial diffusion utilizing the multi-layered Cu-Sn thin film. Jeong et al. [67] proposed pre-annealed multi-layered Sn/Cu/Sn composite preform for fast formation of IMCs at 270 °C for 5 min. The TLPB methods using Ag-Sn [68], Ag-In [68]–[70], Ni-Sn [71], and Au-In [70] are also being developed. Nevertheless, high bonding temperature at 300 °C or higher, long bonding duration, and the limitation of a thin bonding layer, which are required for sufficient diffusion reaction progress, are barriers for industrial application.

1.3.2. Matrix-dilute inclusion composites

Matrix-dilute inclusion composites are a material composed of a conductive matrix and dilute space-filling inclusions. The matrix-dilute inclusion composites are characterized by unconnected inclusions embedded in a topologically interconnected matrix [43]. The electrical and thermal conductivity of the composites primarily depend on the matrix properties. The inclusions are intended to improve the mechanical properties of the matrix. Inclusions within composites are usually intended to reinforce the matrix by their properties of high strength and stiffness. In this study, the definition of the inclusions is extended to be a material embedded in a matrix, intending to modify the matrix properties, namely a material for reinforcement, stiffness reduction, or conductivity enhancement of the matrix. When we discuss the stiffness-reduction composites, pores can be the inclusions. The category of the matrix-dilute inclusion composites is further divided into matrix-particle composites and closed-porous materials. In the following, we discuss the matrix-particle composites (Section 1.3.2 (a)) and closed-porous materials (Section 1.3.2 (b)).

(a) Matrix-particle composites

Matrix-particle composites are composed of isolated inclusions embedded in a matrix material. Quite stiff and nearly insoluble materials such as ceramics are commonly used as the inclusions. The inclusions are intended to inhibit matrix deformation by their rigid properties and the growth of coarse grains by their action as sites for heterogeneous nucleation. In addition, highly-conductive inclusions can be introduced to improve thermal and electrical matrix conductivity. Matrix-particle composites may emerge at various scales, depending on the size of the inclusions.

Inclusion-reinforced solders are being researched as matrix-particle composites for electronic interconnections. Guo et al. [72], [73] developed composite Sn-Ag solders reinforced with micron-sized particles of Ni, Cu, and Ag, where creep behavior of these composite solders was investigated at 25, 65, and 105 °C. Furthermore, composite solders reinforced with nanoparticles of Al_2O_3 [74]–[77], TiO_2 [77]–[79], Fe_2O_3 [80], SiC [81] have recently been researched. These nanoparticles of oxides or carbides with high melting temperatures suppress grain growth and therefore provide the formation of small precipitated IMCs within solders. Li et al. [74] successfully synthesized composite solder reinforced with 1, 3, and 5% of Al_2O_3 nanoparticles, which increased yield and ultimate tensile strength. Tsao et al. [75], [76] successfully blended Sn-3.5Ag-0.5Cu composite solders reinforced with 0.25, 0.5, and 1 wt.% of Al_2O_3 nanoparticles, and revealed the microstructure composed of both superfine nano-Ag_3Sn and wider eutectic areas in the solder matrix, where Al_2O_3 nanoparticles were dispersed both at and along the grain boundary regions. These nanoparticle-reinforced solders showed higher microhardness, higher strength, and lower ductility compared to monolithic Sn-3.5Ag-0.5Cu solder. Sn-Ag solders reinforced with TiO_2 [77]–[79], Fe_2O_3 [80], or SiC [81] nanoparticles also provided higher hardness and strength by the morphology with fine-grained precipitates. The strengthening effects of these matrix-particle composites are understandable by the theory of dispersion strengthening.

Matrix-particle composites composed of metal particles embedded within an IMC matrix has recently emerged. The composites are obtained by transient liquid phase sintering (TLPS) utilizing powder-based bonding materials. In comparison with the interconnection by TLPB, as shown in Section 1.3.1, the powder-base materials utilization enables the reduction of bonding duration by increasing the area of interfacial diffusion and a thicker bonding layer. Greve et al. [82] developed a bonding paste consisting of Cu and Sn particles for a die-attachment of power modules, where high joint strengths were obtained at 600 °C by using the material with a mixing ratio of Cu at 60 wt%. Additionally, higher joint strengths were achieved by the Ni addition to the Cu-Sn paste [83]. Liu et al. [84]–[86] showed the temperature-resistant joints bonded at a lower temperature and shorter bonding process by utilizing Sn-coated Cu particles as a bonding material. Hu et al. [87] developed the bonding film, as shown in Fig. 1.6, produced by the pressurization of Sn-coated Cu particles at room temperature, which enabled void formation reduction and a lower and shorter condition (temperature: 280 °C, pressure: 0.5 MPa) during the bonding process. Furthermore, the possibility for power module applications was demonstrated from a thermal and electrical characteristics point of view. Shao et al. [88] developed the new TLPS process through the capillary action of liquid Sn into a porous Cu film, which realized a well-densified structure even with a relatively low bonding pressure of 0.3 MPa. These TLPS bonding layers, as described above, consist of Cu-Sn IMCs and remaining Cu particles (and sometimes pores). Additionally, Feng et al. [123] demonstrated that the Ni-Sn TLPS joint showed stable strength from room temperature to 350 °C, where the Ni-Sn TLPS bonding layer similarly consists of Ni-Sn IMCs, remaining Ni particles, and pores. Thus, these TLPS layers can be considered as the matrix-particle composites composed of high-melting-point metal particles embedded in an IMC matrix.

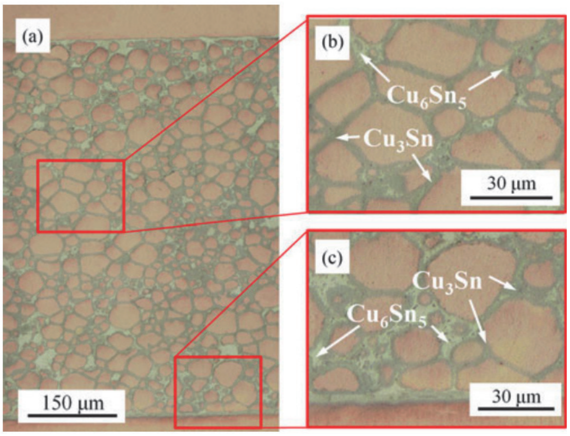

Fig. 1.6. (a) Cross-sectional image of the TLPS joint bonded at 250 °C for 8 min with 0.5 MPa using preformed Cu-Sn film; (b) and (c) higher magnification images of the areas shown by red squares in (a) [87].

(b) Closed-porous materials

Closed-porous materials consist of a matrix material with isolated pores. Fig. 1.7 shows typical three-dimensional (3D) structures obtained by computational modeling, shown in Ref [43], where the structure is known as matrix-dilute pore systems. Nano- or micro-pores are embedded in the matrix. These pores are usually treated as defects, for example, casting defects in the metallic components. However, these isolated pores tend to decrease material stiffness; therefore, these pores can be intentionally introduced into certain materials such as nanoporous metallic glass.

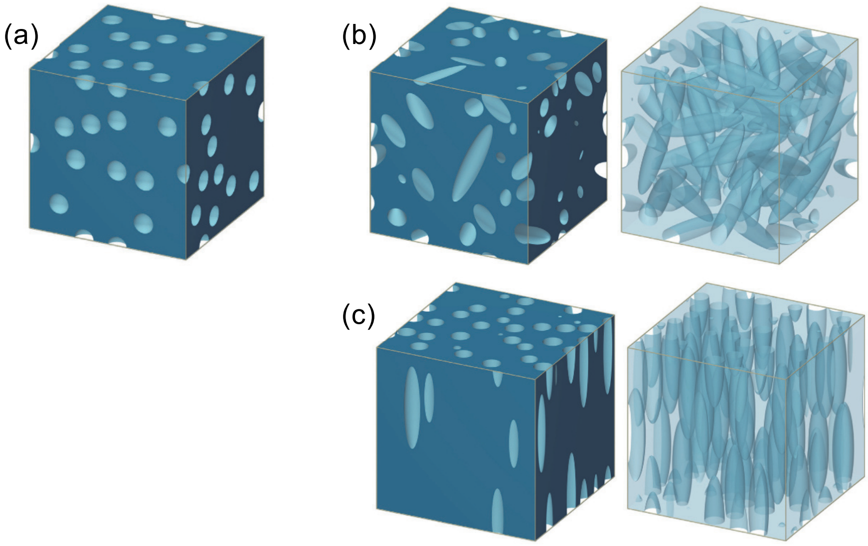

Fig. 1.7. Typical 3D structures of closed-porous materials obtained by computational modeling: (a) randomly arranged spherical pores, (b) randomly oriented elongated ellipsoid pores, and (c) deterministically oriented elongated ellipsoid pores, shown in Ref [43].

Sintered closed-porous materials, which are manufactured by the pressure-assisted sinter bonding process using nanoparticles, are being researched for electronics interconnections, especially power modules. Nanoparticles show the inherent characteristics because of the significantly high surface energy per volume [124]–[126]. The high surface energy is helpful for sinter bonding at a relatively low temperature. Research on bonding technology using nanoparticles started in the early 2000s [89], [90], [92]–[95]. Ag nanoparticles are commonly used for the bonding process [91], [96]–[99], and Cu nanoparticles have also recently been researched [100]–[102]. Additionally, the bonding material of Ag or Cu compounds, such as Ag_2O, Ag_2CO_3, Cu_2O, or Cu_2O, are utilized for sinter bonding through in-situ chemical decomposition reactions [103]–[106]. The pressure-assisted sinter bonding process provides a closed-porous microstructure, consisting of a dense sintered matrix with dilute closed pores. Fig. 1.8 shows the sintering behavior of Ag nanoparticles through pressureless heating in air, shown in our previous study [96]. The Ag nanoparticles began connecting at 200 °C and agglomerated to bulkiness through temperature elevation. The sintered microstructure with closed pores can be seen at a temperature higher than 300 °C. Sintered microstructure strongly depends on temperature and pressure conditions; for example, the bonding temperature and pressure commonly range from 250 to 400 °C and from 5 to 40 MPa, respectively, using Ag nanoparticles. Carr et al. [127] quantitatively characterized the 3D morphology of Ag joints sintered at 240 °C for 3 min under 10 MPa by quantification of the segmented 3D images, where the as-sintered joint mainly embeds closed pores. Zhang et al. [128] reported the averaged volume fraction of pores of the microstructure by pressure-assisted sintering ranged below approximately 20%. Researchers are pursuing improved joint strength by reducing porosity within the closed-porous microstructure by optimizing material characteristics such as particle-size distribution, types of solvent, and bonding conditions such as temperature, pressure, and atmosphere. The sintered closed-porous interconnection material has been reported as already being utilized for power module applications, where excellent conductivity and joint reliability have been demonstrated [128]–[134].

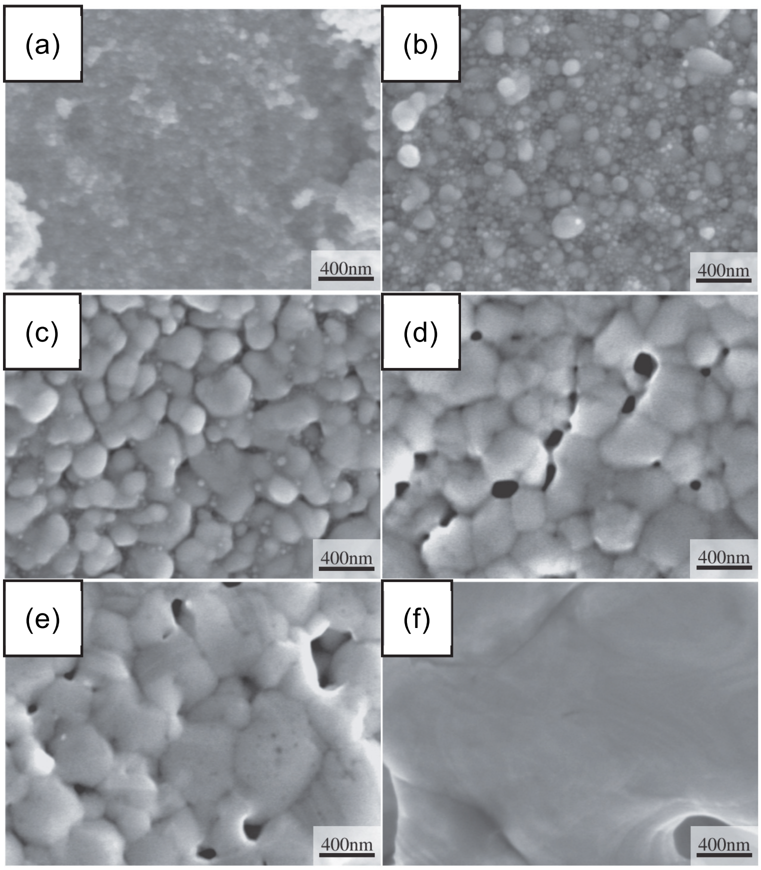

Fig. 1.8. Scanning electron microscope (SEM) images of Ag nanoparticles (a) before and after heating up to (b) 250, (c) 300, (d) 350, (e) 400, and (f) 500 °C [96].

1.3.3. Bicontinuous composites

Bicontinuous composites consist of two constituents, each of which is continuous in space, forming an interpenetrating network. A typical computational-modeled 3D bicontinuous structure is shown in Fig. 1.9. The common feature of all bicontinuous composites is that each of the interpenetrating phases has an open-cell morphology formed of interconnected ligaments [43]. Bicontinuous composites are fabricated to demonstrate outstanding thermal, electrical, and mechanical properties by designing morphological arrangements as well as constituent properties. Regarding electronics interconnection materials, one constituent (primary) works as an electrical and thermal conductive part. In contrast, the secondary constituent acts as a space-filling part or plays both conductive and space-filling roles because of its continuous morphology, which is a different feature from the matrix-dilute inclusion composites (Section 1.3.2). The mechanical properties of the bicontinuous composites depend on the morphology as well as the mechanical properties of both primary and secondary constituents. Simply put, a primary constituent is reinforced or stiffness-reduced by a secondary one. When the secondary constituent is air, the bicontinuous composites are regarded as open-porous materials or open-cellular materials, which are expected to provide significantly low stiffness interconnections. By contrast, relatively stiff materials can be used as the secondary constituents, the morphology of which looks like a skeleton in the body. In this case, the bicontinuous composites are regarded as matrix-skeleton composites, which are defined as the bicontinuous composites with the secondary constituent reinforcing the primary one. Based on this consideration, the category of the bicontinuous composites is further divided into open-porous materials and matrix-skeleton composites. In the following, we discuss matrix-skeleton composites (Section 1.3.3 (a)) and open-porous materials (Section 1.3.3 (b)).

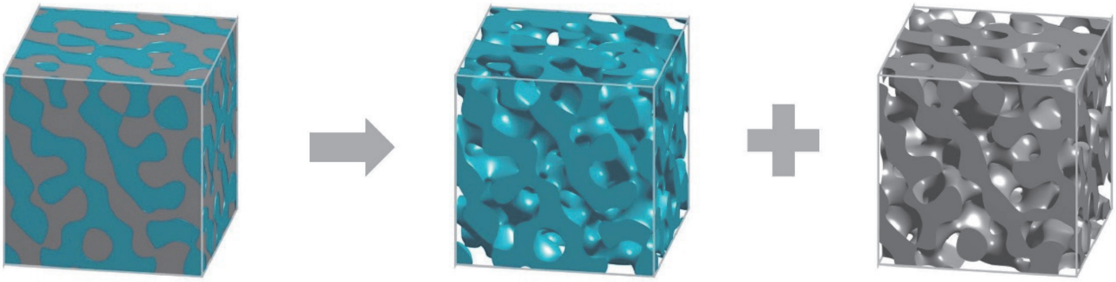

Fig. 1.9. Typical random bicontinuous composite microstructure with each phase of a volume fraction of 50%, shown in Ref [43].

(a) Matrix-skeleton composites

Matrix-skeleton composites are defined as the bicontinuous composites composed of two interpenetrating solids characterized by reinforcement and stiffness-reduction, respectively. Moreover, one solid generally plays the electrical and thermal conductive path role for electronic interconnections. Examples for matrix-skeleton composites are bicontinuous metal-ceramic nanocomposites [135] and polymer/elastomer composites [136]. Here, we discuss sintered conductive adhesives as matrix-skeleton composites.

Sintered conductive adhesives are composed of a skeleton-shaped solid of sintered conductive fillers embedded into a polymer matrix. Jiang et al. [107] reported Ag nanoparticle-filled conductive adhesives with various surfactants of their particles could be achieved with 2×10^{-4} Ω cm. Zhang et al. [108] developed highly conductive polymer nanocomposites, consisting of an epoxy resin, Ag flakes, and incorporated Ag nanoparticles, which showed electrical resistivity of 6.0×10^{-6} Ω cm cured at 260 °C for 10 min. Furthermore, Amoli et al. [109] reported conductive adhesives using Ag nanoparticle-decorated graphene in an epoxy matrix, which showed the electrical resistivity of 4.6×10^{-5} Ω cm at a lower temperature of 220 °C. These highly conductive adhesives have a microstructure, which is a sintered skeleton-shaped solid embedded in a polymer matrix. However, examples, where these adhesives are used for the interconnection of high-temperature power modules, are rarely seen to date.

(b) Open-porous materials

Open-porous materials consist of a solid matrix and continuous space. Fig. 1.10 shows typical 3D open-porous structures obtained by computational modeling, shown in Ref [43], where the structure is known as open-cell material. The inherent feature of the open-porous materials is the morphology of pores, which are continuous in space, compared to the morphology of discontinuous pores in the closed-porous materials (Section 1.3.2 (b)). The volume fraction of the continuous solid part in the open-porous materials is lower than that of the closed-porous materials. The inherent 3D microstructure strongly affects the equivalent mechanical and conductive properties. This microstructure can significantly reduce the interconnection joint stiffness.

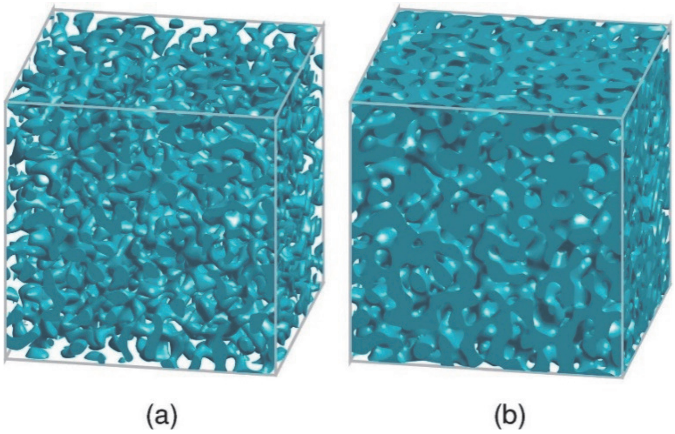

Fig. 1.10. Typical open-porous material microstructures with (a) 20% and (b) 50% solid phase volume fraction, shown in Ref [43].

Sintered open-porous materials are an example of open-porous materials for electronics interconnections. These are commonly obtained by a low-pressure or pressureless sinter bonding process using nano- or microparticles. The closed-porous materials, as discussed in Section 1.3.2 (b), are produced by the well-advanced sintering phenomena through a pressure-assisted bonding process. In contrast, the open-porous materials are fabricated by the intermediate stage of sintering by using a pressureless or low-pressure bonding process. Yu et al. [110] reported that the joint strengths bonded by pressureless sintering of microscale Ag paste showed approximately 15 MPa between 200 and 300 °C for 60 min with Ag-metallized substrates. Kariya et al. [111] evaluated the deformation behavior of open-porous Ag microstructure by using experimental and computational analyses, presenting low Young's modulus and creep deformation enhancement at a lower temperature. Zabihzadeh et al. [112], [113] evaluated the deformation behavior of nano-porous polycrystalline Ag by tensile tests, 3D-tomography, and computational simulations by using image-based reconstruction models. These results provided the macroscopic stress-strain curves and also the microscopic stress and strain distribution within the microstructures with various porosity. Suzuki et al. [114] also demonstrated the open-porous microstructure by using a 3D-sectional observation technique, the deformation behavior of which showed significantly low elastic modulus. They also showed that the increased porosity of sintered Cu open-porous microstructure reduced the elastic modulus by using experimental and computational mechanical testing [115]. As mentioned above, researchers have reported the stiffness-reduced mechanical properties of the sintered open-porous materials. These results suggested the outstanding potential of stiffness-tailored bonding materials. However, the open-porous materials tend to show insufficient joint reliability against thermal cycling operations because of their lower strength.

A solid-state bonding technique by using nanoporous films has been developed for interconnections. Nishikawa et al. demonstrated the nanoporous films of Ag [116]–[118], Au [119], and Cu [120] for high-temperature power module and flip-chip device applications. These nanoporous sheets are fabricated by a dealloying process, which utilizes selective dissolution of electrochemically active elements into the electrolyte solution from a precursor alloy. The dealloying process forms an open-porous structure. For example, the bonding process at 300 °C for 30 min under a pressure of 20 MPa by using the Ag nanoporous sheet enabled a shear strength equivalent to a conventional Pb-based solder [116]. The technique is expected to demonstrate excellent reliability in high-temperature power module applications.

1.4. Objectives and outline

Power modules, being key power electronics devices, are required to achieve power loss reduction, increase switching frequency, raise voltage capability, enhance reliability in a harsh environment, and system miniaturization. Enhancement of interconnection reliability against repetitive thermal stress caused by changes in electric loading or ambient temperature is one of the most challenging issues of power electronics. The maximum junction temperature ($T_{\mathrm{j,max}}$) has recently been shifting from 150 to 175 °C for Si devices, and approaching 200 °C or higher for SiC devices in the near future. Therefore, leading-edge interconnection materials, especially die-attach materials, are strongly required for future applications. The interconnection materials have three main requirements: Heat dissipation performance, joint reliability, and stress-reduction for power chips. The requirements suggest that low Young's modulus, high thermal conductivity, high tensile strength, and high durable temperature are required for the interconnections. Additionally, a lower bonding temperature is favorable for industrial uses. However, a simple monolithic material that can meet all these requirements has not been found. In contrast, NC and MC interconnection materials have a tremendous potential for meeting the requirements of die-attachment for state-of-the-art power modules. A wide variety of NC and MC materials have been reported as interconnection materials, as described in the literature overview in Section 1.3. However, a comprehensive discussion of these NC and MC interconnection materials by a certain methodology focusing on the morphological features has not been thoroughly conducted. Moreover, the compatibility of these NC and MC interconnection materials for power die-attach applications has not been sufficiently discussed.

Based on these considerations, the objectives of this dissertation are to verify NC and MC materials tailored to various requirements for power electronics interconnections by experimental and computational investigations. First, the combination and geometrical arrangement effects of various constituents on their composite properties and joint characteristics are comprehensively discussed by finite element (FE) simulations using the idealized microstructure computational-modeling. Based on the simulation results, we propose the promising NC and MC interconnection materials: Sintered closed-porous Ag material, metallic mesh-embedded solder composite, and Cu-IMC-embedded polymer composite. These NC and MC interconnection materials are evaluated through microstructural observations, mechanical testing, and joint reliability evaluations, as well as FE simulations. These results provide helpful insights about the deformation mechanisms and fracture behaviors of the NC and MC materials, and NC and MC material implementation outlook for future power module applications. The dissertation research flow is shown in Fig. 1.11; and consists of six chapters, with what has preceded being Chapter 1 and the remaining chapters described as follows.

In Chapter 2, a prediction method of NC and MC interconnection materials characteristics are proposed by utilizing the FE simulations using the computationally-modeled idealized microstructure. The effects of the combination and geometrical arrangements of various constituents on their composite properties are comprehensively discussed. Based on these results, we propose the promising NC and MC interconnection materials.

In Chapter 3, a sintered closed-porous Ag material is evaluated for high-temperature die-attach applications of SiC power modules. The effects of the metallurgical and mechanical properties of the sintered Ag materials are evaluated using electron-microscope observations and tensile tests of sintered films at elevated temperatures. Subsequently, the temperature dependence of die-attach reliability is investigated using thermal cycling tests of die-attached specimens composed of SiC power chips and direct bonded copper (DBC) substrates under various temperature conditions.

Finally, the presumed fracture mechanism and the outlook of the implementation of the sintered closed-porous Ag materials for high-temperature power modules are discussed.

In Chapter 4, a metallic mesh-embedded solder composite as a bicontinuous composite is evaluated. The metallic mesh-embedded solder composite consists of Sn-based solder matrix and thin Cu or Ni meshes, which are expected to stabilize the solder matrix against mechanical and thermomechanical loading, and enhance thermal conductivity. Microstructural observation and shear strength tests of such metallic mesh-embedded solder composite joints are evaluated, supported by FE simulations. Moreover, the thermal and thermomechanical resistances of the composite joints to elevated and/or cyclic temperatures are clarified and benchmarked with solder reference joints.

In Chapter 5, a Cu-IMC-embedded polymer composite as a bicontinuous composite is proposed for stiffness-reduced TLPS joints by controlling the microstructural morphology. In this concept, a skeleton shaped microstructure consisting of Cu particles connected with Cu–Sn IMC bridges embedded in a polyimide resin matrix is fabricated by using a Cu-solder-resin composite paste as a bonding material. First, this concept is validated by using mechanical FE simulations of simplified composite models to roughly estimate the composite microstructure impact on the effective mechanical properties. The concept is verified by experimental microstructural analyses of microscope observations and X-ray diffraction analyses. The implementation of the obtained composite joints for power module die-attach is evaluated by thermal aging and cycling tests. Moreover, the unique microstructure is precisely evaluated using FE analysis based on 3D image reconstruction to elucidate their macro- and micro-deformation properties.

In Chapter 6, this dissertation is concluded.

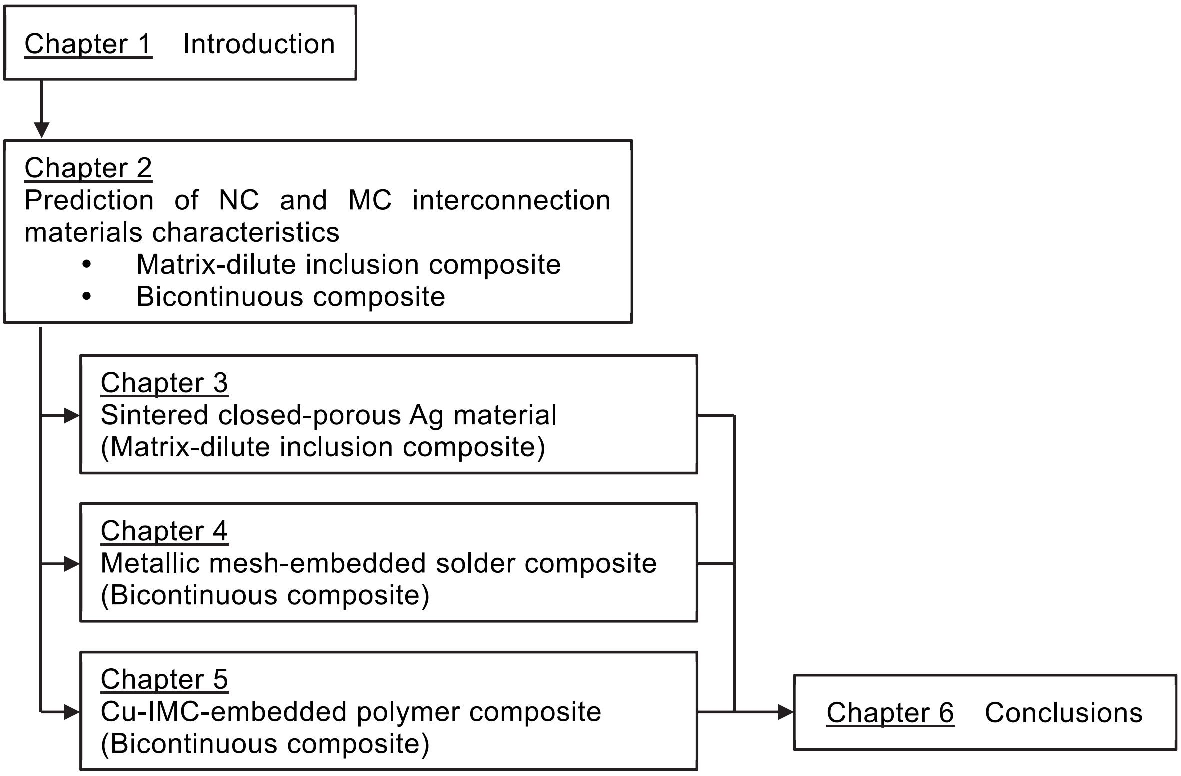

Fig. 1.11. Dissertation flow chart.

References in Chapter 1

[1] R. F. Gibson, “A review of recent research on mechanics of multifunctional composite materials and structures,” *Compos. Struct.*, vol. 92, no. 12, pp. 2793–2810, 2010.

[2] F. Barthelat, “Architectured materials in engineering and biology: Fabrication, structure, mechanics and performance,” *Int. Mater. Rev.*, vol. 60, no. 8, pp. 413–430, 2015.

[3] N. A. Fleck, V. S. Deshpande, and M. F. Ashby, “Micro-architectured materials: Past, present and future,” *Proc. R. Soc. A Math. Phys. Eng. Sci.*, vol. 466, no. 2121, pp. 2495–2516, 2010.

[4] V. Malgras *et al.*, “Templated synthesis for nanoarchitectured porous materials,” *Bull. Chem. Soc. Jpn.*, vol. 88, no. 9, pp. 1171–1200, 2015.

[5] A. Matallana *et al.*, “Power module electronics in HEV/EV applications: New trends in wide-bandgap semiconductor technologies and design aspects,” *Renew. Sustain. Energy Rev.*, vol. 113, pp. 109264–109296, 2019.

[6] M. Gourab and Y. Junji, “Latest Trend and Prospect of Power Module Technology,” *MITSUBISHI DEKI GIHO (in Japanese)*, vol. 92, no. 3, pp. 158–162, 2018.

[7] K. Ryu, M. Noboru, and W. Shunichi, “7th Generation Power Chip Technologies for Industrial Applications,” *MITSUBISHI DENKI GIHO (in Japanese)*, vol. 90, no. 5, pp. 287–290, 2016.

[8] N. Iwamuro, S. Member, and T. Laska, “IGBT History, State-of-the-Art, and Future Prospects,” *IEEE Trans. Electron Devices*, vol. 64, no. 3, pp. 741–752, 2017.

[9] F. J. Niedernostheide, H. J. Schulze, T. Laska, and A. Philippou, “Progress in IGBT development,” *IET Power Electron.*, vol. 11, no. 4, pp. 646–653, 2018.

[10] C. Chen, F. Luo, and Y. Kang, “A Review of SiC Power Module Packaging: Layout, Material System and Integration,” *CPSS Trans. Power Electron. Appl.*, vol. 2, no. 3, pp. 170–186, 2017.

[11] T. Kimoto, “Material science and device physics in SiC technology for high-voltage power devices,” *Japanese J. Appl. Physics*, vol. 54, p. 040103, 2015.

[12] R. Khazaka, L. Mendizabal, D. Henry, and R. Hanna, “Survey of high-temperature reliability of power electronics packaging components,” *IEEE Trans. Power Electron.*, vol. 30, no. 5, pp. 2456–2464, 2015.

[13] J. Fabre, P. Ladoux, and M. Piton, “Characterization and Implementation of Dual-SiC MOSFET Modules for Future Use in Traction Converters,” *IEEE Trans. Power Electron.*, vol. 30, no. 8, pp. 4079–4090, 2015.

[14] X. She, A. Q. Huang, O. Lucia, and B. Ozpineci, “Review of Silicon Carbide Power Devices and Their Applications,” *IEEE Trans. Ind. Electron.*, vol. 64, no. 10, pp. 8193–8205, 2017.

[15] A. Morozumi, Y. Nishimura, Y. Ikeda, E. Mochizuki, and Y. Takahashi, “Packaging Technology for High Temperature Operation of Power Semiconductor Modules,” *J. Japan Inst. Electron. Packag. (in Japanese)*, vol. 17, no. 6, pp. 464–468, 2014.

[16] K. Arai, “Packaging Technologies of Power Module,” in *The 28th Microelectronics Symposium (MES2018) (in Japanese)*, 2018, pp. 93–100.

[17] M. Tanaka, A. Hiruma, A. Umeda, S. Ohkijima, K. Tani, and A. Imura, “Electrification Technologies for Vehicle in DENSO,” *DENSO Tech. Rev.*, vol. 22, pp. 9–20, 2017.

[18] F. Hou *et al.*, “Review of Packaging Schemes for Power Module,” *IEEE J. Emerg. Sel. Top. Power Electron.*, 2019.

[19] B. Hu *et al.*, “Failure and Reliability Analysis of a SiC Power Module Based on Stress Comparison to a Si Device,” *IEEE Trans. Device Mater. Reliab.*, vol. 17, no. 4, pp. 727–737, 2017.

[20] A. Lis, S. Kicin, F. Brem, and C. Leinenbach, “Thermal Stress Assessment for Transient Liquid-Phase Bonded Si Chips in High-Power Modules Using Experimental and Numerical Methods,” *J. Electron. Mater.*, vol. 46, no. 2, pp. 729–741, 2017.

[21] C. Bohm, T. Hauck, A. Juritza, and W. H. Müller, “Weibull statistics of silicon die fracture,” in

6th Electronics Packaging Technology Conference (EPTC 2004), 2004, pp. 782–786.

[22] M. Usui, H. Tanaka, K. Hotta, S. Kuwano, and M. Ishiko, “Mechanical Stress Dependence of Power Device Electrical Characteristics,” *Trans. Inst. Electr. Eng. Japan (in Japanese)*, vol. 128, no. 5, pp. 577–583, 2008.

[23] The Japan Institute of Metals and Materials, *Kinzoku Data Book 2nd Edition (in Japanese)*. Maruzen Publishing Co.,Ltd., 1984.

[24] N. T. S. Lee, V. B. C. Tan, and K. M. Lim, “Structural and mechanical properties of Sn-based intermetallics from ab initio calculations,” *Appl. Phys. Lett.*, vol. 89, no. 14, pp. 4–7, 2006.

[25] G. R. Anstis, P. Chantikul, B. R. Lawn, and D. B. Marshall, “A Critical Evaluation of Indentation Techniques for Measuring Fracture Toughness: I, Direct Crack Measurements,” *J. Am. Ceram. Soc.*, vol. 64, no. 9, pp. 533–538, 1981.

[26] P. Chantikul, G. R. Anstis, B. R. Lawn, and D. B. Marshall, “A Critical Evaluation of Indentation Techniques for Measuring Fracture Toughness: II, Strength Method,” *J. Am. Ceram. Soc.*, vol. 64, no. 9, pp. 539–543, 1981.

[27] X. Deng, M. Koopman, N. Chawla, and K. K. Chawla, “Young’s modulus of (Cu, Ag)-Sn intermetallics measured by nanoindentation,” *Mater. Sci. Eng. A*, vol. 364, no. 1–2, pp. 240–243, 2004.

[28] I. Tsai, E. Wu, S. F. Yen, and T. H. Chuang, “Mechanical properties of intermetallic compounds on lead-free solder by moiré techniques,” *J. Electron. Mater.*, vol. 35, no. 5, pp. 1059–1066, 2006.

[29] G. Gosh, “Elastic properties, hardness, and indentation fracture toughness of intermetallics relevant to electronic packaging,” *J. Mater. Res.*, vol. 19, no. 5, pp. 1439–1454, 2004.

[30] S. Kumar and J. Jung, “Mechanical and electronic properties of Ag3Sn intermetallic compound in lead free solders using ab initio atomistic calculation,” *Mater. Sci. Eng. B Solid-State Mater. Adv. Technol.*, vol. 178, no. 1, pp. 10–21, 2013.

[31] L. Liu, Z. Chen, C. Liu, Y. Wu, and B. An, “Micro-mechanical and fracture characteristics of Cu6Sn5and Cu3Sn intermetallic compounds under micro-cantilever bending,” *Intermetallics*, vol. 76, pp. 10–17, 2016.

[32] Michael Bauccio, *ASM Engineered Materials Reference Book, Second Edition*. 1994.

[33] Y. Imai, “Structure-Property Relationship in Polyimide,” *J. Japan Inst. Electron. Packag. (in Japanese)*, vol. 4, no. 7, pp. 640–646, 2001.

[34] K. Suganuma, T. Sakai, and K. Kim, “Influce of Ag Addition to Sn-Bi Eutectic Alloy on Microstructure and on Mechanical Properties,” *J. Japan Inst. Electron. Packag. (in Japanese)*, vol. 6, no. 5, pp. 414–419, 2003.

[35] L. DU PONT-TORAY CO., “Polyimide film, Kapton,” 2007. .

[36] T. Yamamoto and K. Tsubone, “Assembly Technology Using Lead-free Solder,” *FUJITSU*, vol. 43, no. 1, pp. 50–58, 2007.

[37] M. Nishiura, “Mechanical and Thermal Fatigue Property of Sn Base Solder Alloys,” *J. Japan Inst. Electron. Packag. (in Japanese)*, vol. 3, no. 7, pp. 592–599, 2000.

[38] T. Zhou, T. Bobal, M. Oud, and J. Songliang, “Au/Sn Solder Alloy and Its Applications in Electronics Packaging,” *Intern. Rep. Coining, Inc.*, 1999.

[39] X. Deng, N. Chawla, K. K. Chawla, and M. Koopman, “Deformation behavior of (Cu, Ag)-Sn intermetallics by nanoindentation,” *Acta Mater.*, vol. 52, no. 14, pp. 4291–4303, 2004.

[40] Y. Yao, J. Fry, M. E. Fine, and L. M. Keer, “The Wiedemann-Franz-Lorenz relation for lead-free solder and intermetallic materials,” *Acta Mater.*, vol. 61, no. 5, pp. 1525–1536, 2013.

[41] Y. Ocak, S. Aksöz, N. Maraşli, and K. Keşlioğlu, “Experimental determination of thermal conductivity and solid-liquid interfacial energy of solid Ag3Sn intermetallic in the Sn-Ag-In ternary alloy,” *Intermetallics*, vol. 18, no. 11, pp. 2250–2258, 2010.

[42] N. Jiang, J. A. Clum, R. R. Chromik, and E. J. Cotts, “Thermal expansion of several Sn-based intermetallic compounds,” *Scr. Mater.*, vol. 37, no. 12, pp. 1851–1854, 1997.

[43] S. Bargmann *et al.*, “Generation of 3D representative volume elements for heterogeneous materials: A review,” *Prog. Mater. Sci.*, vol. 96, pp. 322–384, 2018.

[44] I. Shohji, T. Nakamura, F. Mori, and S. Fujiuchi, “Interface Reaction and Mechanical Properties of Lead-free Sn – Zn Alloy / Cu Joints,” *Packag. (Boston, Mass.)*, vol. 43, no. 8, pp. 1797–1801, 2002.

[45] A. Hirose, T. Fujii, T. Imamura, and F. K. Kobayashi, “Influence of Interfacial Reaction on Reliability of QFP Joints with Sn-Ag Based Pb Free Solders,” *Mater. Trans.*, vol. 42, no. 5, pp. 794–802, 2001.

[46] A. Morozumi, H. Hokazono, Y. Nishimura, E. Mochizuki, and Y. Takahashi, “Influence of Antimony on Reliability of Solder Joints Using Sn-Sb Binary Alloy for Power Semiconductor Modules,” *Trans. Japan Inst. Electron. Packag.*, vol. 8, no. 1, pp. 8–17, 2015.

[47] D. G. Ivey, “Microstructural characterization of Au/Sn solder for packaging in optoelectronic applications,” *Micron*, vol. 29, no. 4, pp. 281–287, 1998.

[48] B. S. Lee, C. W. Lee, and J. W. Yoon, “Comparative study of Au–Sn and Sn–Ag–Cu as die-attach materials for power electronics applications,” *Surf. Interface Anal.*, vol. 48, no. 7, pp. 493–497, 2016.

[49] F. Arabi, L. Theolier, D. Martineau, J. Y. Deletage, M. Medina, and E. Woirgard, “Power electronic assemblies: Thermo-mechanical degradations of gold-tin solder for attaching devices,” *Microelectron. Reliab.*, vol. 64, pp. 409–414, 2016.

[50] F. Lang, H. Yamaguchi, H. Ohashi, and H. Sato, "Improvement in joint reliability of SiC power devices by a diffusion barrier between Au-Ge solder and Cu/Ni(P)-metalized ceramic substrates," *J. Electron. Mater.*, vol. 40, no. 7, pp. 1563–1571, 2011.

[51] K. Suganuma and S. Kim, "Ultra heat-shock resistant die attachment for silicon carbide with pure zinc," *IEEE Electron Device Lett.*, vol. 31, no. 12, pp. 1467–1469, 2010.

[52] J. E. Lee, K. S. Kim, K. Suganuma, J. Takenaka, and K. Hagio, "Interfacial properties of Zn-Sn alloys as high temperature lead-free solder on Cu substrate," *Mater. Trans.*, vol. 46, no. 11, pp. 2413–2418, 2005.

[53] Y. Takaku, L. Felicia, I. Ohnuma, R. Kainuma, and K. Ishida, "Interfacial reaction between Cu substrates and Zn-Al base high-temperature Pb-free solders," *J. Electron. Mater.*, vol. 37, no. 3, pp. 314–323, 2008.

[54] Y. Takaku *et al.*, "Interfacial reaction between Zn-Al-based high-temperature solders and Ni substrate," *J. Electron. Mater.*, vol. 38, no. 1, pp. 54–60, 2009.

[55] T. Yamaguchi *et al.*, "Heat dissipative Pb-free bonding technology using Al-rich Zn/Al/Zn clad solder," *Weld. Int.*, vol. 31, no. 11, pp. 846–856, 2017.

[56] T. Yamaguchi *et al.*, "Effects of Bonding Conditions on Bondability Using Zn/Al/Zn Clad Solder," *J. Electron. Mater.*, vol. 44, no. 12, pp. 4769–4778, 2015.

[57] J. N. Lalena, N. F. Dean, and M. W. Weiser, "Experimental investigation of Ge-Doped Bi-11Ag as a new Pb-free solder alloy for power die attachment," *J. Electron. Mater.*, vol. 31, no. 11, pp. 1244–1249, 2002.

[58] J. M. Song, H. Y. Chuang, and Z. M. Wu, "Interfacial reactions between Bi-Ag high-temperature solders and metallic substrates," *J. Electron. Mater.*, vol. 35, no. 5, pp. 1041–1049, 2006.

[59] T. Iseki and M. Takamori, "Development of Bi-Based Pb-Free Solders for High-Temperature," *J. Japan Inst. Electron. Packag. (in Japanese)*, vol. 15, no. 2, pp. 153–157, 2012.

[60] J. Y. Wang, C. M. Chen, and Y. W. Yen, "Interfacial reactions of high-Bi alloys on various substrates," *J. Electron. Mater.*, vol. 43, no. 1, pp. 155–165, 2014.

[61] C. C. Lee and Y. C. Chen, "High temperature tin-copper joints produced at low process temperature for stress reduction," *Thin Solid Films*, vol. 286, no. 1–2, pp. 213–218, 1996.

[62] N. S. Bosco and F. W. Zok, "Critical interlayer thickness for transient liquid phase bonding in the Cu-Sn system," *Acta Mater.*, vol. 52, no. 10, pp. 2965–2972, 2004.

[63] N. S. Bosco and F. W. Zok, "Strength of joints produced by transient liquid phase bonding in the Cu-Sn system," *Acta Mater.*, vol. 53, no. 7, pp. 2019–2027, 2005.

[64] K. Guth *et al.*, "New assembly and interconnect technologies for power modules," in *Integrated Power Electronics Systems (CIPS) 2012 7th InternationalConference*, 2012, vol. 9, pp. 3–7.

[65] K. Guth, N. Heuck, C. Stahlhut, A. Ciliox, N. Oeschler, and I. T. Ag, “End-of-life investigation on the . XT interconnect technology,” in *PCIM Europe 2015*, 2015, pp. 72–79.

[66] S. Fukumoto, M. Matsushima, K. Fujimoto, and A. Tanaka, “Improvement of bondability of copper using multilayer film at low temperature,” in *Annual Meeting of Japan Welding Society (in Japanese)*, 2010.

[67] S. E. Jeong, S. B. Jung, and J. W. Yoon, “Fast formation of Cu-Sn intermetallic joints using pre-annealed Sn/Cu/Sn composite preform for high-temperature bonding applications,” *Thin Solid Films*, vol. 698, no. February, p. 137873, 2020.

[68] A. A. Bajwa, Y. Y. Qin, R. Zeiser, and J. Wilde, “Foil Based Transient Liquid Phase Bonding as a Die-Attachment Method for High Temperature Devices,” in *Proc. 8th International Conferecne on Integrated Power Electronics Systems (CIPS)*, 2014, pp. 25–27.

[69] I. Silver, M. Composites, Y. Chen, W. W. So, C. C. Lee, and S. Member, “A Fluxless Bonding Technology Using,” *IEEE Trans. Components, Packag. Manuf. Technol.*, vol. 20, no. 1, pp. 46–51, 1997.

[70] H. A. Mustain, W. D. Brown, and S. S. Ang, “Transient liquid phase die attach for high-temperature silicon carbide power devices,” *IEEE Trans. Components Packag. Technol.*, vol. 33, no. 3, pp. 563–570, 2010.

[71] S. W. Yoon, M. D. Glover, and K. Shiozaki, “Nickel-tin transient liquid phase bonding toward high-temperature operational power electronics in electrified vehicles,” *IEEE Trans. Power Electron.*, vol. 28, no. 5, pp. 2448–2456, 2013.

[72] F. Guo, J. Lee, S. Choi, J. P. P. Lucas, T. R. R. Bieler, and K. N. N. Subramanian, “Processing and aging characteristics of eutectic Sn-3.5Ag solder reinforced with mechanically incorporated Ni particles,” *J. Electron. Mater.*, vol. 30, no. 9, pp. 1073–1082, 2001.

[73] F. Guo, J. P. Lucas, and K. N. Subramanian, “Creep behavior in Cu and Ag particle-reinforced composite and eutectic Sn-3.5Ag and Sn-4.0Ag-0.5Cu non-composite solder joints,” *J. Mater. Sci. Mater. Electron.*, vol. 12, no. 1, pp. 27–35, 2001.

[74] Z. X. Li and M. Gupta, “High strength lead-free composite solder materials using Nano-Al2O3 as reinforcement,” *Adv. Eng. Mater.*, vol. 7, no. 11, pp. 1049–1054, 2005.

[75] L. C. Tsao, S. Y. Chang, C. I. Lee, W. H. Sun, and C. H. Huang, “Effects of nano-Al2O3 additions on microstructure development and hardness of Sn3.5Ag0.5Cu solder,” *Mater. Des.*, vol. 31, no. 10, pp. 4831–4835, 2010.

[76] T. H. Chuang, M. W. Wu, S. Y. Chang, S. F. Ping, and L. C. Tsao, “Strengthening mechanism of nano-Al 2O 3 particles reinforced Sn3.5Ag0.5Cu lead-free solder,” *J. Mater. Sci. Mater. Electron.*, vol. 22, no. 8, pp. 1021–1027, 2011.

[77] Y. Shi *et al.*, “Creep properties of composite solders reinforced with nano- and microsized particles,” *J. Electron. Mater.*, vol. 37, no. 4, pp. 507–514, 2008.

[78] Y. Tang, G. Y. Li, and Y. C. Pan, “Effects of TiO2 nanoparticles addition on microstructure, microhardness and tensile properties of Sn-3.0Ag-0.5Cu-xTiO2 composite solder,” *Mater. Des.*, vol. 55, pp. 574–582, 2014.

[79] Y. Wen *et al.*, “Reliability enhancement of Sn-1.0Ag-0.5Cu nano-composite solders by adding multiple sizes of TiO2nanoparticles,” *J. Alloys Compd.*, vol. 696, pp. 799–807, 2017.

[80] X. Zhao, Y. Wen, Y. Li, Y. Liu, and Y. Wang, “Effect of γ-Fe2O3 nanoparticles size on the properties of Sn-1.0Ag-0.5Cu nano-composite solders and joints,” *J. Alloys Compd.*, vol. 662, pp. 272–282, 2016.

[81] A. A. El-Daly, W. M. Desoky, T. A. Elmosalami, M. G. El-Shaarawy, and A. M. Abdraboh, “Microstructural modifications and properties of SiC nanoparticles-reinforced Sn-3.0Ag-0.5Cu solder alloy,” *Mater. Des.*, vol. 65, pp. 1196–1204, 2015.

[82] H. Greve, L. Y. Chen, I. Fox, and F. P. McCluskey, “Transient liquid phase sintered attach for power electronics,” in *2013 IEEE 63rd Electronic Components and Technology Conference (ECTC)*, 2013, pp. 435–440.

[83] H. Greve and P. Mccluskey, “Reliability of Sn based LT-TLPS Joints for High Temperature Electronic Systems,” in *CIPS 2014*, 2014.

[84] X. Liu, S. He, and H. Nishikawa, “Thermally stable Cu<inf>3</inf>Sn/Cu composite joint for high-temperature power device,” *Scr. Mater.*, vol. 110, pp. 101–104, 2016.

[85] X. Liu, S. Zhou, and H. Nishikawa, “Thermal stability of low-temperature sintered joint using Sn-coated Cu particles during isothermal aging at 250 °C,” *J. Mater. Sci. Mater. Electron.*, vol. 28, no. 17, pp. 12606–12616, 2017.

[86] X. Liu, S. He, and H. Nishikawa, “Low temperature solid-state bonding using Sn-coated Cu particles for high temperature die attach,” *J. Alloys Compd.*, vol. 695, pp. 2165–2172, 2017.

[87] T. Hu, H. Chen, M. Li, and Z. Zhao, “Cu@Sn Core – Shell Structure Powder Preform for High-Temperature Applications Based on Transient Liquid Phase Bonding,” *IEEE Trans. Power Electron.*, vol. 32, no. 1, pp. 441–451, 2016.

[88] H. Shao, A. Wu, Y. Bao, Y. Zhao, G. Zou, and L. Liu, “Novel transient liquid phase bonding through capillary action for high-temperature power devices packaging,” *Mater. Sci. Eng. A*, vol. 724, no. March, pp. 231–238, 2018.

[89] Z. Z. Zhang and G. Q. Lu, “Pressure-assisted low-temperature sintering of silver paste as an alternative die-attach solution to solder reflow,” *IEEE Trans. Electron. Packag. Manuf.*, vol. 25, no. 4, pp. 279–283, 2002.

[90] A. Hirose, E. Ide, and K. F. Kobayashi, “A Novel Bonding Process Using Nanoparticles,” *J. Japan Inst. Electron. Packag. (in Japanese)*, vol. 7, no. 6, pp. 511–515, 2004.

[91] H. Zheng, D. Berry, K. D. T. Ngo, and G. Q. Lu, “Chip-bonding on copper by pressureless sintering of nanosilver paste under controlled atmosphere,” *IEEE Trans. Components, Packag. Manuf. Technol.*, vol. 4, no. 3, pp. 377–384, 2014.

[92] E. Ide, S. Angata, A. Hirose, and K. F. Kobayashi, “Metal-metal bonding process using Ag metallo-organic nanoparticles,” *Acta Mater.*, vol. 53, no. 8, pp. 2385–2393, 2005.

[93] K.-S. Moon *et al.*, “Thermal behavior of silver nanoparticles for low-temperature interconnect applications,” *J. Electron. Mater.*, vol. 34, no. 2, pp. 168–175, 2005.

[94] J. G. Bai, J. Yin, Z. Zhang, G. Q. Lu, and J. D. van Wyk, “High-temperature operation of SiC power devices by low-temperature sintered silver die-attachment,” *IEEE Trans. Adv. Packag.*, vol. 30, no. 3, pp. 506–510, 2007.

[95] J. G. Bai, J. N. Calata, G. Lei, and G. Q. Lu, “Thermomechanical reliability of low-temperature sintered silver die-attachment,” *Thermomechanical Phenom. Electron. Syst. -Proceedings Intersoc. Conf.*, vol. 2006, no. 3, pp. 1126–1130, 2006.

[96] Y. Akada, H. Tatsumi, T. Yamaguchi, A. Hirose, T. Morita, and E. Ide, “Interfacial Bonding Mechanism Using Silver Metallo-Organic Nanoparticles to Bulk Metals and Observation of Sintering Behavior,” *Mater. Trans.*, vol. 49, no. 7, pp. 1537–1545, 2008.

[97] T. Ogura, M. Nishimura, H. Tatsumi, W. Takahara, and A. Hirose, “Interfacial Bonding Behavior between Silver Nanoparticles and Gold Substrate Using Molecular Dynamics Simulation,” *Mater. Trans.*, vol. 53, no. 12, pp. 2085–2090, 2012.

[98] J. G. Bai, Z. Z. Zhang, J. N. Calata, and G. Q. Lu, “Low-temperature sintered nanoscale silver as a novel semiconductor device-metallized substrate interconnect material,” *IEEE Trans. Components Packag. Technol.*, vol. 29, no. 3, pp. 589–593, 2006.

[99] H. Alarifi, A. Hu, M. Yavuz, and Y. N. Zhou, “Silver nanoparticle paste for low-temperature bonding of copper,” *J. Electron. Mater.*, vol. 40, no. 6, pp. 1394–1402, 2011.

[100] J. Kähler, N. Heuck, A. Wagner, A. Stranz, E. Peiner, and A. Waag, “Sintering of copper particles for die attach,” *IEEE Trans. Components, Packag. Manuf. Technol.*, vol. 2, no. 10, pp. 1587–1591, 2012.

[101] J.-W. Yoon and J.-H. Back, “Effect of Sintering Conditions on the Mechanical Strength of Cu-Sintered Joints for High-Power Applications,” *Materials (Basel).*, vol. 11, no. 11, p. 2105, 2018.

[102] R. Gao, S. He, Y. A. Shen, and H. Nishikawa, “Effect of Substrates on Fracture Mechanism and Process Optimization of Oxidation–Reduction Bonding with Copper Microparticles,” *J. Electron. Mater.*, vol. 48, no. 4, pp. 2263–2271, 2019.

[103] A. Hirose *et al.*, “A novel metal-to-metal bonding process through in-situ formation of Ag nanoparticles using Ag2O microparticles,” *J. Phys. Conf. Ser.*, vol. 165, 2009.

[104] T. Morita and Y. Yasuda, “New bonding technique using copper oxide materials,” *Mater. Trans.*, vol. 56, no. 6, pp. 878–882, 2015.

[105] H. Tatsumi, Y. Akada, T. Yamaguchi, and A. Hirose, “Sintering Mechanism of Composite Ag Nanoparticles and its Application to Bonding Process-Effects of Ag2CO3 Contents on Bondability to Cu,” *Adv. Mater. Process.*, vol. 26–28, pp. 499–502, 2007.

[106] Y. Yasuda, E. Ide, and T. Morita, “Evaluation of Copper Oxide-Based Interconnecting Materials,” *Open Surf. Sci. J.*, vol. 3, no. 1, pp. 123–130, 2010.

[107] H. Jiang, K. S. Moon, J. Lu, and C. P. Wong, “Conductivity enhancement of nano silver-filled conductive adhesives by particle surface functionalization,” *J. Electron. Mater.*, vol. 34, no. 11, pp. 1432–1439, 2005.

[108] R. Zhang, W. Lin, K. S. Moon, and C. P. Wong, “Fast preparation of printable highly conductive polymer nanocomposites by thermal decomposition of silver carboxylate and sintering of silver nanoparticles,” *ACS Appl. Mater. Interfaces*, vol. 2, no. 9, pp. 2637–2645, 2010.

[109] B. Meschi Amoli, J. Trinidad, A. Hu, Y. N. Zhou, and B. Zhao, “Highly electrically conductive adhesives using silver nanoparticle (Ag NP)-decorated graphene: the effect of NPs sintering on the electrical conductivity improvement,” *J. Mater. Sci. Mater. Electron.*, vol. 26, no. 1, pp. 590–600, 2014.

[110] F. Yu, R. W. Johnson, and M. C. Hamilton, “Pressureless Sintering of Microscale Silver Paste for 300 °C Applications,” *IEEE Trans. Components, Packag. Manuf. Technol.*, vol. 5, no. 9, pp. 1258–1264, 2015.

[111] Y. Kariya, H. Yamaguchi, M. Itako, N. Mizumura, and K. Sasaki, “Mechanical Behavior of Sintered Nano-sized Ag Particles,” *J. Smart Process.*, vol. 2, no. 4, pp. 161–165, 2013.

[112] S. Zabihzadeh, S. Van Petegem, M. Holler, A. Diaz, L. I. Duarte, and H. Van Swygenhoven, “Deformation behavior of nanoporous polycrystalline silver. Part I: Microstructure and mechanical properties,” *Acta Mater.*, vol. 131, pp. 467–474, 2017.

[113] S. Zabihzadeh, J. Cugnoni, L. I. Duarte, S. Van Petegem, and H. Van Swygenhoven, “Deformation behavior of nano-porous polycrystalline silver. Part II: Simulations,” *Acta Mater.*, vol. 131, pp. 564–573, 2017.

[114] T. Suzuki *et al.*, “Effect of manufacturing process on micro-deformation behavior of sintered-silver die-attach material,” *IEEE Trans. Device Mater. Reliab.*, vol. 16, no. 4, pp. 588–596, 2016.

[115] T. Suzuki, Y. Yasuda, T. Terasaki, T. Morita, and Y. Kawana, “Macro- and Micro-Deformation Behavior of Sintered-Copper Die-Attach Material,” *IEEE Trans. DEVICE Mater. Reliab.*, vol.

18, no. 1, pp. 54–63, 2018.

[116] M. S. Kim and H. Nishikawa, "Silver nanoporous sheet for solid-state die attach in power device packaging," *Scr. Mater.*, vol. 92, pp. 43–46, 2014.

[117] M. S. Kim and H. Nishikawa, "Effects of bonding temperature on microstructure, fracture behavior and joint strength of Ag nanoporous bonding for high temperature die attach," *Mater. Sci. Eng. A*, vol. 645, pp. 264–272, 2015.

[118] M. S. Kim, K. Matsunaga, Y. H. Ko, C. W. Lee, and H. Nishikawa, "Reliability of Ag nanoporous bonding joint for high temperature die attach under temperature cycling," *Mater. Trans.*, vol. 57, no. 7, pp. 1192–1196, 2016.

[119] W. Fu *et al.*, "Low Temperature Flip Chip Bonding Using Squeegee-Embedded Au Nanoporous Bump Activated by VUV/O3 Treatment," *J. Electron. Mater.*, vol. 47, no. 10, pp. 5952–5958, 2018.

[120] S. Koga, H. Nishikawa, M. Saito, and J. Mizuno, "Fabrication of Nanoporous Cu Sheet and Application to Bonding for High-Temperature Applications," *J. Electron. Mater.*, vol. 49, no. 3, pp. 2151–2158, 2020.

[121] M. Knoerr and A. Schletz, "Power semiconductor joining through sintering of silver nanoparticles: Evaluation of influence of parameters time, temperature and pressure on density, strength and reliability," *Proc. 6th Int. Conf. Integr. Power Electron. Syst.*, pp. 1–6, 2010.

[122] W. D. MacDonald and T. W. Eagar, "Transient liquid phase bonding," *Annu. Rev. Mater. Sci.*, vol. 22, pp. 23–46, 1992.

[123] H. Feng, J. Huang, J. Yang, S. Zhou, R. Zhang, and S. Chen, "A Transient Liquid Phase Sintering Bonding Process Using Nickel-Tin Mixed Powder for the New Generation of High-Temperature Power Devices," *J. Electron. Mater.*, vol. 46, no. 7, pp. 4152–4159, 2017.

[124] R. Kubo, "Electronic properties of small metallic particles," *Phys. Lett.*, vol. 1, no. 2, pp. 49–50, 1962.

[125] M. Takagi, "Electron-Diffraction Study of Liquid-Solid Transition of Thin Metal Films," *J. Phys. Soc. Japan*, vol. 9, no. 3, pp. 359–363, 1954.

[126] J. R. Groza and R. J. Dowding, "Nanoparticulate Materials Densification," *Nanostructured Mater.*, vol. 7, no. 7, pp. 749–768, 1996.

[127] J. Carr, X. Milhet, P. Gadaud, S. A. E. Boyer, G. E. Thompson, and P. Lee, "Quantitative characterization of porosity and determination of elastic modulus for sintered micro-silver joints," *J. Mater. Process. Technol.*, vol. 225, pp. 19–23, 2015.

[128] H. Zhang *et al.*, "Microstructural and mechanical evolution of silver sintering die attach for SiC power devices during high temperature applications," *J. Alloys Compd.*, vol. 774, pp. 487–494,

2019.

[129] U. Scheuermann, “Reliability challenges of automotive power electronics,” *Microelectron. Reliab.*, vol. 49, no. 9–11, pp. 1319–1325, 2009.

[130] C. Gobl and J. Faltenbacher, “Low temperature sinter technology die attachment for power electronic applications,” in *2010 6th International Conference on Integrated Power Electronics Systems*, 2010, pp. 1–5.

[131] A. Large-area, T. G. Lei, J. N. Calata, G. Lu, X. Chen, and S. Luo, “Low-Temperature Sintering of Nanoscale Silver Paste for Attaching Large-Area (>100mm2) Chips,” *IEEE Trans. COMPONENTS Packag. Technol.*, vol. 33, no. 1, pp. 98–104, 2010.

[132] T. Herboth, C. Frilh, M. Gunther, J. Wilde, and R. B. Gmbh, “Assessment of Thermo-Mechanical Stresses in Low Temperature Joining Technology,” in *2012 13th International Conference on Thermal, Mechanical and Multi-Physics Simulation and Experiments in Microelectronics and Microsystems, EuroSimE 2012*, 2012, pp. 1–7.

[133] T. Herboth, M. Guenther, A. Fix, and J. Wilde, “Failure mechanisms of sintered silver interconnections for power electronic applications,” in *2013 IEEE 63rd Electronic Components and Technology Conference (ECTC)*, 2013, pp. 1621–1627.

[134] F. Yu *et al.*, “Reliability of Ag Sintering for Power Semiconductor Die Attach in High-Temperature Applications,” *IEEE Trans. Power Electron.*, vol. 32, no. 9, pp. 7083–7095, 2017.

[135] X. F. Zhang, G. Harley, and L. C. De Jonghe, “Co-continuous metal-ceramic nanocomposites,” *Nano Lett.*, vol. 5, no. 6, pp. 1035–1037, 2005.

[136] L. Wang, J. Lau, E. L. Thomas, and M. C. Boyce, “Co-continuous composite materials for stiffness, strength, and energy dissipation,” *Adv. Mater.*, vol. 23, no. 13, pp. 1524–1529, 2011.

Chapter 2. Prediction of NC and MC interconnection materials characteristics

2.1. Introduction

Researchers have been considering how to describe complicated microscopic behaviors of composite materials, especially deformation behavior, as a simple homogenized model from a macroscopic view. There are various analytical or computational methods for composite material approximation, which is known as homogenization. In the homogenization concept, the complicated composite material microstructure is regarded as the one composed of a repeating unit cell or RVE. The microstructure is approximated as periodic.

Several analytical methods are proposed to predict composite material properties. The simplest classical method is the Rule of Mixtures, which enables prediction of a characteristic from the volume fraction of constituents in a composite. Parallel model (Voigt model) and series model (Reuss model), which are the simplest models, are described as follows:

$$E^{*n} = V_1 {E_1}^n + (1 - V_1) {E_2}^n, \tag{2.1}$$

where E_1, E_2, and E^* are the properties, e.g., Young's modulus of constituents 1 and 2, and the composite, respectively. V_1 is a volume fraction of the first constituent. n is determined with $n = 1$ in the Voigt model or $n = -1$ in the Reuss model. When considering the Young's modulus, it is well known that the values calculated by Voigt and Reuss models are the upper and lower bound of the equivalent value, respectively. The Rule of Mixtures also predicts density, tensile strength, thermal conductivity, or electrical conductivity. This simple approximation is further improved by considering certain idealized assumptions on the microstructure of the composites, such as inclusion shape, distribution, orientation. Moreover, the Hashin-Shtrikman model [1] was also proposed as a modified technique for these methods. Although these methods can roughly predict the effective properties of complicated microstructures, they usually simplify the microstructures and thus do not reflect the actual structures in detail.

A theoretical approach is proposed on micromechanics theories based on Eshelby's average strain estimation for a structure composed of an ellipsoidal inclusion embedded in an infinite medium [2]. The Eshelby's method is available when interactions among inclusions are negligible. Further, the Mori-Tanaka mean-field [3] and self-consistent methods [4] are also well known as micromechanics. Although these methods can predict the effective properties of composite microstructures based on the theoretical understanding, they are usually limited to certain structures and thus are not versatile for wide varieties of actual structures.

A more direct approach is based on computational simulations of microstructures with idealized geometries or actual microstructures obtained by 3D observations. For the computational simulations of the idealized models, various RVE generation methods are proposed by using simple space-filling geometries, such as hexahedral, truncated rhombic dodecahedral, rhombo hexagonal dodecahedral, and cube-and-spheres [5]. These geometries can be created by common computer-aided design (CAD) software. For example, sintered closed- or open-porous materials for electronics interconnections are evaluated by the FE simulations of the models obtained by the idealized computational modeling [6], 3D image-based reconstruction methods [7]–[11], and computer 3D tomography [12], [13]. These computational approaches can be a powerful tool to predict the mechanical and thermal conductive properties of NC and MC interconnections.

In this chapter, FE simulations of a simplified RVE model were carried out to predict the NC and MC interconnection materials characteristics. The impacts of morphology and material properties on equivalent characteristics are thoroughly discussed. Furthermore, the obtained results are verified by comparing previous researches. Based on this prediction method, unique promising NC and MC candidates are proposed.

2.2. FE method for RVEs of composites

2.2.1. FE model

Mechanical and thermal FE simulations of RVEs of matrix-dilute inclusion and bicontinuous composites, as described in Section 1.3, Chapter 1, were performed using Ansys Workbench 18.2. A cubic 3D FE model was set up using 3 × 3 × 3 repeating RVEs, as shown in Fig. 2.1 (a). Fig. 2.1 (b) shows the RVE dimensions, which is composed of three regions: Truncated rhombic dodecahedron with all equal-length sides (Region A), square prism facing to the square-face of Region A (Region B), and a body filling the other RVE space. An RVE has a dimension of the RVE side length, a, and the distance between the square faces of the truncated rhombic dodecahedron, d. The d/a is used for an RVE shape parameter to change the volume fraction V_f of each region in the FE models. Based on this model, the matrix-dilute inclusion and bicontinuous composites are represented by choosing either matrix or inclusion (pore) for each region, as shown in Table 2.1. In the matrix-dilute inclusion composites category, matrix-particle composites are presented by the model consisting of the Region A of inclusions, and the Regions B and C of the matrix. Closed-porous materials are presented by the model consisting of the Region A of pores, and the Regions B and C of the matrix. In the bicontinuous composites category, matrix-skeleton composites are presented by the model consisting of Regions A and B of inclusions, and the Region C of the matrix. Open-porous materials are presented by the model consisting of the Regions A and B of pores, and the Region C of the matrix. By using this modeling method, various NC and MC materials are formed by using this simple common model.

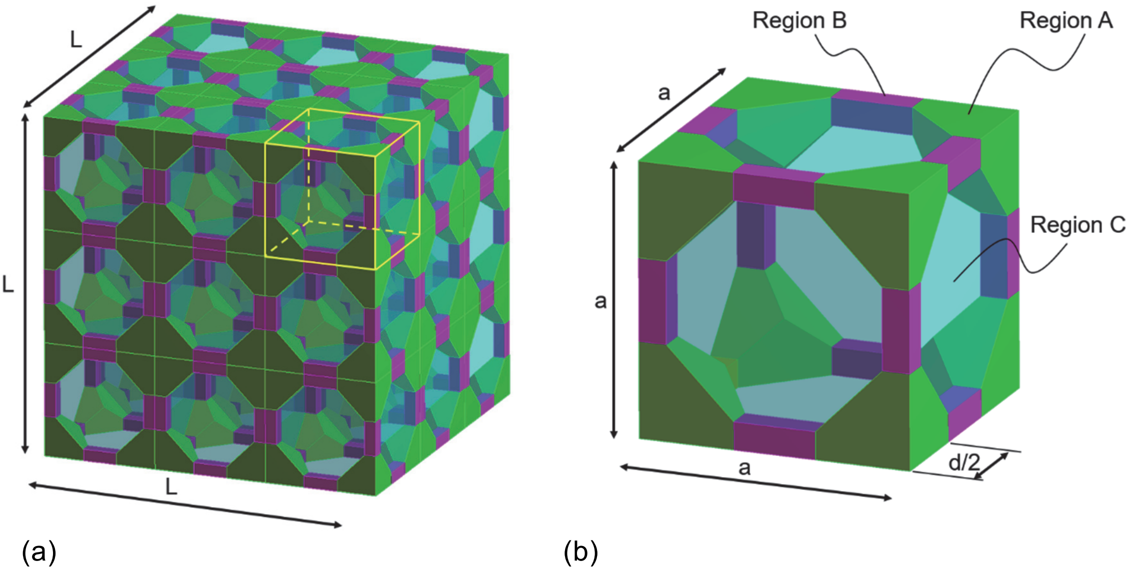

Fig. 2.1. (a) FE model using 3 × 3 × 3 repeating RVEs, and (b) a constituent RVE, which is composed of three regions: Region A; truncated rhombic dodecahedron with all equal-length sides, Region B; square prism facing to the square-face of Region A, and Region C; region filling the remaining RVE space. An RVE has a dimension of the side length of an RVE, *a,* and the distance between the square faces of a Region A, *d*. The *d*/*a* is varied as an RVE shape parameter.

Table 2.1. FE models of matrix-dilute inclusion and bicontinuous composites

Category	Subcategory	Constituents			Model
		Region A	Region B	Region C	example
Matrix-dilute inclusion composites	Matrix-particle composites	Inclusion	Matrix	Matrix	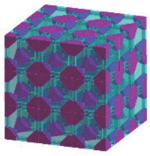
	Closed-porous materials	Pore	Matrix	Matrix	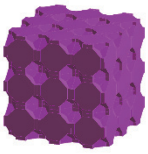
Bicontinuous composites	Matrix-skeleton composites	Inclusion	Inclusion	Matrix	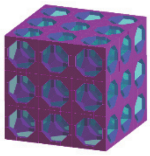
	Open-porous materials	Pore	Pore	Matrix	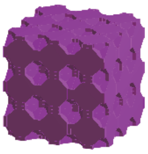

2.2.2. Mechanical FE simulations

The equivalent Young's modulus of the composites is calculated by mechanical FE simulations. The Young's modulus of the matrix and inclusions are E_m and E_i, respectively. The Poisson's ratio of all materials are 0.33. Volume fraction of the particles, skeleton, or pores, V_f, are varied by changing the d/a of the model. In the closed- or open-porous materials, the Young's modulus of the pore-region is zero. The 1/8 model was used for FE analysis considering the symmetry conditions. Ideal contact was assumed between all the interfaces. An external displacement, u, along the x-axis, equivalent to the macroscopic strain of 0.1%, was applied to the yz-surface of the FE model, as shown in Fig. 2.2. The equivalent Young's modulus E^* was calculated from the displacement u and the averaged reaction force F on the surface subjected to external displacement, using the following equations:

$$\sigma = \frac{F}{A} = E^* \cdot \varepsilon = E^* \cdot \frac{u}{L}, \tag{2.2}$$

where σ is tensile stress. A (= L^2) is the cross-sectional area. L is the size of the cubic model. Therefore,

$$E^* = \frac{F}{u \cdot L}. \tag{2.3}$$

Normalized equivalent Young's modulus, E^*/E_m, are used to discuss the impacts of the geometries and the constituent properties on the composite properties. The ratio between Young's modulus of the matrix and inclusions, $E_\mathrm{i}/E_\mathrm{m}$, is used as a matrix-inclusion properties parameter.

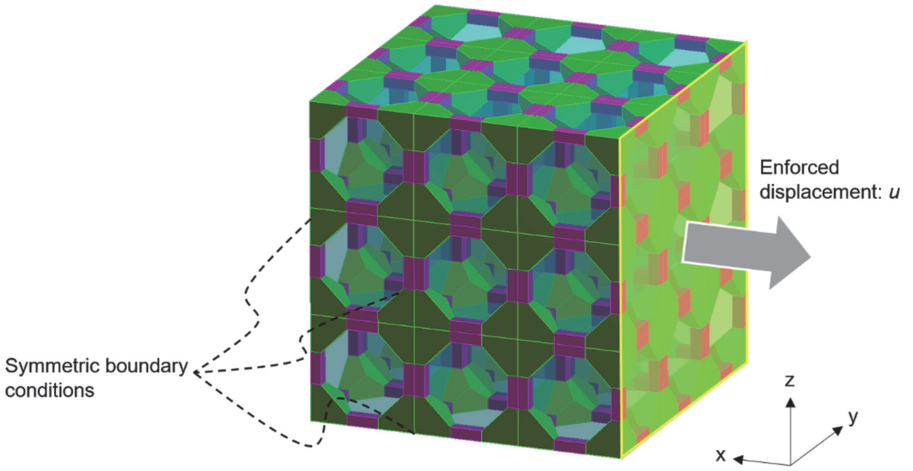

Fig. 2.2. Conditions of mechanical FE simulation.

2.2.3. Thermal FE simulations

Equivalent thermal conductivity of the composites is calculated by steady-state thermal FE simulations. The thermal conductivity of the matrix and inclusions are λ_m and λ_i, respectively. The volume fraction of the particles, skeleton, or pores, V_f, are varied by changing the d/a of the model, the same as the mechanical FE simulations. In the closed- or open-porous materials, the thermal conductivity of the pore-region is zero. Ideal contact was assumed between all the interfaces. Schematic conditions of thermal FE simulations are shown in Fig. 2.3. A constant heat flow Q flows into a base block at one yz-surface, and flows out the other base block at the other yz-surface, along the x-axis. A homogeneous constant temperature T_0 is set on the base block at the yz-surface, where the heat flow Q flows out. An average temperature T as an output parameter is obtained on the other base block at the other yz-surface, where Q flows in. All other surfaces are set in symmetric boundary conditions. The equivalent thermal conductivity λ^* was calculated from the heat flow Q and the average temperature T, using the following equations:

$$q \cdot \left(\frac{L}{\lambda^*} + \frac{L_{base}}{\lambda_{base}}\right) = \frac{Q}{A} \cdot \left(\frac{L}{\lambda^*} + \frac{L_{base}}{\lambda_{base}}\right) = \Delta T, \tag{2.4}$$

where q is heat flux, A (= L^2) is the heat transfer area, L is the heat transfer distance within the RVE,

L_{base} is the heat transfer distance within the base, λ_{base} is the thermal conductivity of the base, and ΔT is the temperature difference between input- and output-surfaces (T - T_0). Therefore,

$$\lambda^* = \frac{Q \cdot L \cdot \lambda_{base}}{L^2 \cdot \lambda_{base} \cdot (T - T_0) - Q \cdot L_{base}}. \tag{2.5}$$

Normalized equivalent thermal conductivity, $\lambda^*/\lambda_{\mathrm{m}}$, is used to discuss the impacts of the geometries and the constituent properties on the composite properties. The ratio between thermal conductivity of the matrix and inclusions, $\lambda_{\mathrm{i}}/\lambda_{\mathrm{m}}$, is used as a matrix-inclusion properties parameter.

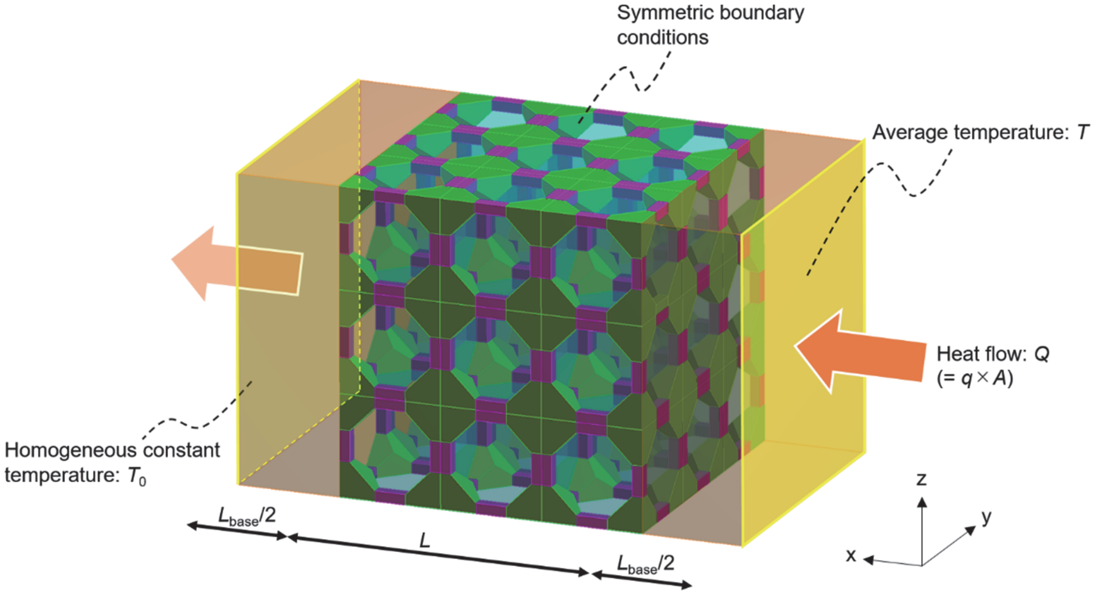

Fig. 2.3. Conditions of steady-state thermal FE simulation.

2.3. Results of FE analysis for RVEs of composites

2.3.1. Mechanical properties of composite materials

Figs. 2.4 and 2.5 show FE model examples of matrix-dilute inclusion and bicontinuous composites, respectively. In the RVE model used in this study, the volume fraction of inclusions V_{f} is geometrically decided to be lower than 50% in these models. The Young's modulus of the inclusions can be chosen to be higher or lower than that of the matrix, intending reinforcement or stiffness-reduction, respectively. Furthermore, the Young's modulus of the pores is assumed to be zero.

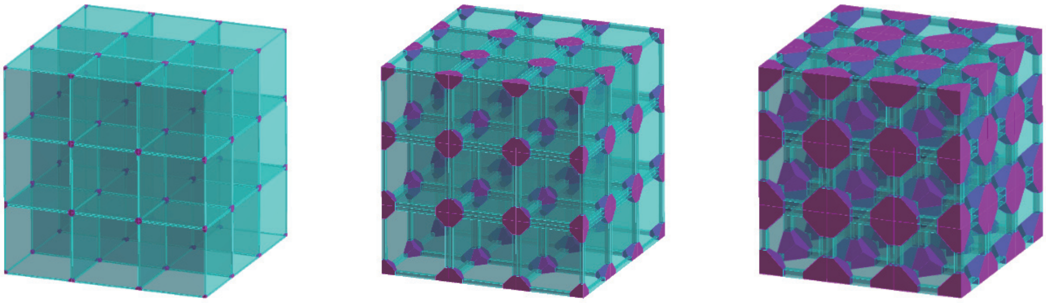

(a) V_f = 0.1%, d/a = 0.10 (b) V_f = 3.3%, d/a = 0.40 (c) V_f = 17.6%, d/a = 0.70

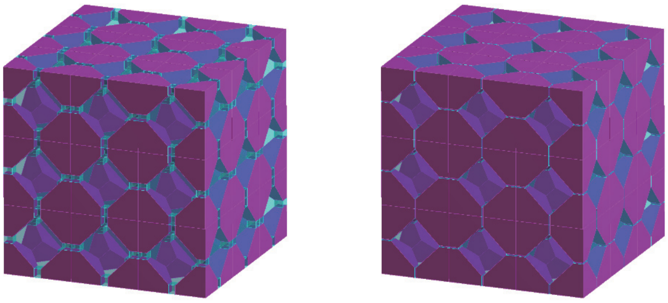

(d) V_f = 37.3%, d/a = 0.90 (e) V_f = 48.2%, d/a = 0.98

Fig. 2.4. Examples of the matrix-dilute inclusion model RVEs with a volume fraction of the inclusions of (a) 0.1, (b) 3.3, (c) 17.6, (d) 37.3, and (e) 48.2%, respectively, where the light-blue region shows matrix, and the pink region shows inclusions.

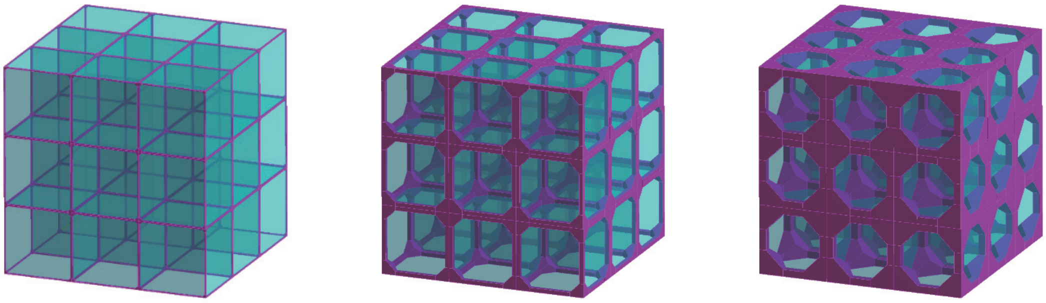

(a) V_f = 0.3%, d/a = 0.10 (b) V_f = 5.7%, d/a = 0.40 (c) V_f = 21.3%, d/a = 0.70

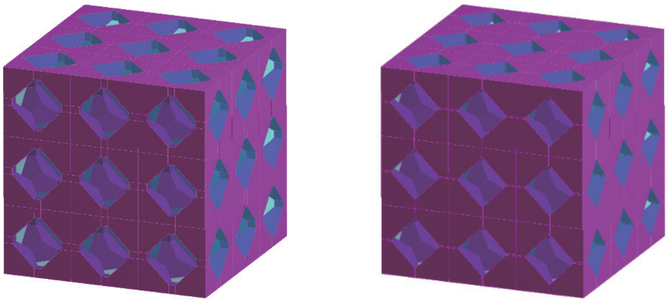

(d) V_f = 39.4%, d/a = 0.90 (e) V_f = 48.7%, d/a = 0.98

Fig. 2.5. Examples of the bicontinuous model RVEs with a volume fraction of the inclusions of (a) 0.3, (b) 5.7, (c) 21.3, (d) 39.4, and (e) 48.7%, respectively, where the light-blue region shows matrix, and the pink region shows inclusions.

The normalized equivalent Young's modulus E^*/E_m for the matrix-dilute inclusion model and the bicontinuous model with varying stiffness ratio E_i/E_m is shown in Figs. 2.6 (a) and (b), respectively. The E_i/E_m is set from 1×10^{-2} to 1×10^{2} including zero. When the E_i/E_m was greater than one, the E^*/E_m of the bicontinuous model was larger than that of the matrix-dilute inclusion model. Moreover, the E^*/E_m difference of both models was larger when the E_i/E_m was larger. Based on these results, it was suggested that the morphology significantly affects the equivalent modulus if the Young's modulus of the inclusions is more than two orders of magnitude greater than that of the matrix. Conversely, when the E_i/E_m was less than one, the E^*/E_m difference for each model was slight. In other words, the morphology had little effect on the equivalent modulus. Moreover, the E^*/E_m of the models with $E_i/E_m = 0$ was almost identical to the E^*/E_m of the models with $E_i/E_m = 1 \times 10^{-2}$. It was suggested that the equivalent modulus of the porous materials was identical to that of the composites including the inclusions more than two orders of magnitude lower than that of the matrix.

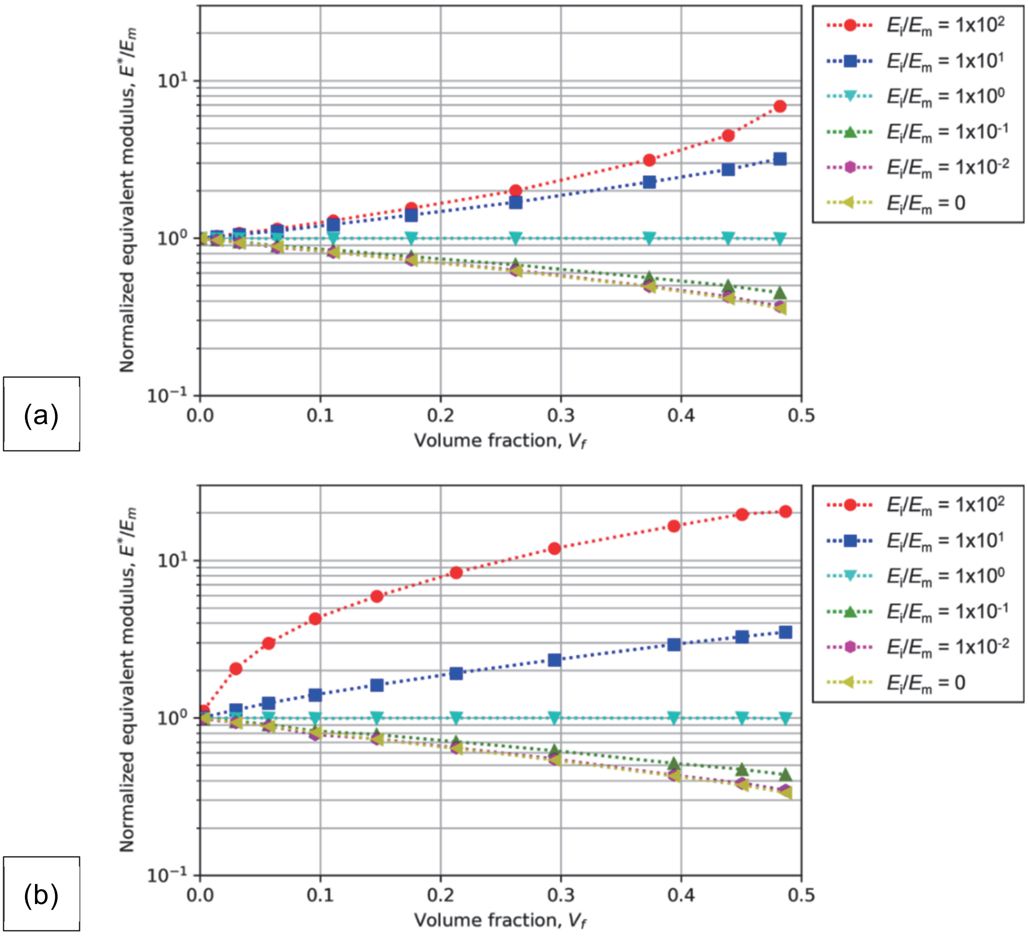

Fig. 2.6. Relationship between normalized equivalent modulus (E^*/E_m) and volume fraction of inclusions (V_f) of (a) matrix-dilute inclusoin model and (b) bicontinuous model, where E_i/E_m is 1×10^2, 1×10^1, 1×10^0, 1×10^{-1}, 1×10^{-2}, and zero, respectively.

(a) $E_i/E_m > 1$

The normalized equivalent Young's modulus (E^*/E_m) was calculated in the case of $E_i/E_m = 1 \times 10^2$, as shown in Fig. 2.7. The calculated lines by Voigt and Reuss models are also shown. The E^*/E_m of both models is monotonically increased by the increase of V_f. All the calculated values existed between the Voigt line (upper bound) and the Reuss line (lower bound) in the entire V_f range. Additionally, the E^*/E_m of the bicontinuous model was always higher than the matrix-dilute inclusion model. This is because the bicontinuous model had relatively large load-carrying volumes parallel to the load-direction, compared to the matrix-dilute inclusion model. Moreover, the brace-like skeletal structure was inferred to further enhance the reinforcement effect. Therefore, a continuous skeleton-shaped inclusion would be more suitable to reinforce the matrix materials.

Fig. 2.8 shows the local distribution of equivalent stress and elastic strain in these simulations. Each model resulted in different stress and strain distributions. In the matrix-dilute inclusion model, overall low stress was shown, and the local-high strain was observed in the matrix. Conversely, in the bicontinuous model, high stress was observed in the inclusion, and the overall low strain was shown. The inclusion in the bicontinuous model mainly carried the load, which was also inferred by the higher equivalent Young's modulus than the matrix-dilute inclusion model. Based on these results, the matrix-dilute inclusion model and the bicontinuous model were suggested to provide a stress- and strain-reduction effect, respectively, in the case of the $E_i/E_m > 1$.

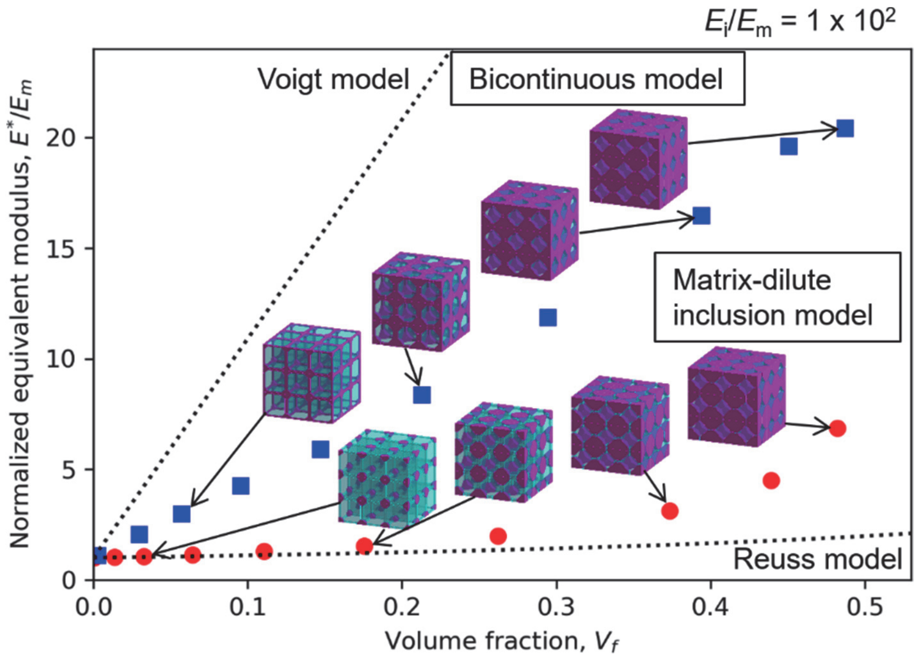

Fig. 2.7. Relationships between normalized equivalent modulus (E^*/E_m) and volume fraction of inclusions (V_f) of matrix-dilute inclusion and bicontinous models, where E_i/E_m is 1×10^2.

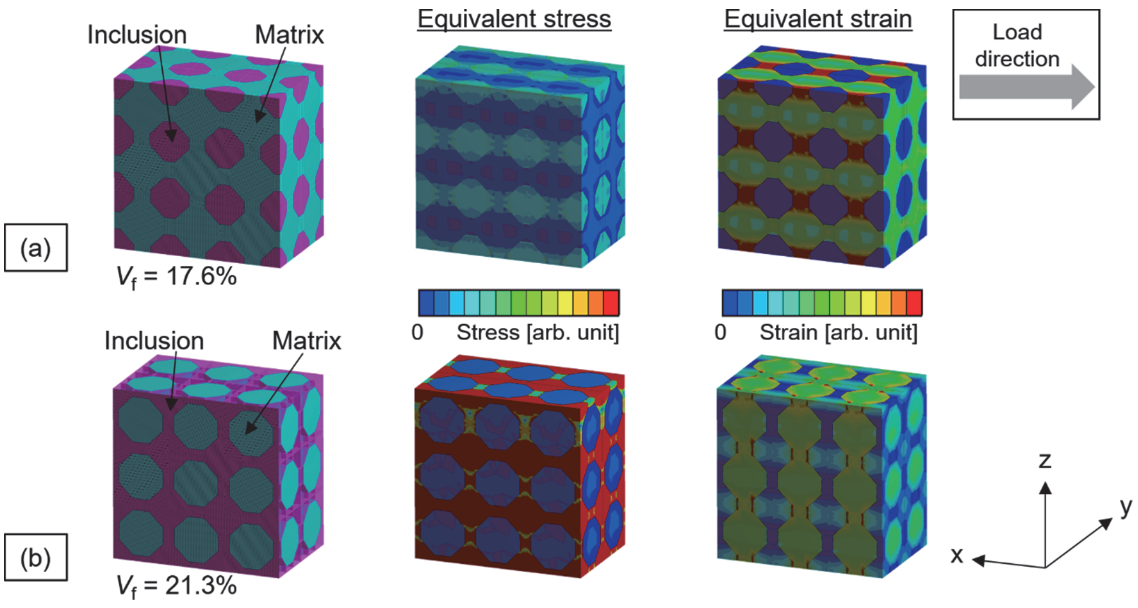

Fig. 2.8. Local distribution of equivalent stress and strain in (a) matrix-dilute inclusion model and (b) bicontinuous model with the inclusion of $E_i/E_m = 1 \times 10^2$.

(b) $E_i/E_m < 1$

Next, the normalized equivalent Young's modulus (E^*/E_m) was calculated in the case of $E_i/E_m = 1 \times 10^{-2}$, as shown in Fig. 2.9. The calculated lines by Voigt and Reuss models are also shown. The E^*/E_m of both models was linearly reduced by the increase in the V_f. As in the case of $E_i/E_m = 1 \times 10^2$, all the calculated values existed between the Voigt line (upper bound) and the Reuss line (lower bound) in the entire V_f range. However, in contrast to the case of $E_i/E_m = 1 \times 10^2$, the difference between both models was slight. In composites containing low stiffness inclusions, the effect of the inclusion morphology on the composite was found to be relatively minor compared to the composites with high stiffness inclusions, as described above. Therefore, it was suggested that the low-stiffness-inclusion volume fraction primarily dominates the composite stress relaxation properties.

Fig. 2.10 shows the local distribution of equivalent stress and elastic strain in these simulations. Each model resulted in different stress and strain distributions. In the matrix-dilute inclusion model, continuous-high stress was observed parallel to the loading direction in the matrix, and the intermittent-high strain was shown in the inclusion. In contrast, in the bicontinuous model, the intermittent-high stress was observed in the matrix, and the continuous-high strain was shown in the inclusion. Based on these results, the matrix-dilute inclusion model and the bicontinuous model were suggested to provide a strain- and stress-dispersion effect, respectively, in the case of $E_i/E_m < 1$.

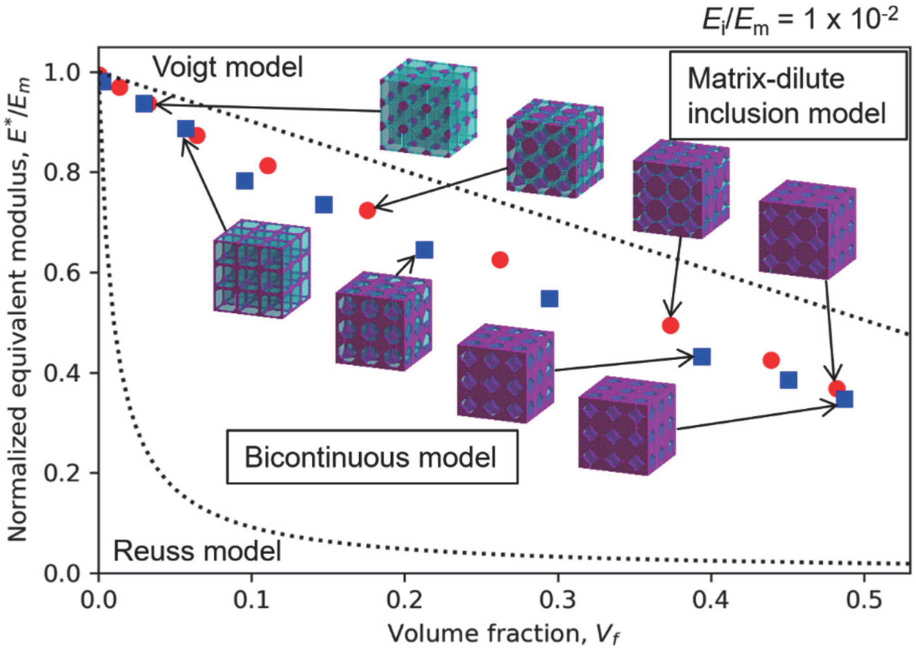

Fig. 2.9. Relationships between normalized equivalent modulus (E^*/E_m) and volume fraction of inclusions (V_f) of matrix-dilute inclusion and bicontinous models, where E_i/E_m is 1 × 10^{-2}.

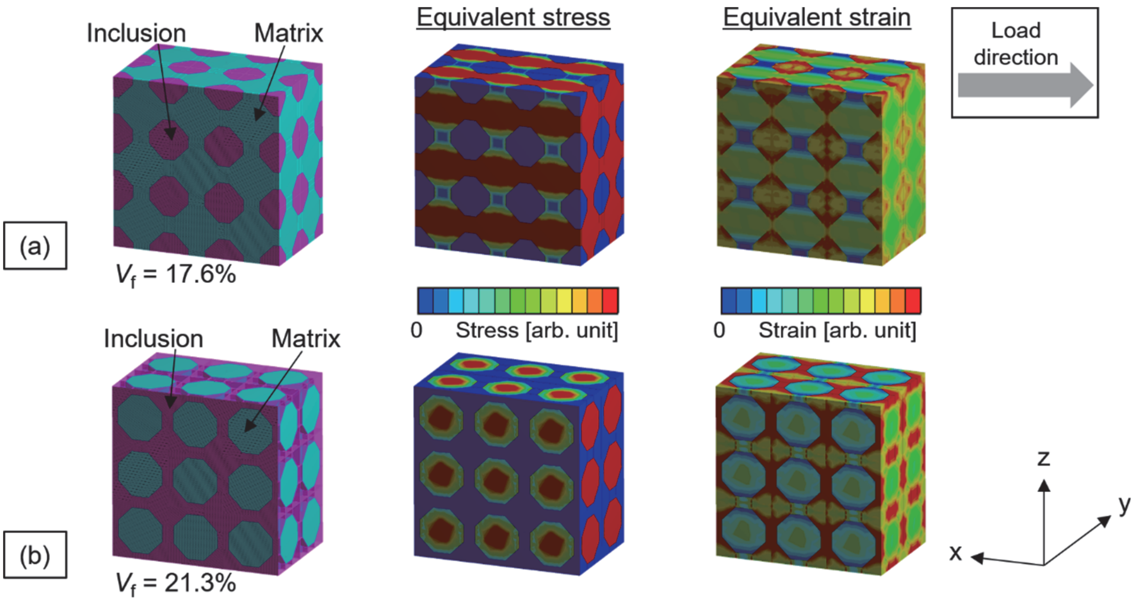

Fig. 2.10. Local distribution of equivalent stress and strain in (a) matrix-dilute inclusion model and (b) bicontinuous model with the inclusion of E_i/E_m = 1 × 10^{-2}.

2.3.2. Thermal properties of composite materials

The normalized equivalent thermal conductivity ($\lambda^{*}/\lambda_{\mathrm{m}}$) for the matrix-dilute inclusion and bicontinuous models was calculated with varying ratio $\lambda_{\mathrm{i}}/\lambda_{\mathrm{m}}$ as shown in Figs. 2.11 (a) and (b), respectively. The $\lambda_{\mathrm{i}}/\lambda_{\mathrm{m}}$ is set from 1×10^{-2} to 1×10^{2} including zero. The $\lambda^{*}/\lambda_{\mathrm{m}}$ of both the matrix-dilute inclusion and bicontinuous models showed a similar relationship to the E^{*}/E_{m}, as mentioned in Section 2.3.1. The $\lambda^{*}/\lambda_{\mathrm{m}}$ of the bicontinuous model was larger than that of the matrix-dilute inclusion model when the $\lambda_{\mathrm{i}}/\lambda_{\mathrm{m}}$ was greater than one, while the difference of the $\lambda^{*}/\lambda_{\mathrm{m}}$ of each model was slight when the $\lambda_{\mathrm{i}}/\lambda_{\mathrm{m}}$ was less than one. Furthermore, the $\lambda^{*}/\lambda_{\mathrm{m}}$ of the models with $\lambda_{\mathrm{i}}/\lambda_{\mathrm{m}} = 0$ was almost identical to the$\lambda^{*}/\lambda_{\mathrm{m}}$ of the models with $\lambda_{\mathrm{i}}/\lambda_{\mathrm{m}} = 1 \times 10^{-2}$. This suggests that the equivalent thermal conductivity of the porous materials was identical to that of the composites including the inclusions more than two orders of magnitude lower than that of the matrix. These understandings were the same for the E^{*}/E_{m}.

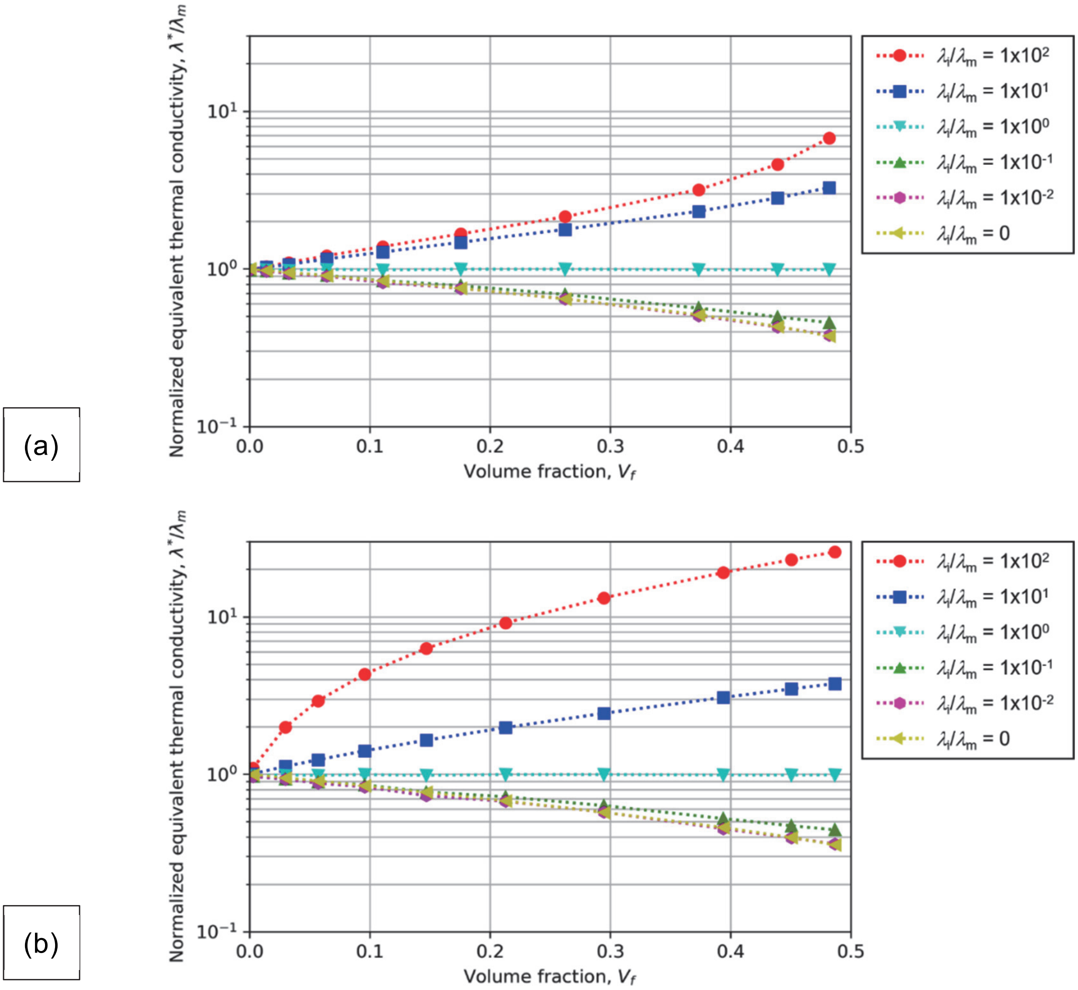

Fig. 2.11. Relationship between normalized equivalent thermal conductivity ($\lambda^{*}/\lambda_{\mathrm{m}}$) and volume fraction of inclusions (V_{f}) of (a) matrix-dilute inclusion model and (b) bicontinuous model, where $\lambda_{\mathrm{i}}/\lambda_{\mathrm{m}}$ is 1×10^{2}, 1×10^{1}, 1×10^{0}, 1×10^{-1}, 1×10^{-2}, and zero, respectively.

(a) $\lambda_i/\lambda_m > 1$

The normalized equivalent thermal conductivity (λ^*/λ_m) was calculated in the case of $\lambda_i/\lambda_m = 1 \times 10^2$, as shown in Fig. 2.12. The calculated lines by Voigt and Reuss models are also shown. The increase in the V_f monotonically increased the λ^*/λ_m of both models. All the calculated values existed between the Voigt line (upper bound) and the Reuss line (lower bound) in the entire V_f range. Furthermore, the λ^*/λ_m of the bicontinuous model was always higher than the matrix-dilute inclusion model. This is because the bicontinuous model had relatively large conductive paths parallel to the heat flow direction, compared to the matrix-dilute inclusion model.

The local distributions of temperature and heat flux along the x-axis are shown in Figs. 2.13 (a) and (b), respectively. Each model resulted in different temperature and heat flux distributions, which indicated the important roles of the inclusions within both models microscopically. In the matrix-dilute inclusion model (Fig. 2.13 (a)), the inclusions temperature was lower than the matrix temperature and the inclusions heat flux was higher than the matrix heat flux on the heat-input surface. Alternatively, the bicontinuous model (Fig. 2.13 (b)) showed the same tendency as the matrix-dilute inclusion model, i.e., the temperature of the inclusions was lower than that of the matrix on the heat input surface and the heat flux of the inclusions was higher than that of the matrix. However, when comparing the two models, marked differences were found. That is, the temperature change along the x-axis was clearly less and the heat flux in the inclusions was clearly larger in the bicontinuous model than in the matrix-dilute inclusion model. These results indicated that the effect of high thermal conductivity inclusions on the equivalent thermal conductivity was more pronounced in the bicontinuous model.

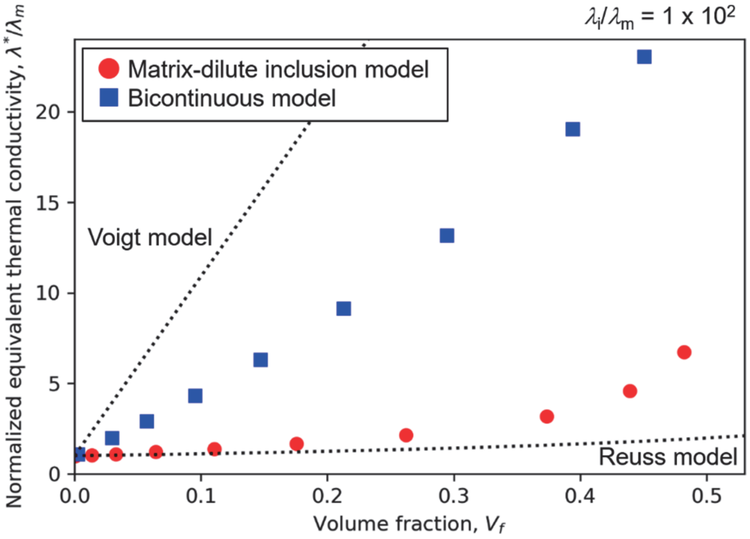

Fig. 2.12. Relationships between normalized thermal conductivity (λ^*/λ_m) and volume fraction of inclusions (V_f) of matrix-dilute inclusion and bicontinous models, where λ_i/ λ_m is 1 × 10^2.

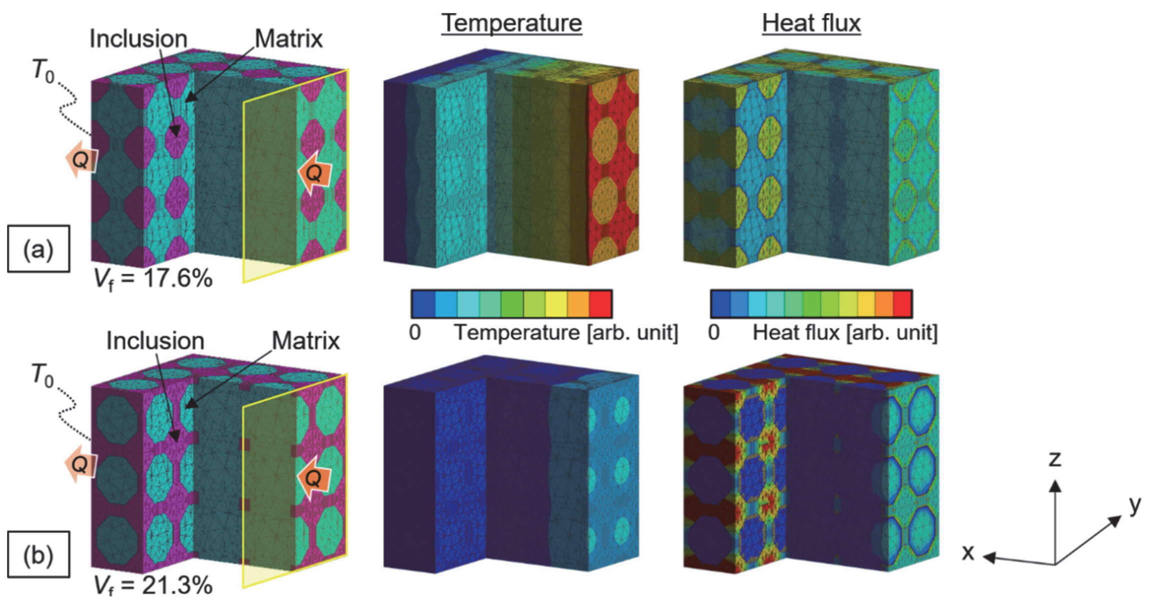

Fig. 2.13. Local distribution of temperature and heat flux along the x-axis in (a) matrix-dilute inclusion model and (b) bicontinuous model with the inclusion of $E_i/E_m = 1 \times 10^2$.

(b) $\lambda_i/\lambda_m < 1$

Next, normalized equivalent thermal conductivity (λ^*/λ_m) was calculated in the case of $\lambda_i/\lambda_m = 1 \times 10^{-2}$, as shown in Fig. 2.14. The calculated lines by the Voigt and Reuss models are also shown. The λ^*/λ_m of both models were reduced by the increase in the V_f in a roughly inverse proportion. As in the case of $\lambda_i/\lambda_m = 1 \times 10^2$, all the calculated values existed between the Voigt line (upper bound) and the Reuss line (lower bound) in the entire V_f range. However, in contrast to the $\lambda_i/\lambda_m = 1 \times 10^2$ case, the difference between both models was slight. In composites containing low thermal conductivity inclusions, the effect of the inclusion morphology on the composites conductive characteristic was found to be relatively minor. Therefore, it was suggested that the volume fraction of the low thermal conductivity inclusions primarily dominates the equivalent thermal conductive properties of the composites.

The local distributions of temperature and heat flux along the x-axis are shown in Figs. 2.15 (a) and (b), respectively. Differences in the temperature and heat flux distributions between both models were slight. In both the matrix-dilute inclusion model (Fig. 2.15 (a)) and the bicontinuous model (Fig. 2.15 (b)), the inclusions temperature was higher than the matrix temperature, and the inclusions heat flux was lower than the matrix heat flux on the heat-input surface. These results suggested that the matrix contributed as the main heat transfer pathway regardless of the inclusion morphology.

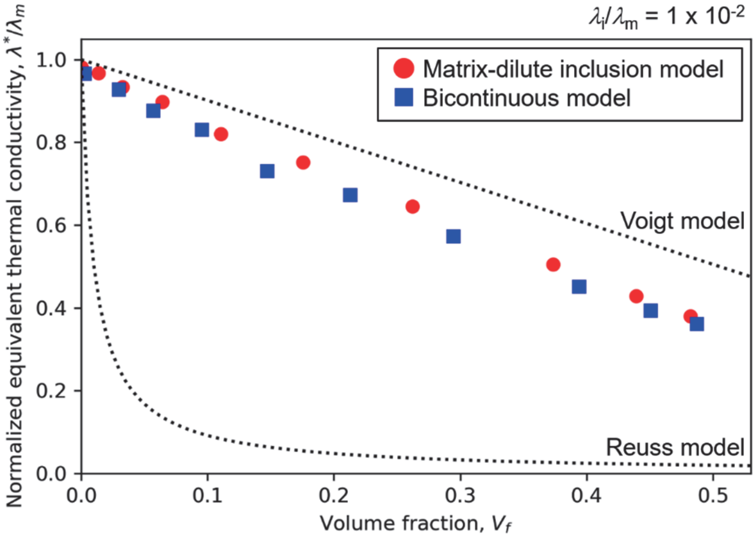

Fig. 2.14. Relationships between normalized thermal conductivity (λ^*/λ_m) and volume fraction of inclusions (V_f) of matrix-dilute inclusion and bicontinous models, where λ_i/λ_m is 1×10^{-2}.

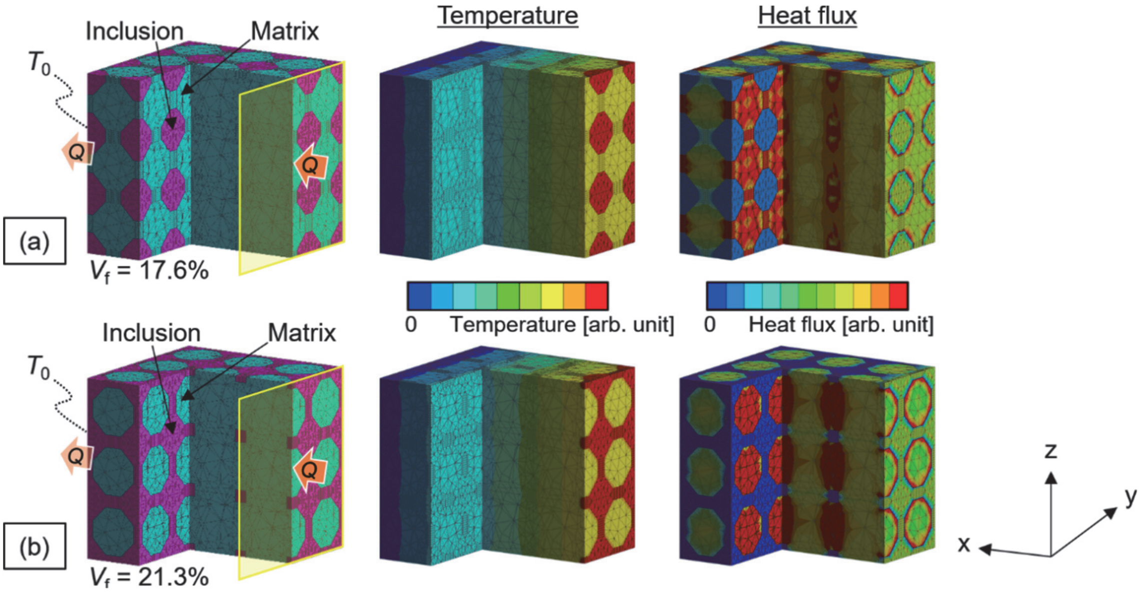

Fig. 2.15. Local distribution of temperature and heat flux along the heat-input direction in (a) matrix-dilute inclusion model and (b) bicontinuous model with the inclusion of $E_i/E_m = 1 \times 10^{-2}$.

2.3.3. Brief summary of FE analysis

Computational calculations using simplified RVE models representing the matrix-dilute inclusion and bicontinuous composites were performed to predict the NC and MC microstructure characteristics for electronics interconnection, as described in Sections 2.3.1 and 2.3.2. In these analyses, the impacts of V_f and E_i/E_m or λ_i/λ_m on the effective Young's modulus or thermal conductivity were evaluated. The results revealed similar trends in effective Young's modulus and thermal conductivity from a macroscopic perspective. When the inclusion properties were greater than those of the matrix, the inclusion effect on the equivalent properties was more pronounced for bicontinuous composites. Conversely, when the inclusion properties were less than those of the matrix, the inclusion effect on the equivalent properties was nearly the same for both composites.

In addition, local stress and strain distributions, or temperature and heat flux distributions suggested the inclusions effect on the equivalent composites characteristics. In the matrix-dilute inclusion model, the hard and soft inclusions provided a stress-reduction effect and a strain-dispersion effect, respectively. Conversely, in the bicontinuous model, the hard and soft inclusions provided a strain-reduction effect and a stress-dispersion effect, respectively. Regarding thermal conductivity, the high-conductivity inclusions improved the equivalent thermal conductivity, especially for bicontinuous composites. Alternatively, the matrix contributed as the main heat transfer pathway within the composites with the low-conductivity inclusions, regardless of the inclusions morphology.

2.4. Discussion

2.4.1. Verification of FE analysis for RVEs of composites

The FE analysis of composites RVEs suggested the effects of the properties and the morphology of the inclusions on the equivalent composite properties. The FE analysis is expected to predict the properties of various composite materials. Here, the equivalent Young’s modulus and thermal conductivity of sintered porous Ag material were calculated as an example of a promising interconnection material.

(a) Equivalent Young’s modulus

First, the equivalent Young’s modulus of porous Ag materials was calculated. The bicontinuous model was used with a Young’s modulus of 83 GPa for bulk Ag. Carr et al. [8] reported the quantitative characterization of porosity and determination of Young’s modulus for sintered porous Ag material. They demonstrated the experimental and computational values of the equivalent Young’s modulus by considering the realistic microstructure obtained by utilizing segmented 3D images. Suzuki et al. [10] evaluated the equivalent Young’s modulus of sintered porous Ag material by a bending test of sintered Ag films. Moreover, the various analytical approximation methods of equivalent modulus for porous materials were proposed. Ramakrishnan and Arunachalam [14] proposed the analytical approximation equation for porous solids (R-A model), as follows:

$$E^* = E_\mathrm{m}\left[\frac{(1 - V_\mathrm{f})^2}{1 + k_\mathrm{E} \cdot V_\mathrm{f}}\right], \tag{2.6}$$

where k_E is described, as follows:

$$k_\mathrm{E} = 2 - 3\nu_\mathrm{m}, \tag{2.7}$$

where ν_m (= 0.37) is the Poisson's ratio of matrix material as bulk Ag. Youssef et al. [15] estimated the modulus by both numerical and analytical approaches. The equivalent Young's modulus of porous Ag was numerically calculated by utilizing the 3D image-based models. The calculated values were compared with the analytically obtained values by the power-law formula, which is one of the analytical approximation methods, as follows:

$$E^* = E_\mathrm{m} \times (1 - V_\mathrm{f})^m, \tag{2.8}$$

where m is the empirically-determined coefficient of 0.463 for porous Ag.

The relationship between equivalent Young's modulus E^* and pores volume fraction V_f of sintered porous Ag material, obtained by FE simulation of the bicontinuous model in this study, has FE simulation [8], [15], experimental [8], [10], and analytical calculation [14], [15] shown in Fig. 2.16. The calculated values by the bicontinuous model in this study showed a similar tendency to the references, where the equivalent Young's modulus was reduced with an increased pores volume fraction. In comparison with the experimental results, the calculated values in this study were higher. It is well known that the equivalent Young's modulus can be predicted by only the pores volume fraction; however, the differences in the simulation and experimental values increased with increased V_f. It indicated that the difference between the real morphology and the simplified regularly arranged morphology of the FE model should be considered for the sintered porous material with a high pores volume fraction.

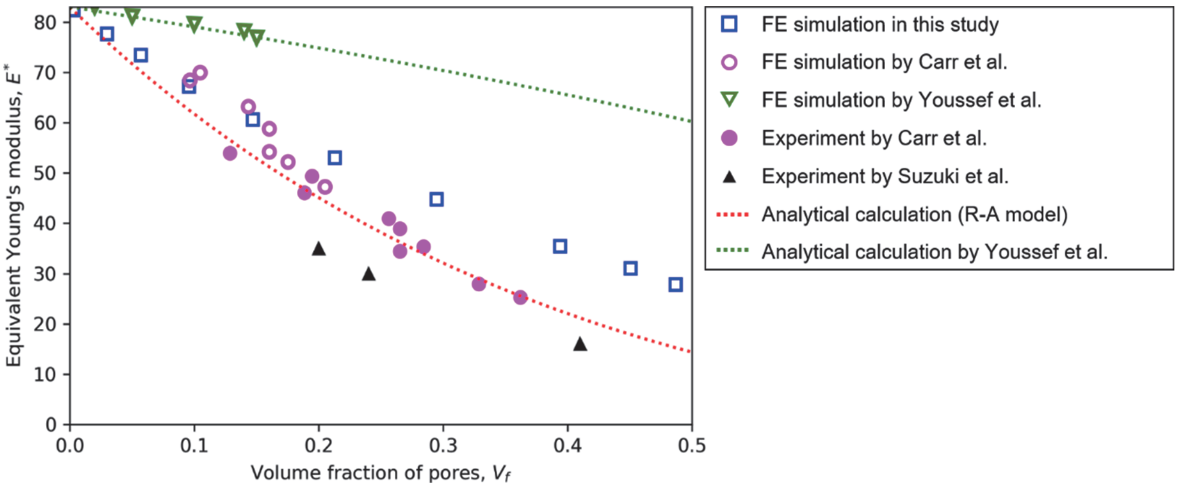

Fig. 2.16. Relationship between equivalent Young's modulus E^* and pores volume fraction V_f of sintered porous Ag material, obtained by FE simulation of bicontinuous model in this study, FE simulation [8], [15], experimental [8], [10], and analytical calculation [14], [15].

(b) Equivalent thermal conductivity

Next, the equivalent thermal conductivity of porous Ag materials was calculated. The bicontinuous model was used with the thermal conductivity of 429 W/m·K for bulk Ag. Many researchers reported the equivalent thermal conductivity of sintered porous Ag materials with a varying pores volume fraction by experiments [15]–[20]. Furthermore, numerical simulation was also evaluated. Signor et al. [21] predicted the equivalent thermal conductivity of sintered porous Ag with varying porosity by the FE simulations of the real 3D morphologies by utilizing segmented 3D images. Moreover, analytical approximation approaches were also evaluated. El Moumen et al. [22] demonstrated the utilization of the Maxwell-Eucken model for approximation of the equivalent thermal conductivity of porous Ag, as follows:

$$\lambda^* = \lambda_\mathrm{m} \frac{2\lambda_\mathrm{m} + \lambda_\mathrm{i} - (2\lambda_\mathrm{m} - \lambda_\mathrm{i}) \cdot V_\mathrm{f}}{2\lambda_\mathrm{m} + \lambda_\mathrm{i} + (\lambda_\mathrm{m} - \lambda_\mathrm{i}) \cdot V_\mathrm{f}}, \tag{2.9}$$

where λ_i is assumed to be zero. Youssef et al. [15] utilized the power-law formula with the empirical coefficient of n = 1.45 for sintered porous Ag, as follows:

$$\lambda^* = \lambda_\mathrm{m} \times (1 - V_\mathrm{f})^n. \tag{2.10}$$

The relationship between equivalent thermal conductivity λ^* and pores volume fraction V_f of sintered porous Ag material, obtained by FE simulation of the bicontinuous model in this study, has FE simulation [21], experimental [15]–[20], and analytical calculation [6], [15] shown in Fig. 2.17. The calculated values by the bicontinuous model in this study agreed well with the other numerical and analytical calculation results in the references, where the equivalent thermal conductivity reduced with an increased pores volume fraction. However, the experimental values were lower than these calculated values, especially in the region of the pores high volume fraction. The FE results using the simplified model in this study are in good agreement with the results using the realistic 3D model in Ref. [21]. Based on this comparison, the experimental thermal conductivity would be affected by the metallurgical characteristics of the inherent nanoparticle-sintered microstructure, e.g., fine grains and numerous grain boundaries, which should be discussed further.

Based on the verification as mentioned above, the FE analysis for RVEs of composites in this study was suggested to be helpful to roughly estimate the equivalent properties of NC and MC interconnection materials although the morphology and metallurgical properties should be further discussed for improved prediction precision.

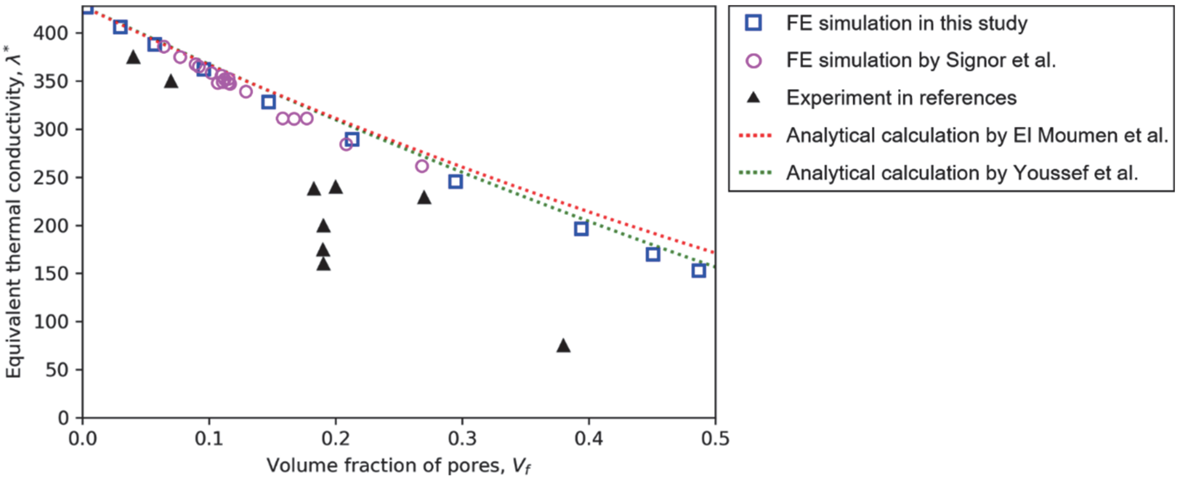

Fig. 2.17. Relationship between equivalent thermal conductivity λ^* and pores volume fraction V_f of sintered porous Ag material, obtained by FE simulation of bicontinuous model in this study, FE simulation [21], experimental [15]–[20], and analytical calculation [6], [15].

2.4.2. Candidates of NC and MC materials for power electronics interconnection

In this section, we intended to derive promising material combinations that could be used for power electronics interconnections. Monolithic interconnection materials must be compromised to satisfy the various favorable properties—low Young's modulus, high thermal conductivity, high tensile strength, and high durable temperature, as shown in Table 2.2. Currently, Pb-5Sn solder is a conventional monolithic material that meets these requirements to some extent, although its use should be restricted because of the large environmental load of Pb. However, tailored NC and MC materials would meet these requirements at a higher level. In Section 1.3, it is evident that Young's modulus, thermal conductivity, and tensile strength have a positive correlation with material durable temperature in existing monolithic materials. Furthermore, thermal conductivity and Young's modulus also tend to be positively correlated. Therefore, material combinations tailored to these requirements would be attractive to the applications.

Constituent candidates for NC and MC interconnection, especially for high-temperature power electronics, are listed as follows:

- Solder alloy,
- heat-resistant polymer,
- sintered metal,
- transient liquid phase sintered IMC.

These constituent candidates are being researched, usually as monolithic materials. However, the hybridization of these monolithic materials has great potential to extend the range of properties. Young's modulus, thermal conductivity, tensile strength, and durable temperature of the representative monolithic materials are listed in Table 2.3. The durable temperature was defined as the melting point for pure metal and solder alloy, the phase transformation temperature for IMC, and decomposition temperature for polymer in this study. From these candidates, Cu, Sn-3Ag-0.5Cu (SAC305), Cu_6Sn_5, and polyimide resin were selected from the perspective of cost, being lead-free, and versatility for electronics interconnection. In addition, sintered porous materials of Ag or Cu, i.e., composites with pores embedded in a high thermally conductive and rigid matrix, were also investigated.

Table 2.2. Favorable properties for interconnection materials, corresponding to the requirements for power electronics interconnections.

Mechanical requirements for power electronics interconnections	Favorable properties
Heat dissipation performance	• High thermal conductivity
Interconnection reliability	• Low Young's modulus • High strength • High-temperature tolerance
Stress-relaxation for power chips	• Low Young's modulus

Table 2.3. Young's modulus, thermal conductivity, and durable temperature of the representative monolithic materials for high-temperature interconnections, referred from Table 1.1 in Section 1.3.

Category	Material	Young's modulus E [GPa]	Thermal conductivity λ [W/m·K]	Tensile strength σ_{UTS} [MPa]	Durable temperature* T_{D} [°C]
Pure metal	Ag	83	429	124	962
	Cu	100	401	213	1085
Solder alloy	SAC305	31	55	52	218
	Pb-5Sn	35	23	18	310
	Au-20Sn	68	57	275	280
IMC	Cu_6Sn_5	102	45	1130	415
Polymer	Polyimide	3	0.2	350	410

*Melting point for pure metals and solder; phase transformation temperature for IMC, decomposition temperature for polymer.

(a) Young's modulus and thermal conductivity

For these selected candidate materials, equivalent Young's modulus and thermal conductivity were numerically calculated by using the bicontinuous RVE model, as described in Section 2.3. The bicontinuous model was used, which is expected to further improve the properties by inclusions. Additionally, those values of closed-porous materials were calculated by the matrix-dilute inclusion RVE model. The volume fraction V_{f} of the inclusions and the pores ranged from 20 to 60%, and from 3 to 20%, respectively. The material combinations of the evaluated composites are described as (*Matrix*, *Inclusion*), as follows: (Ag, open pore), (Ag, closed pore), (Cu, open pore), (Cu, closed pore), (Cu_6Sn_5, Cu), (SAC305, Cu), (SAC305, Cu_6Sn_5), (polyimide, Cu), (polyimide, Cu_6Sn_5), and (polyimide, SAC305).

The relationship between the equivalent thermal conductivity and Young's modulus of representative NC and MC interconnection materials, accompanying the representative monolithic materials, is shown in Fig. 2.18. The area in Fig. 2.18 is divided into four quadrants by the blue lines of the thermal conductivity and Young's modulus of Pb-5Sn solder, which can be considered as a criteria of high-temperature interconnection materials. Promising materials are required to have high thermal conductivity, low stiffness, or both. The first quadrant includes materials with high thermal conductivity; the third quadrant includes materials with low stiffness; the fourth quadrant includes materials with both high thermal conductivity and low stiffness. It was found that the porous material, although rigid, can be expected to have very high thermal conductivity. The difference between the open-porous and closed-porous materials is slight. In particular, it was suggested that the porous Ag material has lower stiffness and more desirable properties compared to Cu. The combination of Cu_6Sn_5 and Cu, generally obtained with pressure-assisted TLPS, was estimated to have relatively good thermal conductivity of 100–200 W/m·K. However, it was suggested that the very high stiffness of this combination was not suitable for power electronics interconnection with high thermal strain. When SAC305 was used as the matrix, relatively high thermal conductivity and low stiffness were expected when Cu was added as the inclusions. When polyimide was used as the matrix, all composites were found to have remarkably low stiffness; therefore, a high stress relaxation property was expected. Moreover, Cu as the inclusion to compensate for the extremely low polyimide thermal conductivity would be helpful.

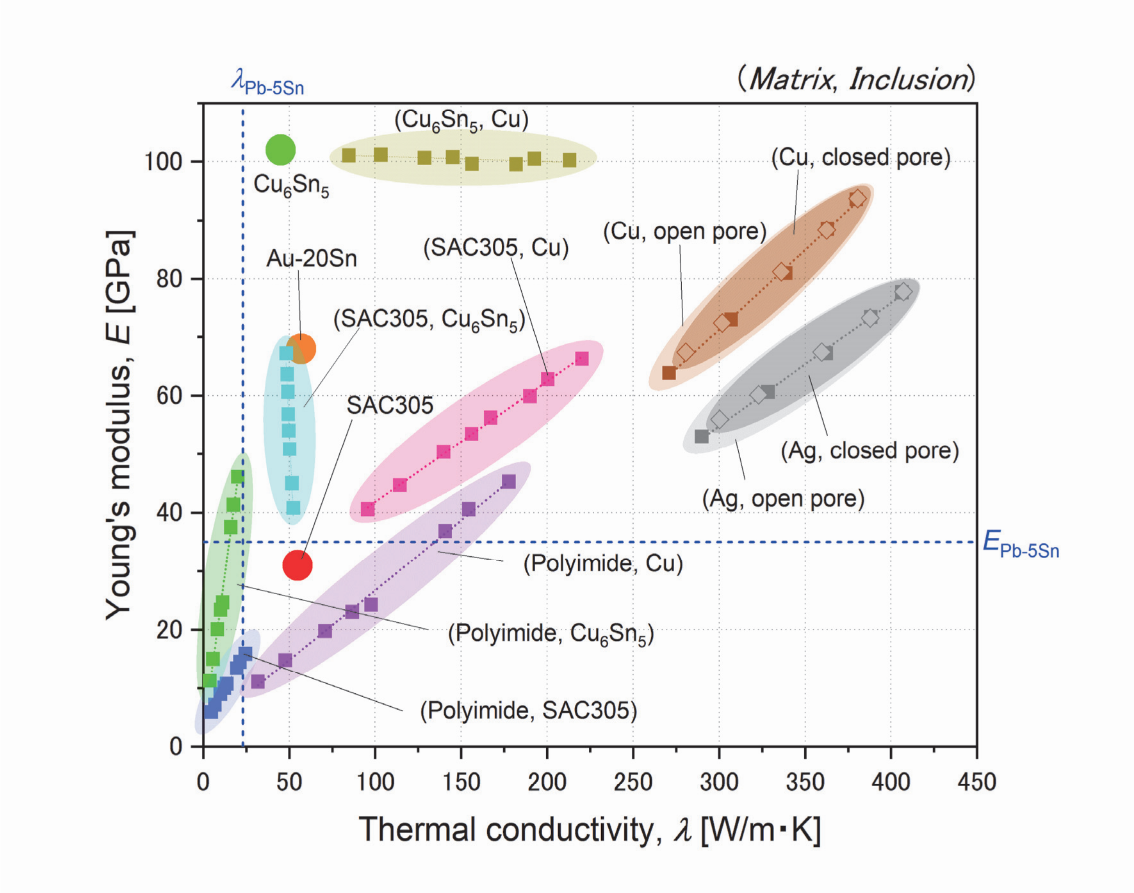

Fig. 2.18. Equivalent thermal conductivity and Young's modulus of representative monolithic and composite materials, as shown by (*Matrix*, *Inclusion*). The values of the composite materials were calculated by FE analysis of the bicontinuous RVE model. Additionally, those of closed-porous materials were calculated by the matrix-dilute inclusion RVE model. The volume fraction V_f of the inclusions and the pores were ranged from 20 to 60%, and from 3 to 20%, respectively.

(b) Strength

The Rule of Mixtures is applied to an equivalent composite strength [23]. The fracture strain of a continuous stiff inclusion is usually smaller than that of a soft matrix. In this case, the composite would fracture when the continuous inclusion fractures. The matrix stress at the inclusion fracture σ_m' is described as follows:

$$\sigma_\mathrm{m}' = E_\mathrm{m}\varepsilon_\mathrm{f,i}, \tag{2.11}$$

where $\varepsilon_\mathrm{f,i}$ is the fracture strain of the inclusion. Eqs. 2.1 and 2.11 lead to the equivalent strength σ^*, as follows:

$$\sigma^* = \sigma_\mathrm{i}V_\mathrm{f} + \sigma_\mathrm{m}'(1 - V_\mathrm{f}), \tag{2.12}$$

where σ_i is the inclusion strength. Therefore,

$$\sigma^* = \sigma_\mathrm{i}V_\mathrm{f} + E_\mathrm{m}\varepsilon_\mathrm{f,i}(1 - V_\mathrm{f}) \tag{2.13}$$

is obtained.

For rough estimation, the equivalent strengths of these NC and MC candidates were calculated by Eq. 2.13, where the $\varepsilon_\mathrm{f,i}$ was assumed to be 0.1%. The relationship between the equivalent strength and Young's modulus of representative NC and MC interconnection materials, accompanying the representative monolithic materials, is shown in Fig. 2.19. The area in Fig. 2.19 is divided into four quadrants by the blue lines of the strengths and Young's modulus of Pb-5Sn solder. High strength and low stiffness properties, presented in the fourth quadrant, would be favorable to power electronics interconnections, suggested by the analytical calculations above. Based on this consideration, the reinforced polyimide composites, i.e., (Polyimide, Cu) and (Polyimide, Cu_6Sn_5) would be promising. Additionally, (SAC305, Cu) and (SAC305, Cu_6Sn_5) could be hopeful because of the high strength and relatively low stiffness.

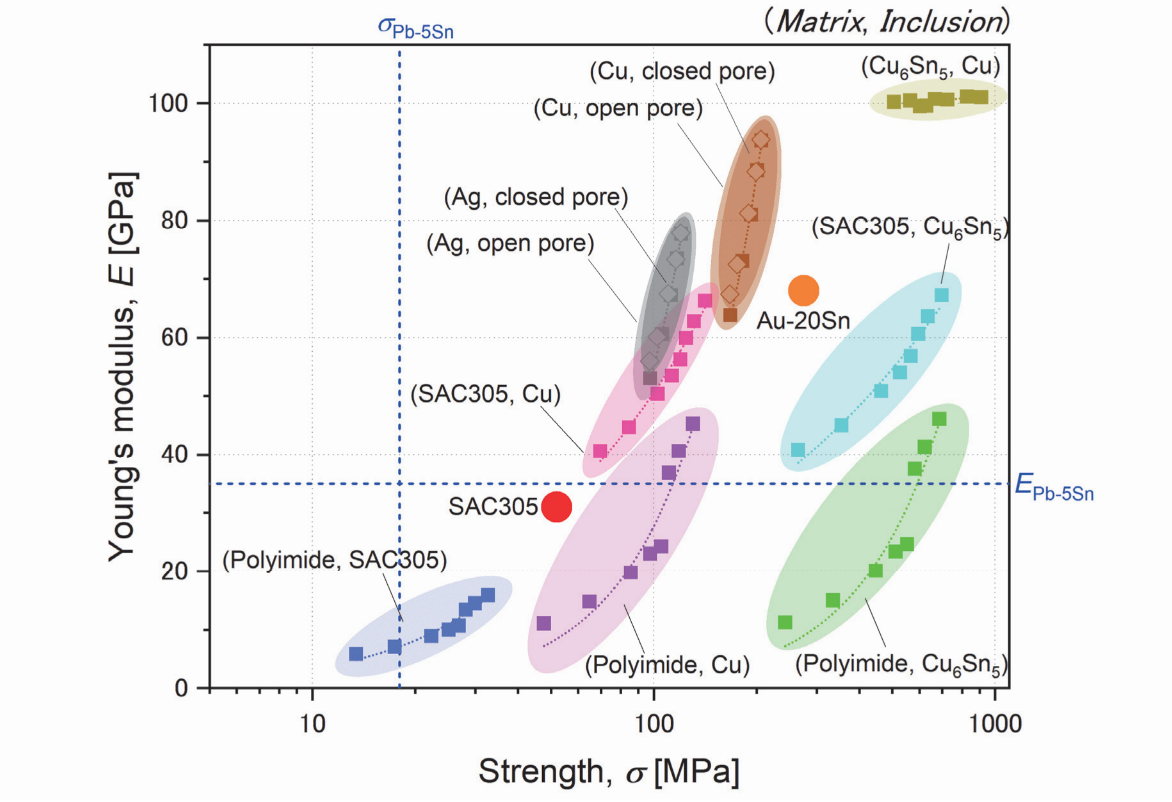

Fig. 2.19. Equivalent strength and Young's modulus of representative monolithic and composite materials, as shown by (*Matrix*, *Inclusion*). The values of the composite materials were calculated by FE analysis of the bicontinuous RVE model for Young's modulus and the Rule of Mixtures for strength. Additionally, those of closed-porous materials were calculated by the matrix-dilute inclusion RVE model. The volume fraction V_f of the inclusions and the pores were ranged from 20 to 60%, and from 3 to 20%, respectively.

(c) Temperature tolerance

The homologous temperature of these NC and MC materials was evaluated. The homologous temperature of NC and MC materials was defined as the ratio of the operating temperature to the lower durable temperature of the constituent materials in Kelvin. The homologous temperatures of the NC and MC materials assuming an operational temperature of 200 °C are shown in Fig. 2.20. The porous Ag and Cu, the melting points of which are significantly high, have low T_h; therefore, high heat resistance can be expected. The Cu_6Sn_5 and polyimide resin, the durable temperatures of which are more than 400 °C, were also expected to have similarly high heat resistance. Conversely, the heat resistance at 200 °C would not be expected for the composites containing SAC305 due to its low durable temperature. In terms of the homologous temperature, it was suggested that the NC and MC materials composed of Cu, Cu_6Sn_5, or polyimide resin are promising as power electronics interconnections above 200 °C.

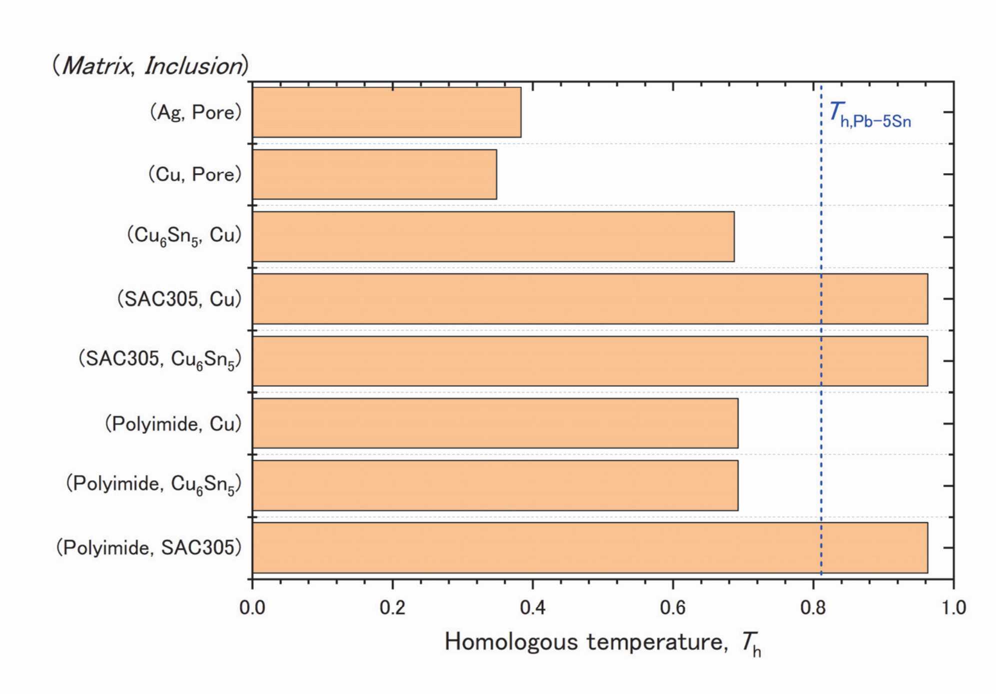

Fig. 2.20. Homologous temperature T_h of NC and MC interconnection materials assuming an operational temperature of 200 °C. The T_h was defined as the ratio of the operating temperature to the lower durable temperature of the constituent materials in Kelvin.

(d) Expected benefits and challenges

Considering the four favorable properties for power electronics interconnections, i.e., low Young's modulus, high thermal conductivity, high strength, and high-temperature tolerance, three promising NC and MC candidates with different characteristics were found as follows:

- Porous Ag material,
- Cu-embedded solder composite,
- Cu (and/or Cu_6Sn_5)-embedded polymer composite.

The estimated properties of these candidates are compared in Table 2.4. The porous Ag material was estimated to provide high thermal conductivity, high strength, and highly durable temperature. It should be beneficial to state-of-the-art high-temperature SiC power electronics interconnections. However, high stiffness would be an issue for the porous Ag material. The thermo-mechanical loading on a power chip and substrate due to thermal strain needs to be studied in detail.

The Cu-embedded solder composite was estimated to have moderately high strength and thermal conductivity. It can replace conventional solders while improving joint properties. In the solder-based composite, however, the heat tolerance may be limited by the solder matrix. In particular, the changes in metallurgical microstructure and the decrease in joint strength against thermal loading should be discussed in detail.

The Cu (and/or Cu_6Sn_5)-embedded polymer composite was estimated to have remarkably low stiffness and high durable temperature. This would be promising for power electronics interconnections, which require high stress-relaxation. Contrary, the polymer matrix would limit the composite thermal conductivity and strength because of its poor properties. Therefore, thermal and mechanical characteristics should be verified.

Table 2.4. Expected benefits of NC and MC candidates for power electronics interconnections.

NC and MC candidates	Favorable properties			
	Low Young's modulus	High thermal conductivity	High strength	High-temperature tolerance
Porous Ag material		✓	✓	✓
Cu embedded solder composite		✓	✓	
Cu (and/or Cu_6Sn_5)-embedded polymer composite	✓			✓

2.5. Conclusions

In this chapter, equivalent Young's modulus and thermal conductivity were estimated by FE simulations using simplified RVE models representing the matrix-dilute inclusion composite and the bicontinuous composite. The properties impacts and the volume fraction of inclusions on the equivalent properties were discussed. Based on the FE simulations, it was suggested that the bicontinuous morphology would further enhance the equivalent properties of NC and MC materials. From this study, three promising NC and MC candidates with different characteristics were found, as follows:

(a) Porous Ag material: Excellent thermal conductivity, durable temperature, and strength,

(b) Cu-embedded solder composite: Moderately high thermal conductivity and strength,

(c) Cu (and/or Cu_6Sn_5)-embedded polymer composite: Low stiffness and high durable temperature.

The porous Ag material, Cu-embedded solder composite, and Cu-IMC-embedded polymer composite are further researched in Chapters 3, 4, and 5, respectively.

References in Chapter 2

[1] Z. Hashin and S. Shtrikman, “A variational approach to the theory of the elastic behaviour of multiphase materials,” *J. Mech. Phys. Solids*, vol. 11, no. 2, pp. 127–140, 1963.

[2] J. D. Eshelby, “The determination of the elastic field of an ellipsoidal inclusion , and related problems,” *Proc. R. Soc. Lond. A. Math. Phys. Sci.*, vol. 241, pp. 376–396, 1957.

[3] T. Mori and K. Tanaka, “Average stress in matrix and average elastic energy of materials with misfitting inclusions,” *Acta Metall.*, vol. 21, no. 5, pp. 571–574, 1973.

[4] R. Hill, “A self-consistent mechanics of composite materials,” *J. Mech. Phys. Solids*, vol. 13, no. 4, pp. 213–222, 1965.

[5] S. Bargmann *et al.*, “Generation of 3D representative volume elements for heterogeneous materials: A review,” *Prog. Mater. Sci.*, vol. 96, pp. 322–384, 2018.

[6] A. El Moumen, T. Kanit, A. Imad, and H. El Minor, “Computational thermal conductivity in porous materials using homogenization techniques: Numerical and statistical approaches,” *Comput. Mater. Sci.*, vol. 97, pp. 148–158, Feb. 2015.

[7] Y. Kariya, H. Yamaguchi, M. Itako, N. Mizumura, and K. Sasaki, “Mechanical Behavior of Sintered Nano-sized Ag Particles,” *J. Smart Process.*, vol. 2, no. 4, pp. 161–165, 2013.

[8] J. Carr, X. Milhet, P. Gadaud, S. A. E. Boyer, G. E. Thompson, and P. Lee, “Quantitative characterization of porosity and determination of elastic modulus for sintered micro-silver joints,” *J. Mater. Process. Technol.*, vol. 225, pp. 19–23, 2015.

[9] A. Gillman, M. J. G. H. Roelofs, K. Matouš, V. G. Kouznetsova, O. van der Sluis, and M. P. F. H. L. van Maris, “Microstructure statistics–property relations of silver particle-based interconnects,” *Mater. Des.*, vol. 118, pp. 304–313, 2017.

[10] T. Suzuki *et al.*, “Effect of manufacturing process on micro-deformation behavior of sintered-silver die-attach material,” *IEEE Trans. Device Mater. Reliab.*, vol. 16, no. 4, pp. 588–596, 2016.

[11] T. Suzuki, Y. Yasuda, T. Terasaki, T. Morita, and Y. Kawana, “Macro- and Micro-Deformation Behavior of Sintered-Copper Die-Attach Material,” *IEEE Trans. DEVICE Mater. Reliab.*, vol. 18, no. 1, pp. 54–63, 2018.

[12] S. Zabihzadeh, S. Van Petegem, M. Holler, A. Diaz, L. I. Duarte, and H. Van Swygenhoven, “Deformation behavior of nanoporous polycrystalline silver. Part I: Microstructure and mechanical properties,” *Acta Mater.*, vol. 131, pp. 467–474, 2017.

[13] S. Zabihzadeh, J. Cugnoni, L. I. Duarte, S. Van Petegem, and H. Van Swygenhoven, “Deformation behavior of nano-porous polycrystalline silver. Part II: Simulations,” *Acta Mater.*, vol. 131, pp. 564–573, 2017.

[14] N. Ramakrishnan and V. S. Arunachalam, “Effective elastic moduli of porous solids,” *J. Mater.*

Sci., vol. 25, no. 9, pp. 3930–3937, 1990.

[15] T. Youssef *et al.*, “Power modules die attach: A comprehensive evolution of the nanosilver sintering physical properties versus its porosity,” *Microelectron. Reliab.*, vol. 55, no. 9–10, pp. 1997–2002, 2015.

[16] A. a Wereszczak, D. J. Vuono, H. Wang, and M. K. Ferber, “Properties of Bulk Sintered Silver As a Function of Porosity,” ORNL/TM-2012/130, 2012.

[17] J. G. Bai, Z. Z. Zhang, J. N. Calata, and G. Q. Lu, “Low-temperature sintered nanoscale silver as a novel semiconductor device-metallized substrate interconnect material,” *IEEE Trans. Components Packag. Technol.*, vol. 29, no. 3, pp. 589–593, 2006.

[18] S. Wang, M. Li, H. Ji, and C. Wang, “Rapid pressureless low-temperature sintering of Ag nanoparticles for high-power density electronic packaging,” *Scr. Mater.*, vol. 69, no. 11–12, pp. 789–792, 2013.

[19] P. Rajaguru, H. Lu, and C. Bailey, “Sintered silver finite element modelling and reliability based design optimisation in power electronic module,” *Microelectron. Reliab.*, vol. 55, no. 6, pp. 919–930, 2015.

[20] F. Le Henaff, S. Azzopardi, E. Woirgard, T. Youssef, S. Bontemps, and J. Joguet, “Lifetime Evaluation of Nanoscale Silver Sintered Power Modules for Automotive Application Based on Experiments and Finite-Element Modeling,” *IEEE Trans. Device Mater. Reliab.*, vol. 15, no. 3, pp. 326–334, 2015.

[21] L. Signor *et al.*, “Evolution of the Thermal Conductivity of Sintered Silver Joints with their Porosity Predicted by the Finite Element Analysis of Real 3D Microstructures,” *J. Electron. Mater.*, vol. 47, no. 7, pp. 4170–4176, 2018.

[22] J. H. Choi, K. Ryu, K. Park, and S. J. Moon, “Thermal conductivity estimation of inkjet-printed silver nanoparticle ink during continuous wave laser sintering,” *Int. J. Heat Mass Transf.*, vol. 85, pp. 904–909, 2015.

[23] H. Fukuda, “An introduction to composite dynamics. Chapter 1. Basic theories of elasticity and material dynamics for composite dynamics,” *J. Japan Soc. Compos. Mater. (in Japanese)*, vol. 23, no. 1, p. 19, 1996.

Chapter 3. Sintered closed-porous Ag material (Matrix-dilute inclusion composite)

3.1. Introduction

Chapter 2 suggests that the porous Ag material provides high thermal conductivity, high strength, and highly durable temperature. It should be beneficial to state-of-the-art high-temperature SiC power electronics interconnections. Contrary, the high stiffness of the porous Ag material would be an issue against thermal strain. Excessive stiffness may lead to joint failure or fatal deformation. Therefore, its mechanical characteristics and applicability to high-temperature interconnections should be studied.

Some studies have reported the mechanical properties of sintered Ag materials [1]–[6]; however, there have been few studies conducted on the effect of metallurgical and mechanical properties on die-attach reliability. The authors have previously investigated the bonding reliability and fracture behavior of a die-attach layer of sintered Ag joints for high-temperature power modules under thermal cycling tests. We found that the die-attach layer achieved a bonding reliability superior to that of conventional solder joints. Furthermore, cracks mainly propagated into sintered Ag joints [7]. Thus, it was determined that the metallurgical and mechanical properties of sintered Ag joints have a great impact on bonding reliability.

In this chapter, we investigated the effects of the metallurgical and mechanical properties of sintered Ag joints on bonding reliability. First, the metallurgical structure of sintered Ag materials was observed using electron microscopy. Second, the mechanical properties of the sintered Ag materials were evaluated using tensile tests of dumbbell-shaped sintered Ag films at elevated temperature. Third, the temperature dependence of die-attach reliability was investigated using thermal cycling tests of die-attached specimens composed of SiC power chips and DBC substrates under various temperature conditions. In addition, the dependence of bonding reliability on the microstructure was also examined. Finally, we determined the presumed fracture mechanism and described its advantages and potential issues for power electronics interconnections.

3.2. Experimental method

3.2.1. Tensile test of sintered Ag nanoparticles

A commercial Ag nanoparticle paste was used in this study. It was composed of Ag nanopaticles of approximately 20 nm in diameter, covered with an organic protective layer in an organic solvent. Ag nanoparticle paste was printed on a glass plate with the shape shown in Fig. 3.1. The paste was dried at 130°C for 30 min, after which it was sintered at 260 °C for 90 s with a bonding pressure of 10 or 30 MPa between the glass plates. The thickness after sintering was approximately 50 μm. The specimens were annealed at 350 °C for 1 h in N_2 atmosphere after sintering in comparison with the as-sintered specimens. Fabricated test specimens were removed carefully from the glass plate using a cutter blade for tensile tests.

The tensile test specimens were investigated using a scanning electron microscope (SEM), electron back-scatter diffraction analysis (EBSD), and a transmission electron microscope (TEM). Center area of the cross section across the tensile test direction was observed. The volume fraction of pores was obtained from the SEM images binarized using image editing software. The specimens for TEM were prepared using electrochemical polishing and ion milling. The tensile specimens were tested at 25, 100, 150, 180, 250, and 300 °C using a universal testing machine with an initial strain rate of 10^{-3} /s. Three specimens of each type were tested. The fracture surfaces of the specimens were observed with SEM.

3.2.2. Thermal cycling test of die-attached specimen

High-speed thermal cycling tests were performed to evaluate the die-attach reliability between SiC power chips and DBC substrates composed of two 0.3-mm-thick Cu electrodes bonded to a 0.6-mm-thick Si_3N_4 substrate. Fig. 3.2 shows the graphical illustration of the die-attached specimen for the thermal cycling tests. The power chips with dimensions of approximately 10 mm × 10 mm × 0.3 mm were sintered on DBC substrates at 260 °C for 90 s with a bonding pressure of 10 or 30 MPa. Die-attached specimens annealed at 350 °C for 1 h in N_2 atmosphere were also prepared for comparison with the as-sintered specimens. The thickness of the die-attached layer is approximately 50 μm.

The temperature profiles of the thermal cycling tests are shown in Fig. 3.3. The tests were conducted at temperatures of $T_{\max}$ = 200 °C and 250 °C with temperature amplitudes of ΔT = 150 °C. The cross-section of the die-attached layer before/after thermal cycling tests were observed by SEM.

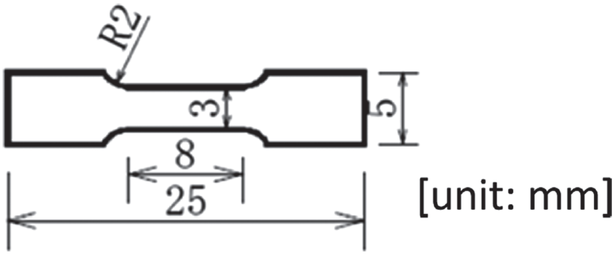

Fig. 3.1. Schematic of a tensile test specimen.

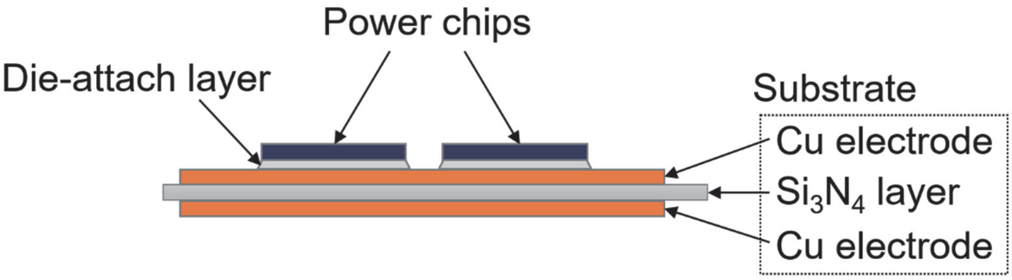

Fig. 3.2. Illustration of a die-attached specimen.

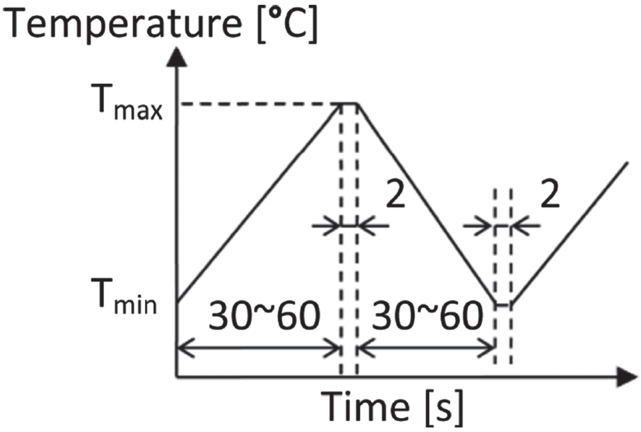

Fig. 3.3. Thermal profile of a thermal cycle test with T_{max} of 200 and 250 °C and ΔT of 150 °C.

3.3. Results

3.3.1. Microstructure of sintered Ag nanoparticles

Fig. 3.4 shows SEM images of the as-sintered tensile test specimens with bonding pressures of 30 and 10 MPa, and the 350-°C-annealed specimen after sintering at 10 MPa. The SEM images indicate that coarse pores disappeared with increasing bonding pressure. In addition, the annealing process produced coarsening of grains, coalescence of pores, and disappearance of minute pores. The porosity of the as-sintered at 30 and 10 MPa, and the annealed specimens were 8, 16, and 19%, respectively.

The crystal structure of the as-sintered specimen at 30 and 10 MPa, and the 350-°C-annealed specimen after sintering at 10 MPa were observed using EBSD and TEM. EBSD images as shown in Fig. 3.5 revealed that the as-sintered specimen showed a nanocrystalline structure with a grain size of approximately 150 nm, whereas the 350-°C-annealed specimen showed the grains of several microns. Moreover, TEM images as shown in Fig. 3.6 revealed that a crystalline structure without both apparent defects and inclusions was observed at the grain boundaries, and no unique structures were detected from the bright-field images and the diffraction patterns around the grain boundaries.

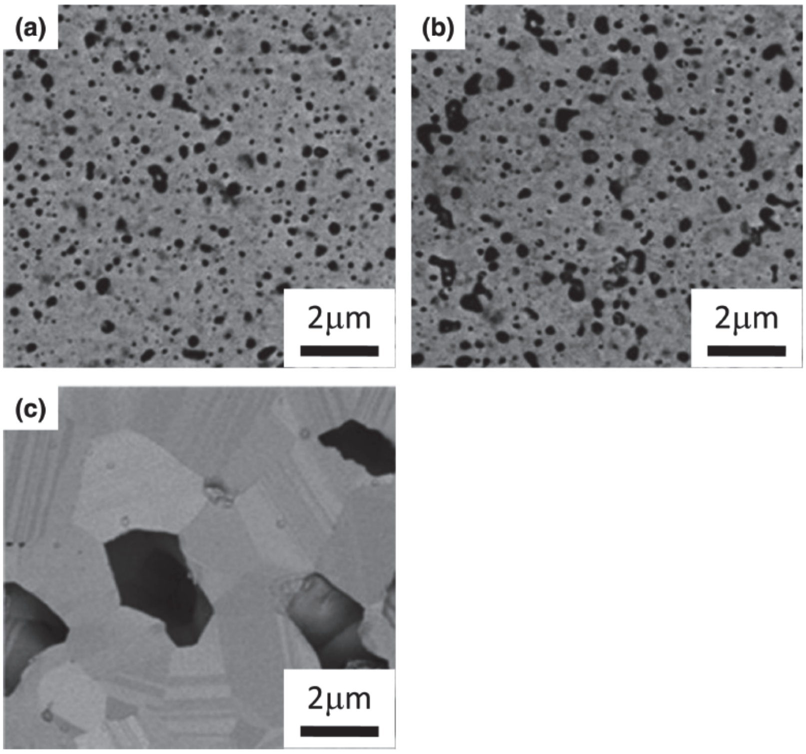

Fig. 3.4. SEM images of an as-sintered specimen with a bonding pressure of (a) 30 MPa and (b) 10 MPa, and (c) specimen annealed at 350 °C after sintering at 10 MPa.

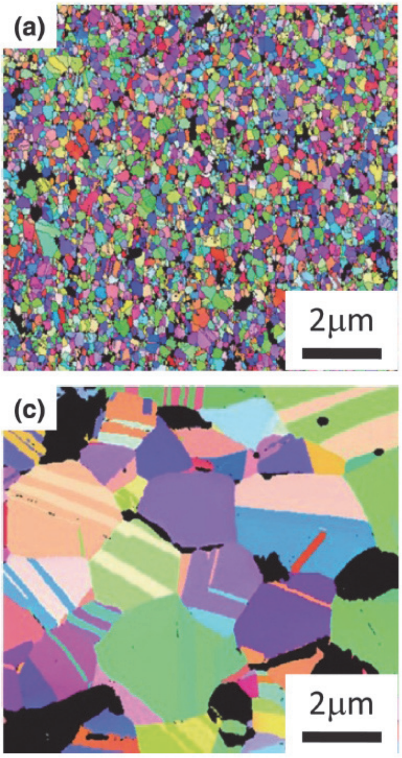

Fig. 3.5. EBSD images of an as-sintered specimen with a bonding pressure of (a) 30 MPa and (b) 10 MPa, and (c) specimen annealed at 350 °C after sintering at 10 MPa.

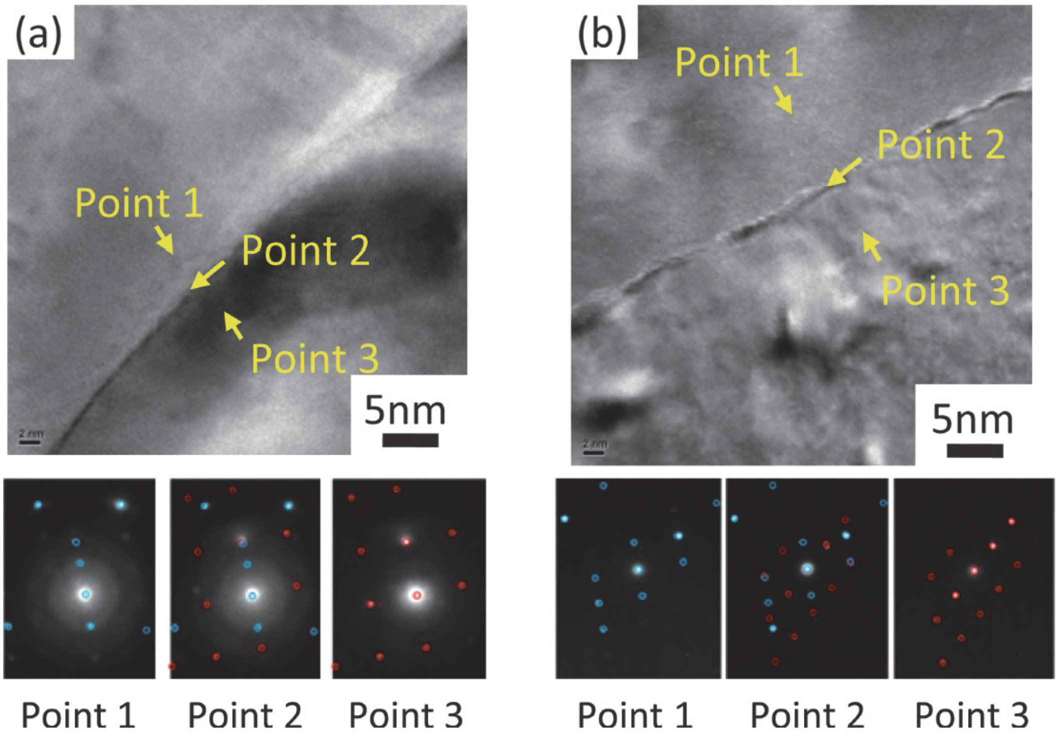

Fig. 3.6. TEM images of (a) as-sintered specimen with a bonding pressure of 10 MPa and (b) specimen annealed at 350 °C after sintering at 10 MPa. The insets show the diffraction patterns around grain boundaries.

3.3.2. Mechanical properties and fracture behavior

Tensile engineering stress–strain curves tested at room temperature (RT) are shown in Fig. 3.7. The ductility of the as-sintered specimens was extremely low. Furthermore, the increase of bonding pressure increased the tensile strength. The Young's modulus of the as-sintered specimens with a bonding pressure of 10 and 30 MPa were 9 and 11 MP, respectively. These values were remarkably lower than the values estimated by the FE simulations in Chapter 2. Additionally, annealing at 350 °C increased the ductility and decreased the tensile strengths.

Fig. 3.8 shows the fracture surfaces of the specimens after tensile tests at RT. Dimpled fractures were observed in both the as-sintered and annealed specimens. The dimple fracture size decreased as the bonding pressure increased, which leads to increased tensile strengths. Furthermore, the comparison between the as-sintered specimens and the annealed one showed that the correlation of grain size to dimple size was clarified.

Tensile engineering stress–strain curves tested at elevated test temperatures are shown in Figs. 3.9 and 3.10, respectively. Tensile strengths decreased and elongation apparently increased as the test temperature increased. Moreover, the tensile strengths with a bonding pressure of 10 MPa were equivalent to that of 30 MPa at elevated temperature. Fig. 3.11 shows the fracture surface tested at 300 °C. Apparent dimples were not observed. In indicated that the fracture mode changed through temperature variation.

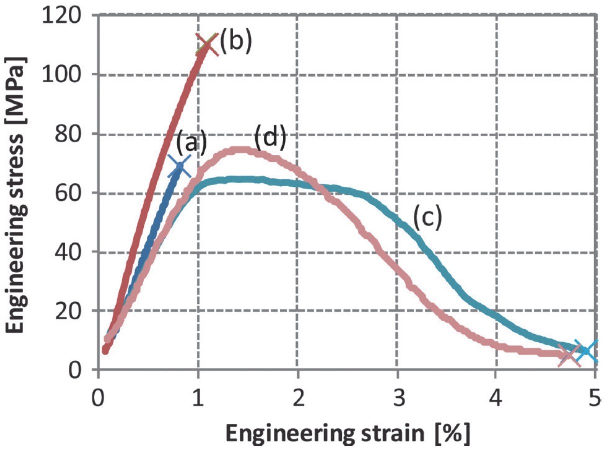

Fig. 3.7. Tensile engineering stress–strain curves of the as-sintered specimen with a bonding pressure of (a) 10 MPa and (b) 30 MPa, and the 350-°C-annealed specimen after sintering with a bonding pressure of (c) 10 MPa and (d) 30 MPa with a strain rate of 1×10^{-3} /s at RT.

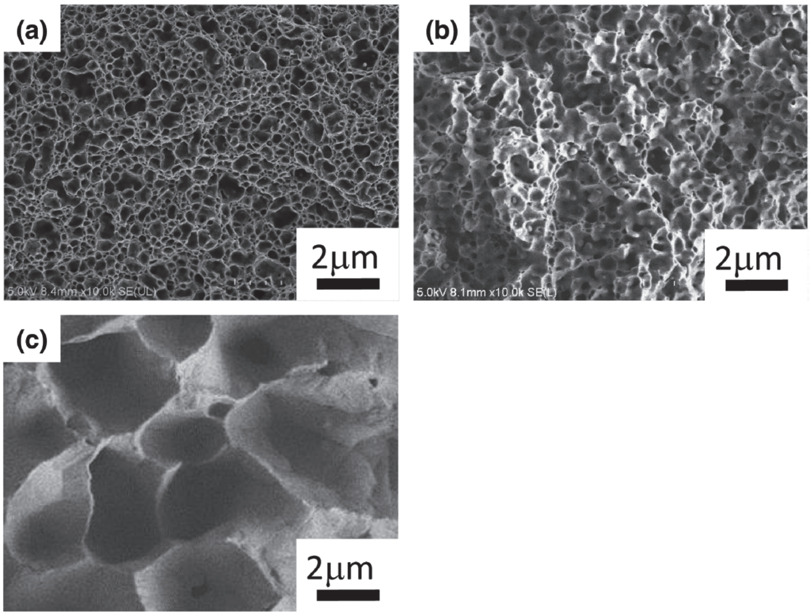

Fig. 3.8. Fracture surfaces of the as-sintered specimen with a bonding pressure of (a) 30 MPa and (b) 10 MPa, and (c) the specimen annealed at 350 °C after sintering at 10 MPa.

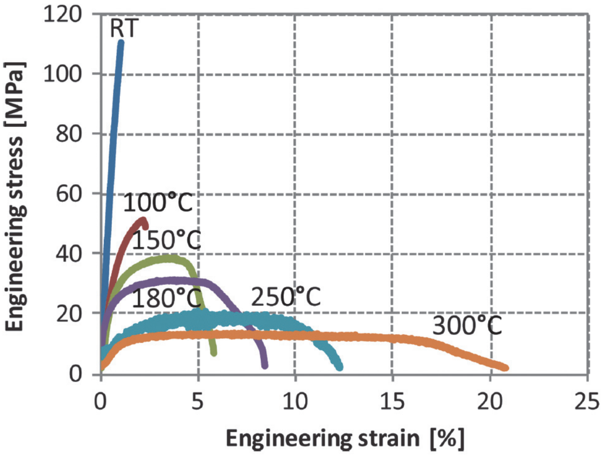

Fig. 3.9. Tensile engineering stress–strain curves of as-sintered specimen with a bonding pressure of 30 MPa tested at RT, 100, 150, 180, 250, and 300 °C with a strain rate of 1×10^{-3} /s.

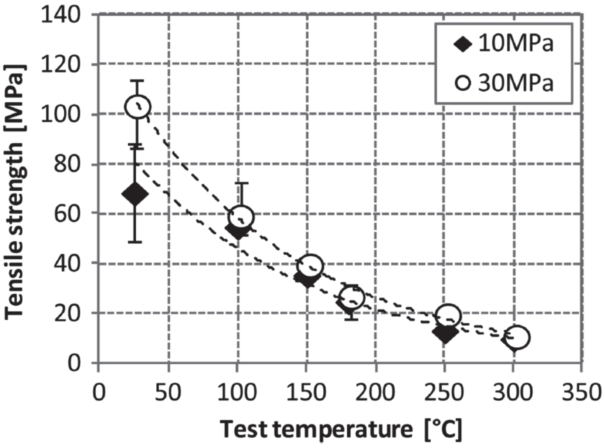

Fig. 3.10. Tensile strength of as-sintered specimens with a bonding pressure of 10 or 30 MPa as a function of test temperature from RT to 300 °C. Error bars represent the maximum and minimum values of each test condition.

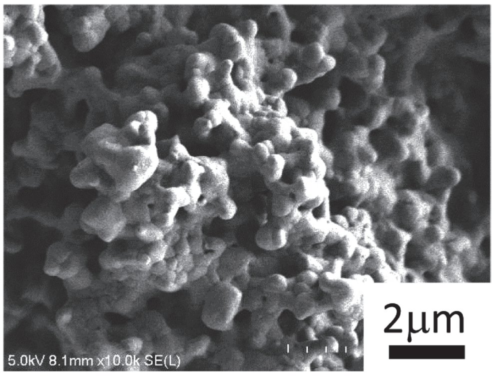

Fig. 3.11. Fracture surface of the as-sintered specimen with a bonding pressure of 10 MPa tested at 300 °C.

3.3.3. Fracture behavior of the die-attached specimens in thermal cycling tests

Fig. 3.12 shows SEM images of the cross section of die-attached layer bonded at 30 and 10 MPa, and the one annealed at 350 °C after bonding at 30 MPa, after 8000 thermal cycles at the temperature range of 100 °C to 250 °C. Undulated surface of a Cu electrode on a DBC substrate was observed on each specimen. The as-sintered die-attached specimen bonded at 30 MPa, as shown in Fig. 3.12 (a), showed excellent joint reliability at such extreme high-temperature cycling, where only slight vertical cracks were observed. This as-sintered joint of 30 MPa would maintain its favorable interconnection even after 250-°C-thermal cycles. The result verified the applicability of the sintered closed-porous Ag material to high-temperature SiC power electronics interconnections at 250 °C. In contrast, the as-sintered specimen bonded at 10 MPa, as shown in Fig. 3.12 (b), showed vertical cracks, pore expansion, and some horizontal cracks in places, which could impair its heat and electrical dissipation performance. Furthermore, the annealed specimen bonded at 30 MPa, as shown in Fig. 3.12 (c), showed severe vertically-horizontally connected cracks. This result suggests the validity of the as-sintered microstructure, i.e., the nanocrystalline and minute-pore-dispersed microstructure.

In order to clarify the effect of the maximum temperature of the thermal cycling tests, the die-attached specimen bonded at 30 MPa was evaluated at the temperature range of 50 to 200 °C. The result after 8000 cycles is shown in Fig. 3.13. A surface of a Cu electrode was observed to be almost flat. It shows the Cu electrode hardly deformed during cycles at $T_{\max}$ of 200 °C. Also, no cracks were observed. The results shown in Fig. 3.12 (a) and Fig. 3.13 indicate that the elevation of test temperature reduced crack resistance with plastic deformation of the sintered Ag layer and the Cu electrode of the DBC substrate.

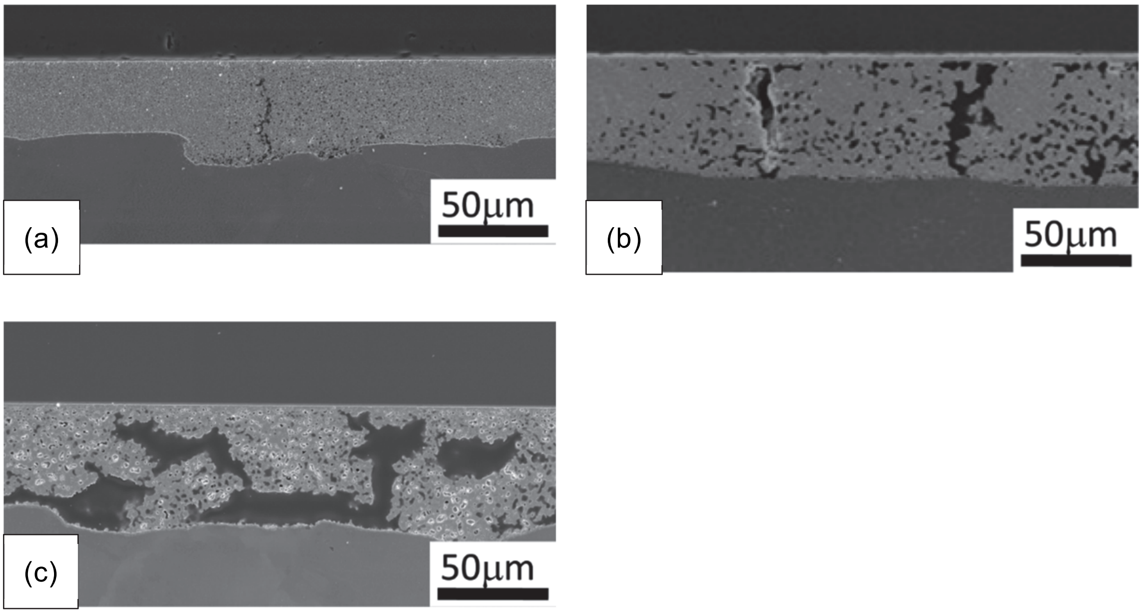

Fig. 3.12. Cross section of the as-sintered specimen with a bonding pressure of (a) 30 and (b) 10 MPa, and (c) the specimen annealed at 350 °C after bonding at 30 MPa and 8,000 thermal cycles at 100-250 °C.

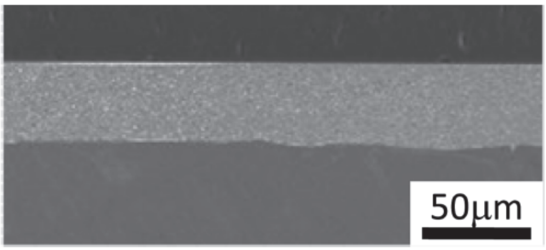

Fig. 3.13. Cross section of the as-sintered specimen with a bonding pressure of 30 MPa after 8,000 thermal cycles at 50-200 °C.

3.4. Discussion

3.4.1. Metallurgical and mechanical characteristics

The results of the tensile tests at RT, showing dimpled fracture behavior, indicated that plastic deformation occurred from the microscopic mechanism of ductile cracking, although the stress-strain curves of the as-sintered specimens seemed brittle as shown in Fig. 3.7. In nanocrystalline (grain size: ~250 nm) and ultrafine-grained metals (grain size: 250~1,000 μm), intragranular dislocation activity is limited, and the grain-boundary shear is considered to be the main mechanism of deformation [8]. A lack of strain hardening after an initial small deformation, which is known for nanocrystalline and ultrafine-grained metals, leads to strain localization under tensile loads [8]–[10]. Thus, it is assumed that the sintered Ag materials exhibit inherent mechanical properties in nanocrystalline metals.

Researchers reported the Young's modulus of sintered porous Ag materials. Herboth et al. [1], [2] obtained the Young's modulus of 10–40 GPa by tensile tests of the as-sintered specimens, which have the porosity of 3 and 15 vol%. Kraft et al. [6] showed the values ranged from 30–60 GPa by nanoindentation method, where the specimens were sintered with a pressure ranged from 1 to 20 MPa. Kariya et al. [4] obtained the value of 22 GPa by tensile test using sintered Ag films. Suzuki et al. [5] showed the values of 16–35 GPa by mechanical bending tests using the similar sintered films. These experimental researches, including our study, provided a wide range of experimental values of Young's modulus, which are remarkably lower than the calculated value in Chapter 2. This comparison indicates the impact of the inherent unclear mechanism of nanocrystalline sintered porous Ag materials, which is of particular interest in future work.

The tensile tests at elevated temperatures revealed that the sintered Ag materials showed apparent temperature-dependent mechanical properties. The temperature dependences of tensile strengths and the transformation of fracture behavior to intergranular fracture with temperature elevation are known in Ag [11], which indicating that intergranular fracture was also dominant for the sintered Ag materials. In addition, the onset of creep deformation of sintered nano-Ag materials [2], [4] and other fcc nanocrystalline metals, such as Cu [12], at RT caused by the Coble creep deformation mechanism has been reported based on the finding of the temperature dependency and the strain rate dependency. The sintered Ag materials in this research also might have shown the creep deformation at low temperatures driven by intergranular diffusion.

3.4.2. Thermal cycling reliability

Based on the metallurgical and mechanical properties of the as-sintered and annealed specimens, the bonding reliability through thermal cycling of die-attached joints were evaluated. The results showed the lower bonding pressure reduced crack resistant. Furthermore, the annealed specimen showed obvious cracks propagated. These results indicate that the coalescence of pores and/or the coarsening of grains decreased the die-attached reliability.

Thermal strains generated at the die-attached layer during thermal cycling tests were estimated using a closed-form solution of the thermo-elastoplastic strains [13]. Based on this estimation, the strain generated during thermal cycling tests with ΔT = 150 °C was found to be macroscopically within the elastic region when the yield stress of the die-attached layer was above 16 MPa. In this case, a maximum strain of 0.37% was estimated to have been generated during the thermal cycling tests. The estimation supposed that the plastic deformation occurred over the entire area of the die-attached layer at $\geq$ 250 °C based on the results of the tensile tests. The estimation, which revealed that the strain was within the elastic region at the temperature range of 50 °C to 200 °C, agreed with the results of the thermal cycling tests; it showed no cracks. In addition, it was estimated that the reduction of crack resistance was caused by plastic deformation at the temperature range of 100 °C to 250 °C. From the perspective of the microstructure, it was supposed that coarse pores induced fracture by stress concentration around them. Additionally, coarsening of grains through annealing presumed to reduce the crack resistance because of the offset of creep deformation in contrast with nanocrystalline metals.

Fig. 3.14 shows the presumed fracture mechanism based on the results of Figs. 3.12 and 3.13. Submicron-sized pores are dispersed in the die-attached layer at initial state. At the heating step, compressive strain occurs at the sintered Ag layer and the Cu electrode of the DBC substrate. During these steps, the plastic deformation of the Cu electrode, which softens at > 200 °C, coincided with the plastic deformation of the sintered Ag layer. At the following cooling step, tensile strain was generated. The tensile strain was locally large because of the inhomogeneity of the plastic deformation of the Cu electrode. Therefore, plastic deformation occurred locally in the sintered Ag layer with the expansion of the pores. Repetitive thermal cycles increased the amount of plastic deformation and the pore expansion as shown in Fig. 3.12. As a result, both vertical and horizontal cracks occurred, since the expanded pores were connected.

Given the fracture mechanism, it is understandable through the thermal cycling tests that the crack resistance was reduced by the increased amount of plastic deformation of the Cu electrode arising from the increased test temperature or thermal stress. With regard to the microstructure, the nanocrystalline structure and minute pore dispersion improve the bonding reliability, as mentioned previously. To achieve greater bonding reliability at higher temperature, the inhibition of coarsening of grains and pores, which might induce plastic deformation, would be important.

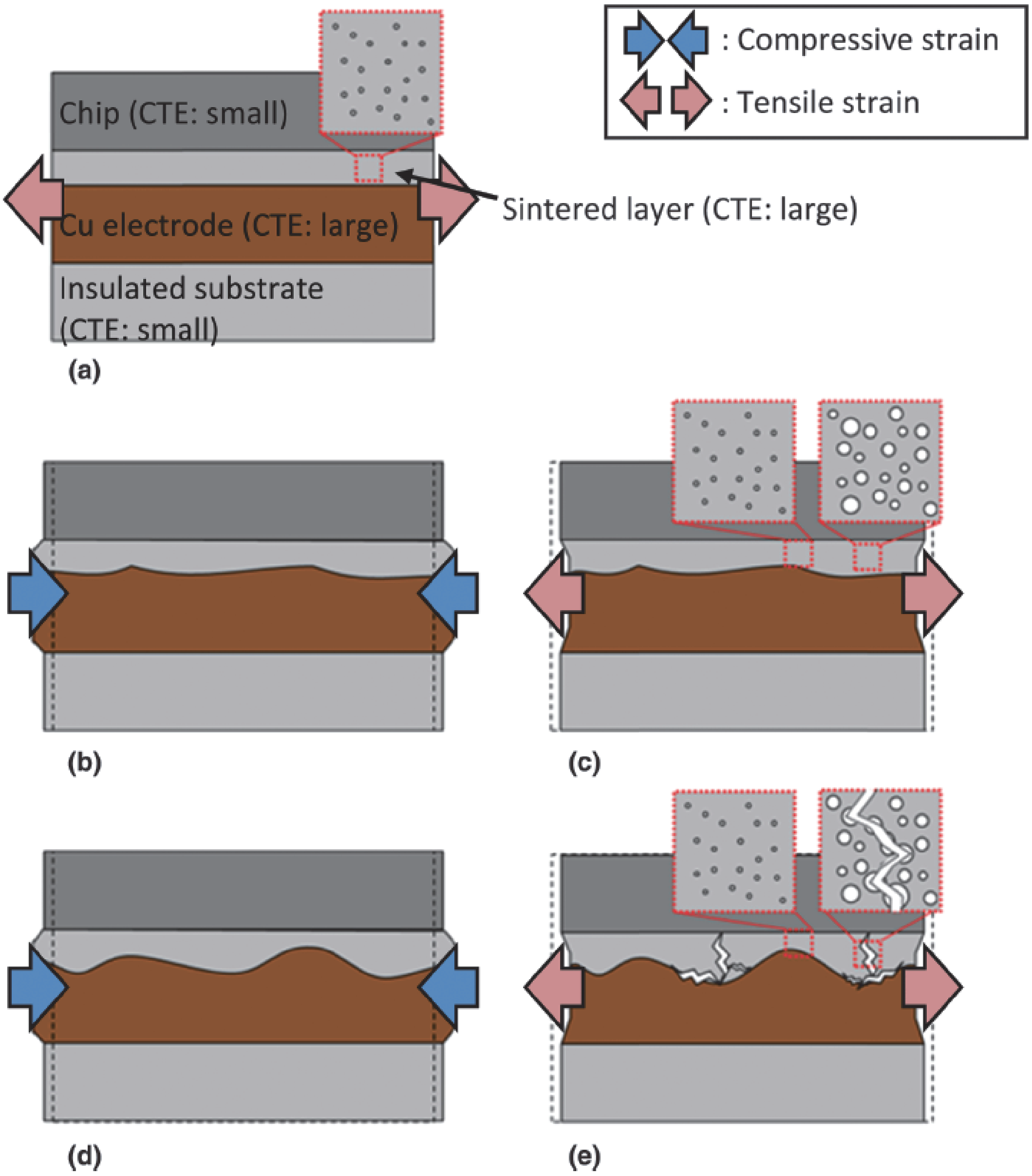

Fig. 3.14. Schematic of the fracture mechanism of the die-attached layer during a thermal cycle test. (a) Nanosized pores are dispersed in a sintered Ag layer at the initial state. (b) At the heating step, plastic deformation of the Cu electrode and sintered Ag layer occur through compressive strain. (c) At the cooling step, the generated strain is lower than tensile strain; however, expansion of pores occurs locally. (d) Repetitive thermal cycles increase the amount of plastic deformation. (e) Both vertical and horizontal cracks occur, since the expanded pores are connected. Moreover, coarse pores and micro-sized grains reduce crack resistance.

3.4.3. Advantages and potential issues

The characteristics of the sintered closed-porous Ag material revealed in this study are described, as follows:

- Young's modulus of 10–60 GPa, provided in this study and Refs. [1], [2], [4]–[6],
- thermal conductivity of 240 W/m·K [14],
- strength of 70–110 MPa, obtained by tensile test of sintered films, and
- durable temperature of 250 °C.

This material showed significantly high strength and was verified a high-temperature operation at a maximum temperature of 250 °C. It was also found to have a lower stiffness than estimated from the porosity. However, the mechanical properties with low elongation were revealed from a macroscopic perspective. Additionally, from an industrial point of view, the high cost of Ag-nanoparticle paste and the complexity of this sintering method, which requires high pressures, are assumed to be barriers to industrial applications. The advantages and potential issues of this material can be described, as follows:

- Advantages;
  - ➢ Excellent interconnection reliability and
  - ➢ excellent heat dissipation performance.
- Potential issues;
  - ➢ High material cost.

Considering these features, the sintered closed-porous Ag materials would be appropriate to the high-temperature interconnections, loaded by moderately low thermal strain, such as state-of-the-art SiC power module die-attachments. Further expansion of applications of the sintered Ag materials for electronics interconnections require simplified bonding process, such as pressureless process, and lower cost bonding material. Additionally, further experimental investigation on the impacts of the inherent nanocrystalline microstructure on the various properties is of particular interest.

3.5. Conclusions

This chapter demonstrated the mechanical characteristics and applicability to power electronics interconnections of the sintered closed-porous Ag material, fabricated by a sintering process at 260 °C with a bonding pressure of 10–30 MPa. Metallurgical and mechanical properties of this material were investigated, and the die-attach reliability was tested under different thermal cycling conditions. Nanocrystalline and coarsened microstructures were observed in the as-sintered and annealed state, respectively. TEM images showed a favorable crystalline structure along the grain boundaries regardless of whether annealing took place. Tensile tests revealed that the as-sintered Ag materials macroscopically showed low ductility compared with the annealed specimen at RT. The Young's modulus in the as-sintered state was lower than the estimated value in Chapter 2. Moreover, temperature-dependent mechanical properties were revealed in the as-sintered specimens. It was inferred that the as-sintered Ag materials showed the inherent mechanical properties of nanocrystalline metals.

The as-sintered die-attached specimen bonded at 30 MPa showed excellent joint reliability under thermal cycling test at a peak temperature of 250 °C, where only slight vertical cracks were observed. The as-sintered joint of 30 MPa would maintain its favorable interconnection even after 250-°C-thermal cycles. Furthermore, no cracks were observed at 50–200 °C. These test results indicate that the elevation of test temperature reduced crack resistance. Additionally, based on the comparison between the as-sintered and annealed states, thermal cycling fracture mechanism of this material was presumed. These evaluations suggest the favorable application of the porous Ag material to the high-temperature interconnections, such as state-of-the-art SiC power module die-attachments.

References in Chapter 3

[1] T. Herboth, C. Frilh, M. Gunther, J. Wilde, and R. B. Gmbh, "Assessment of Thermo-Mechanical Stresses in Low Temperature Joining Technology," in *2012 13th International Conference on Thermal, Mechanical and Multi-Physics Simulation and Experiments in Microelectronics and Microsystems, EuroSimE 2012*, 2012, pp. 1–7.

[2] T. Herboth, M. Guenther, A. Fix, and J. Wilde, "Failure mechanisms of sintered silver interconnections for power electronic applications," in *2013 IEEE 63rd Electronic Components and Technology Conference (ECTC)*, 2013, pp. 1621–1627.

[3] Y. Tan, X. Li, and X. Chen, "Fatigue and dwell-fatigue behavior of nano-silver sintered lap-shear joint at elevated temperature," *Microelectron. Reliab.*, vol. 54, no. 3, pp. 648–653, 2014.

[4] Y. Kariya, H. Yamaguchi, M. Itako, N. Mizumura, and K. Sasaki, "Mechanical Behavior of Sintered Nano-sized Ag Particles," *J. Smart Process.*, vol. 2, no. 4, pp. 161–165, 2013.

[5] T. Suzuki *et al.*, "Effect of manufacturing process on micro-deformation behavior of sintered-silver die-attach material," *IEEE Trans. Device Mater. Reliab.*, vol. 16, no. 4, pp. 588–596, 2016.

[6] S. Kraft, S. Zischler, N. Tham, and A. Schletz, "Properties of a novel silver sintering die attach material for high temperature - high lifetime applications," pp. 242–247, 2013.

[7] K. Y. Tatsumi Hiroaki, Kumada Sho, Yokomura Nobuo, Hino Yasunari, "Reliability of Sintered

Bonding Layer Using Silver Nanoparticles Under Cyclic Thermal Shock Test," in *The national meeting of Japan Welding Society*, 2014, pp. 104–105.

[8] M. A. Meyers, A. Mishra, and D. J. Benson, "Mechanical properties of nanocrystalline materials," *Prog. Mater. Sci.*, vol. 51, no. 4, pp. 427–556, 2006.

[9] Q. Wei, S. Cheng, K. T. Ramesh, and E. Ma, "Effect of nanocrystalline and ultrafine grain sizes on the strain rate sensitivity and activation volume: Fcc versus bcc metals," *Mater. Sci. Eng. A*, vol. 381, no. 1–2, pp. 71–79, 2004.

[10] S. Cheng *et al.*, "Tensile properties of in situ consolidated nanocrystalline Cu," *Acta Mater.*, vol. 53, no. 5, pp. 1521–1533, 2005.

[11] R. Carreker, "Tensile Deformation of Silver as a Function of Temperature, Strain Rate, and Grain Size," *J. Met.*, pp. 112–115, 1957.

[12] A. H. Chokshi, A. Rosen, J. Karch, and H. Gleiter, "On the validity of the hall-petch relationship in nanocrystalline materials," *Scr. Metall.*, vol. 23, no. 10, pp. 1679–1683, 1989.

[13] A. Yasukawa, "Closed-Form Solution for Thermo-Elastoplastic Strains in Semiconductor Chip Bonding Structures," *JSME Int. journal. Ser. A, Mech. Mater. Eng.*, vol. 36, no. 4, pp. 374–381, 1993.

[14] U. Scheuermann, "Reliability challenges of automotive power electronics," *Microelectron. Reliab.*, vol. 49, no. 9–11, pp. 1319–1325, 2009.

Chapter 4. Metallic mesh-embedded solder composite (Bicontinuous composite)

4.1. Introduction

Chapter 2 suggests the Cu-embedded solder composite was estimated to have high strength and thermal conductivity. It can replace conventional solders while improving joint properties. Contrary, the heat tolerance may be limited by the solder matrix. In particular, the changes in metallurgical microstructure and the decrease in joint strength against thermal loading should be discussed in detail. The material, bonding process, and the verification of this concept is investigated in this chapter.

Die-attach techniques for power modules are subject to continuous research and development that aims at miniaturization and ever-increasing power densities with lead-free, low-temperature joining solutions. Such multi-layered assemblies consist of dissimilar materials and suffer from time-dependent thermomechanical degradation during service under elevated and cyclic temperatures. Soldering can generally meet the requirements for large-scale production, and previous studies have investigated and improved various facets of solder joints.

Because interfacial IMC layers are prone to crack initiation and failure, degraded mechanical properties have been observed with, for instance, increasing interfacial IMC layer thicknesses and larger amounts of electroless Ni-P within the metallization system [1]–[5]. By contrast, the roughness of the IMC layer has been shown to improve the joint strength [2]. In addition, varying the chemical composition of widely-used lead-free Sn-based solder alloys has strengthened the joint by adding or modifying the content of alloying elements such as Ag, Ni, Bi, In, Sb, or Ce [6]–[11]. The enhanced resistance to mechanical and thermomechanical loading has been mainly attributed to solution- or precipitation-strengthening and optimized interfacial reaction conditions. Although the high melting temperatures of Zn- or Au-based solders [12]–[15] are expected to improve temperature resistance, the bonding temperature must also be raised above the melting point. Other studies have achieved mechanical reinforcement of solder joints by adding nano-sized materials such as Fe_2O_3, TiO_2, and SiC particles or graphene flakes [16]–[20].

Because soldered interconnections in power modules are exposed to elevated and cyclic temperatures, the time-dependent (creep) and time-independent (plastic) responses of solders have been investigated under these service conditions [21]–[24]. Sn-based solders have been found to obey power-law breakdown characteristics during creep [25], [26]. Recrystallized grain boundaries at positions of high stress, i.e., typically near semiconductor chip interfaces, have been identified as crack initiation sites [27], [28]. FE simulations have been applied to calculate local stresses and strains in solder joints to feed reliability models and to perform lifetime predictions and design optimization [29]–[32].

The approach presented here applies novel composite structures that consist of Sn-based solder and thin metallic meshes. The load-carrying matrix phase is composed of ductile solder, and the integration of the metallic mesh was expected to stabilize the solder against mechanical and thermomechanical loading and to increase the thermal conductivity of the joint. This work is motivated by other well-known composites, such as metal-matrix composites (MMCs) or fibre-reinforced polymers (FRPs), which beneficially combine the properties of the individual materials. In this chapter, this concept is verified through the microstructural and mechanical evaluation of such metallic mesh-embedded solder (solder-mesh) composite joints by microstructural observation and shear strength tests. The mechanical and thermal characteristics of the composite joints are supported by FE simulations. Moreover, the thermal and thermomechanical resistances of the solder-mesh composite joints to elevated and/or cyclic temperatures are clarified and benchmarked with solder reference joints.

4.2. Experimental method

4.2.1. Microstructural and mechanical characterization

Soldering was conducted with Cu substrates that had dimensions of 20 × 20 × 0.8 mm and 10 × 10 × 0.8 mm, respectively, and 99.96% purity. Cu and Ni meshes were cut into sizes that were slightly larger than the cross-sectional area of the smaller Cu substrate. The Cu and Ni meshes had filament diameters d of 75 and 65 μm, mesh thicknesses t of 180 and 160 μm, and mesh widths w of 430 and 340 μm, respectively. Commercial SAC305 solder paste with approximately 11% flux was applied on the bonding surface of the lower substrate as well as on the metallic mesh. The preform-like layer of metallic mesh and solder paste was placed between the Cu substrates. A schematic of the Cu-Cu specimen is shown in Fig. 4.1 (a), including the relevant geometric features. Figs. 4.1 (b) and (c) show top views of the Cu and Ni meshes, respectively, used in this study. Samples assembled with only SAC305 solder paste were used as references. Pressureless bonding was conducted in a reflow furnace (UniTemp GmbH) at a holding temperature of 240 °C for 60 s under N_2 (process type 1). Another set of parameters was identified as the result of a systematic process optimization. This process (type 2) was also run at 240 °C as the process atmosphere but switched from N_2 to vacuum. The microstructures of the Cu-SAC305-Cu, Cu-Ni mesh/SAC305(NMS)-Cu, and Cu-Cu mesh/SAC305(CMS)-Cu samples were analyzed by optical microscopy (OM, Olympus SZX7) and SEM (Hitachi S-3000H) after conventional metallographic preparation (grinding and polishing) and ion beam cross-section cutting (JEOL SM-09010), respectively. The joined assemblies were subjected to shear tests with a cross-head speed of 0.01 mm/s. The shear strengths were obtained from five samples for each joint type. The analyses of the fracture surfaces were performed by OM and SEM, respectively.

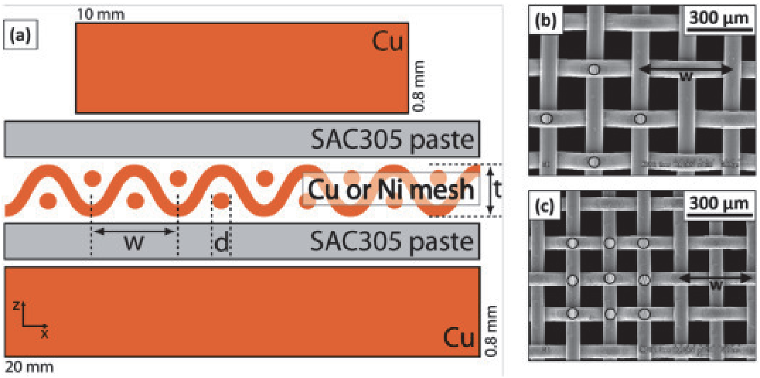

Fig. 4.1. (a) Schematic of Cu-Cu specimen using Cu or Ni mesh and SAC305 solder, including dimensions and geometric parameters. SE micrograph (top view) of (b) Cu mesh and (c) Ni mesh; round spots indicate CMS and NMS fracture locations (cf. Section 4.4.3).

4.2.2. Thermal aging test

The Cu-to-Cu samples with SAC305 solder (reference), CMS, and NMS bonding layers were produced with Type 2, as described above. These samples were exposed to a constant, elevated temperature of 150 °C for 500 h and 1000 h. The annealing test was performed under atmospheric conditions (Espec STH-120). Before and after annealing, five samples of each joint type were subjected to shear tests with a crosshead speed of 0.01 mm/s. The fracture surfaces were investigated by OM and SEM. Simultaneously, the microstructural features of the annealed samples were probed by SEM with mainly backscattered electron (BSE) contrast after the cross-sections had been ground and polished.

4.2.3. Thermal cycling test

Si chips were bonded to the DBC substrates with the SAC305 solder, CMS, and NMS composites. The Si chips had dimensions of 15 × 15 × 0.2 mm and Ni/Au (2/0.1 µm) top metallizations. Each DBC substrate was composed of a 0.63 mm Si_3N_4 ceramic sandwiched between two 0.3 mm Cu layers. The quarter-symmetrical schematic of a Si-to-DBC sample is shown in Fig. 4.2. Three Si-to-DBC samples of each variant were subjected to up to 8000 short temperature cycles. The temperature oscillated between 80 °C and 200 °C when the bottom sides of the samples were heated and cooled on two different plates within 20 s and 16 s, respectively. K-type thermocouples were attached on top of the Si chips using Kapton tape to ensure that the target temperatures were reached during the tests.

The quality of the bonding layers was investigated by non-destructive scanning acoustic tomography (SAT, Hitachi FineSAT) with a 75 MHz transducer in the as-bonded state and after a defined number of temperature cycles. The unbonded (or deteriorated) areas were quantified based on the contrast in the binary SAT images using ImageJ software. The degradation behaviors of the SAC305, CMS, and NMS composite joints were also investigated by SEM and BSE imaging of the cross-sections after temperature cycling. The chemical compositions of the IMC layers and solder matrices were analyzed by energy-dispersive X-ray spectroscopy (EDX, EDAX).

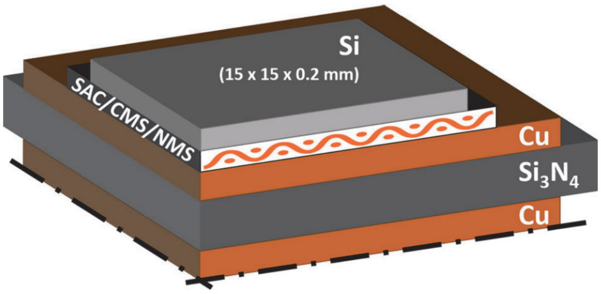

Fig. 4.2. Illustration of Si-DBC specimen interconnected with SAC305, NMS, or CMS composite.

4.3. Finite element analysis

4.3.1. Thermal simulation

Miniaturized 3D thermal FE models of the CMS and NMS systems were set up according to Fig. 4.3 (a). The mesh inlet with 5 × 5 interconnection points is shown separately in Fig. 4.3 (b). The geometries and dimensions from the experimental section were implemented considering the relevant thermal properties, i.e. the heat capacities C_p (Cu: 0.385, Ni: 0.502, SAC305: 0.23 J/g·K) and the thermal conductivities λ (Cu: 400, Ni: 90, SAC305: 55 W/m·K) of the materials. The averaged element size was chosen as 10 and 25 μm for the mesh inlet and solder matrix, respectively, which lead to a total element number of 400,000. The flanks of the layer were modeled as adiabatic. The thickness of the composite structure was systematically increased from 170 μm, i.e. the lower boundary given by the thickness of the mesh inlet, up to 300 μm.

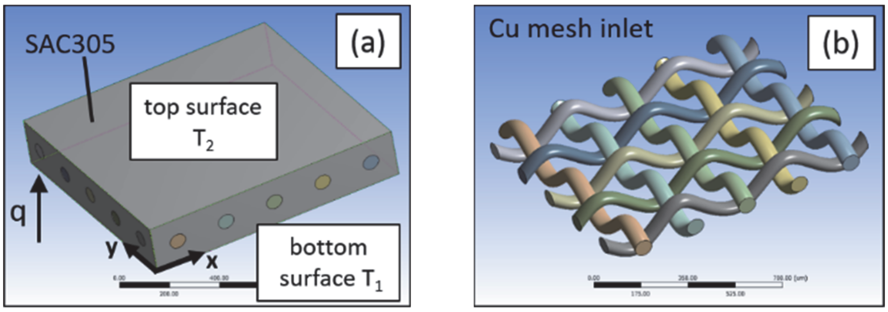

Fig. 4.3. FE model of (a) CMS, (b) mesh inlet with 5 × 5 interconnection points.

A constant heat flux q is applied on the bottom surface of the FE composite model for 2 s until equilibrium conditions are reached. The temperature fields on the bottom and top surface T_1(x,y) and T_2(x,y) are calculated. Fourrier’s law for stationary solutions is used to calculate the theoretical thermal conductivity λ in z-direction, as follows:

$$\lambda_z = \frac{q \cdot D}{\frac{1}{A_1}\iint_{btm} T_1(x,y)dxdy - \frac{1}{A_2}\iint_{top} T_2(x,y)dxdy}, \qquad (4.1)$$

where A is the surface area and D is the layer thickness. The thermal resistance R_{th} is the reciprocal value of λ_z.

4.3.2. Shear test simulation

3D FE models of the Cu-SAC305-Cu, Cu-CMS-Cu, and Cu-NMS-Cu systems were established using Ansys Workbench 17.2. The model is shown in Fig. 4.4 (a). The solder joint was modeled with miniaturized dimensions of 1.1 × 1.1 × 0.23 mm. The metallic mesh, as illustrated in Fig. 4.4 (c), was integrated with 5 × 5 interconnection points in the solder layer, considering the experimental geometric dimensions described in Section 4.2.1. Based on the experimental observations presented in Section 4.4.3, boundary conditions fixed the relative motion of parallel and perpendicular filaments at the intersection points. Ideal contact was assumed at the Cu substrate-SAC305 solder and the solder-metallic mesh interfaces. The model was meshed with a combination of hexagonal and tetrahedral elements. The averaged element edge length was set at 25 and 50 μm for the joint (SAC305 and metallic mesh) and Cu substrates, respectively, which resulted in 160,000 elements. The mechanical behaviors of Cu, Ni, and SAC305 solder were represented by the elasto-plastic properties summarized in Table 4.1. Circular defects with 600 μm diameters were added in the joint center as shown in Fig. 4.4 (b) to elucidate the impact of residues on the fracture behavior. The upper Cu substrate was loaded with a shear force that provoked strain-to-failure within the SAC305 solder, while the lower substrate was fixed against translational and rotational motion through boundary conditions. The linear-elastic response of the solder-metallic mesh layer is anisotropic. The elasticity parallel to the filaments can be approximated by the Voigt model while the direction perpendicular to the filaments is assumed to obey the Reuss model.

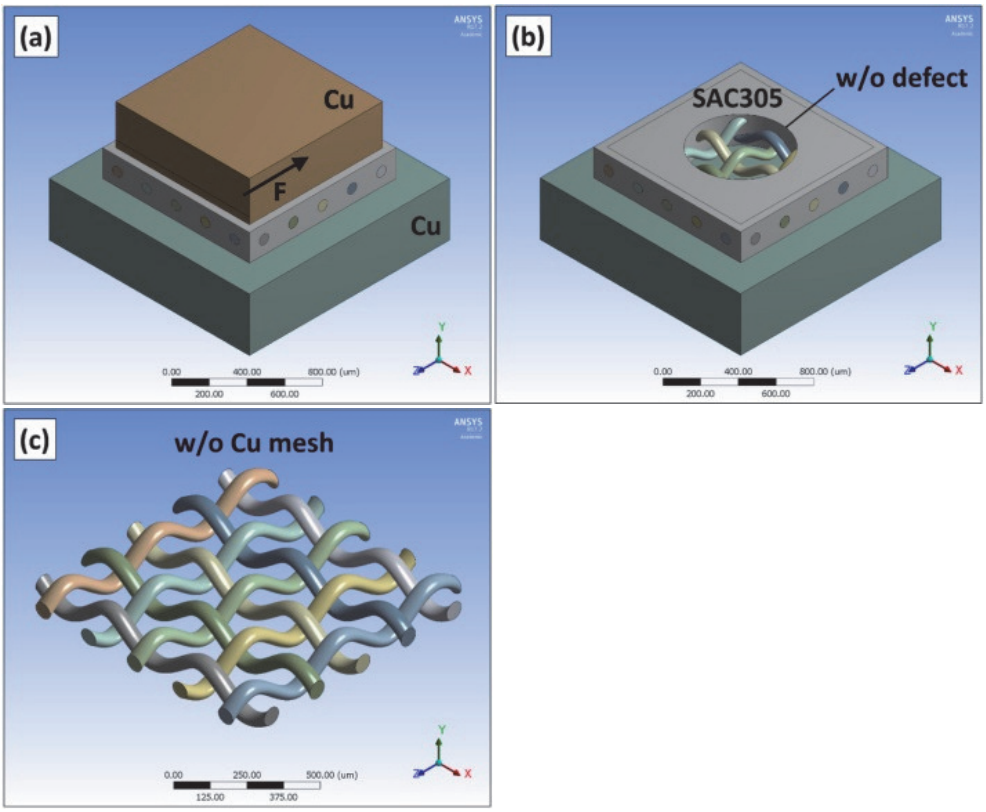

Fig. 4.4. FE shear test model showing: (a) the joined Cu-Cu specimen, (b) a central defect within the SAC305 solder, and (c) the structure of a 5 × 5 Cu mesh within the SAC305 solder.

4.3.3. Thermal cycling simulation

The model is shown in Fig. 4.5 (a) and consists of SAC305 solder, CMS, and NMS composite layers sandwiched between a Si chip and Cu layer. Miniaturized dimensions of 1.0 × 1.0 × 0.2 mm, 1.1 × 1.1 × 0.2/0.32 mm, and 1.5 × 1.5 × 0.3 mm were chosen for the Si chip, composite or solder joint, and Cu metallization, respectively, which were assumed to represent the (thermo-)mechanical characteristics of the experimental assembly fairly. The bonding layer thickness was selected as 200 μm or 320 μm. The Cu and Ni mesh inlets in Fig. 4.5 (b) have 5 × 5 interconnection points. Boundary conditions fixed the relative motions of the parallel and perpendicular filaments at the intersection points because these locations were found to be bonded through IMC formation, based on the experimental observations presented in Section 4.4.3. The boundary conditions were also applied to the bottom side of the Cu layer to block any translational and rotational motion. Ideal contact was assumed at the SAC305–Cu substrate, SAC305–Si chip, and solder–mesh interfaces. The model was meshed with hexagonal and tetragonal elements that had average edge lengths of 25 μm and 50 μm in the joint and substrates, respectively. The FE assembly was loaded with a temperature–time sequence that mimicked the short temperature cycling conditions described in Section 4.2.3. The calculations were performed for five steady-state cycles in which the temperature oscillated between 80 °C and 200 °C and the upper and lower temperature limits were approached asymptotically within 20 s and 16 s during heating and cooling, respectively (cf. Fig. 4.31).

The Si chip was modeled as linear-elastic. The thermo-mechanical responses of the Cu and Ni filaments as well as the Cu layer were approximated based on their elasto-plastic properties. Visco-elasto-plastic properties with hyperbolic sine (sinh) power-law breakdown characteristics were considered for the SAC305 solder matrix;

$$\frac{d\varepsilon}{dt} = C \cdot \left[\sinh\left(\alpha \cdot \sigma_{\mathrm{eq}}\right)\right]^{n} \cdot \exp\left(\frac{-Q_{\mathrm{a}}}{R \cdot T}\right), \tag{4.2}$$

where, $d\varepsilon/dt$ is the creep strain rate, σ_{eq} is the equivalent stress, C and α are multipliers, n is the stress exponent, Q_{a} is the activation energy, R is the universal gas constant, and T is the temperature. Most of the properties were temperature-dependent. Selected relevant physical parameters used in this study are summarized in Tables 4.1 and 4.2.

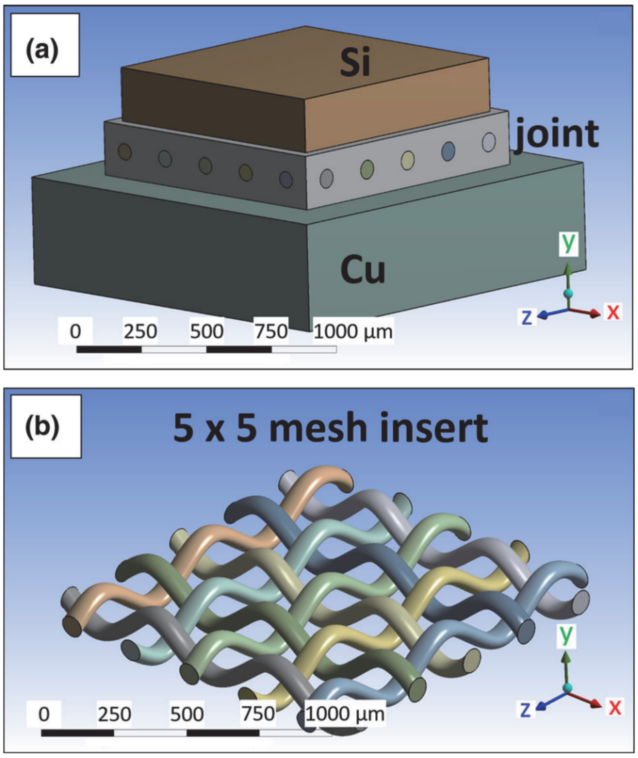

Fig. 4.5. (a) Si-Cu FE model for temperature cycling simulations, (b) 5 × 5 mesh insert within the solder.

Table 4.1. Summary of selected physical properties used in this study; data from Refs. [21], [23], [24], [33]

Material	Young's Modulus E (GPa)	Yield Strength σ_Y (MPa)	Ultimate Tensile Strength σ_{UTS} (MPa)	CTE α_{th} (10^{-6}/°C)
Si	112	--	--	2.6 (RT) 3.5 (250 °C)
Ni	207 (RT)	103	387	13.1
Cu	96 (0 °C) 88 (300 °C)	52 (0 °C) 42 (300 °C)	240 (0 °C) 178 (300 °C)	16.7
SAC305	46 (RT) 35 (100 °C) 4 (200 °C)	45 (RT) 15 (125 °C) 3 (200 °C)	58 (RT) 23 (125 °C) 4 (200 °C)	21.2 (RT) 22.0 (100 °C) 22.5 (200 °C)

Table 4.2. Hyperbolic sine creep parameters for SAC305 solder; data from Ref. [26]

C (s^{-1})	α (MPa^{-1})	n (-)	Q_a (kJ/mol)
2631	0.0453	5	52.4

4.4. Results

4.4.1. Experimental microstructure and proof of concept

Fig. 4.6 shows the cross-section of a Cu-SAC305-Cu joint after process type 1, with BSE contrast. Characteristic scallop-like Cu_6Sn_5 IMCs with thicknesses of approximately 2 μm evolved at the substrate-to-solder interfaces. The total joint thickness was measured to be 30 μm, and submicrometer-sized Kirkendall voids were found to be present within the IMC layer.

Fig. 4.7 (a) confirms that the Ni mesh generally integrated well in the solder layer, with almost no bonding defects at the NMS interface. The interfacial reaction layer between the substrate and solder was not affected when a Ni mesh was added into the solder joint, as shown in Fig. 4.7 (b). The high-magnification BSE images in Figs. 4.7 (c) and (d) reveal the formation of elongated and faceted Ni_3Sn_4 IMC at the NMS interfaces. Parallel and perpendicular filaments were bonded to each other at intersection points through the formation of the Ni_3Sn_4 IMC. This interconnection is assumed to result in a stiffening effect. The joint thickness that formed under the type 1 process conditions was determined to be 210 μm.

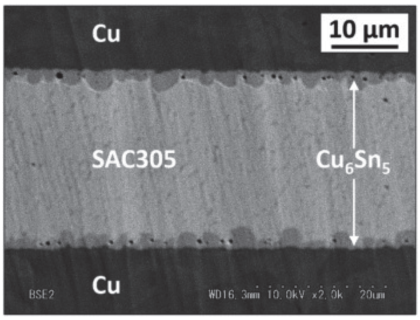

Fig. 4.6. BSE micrograph of a Cu-Cu joint soldered with SAC305 (reference).

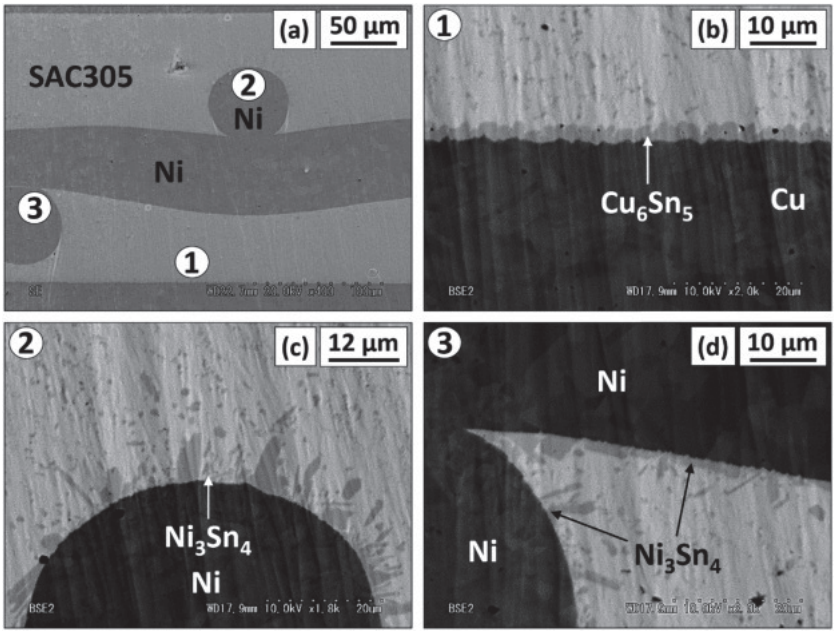

Fig. 4.7. BSE and SE micrographs of a Cu-Cu joint soldered with NMS composite: (a) the whole joint, (b) at the Cu substrate-SAC305 interface (pos. 1), (c) at the NMS interface (pos. 2), and (d) at the point between SAC305 and two intersecting Ni filaments (pos. 3).

Fig. 4.8 (a) confirms the favorable compatibility of the CMS composites. Scallop-like Cu_6Sn_5 IMCs with thicknesses of approximately 2 μm were observed at the substrate-solder and CMS interfaces, as shown in Figs. 4.8 (b) through (d). Fig. 4.8 (d) also shows that the parallel and perpendicular filaments were bonded to each other through IMC formation. The CMS joint thickness was measured to be 220 μm. Both CMS and NMS composite joints had joint thicknesses that were slightly larger than the metallic mesh thicknesses because an approximately 20–30-μm thick, continuous SAC305 solder layer formed between the metallic mesh and the upper and lower substrate under the pressureless conditions.

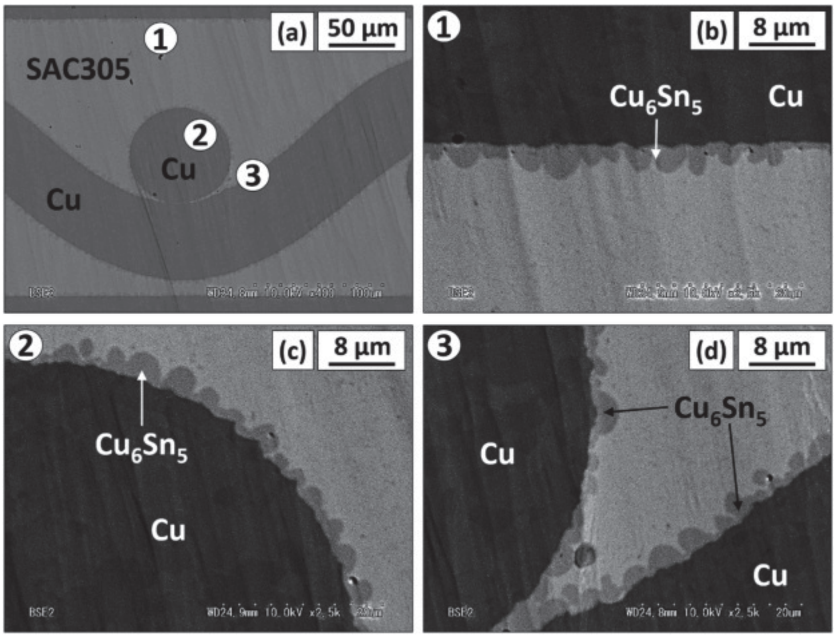

Fig. 4.8. BSE micrographs of a Cu-Cu joint soldered with CMS composite: (a) the whole joint, (b) at the Cu substrate-SAC305 interface (pos. 1), (c) at the CMS interface (pos. 2), and (d) at the point between SAC305 and two intersecting Cu filaments (pos. 3).

A favorable joint quality with homogeneous joint thickness and pronounced fillet formation can be observed from the full cross-section OM images shown in Fig. 4.9, where the solder-metallic mesh composite joints are shown with Ni mesh in Figs. 4.9 (a) and (b) and with Cu mesh in Figs. 4.9 (c) and (d). The woven structures of the metallic meshes differ slightly from each other. Both joints in Fig. 4.9 were produced with process type 2 parameters. These results confirm the feasibility of the proposed concept. The microstructural features after process type 2 were identical to those described above for process type 1 in Figs. 4.6 through 4.8. The difference between process types 1 and 2 will be addressed in the following section.

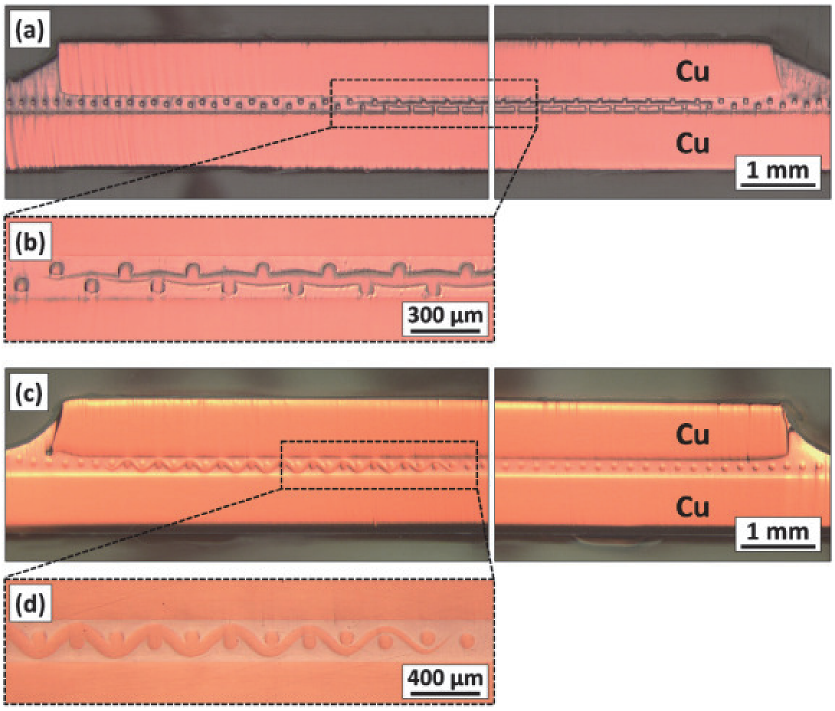

Fig. 4.9. Full cross-section and magnified OM micrographs of Cu-to-Cu joints fabricated by process type 2 using (a) and (b) NMS composite, and (c) and (d) CMS composite.

4.4.2. Thermal characteristic

The calculated temperature fields on the bottom and top surface T_1(x,y) and T_2(x,y), respectively, are shown in Figs. 4.10 (a) and (b). Spots with a slightly lower temperature are more or less homogeneously distributed on the surfaces. These local heat sinks are assigned to positions where the wavy mesh has a shorter distance to the surface compared to the surrounding volume and the Cu filaments serve as effective paths for heat transport. The calculated thermal conductivity and thermal resistance for the solder-mesh composite joints are plotted in Figs. 4.11 (a) and (b), respectively. High equivalent thermal conductivities of the mesh-SAC305 composites, particularly Cu mesh, were demonstrated. The equivalent thermal conductivity decreased with increase in the layer thickness because of the reduction of mesh volume fraction. The high λ-value of Cu enhances the overall conductivity of the Cu mesh/SAC305 composites compared to SAC305 layers with the same thickness. In other words, a 100 µm thick SAC305 layer should have a thermal resistance similar to a 230 µm Cu mesh/SAC305 composite layer. On the contrary, a Ni mesh inlet is not expected to significantly increase thermal conductivity.

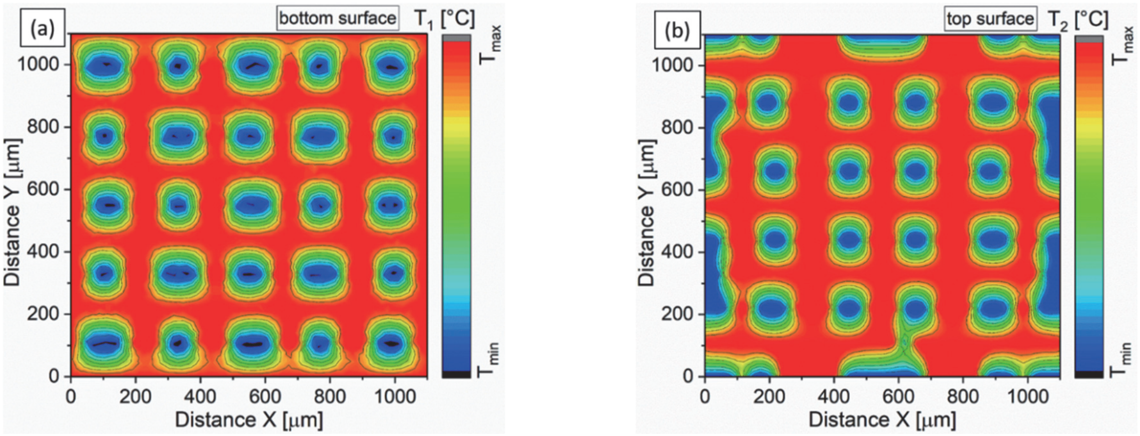

Fig. 4.10. Calculated temperature distribution on the (a) bottom and (b) top surface of a CMS joint.

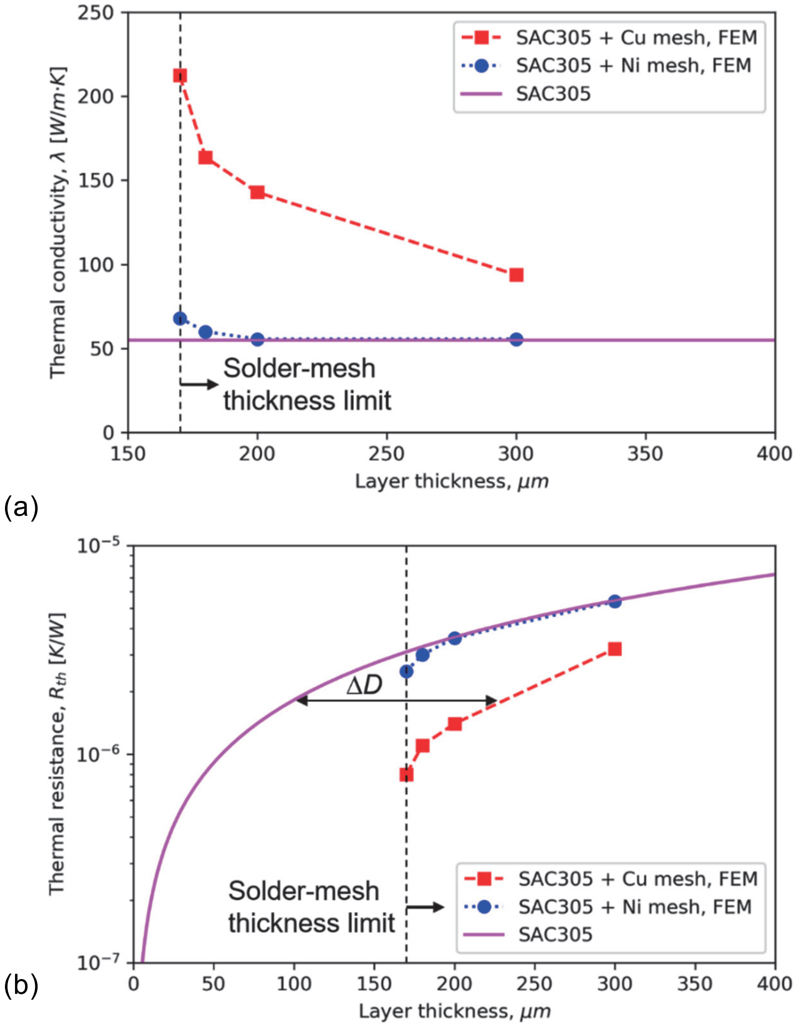

Fig. 4.11. Evolution of (a) thermal conductivity and (b) thermal resistance for SAC305, Cu mesh/SAC305 and Ni mesh/SAC305 composites as a function of layer thickness.

4.4.3. Shear strength and fracture

(a) Experimental results

The shear strengths of process type 1 samples were measured to be 32 ± 1.8, 33.7 ± 1.3, and 35.3 ± 1 MPa for joints consisting of SAC305, NMS, and CMS composites, respectively. The fracture surface analysis of the SAC305 joint indicated a steady fracture path throughout the soldered layer, as shown in the OM overview in Fig. 4.12 (a). Cracking occurred within the solder joint in the vicinity of the interface extending toward the upper or lower Cu substrate. Ductile fracture features, i.e. dimples, were found on the fractured solder layer, as shown in Fig. 4.12 (b). The solder layer contained spherical defects, as exemplified in Fig. 4.12 (c) by the un-bonded spot with a diameter of approximately 500 µm. The brighter contrast at the defect periphery is caused by the charging effects of polymeric residues in the joint.

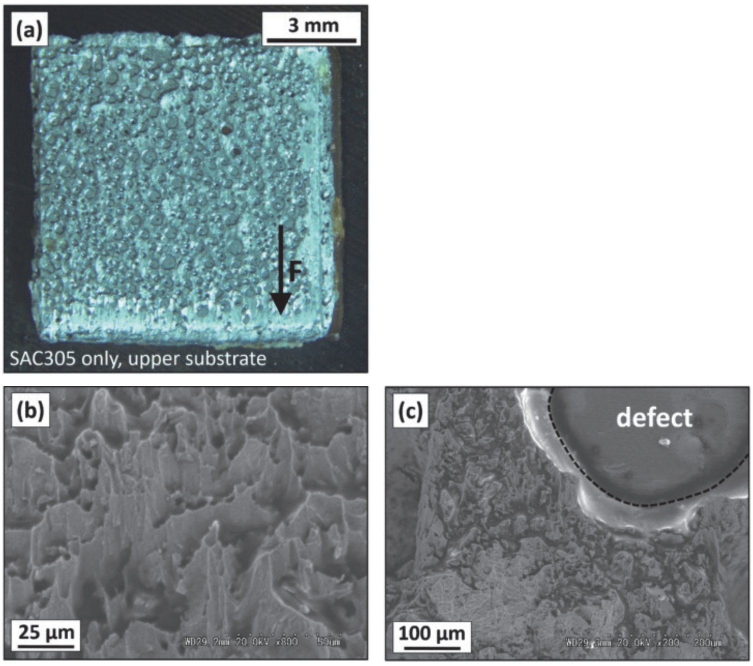

Fig. 4.12. Fracture surface of process type 1 Cu-Cu joint soldered with SAC305 showing: (a) OM micrograph of the whole upper fracture surface; and SEM images of (b) dimples in the SAC305 solder and (c) a circular defect surrounded by a ring of residue with brighter contrast.

The fracture surface of the process type 1 joint with Cu mesh shown in Fig. 4.13 (a), was divided into region A with ductile features and region B where cracking occurred along the solder-metallic mesh interface, as shown in Fig. 4.13 (b). Fig. 4.13 (c) shows that the filaments are cut in the transition zone from A to B despite the higher specific strength of Cu compared to SAC305. Fracture was initiated at the joint edge, and the crack propagated between the metallic mesh and upper substrate up to the transition zone, where the mesh was cut and the cracking path diverged down toward the lower substrate. Filaments that were positioned perpendicular to the shear load were bent toward the Cu substrate with an approximately 45°-angle, as can be seen in Fig. 4.13 (d). By contrast, filaments parallel to the external load fractured without being bent, as shown in Fig. 4.13 (c). Residues were found at the transition zone from A to B, as indicated by the darker contrast in in Fig. 4.13 (c). Such residues were preferentially located where the metallic mesh was cut. The replacement of the Cu mesh by the Ni mesh resulted in identical fracture features. These fracture characteristics will be discussed below.

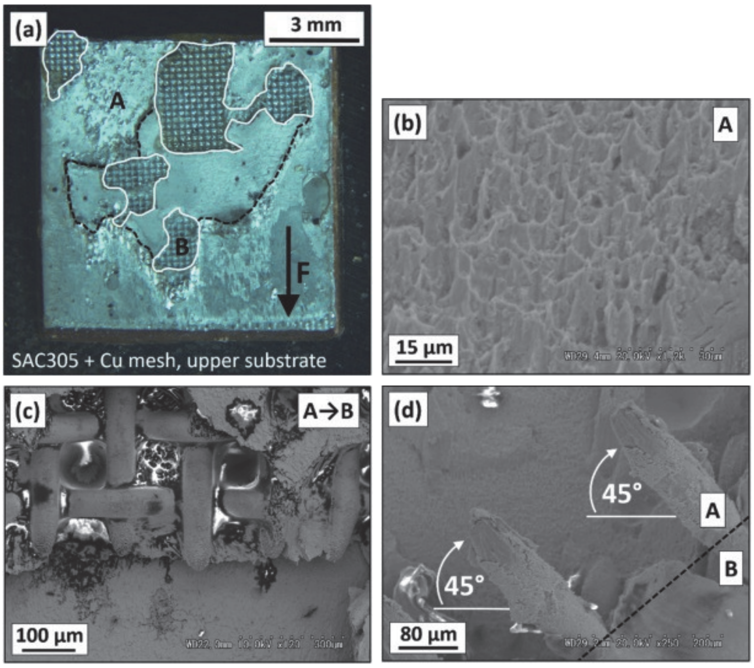

Fig. 4.13. Fracture surface of process type 1 Cu-Cu joint soldered with Cu mesh-SAC305 composite showing (a) OM micrograph of the whole upper fracture surface; and SEM images of (b) dimples in the SAC305 solder; and SEM images of mesh and fractured Ni filaments (c) parallel and (d) perpendicular to the loading direction with spots of residues.

With the type 2 process, the shear strength increased to 44.1 ± 6 (+38%), 44.7 ± 4.7 (+33%), and 51.4 ± 3.2 (+46%) for joints with SAC305, NMS, and CMS composites, respectively. Fig. 4.14 visualizes the averaged shear strength for the three different joint architectures after process types 1 and 2, showing a higher shear strength tendency for CMS composite joints. In other words, the Cu mesh yielded a reinforcement effect and increased the strength by 16% compared to the reference SAC305 solder joint.

Different fracture characteristics were found for the SAC305 joint, and the fracture surface of the upper and lower substrates could be subdivided into regions A, B, C, and D, as shown in Figs. 4.15 (a) and (b). Close to the loaded edge in region A, an adhesive and brittle fracture initiated at the Cu_6Sn_5 IMC-SAC305 interface of the upper substrate, as can be seen in Fig. 4.15 (c). The fracture behavior switched to a ductile and cohesive mode in region B, as can be inferred from the dimples in Fig. 4.15 (d). The crack propagated in the vicinity of the upper substrate. Although the fracture mode remained ductile in region C, the cracking path moved toward the lower substrate, as illustrated in Fig. 4.15 (e). Brittle and adhesive cracking toward the lower substrate again occurred at the end opposite to the load introduction, in region D. The area fraction of ductile failure (in B+C) was measured to be 78%.

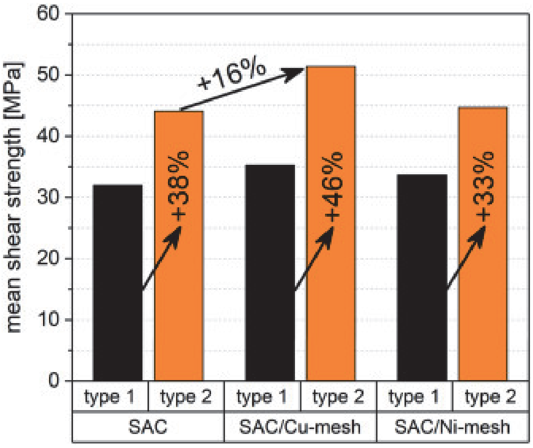

Fig. 4.14. Comparison of mean shear strengths among joints with SAC305, CMS, and NMS composites fabricated by process types 1 and 2.

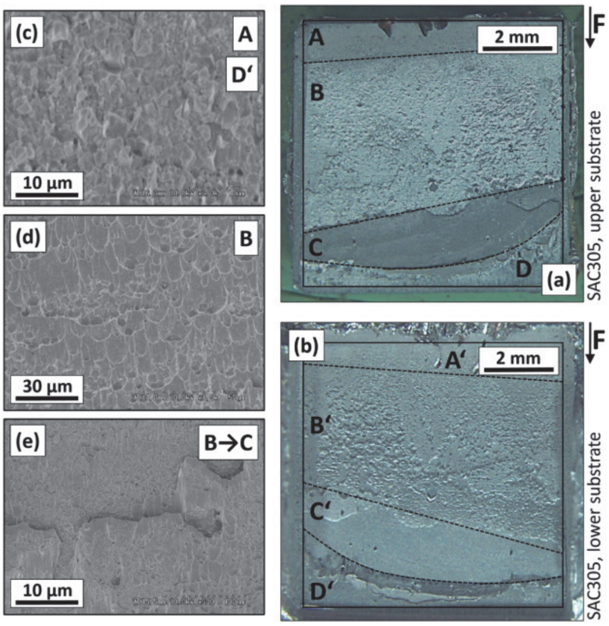

Fig. 4.15. Fracture surface of process type 2 Cu-Cu joint soldered with SAC305, showing OM micrographs of the whole (a) upper fracture surface and (b) lower fracture surface; SEM images of (c) brittle fracture in region A (also representative for region D′), (d) ductile fracture in region B; and (e) transition from regions B to C.

A highly structured fracture pattern can be observed from the upper and lower fracture surfaces of the CMS joint in Figs. 4.16 (a) and (b). Adhesive and brittle fracture initiation appeared at the loaded edge toward the upper substrate, as shown in Fig. 4.16 (c); this region was defined as region

A. In accordance with the SAC305 joint, the failure mode changed from brittle to ductile in region B, as suggested by Fig. 4.16 (d). A rough pattern appeared during the transition from regions B to C, as shown in Fig. 4.16 (e). The largest part of the fracture surface can be described by the characteristics found in region C (or C'). A well-structured pattern was observed in this zone, which represents the integrated Cu mesh. Periodic features in Fig. 4.16 (f) can be ascribed to the mesh width *w*. The higher magnification in Fig. 4.16 (g) clarifies that the fracture path tore holes down to the metallic mesh at locations where the mesh and the upper substrate were closest to each other. The surrounding fracture within the SAC305 solder contained ductile features. Further magnification in Fig. 4.16 (h) finally reveals ductile and brittle fracture on the peak area of the Cu mesh, which is attributed to interfacial failure between Cu_6Sn_5 IMC on the Cu mesh and the SAC305 solder. In contrast to the corresponding joint fabricated by process type 1 as shown in Fig. 4.13, the metallic mesh in the joint fabricated by process type 2 was not cut and fracture consequently occurred between the mesh and the upper substrate throughout the joint. The characteristic region C covered an area fraction of 76%. When only region C was considered, the area fraction of CMS fracture spots (cf. Fig. 4.16 (g)) was 13%.

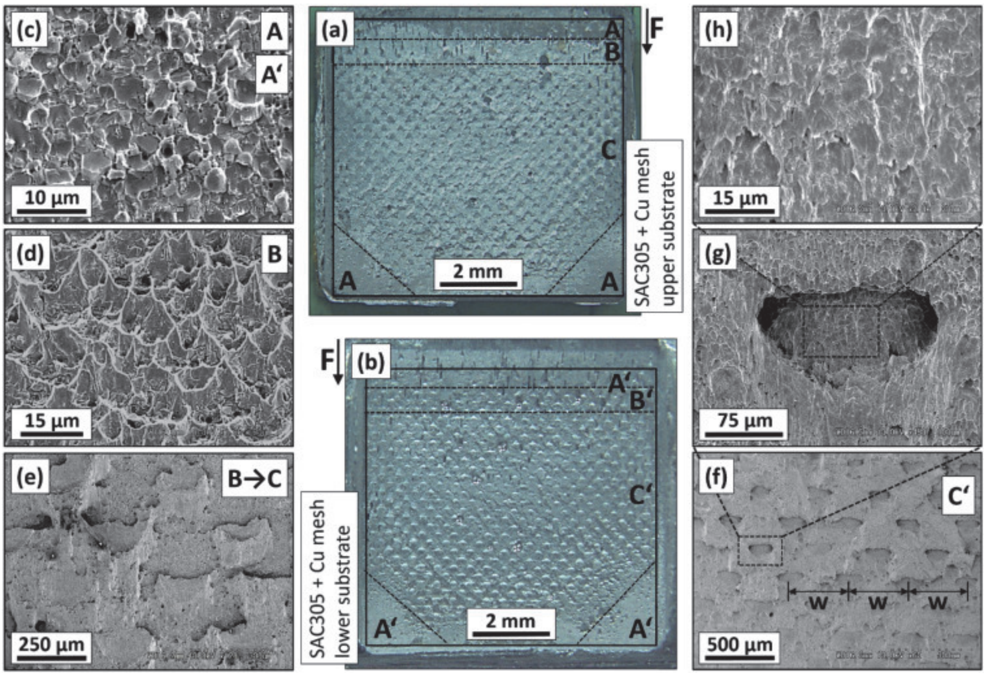

Fig. 4.16. Fracture surface of process type 2 Cu-Cu joint soldered with CMS composite, showing OM micrographs of the whole (a) upper fracture surface and (b) lower fracture surface; SEM images of (c) brittle fracture in region A (also representative for region A′), (d) ductile fracture in region B, and (e) transition from regions B to C; and (f) mesh-induced fracture pattern in region C′ with magnified view in (g) and (h).

The NMS joint fracture surfaces of the upper and lower substrates can also be subdivided into regions A, B, and C, according to Figs. 4.17 (a) and (b). The initial brittle interfacial fracture (A) in Fig. 4.17 (c) was followed by a ductile fracture within the solder (B), as shown in Fig. 4.17 (d), and then by the characteristic solder-metallic mesh fracture pattern (C), as shown in Figs. 4.17 (e) through (g). In contrast to the CMS joint, the area fraction of the solder-mesh fracture (C) was significantly reduced to 45%. Within region C, the area fraction of NMS fracture spots was higher, 30%, possibly because of the flatter structure of the Ni mesh. Because of the vacuum step added to the bonding process, very few residues appeared in any of the joint architectures, SAC305, NMS, or CMS.

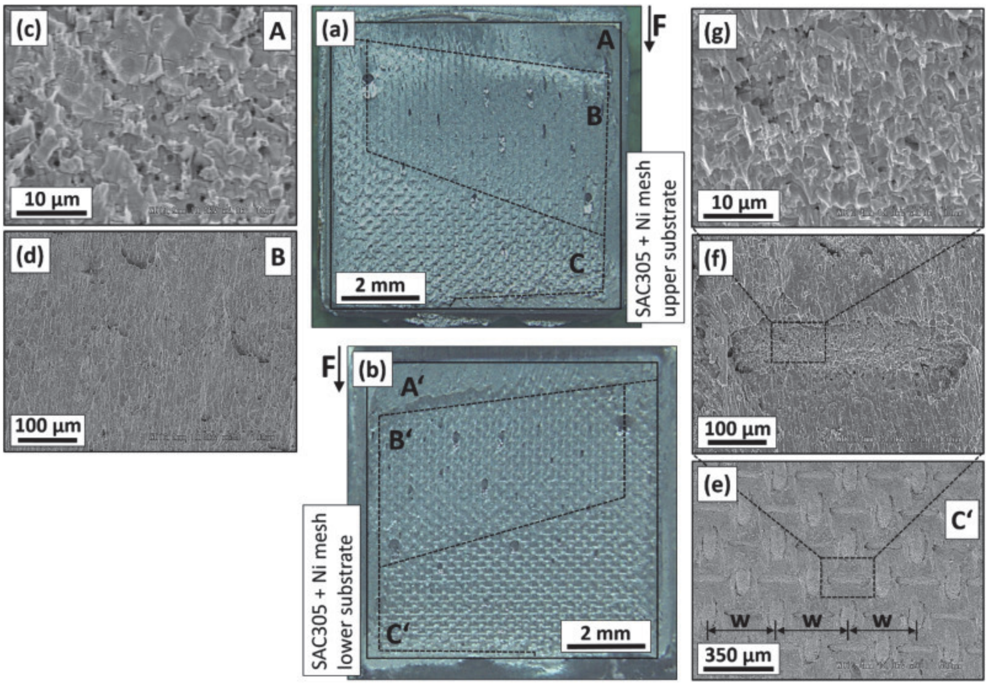

Fig. 4.17. Fracture surface of process type 2 Cu-Cu joint soldered with NMS composite, showing OM micrographs of the whole (a) upper fracture surface and (b) lower fracture surface; SEM images of (c) brittle fracture in region A, (d) ductile fracture in region B, and (e) mesh-induced fracture pattern in region C′ with magnified view in (f) and (g).

(b) Finite element results

Fig. 4.18 visualizes the Mises stress distribution on a Cu mesh inlet integrated in the SAC305 solder joint. In both cases, an external load was applied on the Cu substrate that locally (close to the loaded edge) provoked the fracture strain of approximately 30% within the SAC305 solder. For better visibility, the display of stresses in the solder as well as the upper and lower substrate was deactivated. Fig. 4.18 (a) shows that the Mises stress distributed relatively homogeneously across the mesh structure with average values of approximately 100 MPa. Local stress peaks up to 150 MPa are marked by the dashed rings located on distinct points of the metallic mesh surface where the distance between the mesh and the upper substrate was shortest. These stress peaks are in good agreement with the fracture characteristics observed in Figs. 4.16 (f) through (h) and Figs. 4.17 (e) through (g), where interfacial fractures occurred. By contrast, as shown in Fig. 4.18 (b), the stress distribution changed significantly when the solder-metallic mesh joint contained a central defect. This simulation considered the appearance of residue spots based on the experimental results presented in Fig. 4.13. Filaments within the defect were almost not loaded because they could deform freely. However, parts of filaments in the vicinity of the defect-solder interface become more strongly stressed. These locations are highlighted in the figure with dashed circles. Although the absolute Mises stress values of approximately 150 MPa, which were above the material's yield strength, were similar to the defect-free case, the full volume of the filaments was now locally subjected to the stress peaks. Filaments parallel to the load direction were predominantly loaded.

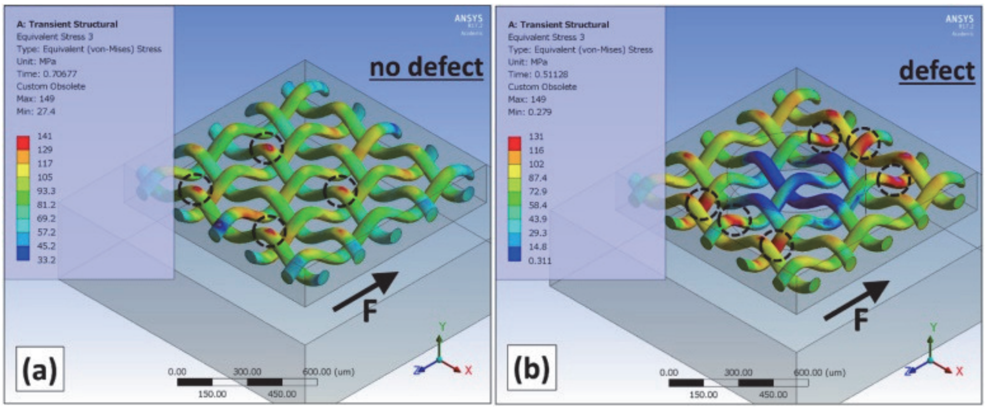

Fig. 4.18. Mises stress distributions in the Cu filaments for joints (a) without defects and (b) with defects, both loaded to the strain-to-fracture of SAC305 solder; dashed circles indicate spots of highest stress.

The evolution of equivalent plastic strain in the SAC305 solder was analyzed as a function of the applied external stress. Solder-mesh composite joints with and without central defects were compared to the corresponding SAC305 counterparts. Fig. 4.19 shows a plot of the normalized equivalent plastic strain versus the normalized external stress for direct comparison. A value of 1 for the normalized strain was equivalent to the strain-to-failure and indicated fracture. The results suggested that the defect-free solder-metallic mesh composite joints provided the highest resistance against mechanical shear loading. The defect-free SAC305 joints were expected to fail under an external load that was approximately 5% lower. Similar characteristics could be derived for the flawed soder-mesh and solder joints, and their strengths clearly decreased. These results indicated that a metallic mesh inlet could slightly reinforce a solder joint, probably through a stiffening effect that was probably also related to the IMC interconnection of parallel and perpendicular filaments during bonding.

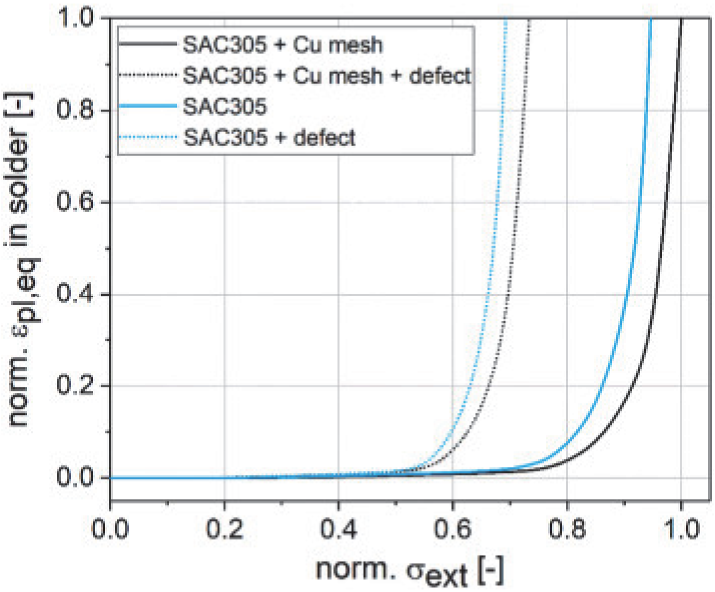

Fig. 4.19. Comparison of calculated normalized equivalent plastic strain over normalized external stress for Cu-Cu joints w/o Cu mesh and w/o central defect.

4.4.4. Resistance against elevated temperature

The Cu-SAC305-Cu samples had 2-μm-thick Cu_6Sn_5 IMC layers after bonding, as shown in Section 4.4.1. The exposure to 150 °C for 1000 h caused IMC layer thickening to approximately 9 μm at the Cu substrate–SAC305 solder interface, while the IMC layer could be divided into approximately equal portions of Cu_6Sn_5 and Cu_3Sn (ratio 1:1), as shown in Fig. 4.20. The remaining SAC305 solder layer was 10–15 μm thick.

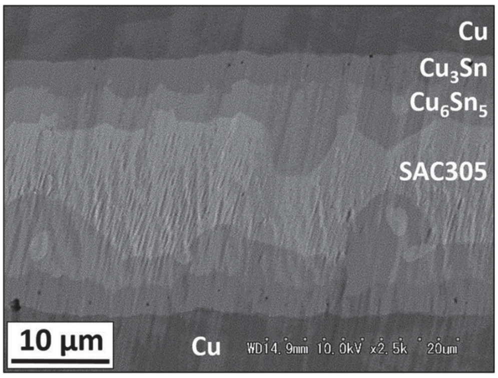

Fig. 4.20. BSE micrograph of a Cu-SAC305-Cu joint annealed for 1000 h at 150 °C.

Good structural integrity is evident in the whole cross-sectional SEM image of the NMS joint after annealing at 150 °C for 1000 h in Fig. 4.21 (a). The average IMC thickness at the Cu substrate–solder interface in Fig. 4.21 (b) was measured to be 7.5 μm. However, the ratio between Cu_6Sn_5 and

Cu_3Sn in the IMC was shifted to 4:1. Some defects, which seemed to be caused by spalling effects, formed at the interface between the Ni_3Sn_4 IMC and solder, as can be seen in Fig. 4.21 (c).

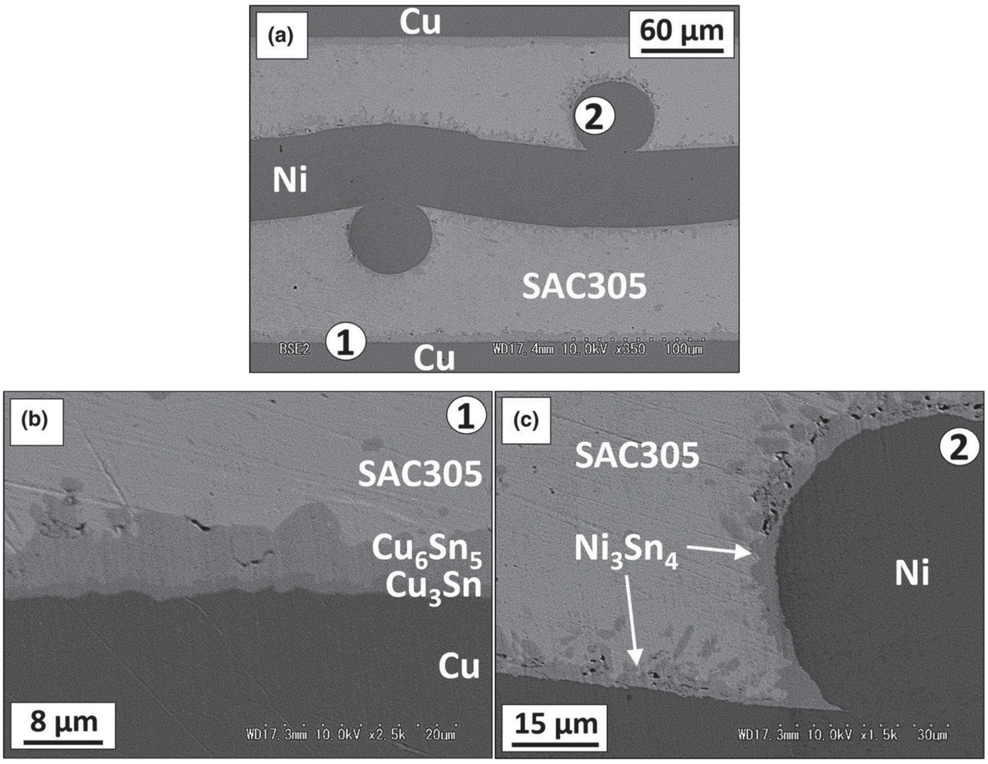

Fig. 4.21. BSE micrographs of a Cu-Cu joint soldered with NMS composite annealed for 1000 h for 150 °C (a) as a whole joint, (b) at the Cu substrate–SAC305 interface (pos. 1), and (c) at the triple point between SAC305 and two intersecting Ni filaments (pos. 2).

No significant structural degradation is observable in the CMS composite joint after 1000 h of annealing in Fig. 4.22 (a). The total thickness of the IMC layer at the substrate–solder interface in Fig. 4.22 (b) evolved to 6 μm, containing equal portions of Cu_6Sn5 and Cu_3Sn (1:1). The IMC layer at the solder–mesh interface in Fig. 4.22 (c) also consists of equal fractions of Cu_6Sn_5 and Cu_3Sn IMC and has a total thickness of 6.5 μm. Minor defects preferably occurred at the solder–IMC interface possibly because of mismatched thermal expansion or lattice structure (cracking, delamination) or unbalanced interdiffusion (Kirkendall voiding). Comparison of the microstructural features of the SAC305, NMS, and CMS joints after annealing proves that the metallic mesh inlet impacts the appearance of interfacial defects and the IMC ratios.

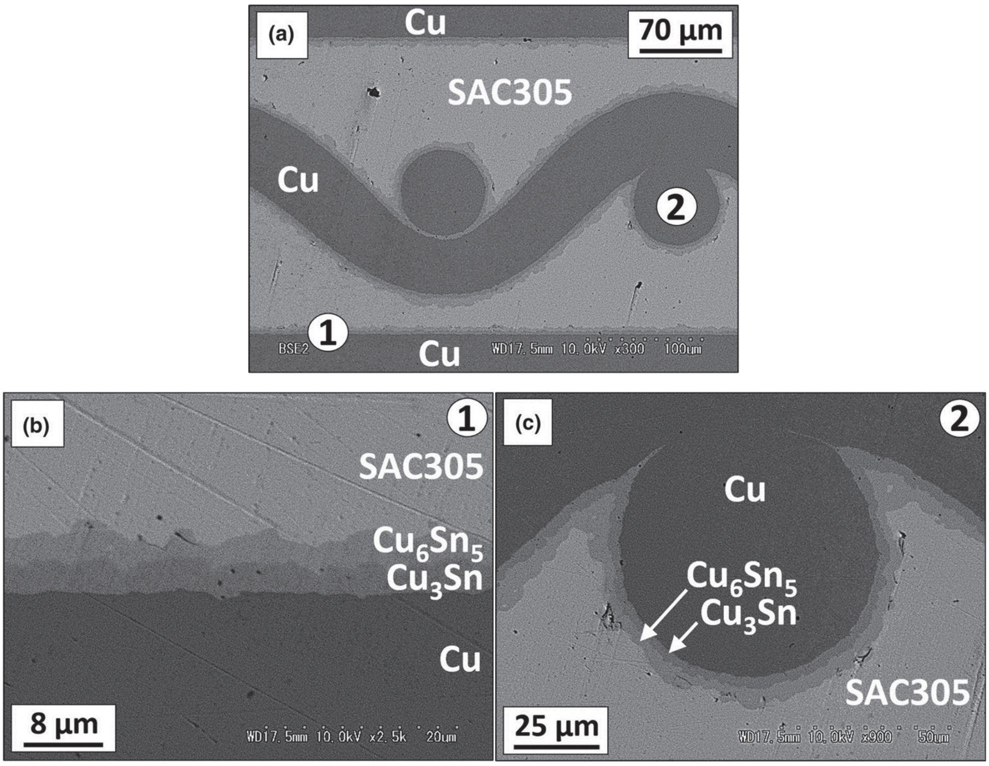

Fig. 4.22. BSE micrographs of a Cu-Cu joint soldered with CMS composite annealed for 1000 h for 150 °C (a) as a whole joint, (b) at the Cu substrate–SAC305 interface (pos. 1), and (c) at the triple point between SAC305 and two intersecting Cu filaments (pos. 2).

The shear strength evolution is plotted in Fig. 4.23 as a function of the type of bonding layer and annealing time. The shear strength of the SAC305 joints decreases from 44.1 ± 6 MPa to 36.4 ± 3.4 MPa after 500 h of annealing and recovers to 43.3 ± 7 MPa after 1000 h. It is assumed that IMC bridges locally connected both substrates, increasing the strength after the longer annealing time. The fracture surface analysis results in Fig. 4.24 reveal that ductile cracking behavior is preferable within the SAC305 solder layer in region B, as can be seen in Fig. 4.24 (c). A small fraction of the surface close to the shear load introduction was assigned to brittle and interfacial fracturing along the IMC layer in region A based on Fig. 4.24 (b). Another area in Fig. 4.24 (d) was marked as region C, where mixed-mode ductile and brittle failure was identified.

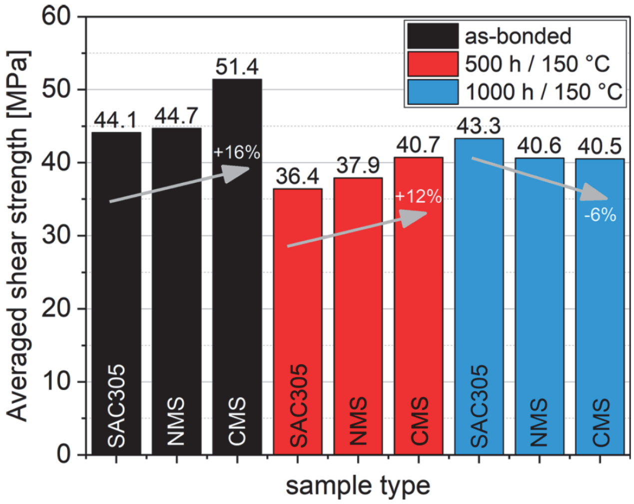

Fig. 4.23. Comparison of average shear strengths between joints with SAC305, CMS, and NMS composites, as-bonded and after annealing at 150 °C for 500 h and 1000 h.

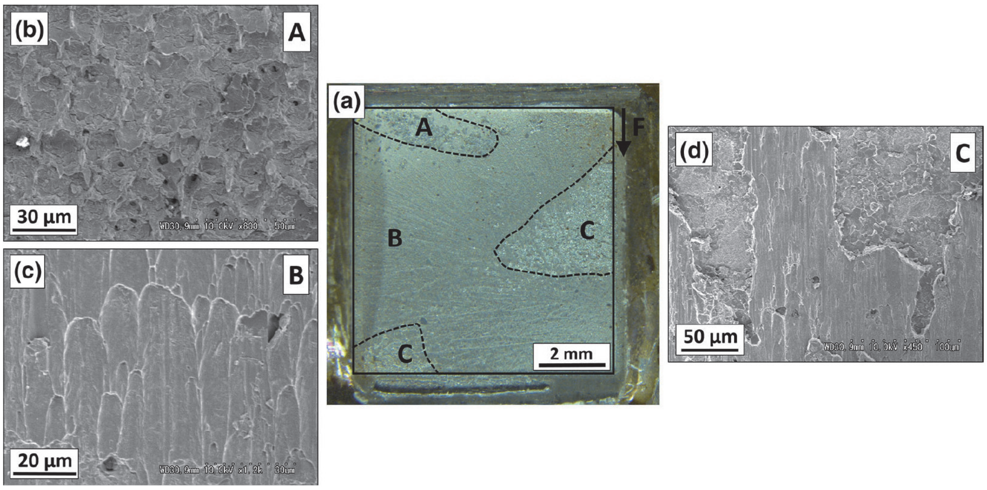

Fig. 4.24. Fracture surface of a Cu-SAC305-Cu joint annealed for 1000 h at 150 °C with (a) an OM micrograph of the whole lower substrate and SE micrographs of the (b) brittle fracture in region A, (c) ductile fracture in region B, and (d) mixed fracture mode in region C.

The NMS composite joints experienced a strength decrease from 44.7 ± 4.7 MPa to 37.9 ± 4.9 MPa after annealing for 500 h and slight recovery up to 40.6 ± 2.3 MPa after 1000 h. The fracture analysis in Fig. 4.25 proves that the cracks predominantly propagated through the SAC305 solder with ductile deformation features. The dimples in region B are evident in Fig. 4.25 (c). Only a weak interaction between the Ni mesh inlet and cracking path was derived from the checkered pattern in region B, which mirrors the geometry of the mesh in Fig. 4.25 (a). The interaction among the cracking path, mesh, and solder was much more pronounced in the as-bonded state when the fracture surface was covered with holes where cracking of the solder–mesh interface occurred. This fracture mode was described in detail in [38], where it was stated that this mode locally enhances the fracture resistance, which would explain the higher shear strength in as-bonded conditions. In the comparably small region A, the fracturing proceeded along the solder–mesh interface, as shown in Fig. 4.25 (b). This fracture type was probably triggered by the interfacial defects between the Ni_3Sn_4 IMC on the mesh and the SAC305 solder, according to Fig. 4.25 (c).

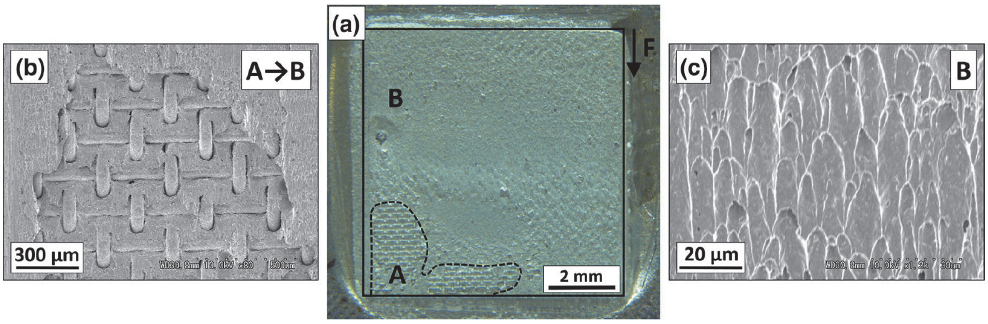

Fig. 4.25. Fracture surface of a Cu-Cu joint soldered with NMS composite annealed for 1000 h at 150 °C showing (a) an OM micrograph of the lower substrate and SE micrographs of the (b) interfacial solder–mesh fracture in region A and (c) ductile fracture in region B.

The greatest decrease in shear strength was measured for the CMS composite joints, when it decreased by approximately 10 MPa to 40.7 ± 1.7 MPa after 500 h. However, the strength remained nearly unchanged thereafter and was measured to be 40.5 ± 2.6 MPa after 1000 h. Figs. 4.26 (a) and (c) confirm the presence of mainly ductile deformation features in region B, which were caused by cohesive fracturing within the SAC305 solder. The magnified view of region A in Fig. 4.26 (b) shows a mesh-induced fracture pattern that suggests that the mesh contributed to the fracture behavior. In accordance with the NMS joints, this effect was strongly weakened after annealing for 1000 h compared to that in the as-bonded case, as discussed in Section 4.4.3, which probably also explains the strength decrease during annealing.

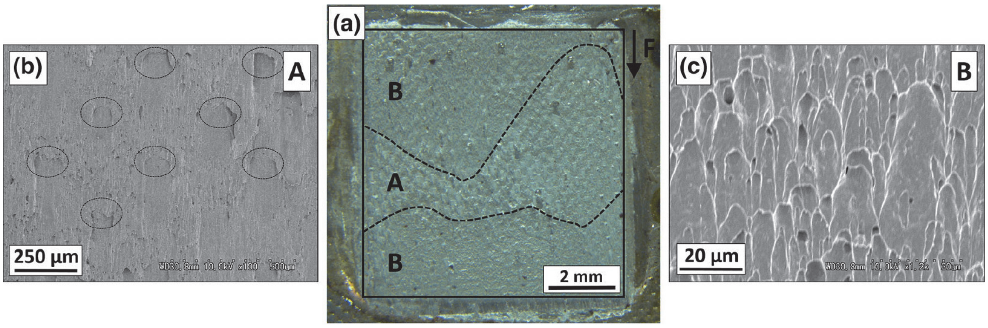

Fig. 4.26. Fracture surface of a Cu-Cu joint soldered with CMS composite annealed for 1000 h at 150 °C showing (a) an OM micrograph of the lower substrate and SE micrographs of the (b) ductile fracture with weak solder–mesh interaction region A marked by dashed circles and (c) solely ductile fracture in region B

In summary, the solder-mesh composite joints provided sufficient resistance against an elevated temperature of 150 °C for up to 1000 h with shear strengths greater than 40 MPa. The shear strengths of the SAC305, NMS, and CMS joints were similar after 1000 h of annealing, which was probably because of the similar fracture characteristics with predominant ductile and cohesive cracking within the SAC305 solder alloy. It seemed that the beneficial effects of particularly the CMS composites on the as-bonded shear strength vanished after annealing. However, the mesh inlets did not negatively influence the mechanical properties.

4.4.5. Reliability during temperature cycling

(a) Experimental results

Oscillating temperatures between 80 °C and 200 °C with a short cycle time of 37 s were applied to the Si-to-DBC samples. SAC305 solder joints with 180 µm and 110 µm thicknesses were used as references, and their performances were compared to those of 360- and 320-µm-thick NMS and CMS composite joints. The SAT images of these six cases in Fig. 4.27 track the deterioration from the as-bonded state until up to 8000 cycles. The flawed areas in the as-bonded SAC305 solder and solder-mesh composite joints were determined to constitute 0.5% or less of the total areas.

The results of quantitative analysis via SAT are plotted in Fig. 4.28. Rapid degradation of the SAC305 joints in Figs. 4.27 (a) and (b) after 2000 cycles resulted in unbonded areas of 11.7% and 7.1% with joint thicknesses of 110 µm and 180 µm, respectively. Pronounced deterioration at the edges and in the centers of the joints are identifiable in the SAT images. The SAC305 joints were classified as “failed” because a delaminated area between 5 and 10% is commonly used as failure criterion in high power applications. The SEM cross-section of the thicker (180-µm-thick) SAC305 joint after 2000 short cycles is shown in Fig. 4.29 (a). The cut plane of the SEM image corresponds to the A-A line in Fig. 4.27. Cracks appear to have propagated along the Si chip and apparently were initiated at the edges. Higher magnification revealed that the crack partly moved through the IMC layer on the chip side and partly along the IMC–solder interface. In the central part of the joint, characteristic cracking behavior occurred within the IMC layer or at the chip–IMC interface. The average IMC layer thickness after 2000 cycles was measured to be 7 µm, and its chemical composition was 48 at% Sn, 38 at% Cu, and 14 at% Ni. The solder matrix nearby was found to have a total of 4 at% of Cu, Ni, and Ag in solution. Ag_3Sn-type IMC particles with diameters less than 5 µm and minor fractions of Cu and Ni were embedded in the solder matrix.

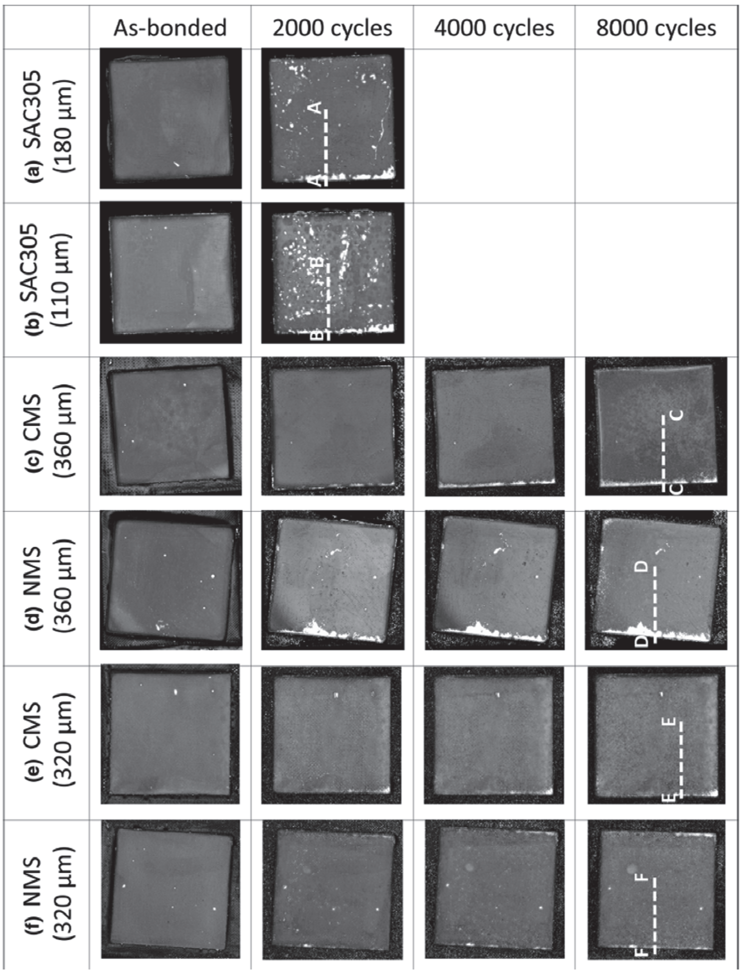

Fig. 4.27. SAT images of Si-to-DBC samples joined with SAC305 (a) 110 µm and (b) 180 µm thick and with (c) and (e) CMS and (d) and (f) NMS composites 360 µm and 320 µm thick after 0, 2000, 4000, and 8000 short cycles between 80 °C and 200 °C; white color indicates unbonded area.

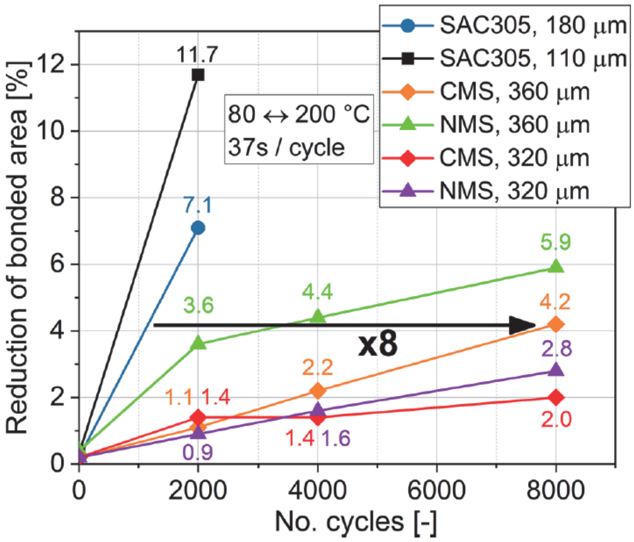

Fig. 4.28. Reduction of the bonded areas in Si-to-DBC samples as a function of the number of short cycles, derived from the SAT images in Fig. 4.27.

The SEM cross-section of the thinner (110-µm-thick) SAC305 joint after 2000 cycles along the B-B line can be seen in Fig. 4.29 (b). The cracking characteristics are similar to those described above for the thicker SAC305 joint. Additional vertical cracks are evident close to the edge of the joint. The IMC layer thickness at the chip side was determined to be 8 µm with a chemical composition of 48 at% Sn, 38 at% Cu, and 14 at% Ni. The solder matrix had approximately 4 at% of Cu, Ni, and Ag in solution, and Ag_3Sn-like IMCs were more or less homogeneously distributed within.

The 360-µm-thick CMS composite joints depicted in Fig. 4.27 (c) deteriorated much more slowly, and the unbonded area in the SAT image after 8000 cycles was measured to be 4.2% of the total area. Moreover, the degradation occurred only at the joint edges. The SEM cross-section along the C-C line after 8000 cycles in Fig. 4.29 (c) reveals that cracking was initiated at the edge of the interconnection. The cracking path propagated along the Si chip interface and significantly interacted with the Cu mesh inlet. Thus, the degradation toward the center of the joint proceeded more slowly. The IMC layer between the Si chip and SAC305 solder reached a thickness of 8 µm after 8000 cycles and had a chemical composition of 48 at% Sn, 38 at% Cu, and 14 at% Ni. The solder matrix contained 4 at% of the alloying elements Cu, Ni, and Ag, with Ag_3Sn-type IMCs distributed. The results of the degradation of the Si-to-DBC interconnections in Fig. 4.28 highlight that the 360-µm-thick CMS joints enhanced the lifetime by a factor of 8 compared to that of the 180-µm-thick SAC305 joint which was classified as failed.

Similar characteristics were found for the 360-µm-thick NMS joint depicted in Fig. 4.27 (d). The bonded area after 8000 cycles was reduced by almost 6%. Although the Ni mesh was located close to the DBC side, the cracking was affected by the mesh. It started at the joint edge and mainly propagated close to the Si chip interface, but the path also was distracted down to the mesh according to the SEM image along the D-D line in Fig. 4.29 (d). Local SEM and EDX analyses revealed a 5-µm-thick IMC layer on the chip side after 8000 cycles, which was composed of 49 at% Sn, 33 at% Cu, and 18 at% Ni. The surrounding Sn-based solder matrix had approximately 4 at% of Cu, Ni, and Ag in solution with Ag_3Sn IMCs spread within.

The fraction of the unbonded area after 8000 cycles was determined to be 2.8% and 2.0% for the 320-µm-thick CMS and NMS composite joints in Figs. 4.27 (e) and (f), respectively. The SAT images suggest that the edges of the thinner composite joints were more resistant to temperature-induced deterioration. The cross-section of the cycled CMS joint along the E-E line in Fig. 4.29 (e) qualitatively suggests stronger distraction of the cracking path even down to the lower substrate. In the case of the thinner NMS joint in Fig. 4.29 (f), the mesh was located close to the Si chip, which apparently prevented the crack from propagating along the F-F cut line. The results of further analyses of the IMC layer thicknesses and chemical compositions in the 320-μm-thick solder–mesh composite joints did not differ from those of the 360-μm-thick joints described above.

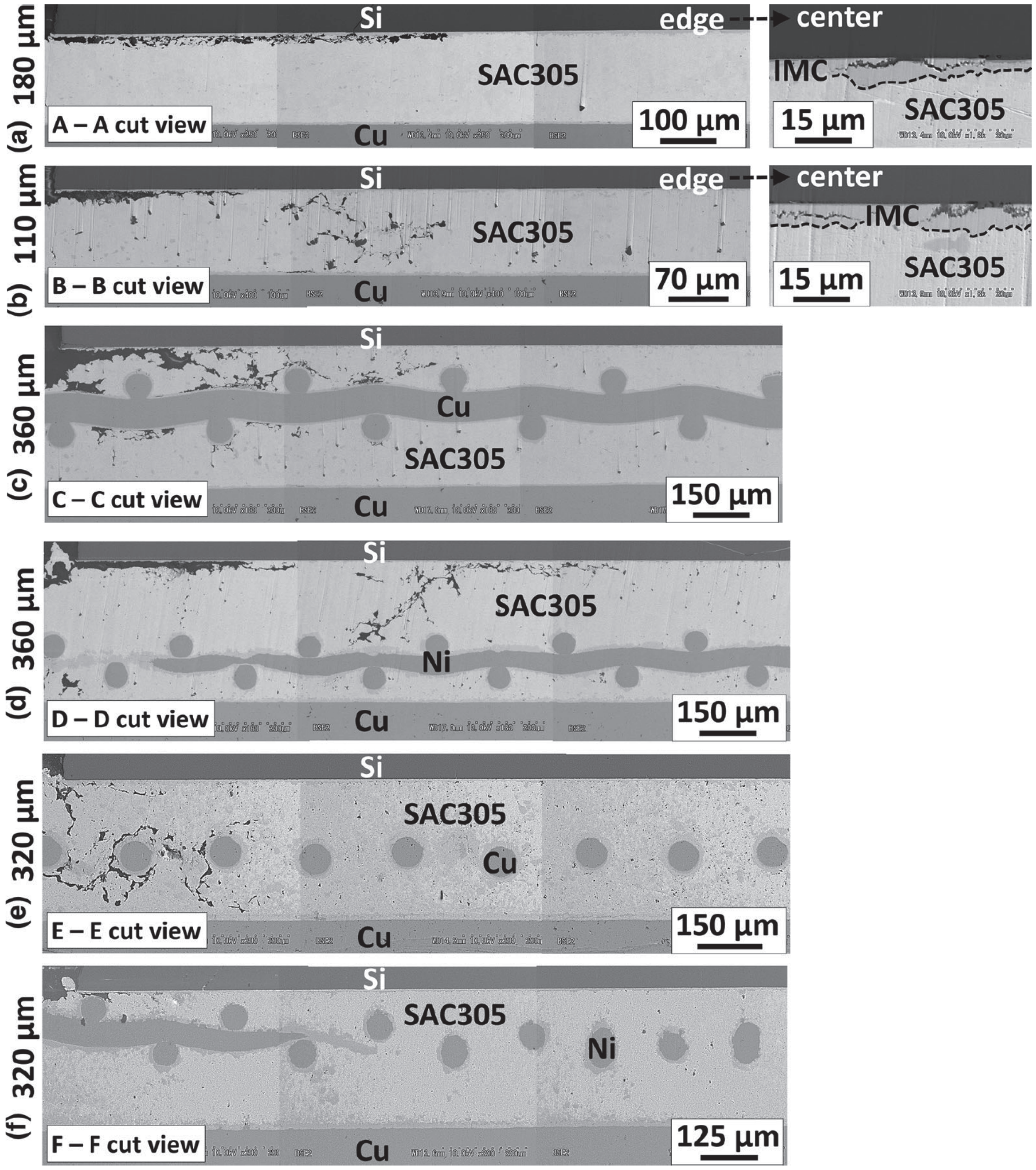

Fig. 4.29. Cross-sections of Si-to-DBC samples with (a) 180-μm-thick and (b) 110-μm-thick SAC305 solder joints after 2000 short cycles, 360-μm-thick (c) CMS and (d) NMS composite joints, and 320-μm-thick (e) CMS and (f) NMS composite joints after 8000 short cycles along the A-A, B-B, C-C, D-D, E-E, and F-F lines in Fig. 4.27.

(b) Finite element results

Fig. 4.30 shows the distributions of the total inelastic (creep and plastic) Mises strain in 200-µm-thick bonding layers between the Si chip and Cu metallization after five calculated temperature cycles between 80 °C and 200 °C. The implemented temperature–time sequence is plotted in Fig. 4.31 and approximates the experimental cycling conditions. The SAC305 solder interconnection suffered from strain peaks at the joint edges and corners, as can be seen in Fig. 4.30 (a). The lowest strains were calculated in the center of the joint, with half the magnitudes of those in the outer areas. Consequently, crack initiation and degradation were mainly expected at or close to the Si–solder interface in the joint periphery. This failure behavior was identified using the experimental SAT and SEM results presented in Figs. 4.27, 29 (a) and (b). Based on the results in Fig. 4.31, the local loading state was characterized by a normalized strain increase rate of 0.176 per cycle.

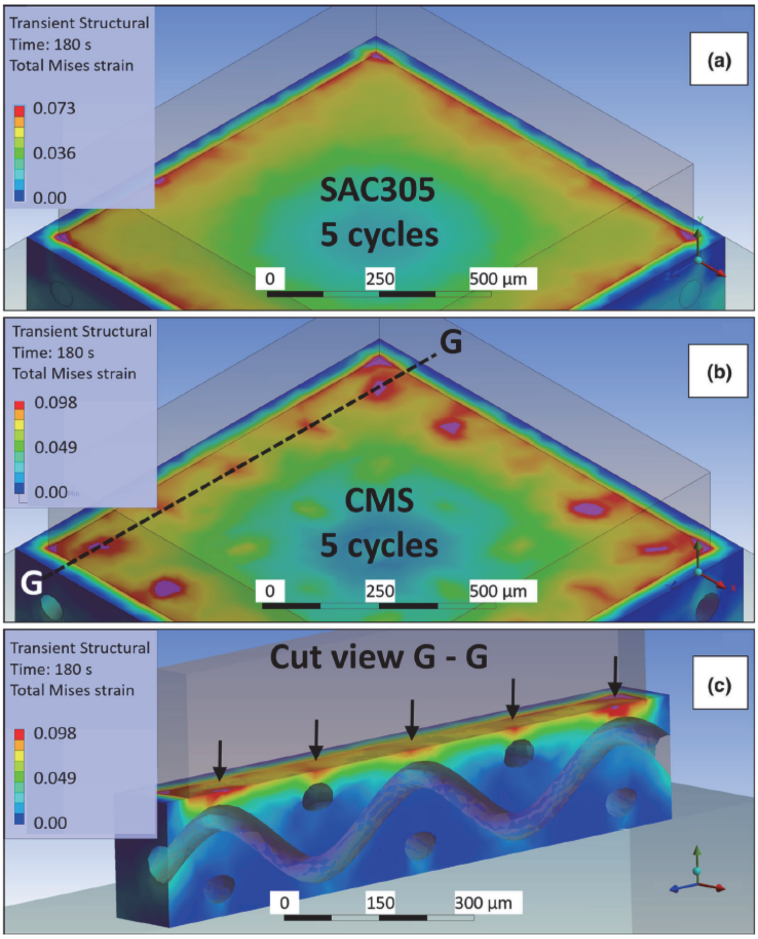

Fig. 4.30. Calculated total Mises strain after five temperature cycles at the Si–solder interface for (a) SAC305 and (b) CMS composite and (c) in the cut view along the G-G line.

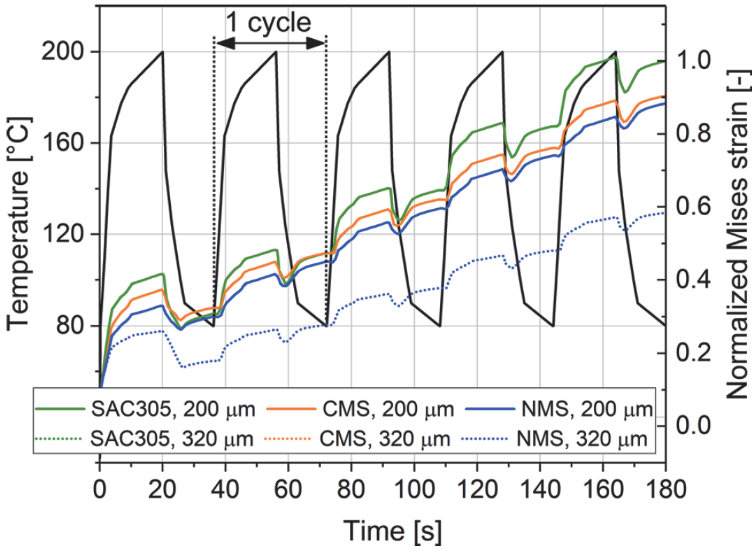

Fig. 4.31. Evolution of calculated normalized Mises strains in SAC305, CMS, and NMS composite joints with 200 μm and 320 μm thicknesses during five temperature cycles.

Fig. 4.30 (b) shows the Mises strain distribution after five calculated cycles between 80 °C and 200 °C in a 200-μm-thick CMS composite joint, which is also representative of NMS composite joints. Pronounced differences in the local loading state are evident when additional strain peaks appear in defined spots near the edges. The cut view along the G-G line in Fig. 4.30 (c) clarifies that these spots emerged where the wavy mesh inlet had the shortest distance to the Si chip. In Section 4.4.3, these locations were found to provide a locally enhanced resistance against crack propagation under quasistatic shear loading. This feature can at least partly explain the significantly slower degradation of solder-mesh composite joints compared to SAC305 solder joints. Fig. 4.30 (c) also indicates that these strain peaks filled out the volume between the mesh inlet and Si interface. This interaction between the multi-layered system and mesh inlet may distract the cracking path from the Si interface down to the mesh inlet, as shown in Figs. 4.29 (c) through 4.29 (f). These cracking characteristics resulted in a path longer than that along the Si chip in the solder joints. Analysis of the FE simulation results in Fig. 4.31 suggested that the normalized inelastic Mises strain in the solder matrix increased by 0.147 and 0.143 per cycle in the CMS and NMS composite joints, respectively, which is equivalent to reduction of the strain load by 16% and 18% compared to that in the SAC305 joint. These results are related to the lower thermal expansion of the mesh inlet, which effectively decreased the thermal expansion of the solder-mesh composite layer. The mesh and solder matrix strongly interacted with each other in the Si-to-DBC assembly during temperature cycling. Fig. 4.32 (a) shows the initial shape of the Cu mesh in the FE model before the simulations. Fig. 4.32 (b) shows the mesh inlet with strongly amplified deformation after five calculated thermal cycles. Plastic strain in the Cu mesh provoked a stretching effect. Although the local plastic strain in the mesh was calculated to be only 0.0075% per cycle, the linear extrapolation to 8000 cycles resulted in a theoretical accumulated value of 60%. It was assumed that the mesh inlet served as a “damper” that partly absorbed the strain loading during temperature cycling and distracted the cracking path.

On the contrary, almost identical normalized strain increase rates of 0.103 per cycle were calculated from Fig. 4.31 for the 320-μm-thick SAC305, CMS, and NMS joints. This result confirms that thicker solder joints provide better reliability, which was experimentally observed for the 100 μm and 180 μm thicknesses. The strain distributions in the 320-μm-thick SAC305 and solder–mesh composite joints are comparable to that in Fig. 4.30 (a), with peaks located at the edges and corners. The interaction between the mesh and solder was also weakened when a plastic strain increase of 0.0036% per cycle was calculated in the mesh. These results strongly indicate that the distance between the mesh and chip interface is essential for composite joint reliability.

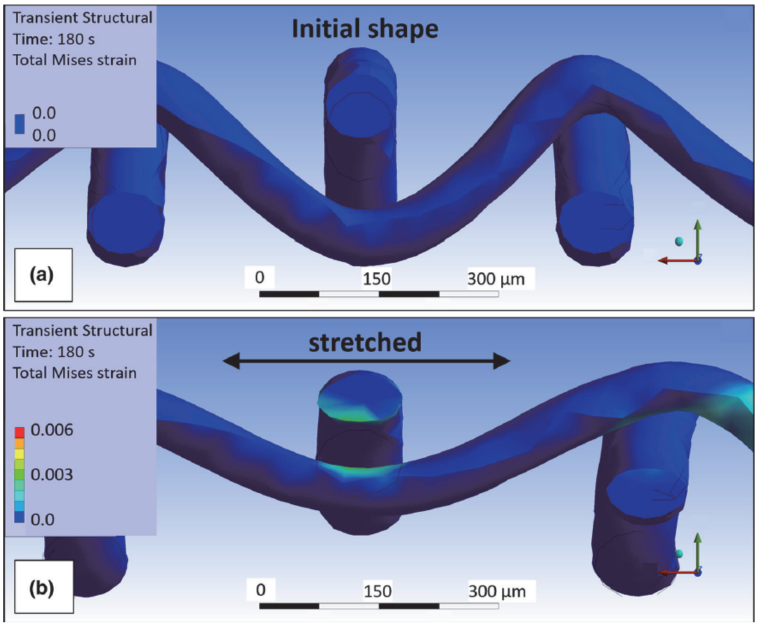

Fig. 4.32. Cross-sectional view, calculated equivalent plastic strain, and mesh shape (a) in the initial state and (b) after five temperature cycles (deformation highly scaled up).

4.5. Discussion

4.5.1 Joint characteristics

The process parameters were successfully optimized in Section 4.4.1 and 4.4.3 such that residues were removed from the joined volume and the shear strength significantly increased. The vacuum step helped to remove residues from the joined volume. The fracture mechanisms were clarified by the combination of OM and SEM inspection as well as FE simulations. Fig. 4.33 schematically summarizes the three cases: the Cu-Cu joints using only SAC305 solder in Fig. 4.33 (a), CMS or NMS composites fabricated by process type 2 in Fig. 4.33 (b), and CMS or NMS composites before process optimization (process type 1) in Fig. 4.33 (c). The solder joint predominantly fractured in a ductile-cohesive mode within the soldered layer, and crack propagation occurred toward one or the other substrate.

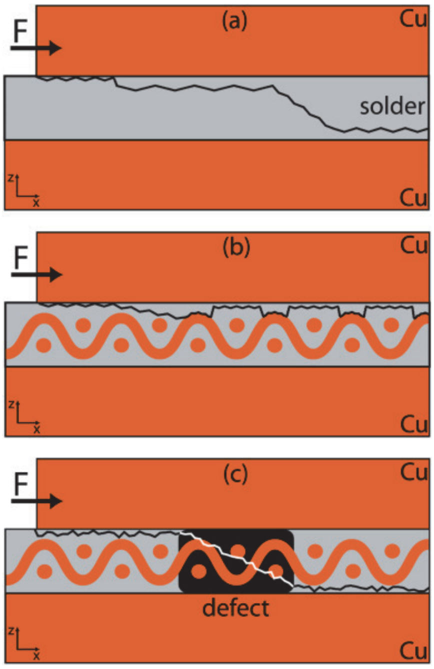

Fig. 4.33. Schematic of fracture path through shear loaded Cu-to-Cu joints with (a) SAC305 solder, (b) defect-free solder-mesh composite, and (c) solder-mesh composite including larger defects.

The shear test results showed that the CMS composite joints exceeded the strength of the SAC305 joint by 16%. However, the FE simulations and analyses in Figs. 4.18 and 4.19 suggest a strength increase of only approximately 5%. This reinforcement is interpreted as the result of a stiffening effect. The plot in Fig. 4.19 indicates that the integration of a metallic mesh slightly delays the initiation and critical stage of plastic material flow. The remaining 11% are likely related to differences in the fracture behaviors of solder and CMS joints that are not captured by the FE simulations. The schematic in Fig. 4.33 (b) shows the crack propagation within a defect-free (process type 2) solder-metallic mesh composite joint, as deduced from Figs. 4.16 and 4.17 in

Section 4.4.3. Beyond the small volume of interfacial crack initiation at the loaded edge, the fracture path switches to a very consistent pattern that forms because of the alternating cracking within the SAC305 solder and at the solder-metallic mesh interface. The area of ductile fracture in the SAC305 joint (78%), denoted as regions B and C in Fig. 4.15, is comparable to that of region C for the combined solder and solder-metallic mesh fracture in Fig. 4.16 (76%). The fracture region C of the CMS joint can be further divided into a fraction with failure in the solder, $A_{f,S}$ (87%), and another fraction, $A_{f\text{-}S\text{-}M}$ (13%), where failure occurs at the solder-metallic mesh interface. The Cu mesh inlet would contribute to the strength increase by a stiffening effect (5%) and a locally enhanced fracture resistance (11%). Interestingly, the Cu mesh and the upper substrate do not need to be in direct contact to provoke the local cracking at the solder-metallic mesh interface. However, the experimental observations are in good agreement with the FE simulations in Fig. 4.18 (a), which highlight local interfacial stress peaks on the Cu mesh where the solder-metallic mesh fracture occurs.

The analysis above was also applied to the NMS composite joints. Simulations demonstrated that the stiffening effect also stabilized the solder and led to a reinforcement of 5%. Because the experimental strength was similar, i.e. only 1% higher, to that of the SAC305 solder joints, a local fracture-induced strength degradation must have been involved. $A_{f,S}$ and $A_{f,S\text{-}M}$ were measured as 0.7 and 0.3, respectively, because of the different architecture of the Ni mesh according to Figs. 4.1 (b) and (c). Moreover, the NMS fracture was located at all intersection points of the Ni mesh whereas the CMS fracture appeared at every second intersection, as indicated by the round spots in Figs. 4.1 (b) and (c). In comparison with the SAC305 solder joints, the Cu mesh inlets resulted in stiffness and fracture-induced reinforcement. In the case of Ni meshes, the stiffness increase alone compensated for the local weakening of the fracture strength. This explanation is partially verified by various other studies that demonstrate the enhanced brittleness and lower strength of Ni_3Sn_4 IMC compared to, for instance, Cu_6Sn_5 or Ag_3Sn IMC [34], [35]. Although the type of interfacial IMC is expected to be largely responsible for the fracture and strength of solder-metallic mesh joints, the slightly different woven structures of the Cu and Ni meshes may have an additional effect on the joint strength.

The third case in Fig. 4.33 (c) represents a solder-metallic mesh composite joint with defects (residues) as they were found after process type 1. By combining the experimental and numerical results, these residues can be concluded to trigger the cutting of the metallic mesh inlet. SEM analyses identified residues located at the cut edges of the metallic mesh, and the FE simulations demonstrated volumetric stress peaks above the material's yield strength in the filaments parallel to the loading direction and in the vicinity of the defect-solder interface. These results indicate that parallel filaments will be the primary fracture sites. Subsequent secondary fracture occurs in filaments perpendicular to the load, which is why these filaments are bent with an approximately 45° angle, as shown in Fig. 4.13 (c), because the upper substrate likely gets lifted. This study could optimize the process conditions and eliminate the fracture mode shown in Fig. 4.33 (c). However, this effect can be useful to evaluate the process and joint quality when, for instance, some aspect of the metallic mesh geometry is changed, such as the mesh width or the filament diameter. The metallic mesh inlet would typically not be cut in defect-free solder- metallic mesh joints because of the higher specific strength of such joints.

4.5.2. Impact of metallic-mesh inlet on joint reliability

This research has proven that solder-mesh composite solutions can significantly improve the lifetimes of Si-to-DBC interconnections as they are used in power module applications. The tested joints were able to resist 8000 short temperature cycles with a peak temperature of 200 °C and a temperature amplitude of 120 °C. The joints provide long-term resistance up to 200 °C, which is only 18 °C below the solidus temperature of the SAC305 solder matrix. Since the SAC305 reference joints deteriorated much faster, the mesh inlet obviously enhanced the performance. Here, we discuss the key influencing factors based on the study.

(a) IMC thickening

The SAC305 joints in the Si-to-DBC samples strongly suffered from degradation at the Si interface. Figs. 4.29 (a) and (b) confirm that cracking preferentially propagated through or close to the IMC layer on the Si chip. The solder-mesh composite joint slowed down the degradation at the edges and prevented the interconnection from failing in the central parts. An 8-μm-thick IMC layer emerged in the thinner (110-μm-thick) SAC305 and CMS composite joints after 2000 and 8000 cycles, respectively. Furthermore, the NMS joints only formed 5-μm-thick IMC layers after 8000 cycles. The results of the annealing experiments confirmed the influence of the mesh on the IMC growth when the Cu-Sn ratio in the IMC on the substrate side varied with the mesh material. It is known that (near-)IMC regions become more susceptible to cracking with increasing IMC thickness [2], [5], which can particularly explain the brittle cracking within the IMC layers in the centers of the SAC305 joints in Figs. 4.27 (a), (b), and 4.29 (a) and (b). Thus, the reduced IMC growth rates in the solder–mesh composite joints helped improve the reliability due to the presence of the Cu and Ni meshes, respectively. These aspects require further investigation.

(b) Reduction of thermal expansion

The FE simulation results in Figs. 4.30 and 4.31 reveal that lower strain rates per temperature cycle evolve in solder-mesh composite joints than in solder joints with 200 µm joint thickness. The effect on the reliability can be estimated by using, for instance, the lifetime model developed by Coffin-Manson:

$$N_f = A \cdot \Delta\varepsilon_{\mathrm{ie}}^{b}, \tag{4.3}$$

where N_f is the number of cycles to failure, $\Delta\varepsilon_{\mathrm{ie}}$ is the strain increase per cycle, and A and b are the material-dependent lifetime coefficient and exponent, respectively. The value of b for SAC305 solder can be narrowed down to a range between -1 and -2 [36]. Thus, a reduction of $\Delta\varepsilon_{\mathrm{ie}}$ by 16% and 18%, as suggested by the FE simulation results for CMS and NMS vs. SAC305 joints in Section 4.4.5, yields a lifetime increase by a factor of 1.19–1.42 for CMS composites and 1.22–1.49 for NMS composites. Similar methods of assessing the lifetimes of solder joints have been successfully used in various other studies [29]–[32], [36]. The positive effect is caused by the thermal expansion coefficients of Cu and Ni being lower than that of SAC305 according to Table 4.1. The mesh inlet decreased the thermal expansion of the solder material in its vicinity. The sphere of influence is locally restricted, and the positive impact of the mesh on the critical stress and strain state at the Si interface depends on the distance between the mesh and Si chip. According to the FE results in Fig. 4.31, only the thinner 200-µm-thick composite joints benefitted from reduced strain increase rates relative to those of the SAC305 counterparts, whereas the near-interface solder alloys in the thicker 320-µm-thick composite joints suffered from the same loading without the mesh. Near-interface stress reduction delays solder grain coarsening and cracking along grain boundaries, as described in [27], [28]. Although a miniaturized model was used and the results cannot be directly scaled up for the real geometry, this effect only contributes partly to the enhanced reliability.

(c) Cracking and degradation characteristics

The reliability of soldered semiconductor chips typically improves with increasing solder joint thickness, which is in agreement with our experimental observations of 110- and 180-µm-thick SAC305 solder joints and the results in Section 4.4.5. The solder-mesh composite joints had greater thicknesses of 320 µm and 360 µm. However, it is not likely that a joint thickness increase by a factor of 2 (180-µm-thick SAC305 vs. 360-µm-thick CMS) resulted in lifetime enhancement by a factor of 8, as shown in Fig. 4.28. Moreover, solder-mesh composite joints apparently do not obey the classical thickness-vs.-lifetime relationship. The thinner 320-µm-thick solder–mesh composite joints deteriorated more slowly than the thicker 360-µm-thick ones during short cycles with T_{max} =

200 °C. It is assumed that the inverse thickness-vs.-lifetime correlation is linked to the interaction between the cracking path and mesh. This hypothesis is supported by Fig. 4.29 (c), which reveals the massive interaction between the crack and Cu mesh. The mesh and Si chip were separated by 65 µm. Many branches formed in the near-edge solder. On the contrary, the larger distance of 180 µm between the Ni mesh and Si chip in Fig. 4.29 (d) led to a significantly weakened impact on the cracking path. Consequently, the cracking could propagate more easily, i.e., farther, along the Si interface during the same number of cycles. This hypothesis was supported by the thinner 320-µm-thick composite joints. The CMS joint provoked the cracking path to reach even the lower substrate side in Fig. 4.29 (e). When the Ni mesh was also located near the Si chip, according to Fig. 4.29 (f), the reliability further improved, leading to an unbonded area of only 2% of the total area after 8000 cycles. The appearance of strain peaks at the positions of shortest distance between the mesh and chip is revealed by the FE simulation results in Fig. 4.30 (c). The enhanced resistance of composite joints against thermal fatigue is in agreement with the quasistatic shear test behavior in Section 4.4.3. It was determined that the mesh provoked a unique cracking behavior with cohesive and interfacial patterns, which was supposed to be more resistant than purely cohesive fracturing within the SAC305 solder. Composite joints tend to be thicker than solder joints, and the thermal or electrical resistance must be considered. The results in Section 4.4.3 showed that CMS joints can outperform SAC305 joints in terms of resistance. A 300-µm-thick CMS joint can be expected to provide the thermal resistance of a 150-µm-thick SAC305 joint. Thus, CMS joints have the potential to improve the heat dissipation into the substrate and heat sink during service. The same power density would lead to lower peak temperatures and thermally induced stresses in the semiconductor chip and joint, which would improve the lifetime. In other words, the devices could be operated with the same lifetime behavior but higher power densities.

(d) Other factors/future work

The mesh material may affect the reliability, although there were no pronounced differences between Cu and Ni. It seems to be essential for the metallic mesh to be bonded metallurgically to the solder, so that the solder–mesh interface does not become severely delaminated through the elevated and cyclic temperatures.

The solder-mesh composite joints with the SAC305 matrix could be operated at a peak temperature of 200 °C, which is only 18 °C below the solidus temperature of the solder. It is of great interest to investigate whether such near-melting operation conditions can be applied to other solder-mesh composites with higher melting points, such as composites with Sn-5Sb (T_S = 237 °C), Bi-11Ag (T_S = 262 °C), Au-20Sn (T_S = 280 °C), or Au-12Ge (T_S = 356 °C) as the matrix material.

Effects on the reliability of these solders in relation to their melting points similar to those observed for SAC305 would significantly push the operation limits towards applications at temperatures far greater than 200 °C.

The Cu and Ni meshes used in this study differed only slightly, and no geometry effects were observed. However, it would be interesting to investigate the effects of different woven architectures. The current study also indicated that the reliabilities and conductivities of solder-mesh composite joints improve with decreasing joint thickness. Therefore, further experimental investigations of the performance of thinner composite joints (with thicknesses of 200–300 μm) is of particular interest.

4.5.3. Advantages and potential issues

The characteristics of the Cu mesh-embedded solder composite revealed in this study are described, as follows:

- Young's modulus of 33 GPa, estimated from the stiffening effect of 5%,
- thermal conductivity of 70–94 W/m·K in the composite thickness of 300–350 μm,
- shear strength of 51 MPa, and
- durable temperature of 200 °C.

This composite material showed higher strength and thermal conductivity, comparing to monolithic SAC305 or Pb-5Sn solders. The composite joint showed high temperature-tolerance against thermal aging at 150 °C and also thermal cycling with peak temperature up to 200 °C despite low durable temperature of the matrix solder. Additionally, from an industrial point of view, relatively low cost and pressureless bonding process would be favorable to expand applications further. In contrast, stiffness was estimated to be increased by metallic mesh inlet, which may be an issue for some applications. The advantages and potential issues of this material can be described, as follows:

- Advantages;
    - ➢ Good interconnection reliability,
    - ➢ good heat dissipation performance, and
    - ➢ low cost of materials and bonding apparatus.
- Potential issues;
    - ➢ Moderate stress relaxation performance for power chips.

Considering the superior characteristics over monolithic solders, achieved by Cu mesh-inlet reinforcement, and its compatibility of conventional solders would be suitable for next-generation interconnections to replace conventional solder in mid-grade automotive power modules. For further expansion of applications of the composite joint, utilization of higher-temperature tolerant solder matrix would be beneficial for future work. Furthermore, softer solder matrix utilization may also enhance stress-relaxation performance for delicate die-attach solutions, which is of particular interest.

4.6. Conclusions

The study verified the favorable compatibility between SAC305 solder and thin metallic Cu and Ni mesh inlets. Residues (defects) within the composite joints were successfully removed through process optimization. The microstructure and formation of IMCs at the solder-substrate and solder-metallic mesh interfaces, i.e. scallop-like Cu_6Sn_5 IMCs with Cu mesh and faceted Ni_3Sn_4 IMCs with Ni mesh, were analyzed. Average shear strengths of 51.4, 44.8, and 44.1 MPa were found for CMS composite, NMS composite, and SAC305 solder joints, respectively. A specific fracture pattern was identified to result from the solder-substrate-mesh interaction, with a cracking path partly within the solder and partly at the solder-metallic mesh interface. These fracture characteristics were clarified by FE simulations that demonstrated the enhanced stiffness (+5%) of the CMS and NMS composite joints. Further contribution to the reinforcement (+11%) was attributed to a locally increased fracture resistance of CMS interfacial fractures. By contrast, local NMS fractures compensated for the enhanced stiffness due to the more brittle characteristics of Ni_3Sn_4 IMC. Thermal FE simulations indicated that in particular CMS composites can reduce the thermal resistance of the interconnections which is equivalent to a better heat dissipation through the bonding layer.

Their long-term stability against a constant elevated temperature of 150 °C was confirmed. Additionally, the composite joints were cycled with peak temperatures up to 200 °C, while the lifetimes improved by factors of 8 (or more) compared to those of the soldered counterparts. Since the peak testing temperature was only 18 °C below the solidus line of the SAC305 solder matrix, the potential of the solder alloy was exploited. The Cu mesh-embedded solder composite is attractive low-cost joining solutions for mid-grade power modules.

References in Chapter 4

[1] A. Sharif and Y. C. Chan, "Effect of substrate metallization on interfacial reactions and reliability of Sn-Zn-Bi solder joints," *Microelectron. Eng.*, vol. 84, no. 2, pp. 328–335, 2007.

[2] T. An and F. Qin, "Effects of the intermetallic compound microstructure on the tensile behavior of Sn3.0Ag0.5Cu/Cu solder joint under various strain rates," *Microelectron. Reliab.*, vol. 54, no. 5, pp. 932–938, 2014.

[3] S. M. Lee, J. W. Yoon, and S. B. Jung, “Electromigration effect on Sn-58 % Bi solder joints with various substrate metallizations under current stress,” *J. Mater. Sci. Mater. Electron.*, vol. 27, no. 2, pp. 1105–1112, 2016.

[4] M. O. Alam, Y. C. Chan, and K. C. Hung, “Reliability study of the electroless Ni-P layer against solder alloy,” *Microelectron. Reliab.*, vol. 42, no. 7, pp. 1065–1073, 2002.

[5] X. Hu, Y. Li, Y. Liu, Y. Liu, and Z. Min, “Microstructure and shear strength of Sn37Pb/Cu solder joints subjected to isothermal aging,” *Microelectron. Reliab.*, vol. 54, no. 8, pp. 1575–1582, 2014.

[6] A. Hirose, T. Fujii, T. Imamura, and F. K. Kobayashi, “Influence of Interfacial Reaction on Reliability of QFP Joints with Sn-Ag Based Pb Free Solders,” *Mater. Trans.*, vol. 42, no. 5, pp. 794–802, 2001.

[7] A. Lis *et al.*, “Finite Element-Assisted Assessment of the Thermo-cyclic Characteristics of Leads Soldered with SnAgCu(+Bi,In) Alloys,” *J. Electron. Mater.*, vol. 46, no. 7, pp. 4326–4343, 2017.

[8] A. A. El-Daly, A. M. El-Taher, and S. Gouda, “Development of new multicomponent Sn-Ag-Cu-Bi lead-free solders for low-cost commercial electronic assembly,” *J. Alloys Compd.*, vol. 627, pp. 268–275, 2015.

[9] X. Tu, D. Yi, J. Wu, and B. Wang, “Influence of Ce addition on Sn-3.0Ag-0.5Cu solder joints: Thermal behavior, microstructure and mechanical properties,” *J. Alloys Compd.*, vol. 698, pp. 317–328, 2017.

[10] Q. B. Tao, L. Benabou, L. Vivet, V. N. Le, and F. B. Ouezdou, “Effect of Ni and Sb additions and testing conditions on the mechanical properties and microstructures of lead-free solder joints,” *Mater. Sci. Eng. A*, vol. 669, pp. 403–416, 2016.

[11] M. Yang *et al.*, “Effects of Ag content on the interfacial reactions between liquid Sn-Ag-Cu solders and Cu substrates during soldering,” *J. Alloys Compd.*, vol. 679, pp. 18–25, 2016.

[12] T. Takahashi, S. Komatsu, H. Nishikawa, and T. Takemoto, “Improvement of high-temperature performance of Zn-Sn solder joint,” *J. Electron. Mater.*, vol. 39, no. 8, pp. 1241–1247, 2010.

[13] S. J. Kim, K. S. Kim, S. S. Kim, C. Y. Kang, and K. Suganuma, “Characteristics of Zn-Al-Cu alloys for high temperature solder application,” *Mater. Trans.*, vol. 49, no. 7, pp. 1531–1536, 2008.

[14] T. Yamaguchi *et al.*, “Heat dissipative Pb-free bonding technology using Al-rich Zn/Al/Zn clad solder,” *Weld. Int.*, vol. 31, no. 11, pp. 846–856, 2017.

[15] C. Leinenbach, F. Valenza, D. Giuranno, H. R. Elsener, S. Jin, and R. Novakovic, “Wetting

and soldering behavior of eutectic Au-Ge alloy on Cu and Ni substrates," *J. Electron. Mater.*, vol. 40, no. 7, pp. 1533–1541, 2011.

[16] X. Zhao, Y. Wen, Y. Li, Y. Liu, and Y. Wang, "Effect of γ-Fe2O3 nanoparticles size on the properties of Sn-1.0Ag-0.5Cu nano-composite solders and joints," *J. Alloys Compd.*, vol. 662, pp. 272–282, 2016.

[17] Y. Tang, G. Y. Li, and Y. C. Pan, "Effects of TiO2 nanoparticles addition on microstructure, microhardness and tensile properties of Sn-3.0Ag-0.5Cu-xTiO2 composite solder," *Mater. Des.*, vol. 55, pp. 574–582, 2014.

[18] G. Chen, L. Liu, V. V. Silberschmidt, C. Liu, F. Wu, and Y. C. Chan, "Microstructural evolution of 96.5Sn–3Ag–0.5Cu lead free solder reinforced with nickel-coated graphene reinforcements under large temperature gradient," *J. Mater. Sci. Mater. Electron.*, vol. 29, no. 7, pp. 5253–5263, 2018.

[19] Y. Wen *et al.*, "Reliability enhancement of Sn-1.0Ag-0.5Cu nano-composite solders by adding multiple sizes of TiO2nanoparticles," *J. Alloys Compd.*, vol. 696, pp. 799–807, 2017.

[20] A. A. El-Daly, W. M. Desoky, T. A. Elmosalami, M. G. El-Shaarawy, and A. M. Abdraboh, "Microstructural modifications and properties of SiC nanoparticles-reinforced Sn-3.0Ag-0.5Cu solder alloy," *Mater. Des.*, vol. 65, pp. 1196–1204, 2015.

[21] P. Lall, S. Shantaram, J. Suhling, and D. Locker, "Effect of aging on the high strain rate mechanical properties of SAC105 and SAC305 leadfree alloys," in *2013 IEEE 63rd Electronic Components and Technology Conference (ECTC)*, 2013, pp. 1277–1293.

[22] A. Nourani and J. K. Spelt, "Combined effect of strain-rate and mode-ratio on the fracture of lead-free solder joints," *Mater. Des.*, vol. 85, pp. 115–126, 2015.

[23] P. Lall, D. Zhang, V. Yadav, and D. Locker, "High strain rate constitutive behavior of SAC105 and SAC305 leadfree solder during operation at high temperature," *Microelectron. Reliab.*, vol. 62, pp. 4–17, 2016.

[24] I. Shohji, T. Yoshida, T. Takahashi, and S. Hioki, "Tensile Properties of Sn-3.5Ag-0.75Cu Lead-free Solders," *Mater. Trans.*, vol. 43, no. 8, pp. 1854–1857, 2002.

[25] S. Wiese *et al.*, "Constitutive behaviour of lead-free solders vs. lead-containing solders - experiments on bulk specimens and flip-chip joints," *Proc. - Electron. Components Technol. Conf.*, vol. 00, no. 1, pp. 890–902, 2001.

[26] P. T. Vianco, "Fatigue and Creep of Lead-Free Solder Alloys," in *Fundamental Properties, Lead-free Solder Interconnect Reliability,* ASM International, 2005.

[27] M. Berthou, P. Retailleau, H. Frémont, A. Guédon-Gracia, and C. Jéphos-Davennel, "Microstructure evolution observation for SAC solder joint: Comparison between thermal

cycling and thermal storage," *Microelectron. Reliab.*, vol. 49, no. 9–11, pp. 1267–1272, 2009.

[28] M. A. Matin, W. P. Vellinga, and M. G. D. Geers, "Thermomechanical fatigue damage evolution in SAC solder joints," *Mater. Sci. Eng. A*, vol. 445–446, no. May 2006, pp. 73–85, 2007.

[29] M. M. Basit *et al.*, "Thermal cycling reliability of aged PBGA assemblies - Comparison of Weibull failure data and finite element model predictions," in *2015 IEEE 65th Electronic Components and Technology Conference (ECTC)*, 2015, pp. 106–117.

[30] U. M. Choi *et al.*, "Power cycling test and failure analysis of molded Intelligent Power IGBT Module under different temperature swing durations," *Microelectron. Reliab.*, vol. 64, pp. 403–408, 2016.

[31] K. N. Tu, "Reliability challenges in 3D IC packaging technology," *Microelectron. Reliab.*, vol. 51, no. 3, pp. 517–523, 2011.

[32] H. B. Qin, W. Y. Li, M. B. Zhou, and X. P. Zhang, "Low cycle fatigue performance of ball grid array structure Cu/Sn-3.0Ag-0.5Cu/Cu solder joints," *Microelectron. Reliab.*, vol. 54, no. 12, pp. 2911–2921, 2014.

[33] W. D. Jenkins, T. G. Digges, and C. R. Johnson, "Tensile properties of copper, nickel, and 70%copper30%nickel and 30%copper70%nickel alloys at high temperatures," *J. Res. Natl. Bur. Stand.*, vol. 58, no. April, pp. 201–211, 1957.

[34] A. Lis, S. Kicin, F. Brem, and C. Leinenbach, "Thermal Stress Assessment for Transient Liquid-Phase Bonded Si Chips in High-Power Modules Using Experimental and Numerical Methods," *J. Electron. Mater.*, vol. 46, no. 2, pp. 729–741, 2017.

[35] N. S. Bosco and F. W. Zok, "Strength of joints produced by transient liquid phase bonding in the Cu-Sn system," *Acta Mater.*, vol. 53, no. 7, pp. 2019–2027, 2005.

[36] T. Hannach, "Ermittlung von Lebensdauergleichungen vom Coffin-Manson- und Morrowtyp für bleihaltige und bleifreie Weichlote durch Kombination von FE und Experiment," Technische Universität Berlin, 2010.

Chapter 5. Cu-IMC-embedded polymer composite (Bicontinuous composite)

5.1. Introduction

Chapter 2 suggests that the Cu (and/or Cu_6Sn_5)-embedded polymer composite provides significantly low stiffness and high durable temperature. It should be beneficial to power electronics interconnections, requiring high stress-relaxation. Contrary, the polymer matrix would limit the composite thermal conductivity and strength because of its poor properties. Additionally, IMC brittle properties should be carefully discussed for repetitive thermo-mechanical loading. Therefore, its thermo-mechanical characteristics and applicability to high-temperature interconnections should be studied.

TLPB has been expected to provide a high temperature endurance in power electronics industries [1]–[6]. High-melting-point materials (Cu, Ag, and Ni) and low-melting-point materials (Sn or In) are supplied as layers that isothermally solidify during processing. A process that uses mixed powders is called TLPS [7]–[9]. In a Cu–Sn system, high-melting-point joints are composed of Cu_6Sn_5 and Cu_3Sn IMCs, which are formed at processing temperatures such as 300 °C. The Cu–Sn system is relatively cost-effective and compatible with the electronics interconnections [10]–[12]. The Cu–Sn IMCs, Cu_6Sn_5 and Cu_3Sn, have phase transformation temperatures of 415 and 640 °C, respectively. Additionally, they have higher mechanical strengths and creep resistances compared to conventional Sn-based solders [13]. Thus, they are suitable as strongly temperature-resistant materials for power electronics applications. However, interfacial IMC layers have commonly been treated as an issue of conventional soldering technologies because they are prone to crack initiation and failure; for instance, the increase in IMC layer thickness degrades the mechanical properties of the joints or bonding reliability because of the quite stiff and brittle properties of Cu–Sn IMCs [14]–[16]. From the point of view of the IMCs morphology, a flat IMC surface reduces the thermal cycling fatigue lifetime of the solder joint [17]. Even in the TLP technologies, the quite stiff and brittle properties of the IMCs cause strength reduction or joint fracture through thermal cyclic operations despite the higher durable temperature of the joints [18]–[22].

In this chapter, we propose a novel approach for stiffness reduction of TLPS joints by controlling the microstructural morphology using a Cu-solder-resin composite paste as the bonding material, where a skeleton shaped microstructure consisting of Cu particles connected with Cu–Sn IMC bridges partially filled with polyimide resin is observed. First, mechanical FE simulations of simplified 2.5-dimensional (2.5D) models of the composite joints are performed to roughly estimate the impact of the composite microstructure on the mechanical properties of the TLPS joints. Next, the evolution of the TLPS Cu–Sn skeleton microstructure during thermal aging is evaluated by shear strength tests, X-ray diffraction analysis, microstructure observation, and a fractographical method. From these results, the microstructural and mechanical evolutions of the TLPS Cu–Sn skeleton joints are discussed.

Subsequently, the unique microstructure of the TLPS joint is precisely evaluated using FE simulations based on 3D image reconstruction to elucidate its macro- and micro-deformation properties. The macroscopic mechanical properties of the TLPS microstructure are estimated through computational tensile tests, where the composites are considered as homogenized materials. The mechanical properties of the materials and the ambient temperature are varied to clarify their effect on the stability of the joint. Structural FE simulations mimicking thermal cycling tests of SiC-die-attached specimens are used to predict their reliability by using the calculated homogenized mechanical properties of the microstructure, which are compared with those obtained by experimental thermal cycling results. In addition, the deformation behavior of the microstructure is investigated to identify crack initiation sites microscopically.

5.2. Experimental method

5.2.1. Cu-solder-resin composite

The Cu-solder-resin composite, investigated in this paper, is a paste that mainly contains Cu particles, SAC305 solder particles, and polyimide-type thermosetting resin. The melting point of the solder is 218 °C. The cure temperature of the polyimide resin is 230–240 °C. The sizes of the Cu particles and solder particles are approximately 10 and 3 μm, respectively. The content of the Cu in wt.% is approximately three times higher than that of the solder, which is designed to consume the solder through the formation of Cu–Sn IMCs. The content of the polyimide resin is approximately 20% in volume within the total of the Cu, solder, and polyimide resin. The polyimide resin is chosen by the curing temperature close to the melting point of the solder and by the soft mechanical properties, whose yield strength is approximately 1 MPa, which was expected to easily deform while embedded within the microstructure of the Cu and IMCs. The decomposition temperature of the polyimide is greater than 400 °C. The paste after the reflow process was observed by FE-SEM (SU8000, Hitachi High-Technologies Corporation).

The thermal conductivity of TLPS films was measured at room temperature. The TLPS films were sintered at 250 °C for 1 min with a heating rate of 30 °C/min from room temperature in a nitrogen atmosphere without pressure. The specimens, which had approximate dimensions of 9 × 9 × 0.5 mm^3, were fabricated by polishing the TLPS films. The thermal diffusivity and specific heat capacity of the specimens were measured using the laser flash method (TC-7000, ULVAC RIKO, Inc.) and differential scanning calorimetry (DSC, DSC7000X, Hitachi High-Technologies Corporation), respectively. Three specimens were analyzed, with the thermal diffusivity obtained from the average of three measurements per specimen. Thermal conductivity λ was calculated as follows:

$$\lambda = \alpha \cdot \rho \cdot c, \tag{5.1}$$

where α, ρ, and c are the thermal diffusivity, apparent density, and specific heat of the TLPS films, respectively.

5.2.2. Thermal aging test

Fig. 5.1 shows an illustration of the die-attached specimen for thermal aging tests. Kovar (Ni–Co–Fe alloy) chips were bonded onto DBC substrates, composed of two 0.3-mm-thick Cu electrodes bonded to a 0.6-mm-thick Si_3N_4 substrate. The chips had dimensions of 7 × 7 × 2 mm^3 and a Ni/Au surface metallization. The thickness of the Ni and Au metallization was 2.0 and 0.1 µm, respectively. Before bonding, the chips were mounted onto the composite paste, which was printed on the substrate with a 100-µm thickness in advance. According to the temperature profile shown in Fig. 5.2, the specimens were preheated at 100 °C for 60 min and bonded at 250 °C for 1 min in a reflow furnace (VSU28, Invacu, Ltd., Burgas, Bulgaria). The preheating step was carried out to evaporate any solvent contained in the paste, which can inhibit from uniform sintering. The heating step was performed in a nitrogen atmosphere. No pressure was applied in this heating process.

The die-attached specimens were subjected to thermal aging testing at 150, 175, and 200 °C for 500 or 1000 h in air. Analyses of the cross-sections and fracture surfaces of the aged specimens were performed by FE-SEM and EDX (EMAX Evolution, HORIBA, Ltd., Kyoto, Japan). The crystal structure of each phase in the TLPS layer was identified by X-ray diffraction (XRD; D8 DISCOVER, Bruker Corporation, Billerica, MA, USA) apparatus, as shown in Fig. 5.3. The specimens for XRD were prepared by a tilted cross-sectioning method for resin-molded specimens. The die-attached specimens were subjected to shear tests with a cross head speed of 100 µm/s at room temperature by a bond tester (CONDOR 150, XYZTEC). The average value of the two samples was regarded as the shear strength. After the shear test, the fracture surfaces were analyzed using FE-SEM and EDX.

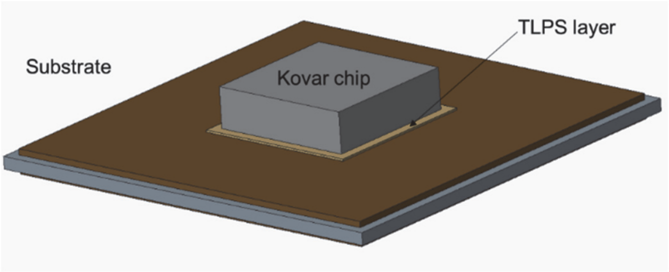

Fig. 5.1. Illustration of a die-attached specimen.

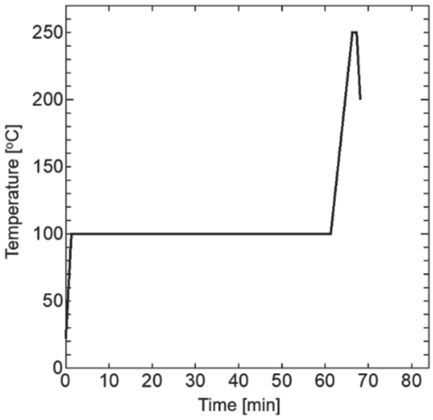

Fig. 5.2. Temperature profile during bonding process.

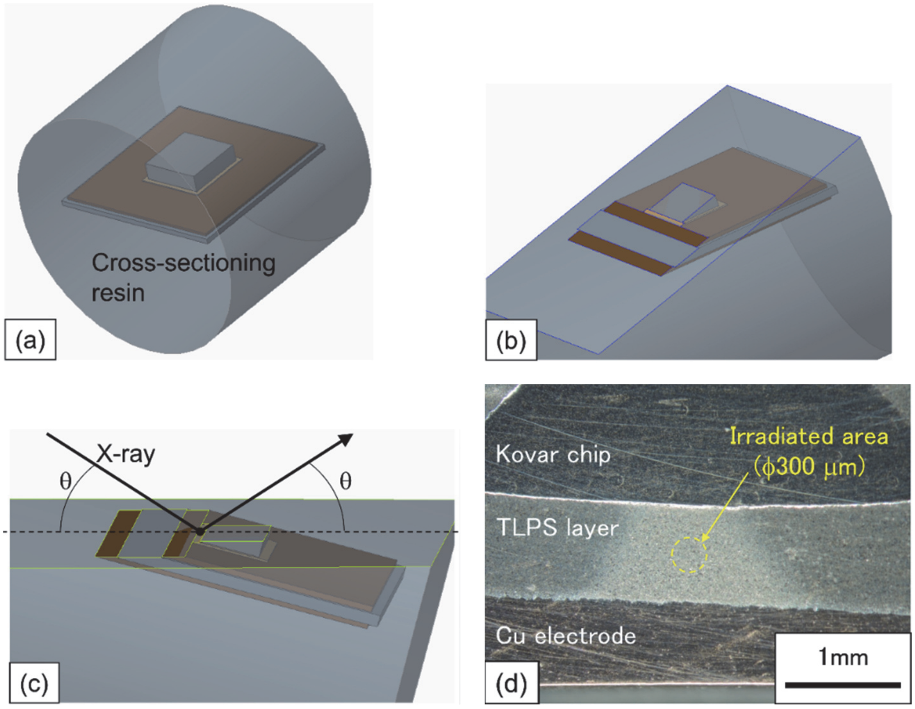

Fig. 5.3. XRD method using tilted cross-sectioning: (a) Before cross-sectioning, (b) after cross-sectioning, (c) schematic of XRD arrangement, and (d) irradiated area of the TLPS layer.

5.2.3. Thermal cycling test

Fig. 5.4 shows an illustration of the SiC-die-attached specimen for thermal cycling tests. SiC power chips were bonded onto the DBC substrates. The power chips had approximate dimensions of 8 × 8 × 0.3mm^3 and a Ni/Au surface metallization. The preheating and reflow steps based on the temperature profile, as mentioned in Section 5.2.2, were carried out using a reflow furnace (MICROView core9046a, CORES Corporation).

Thermal cycling tests of the die-attached specimens were performed using a thermal cycling chamber (TSA-73EH, ESPEC CORP.) in the temperature range from −55 °C to 175 °C with a dwell time of 15 min at both minimum and maximum temperatures. The die-attached specimens bonded by a commercial SAC305 solder paste were also subjected to the thermal cycling tests for comparison. Six joints of each type were tested. Nondestructive observations of the die- attached layers were performed every 300 thermal cycles using SAT (FineSAT III, Hitachi Power Solutions Co., Ltd.). The resolution of the SAT we used is estimated to be 0.1 mm × 0.1 mm. The ratio of unbonded areas was obtained from the SAT images binarized using image editing software. After thermal cycling tests, a representative joint was selected from the six joints of each type, and cross-sectional SEM images were recorded.

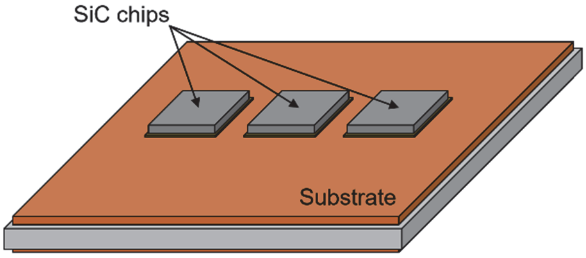

Fig. 5.4. Illustration of a SiC-die-attached specimen.

5.3. Finite element analysis

5.3.1. Simplified 2.5D model

Mechanical FE simulations of simplified model of the TLPS joint were performed using Ansys Workbench 17.2. A 2.5D FE model was set-up and consisted of the SiC chip, the Cu electrode of the DBC substrate, and the joint in between the chip and electrode. The complex microstructure of the joint was simplified by modeling Cu particles, connected by Cu_6Sn_5 IMCs, as homogeneously distributed within the polyimide resin matrix. Elasto-plastic properties were considered for the Cu and polyimide resin, whereas the SiC and IMC were modeled as linear-elastic. The relevant parameters of the materials are summarized in Table 5.1 [23]–[25]. The parameters of the polyimide resin were measured by tensile tests of the cured polyimide resin film.

The 2.5D FE model is illustrated in Fig. 5.5. Ideal contact was assumed between all interfaces. The model consists of cubic elements with an average edge length of 3 and 1 μm in the joint and the substrates, respectively. A systematic numerical parameter study was performed in which the single Cu particles were increasingly linked to each other and to both substrates by primary (vertical) and secondary (horizontal) IMC interconnections. An external force *F* was applied to the upper SiC chip in order to mimic the shear test conditions. The force *F* was an input parameter, whereas the displacement of the upper substrate *u* was obtained during the simulation.

Table 5.1. Summary of relevant properties of materials [23]–[25].

Material	Young's modulus E [GPa]	Yield strength σ_y [MPa]	Ultimate tensile strength σ_{UTS} [MPa]
SiC	410	--	--
Cu_6Sn_5	102	--	--
Cu	100	53	240
Resin	0.06	1	4

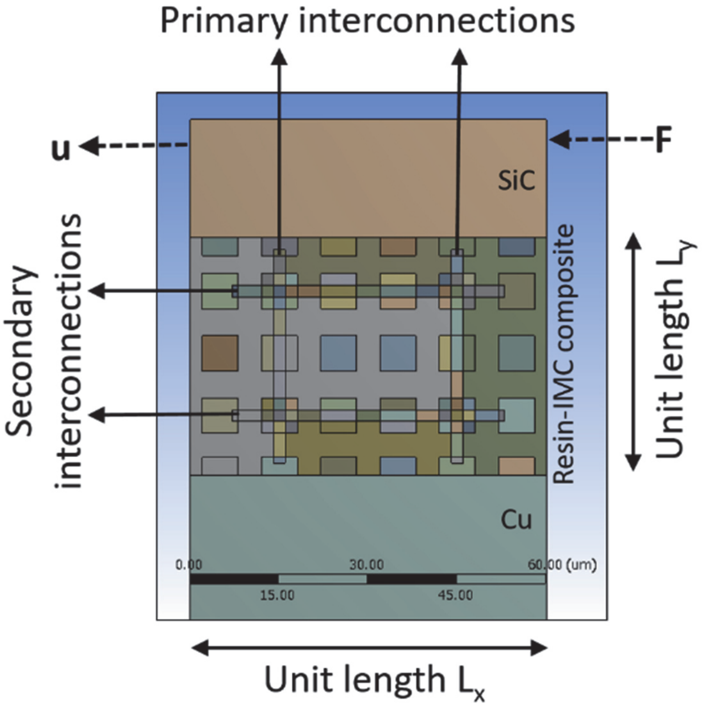

Fig. 5.5. 2.5D FE model of a SiC-Cu joint with Cu particles embedded in resin and connected by primary and secondary IMC interconnections.

5.3.2. 3D-image-reconstructed model

(a) Modeling of the Cu-IMC-resin microstructure based on 3D image reconstruction

3D image reconstruction of the serial cross-sectional SEM images provided useful insights about the mechanical properties of the Cu-IMC-resin microstructure. Fig. 5.6 shows the segmentation flow of these images. The resolution of the original SEM images was 0.06 μm/pixel. These images were segmented into three regions, which were Cu, IMCs, and polyimide resin, based on their brightness using a commercial image processing software, Amira, as shown in Figs. 5.6 (b) and (c). The subsequent steps were performed by an image processing and meshing software, Scan IP, Simpleware. These steps included resizing of the images into the resolution of 0.5 μm/pixel and Gaussian smoothing, as shown in Fig. 5.6 (d). The latter was done to reduce the number of FE mesh cells. Finally, the images were resegmentated to remove the tiny cavities and islands, whose sizes were approximately less than 1 μm, as shown in Fig. 5.6 (e). Figs. 5.7 and 5.8 show the reconstructed cubic 3D model with sizes of 15 and 50 μm, respectively. These models were composed of quadratic hexahedral elements, where the number of nodes and elements in the 15- and 50-μm-sized model were 118,305 and 65,919, and 1,535,038 and 833,105, respectively. The volume fractions of Cu, IMC, and polyimide resin in the latter model were 24.0, 32.7, and 43.3%, respectively.

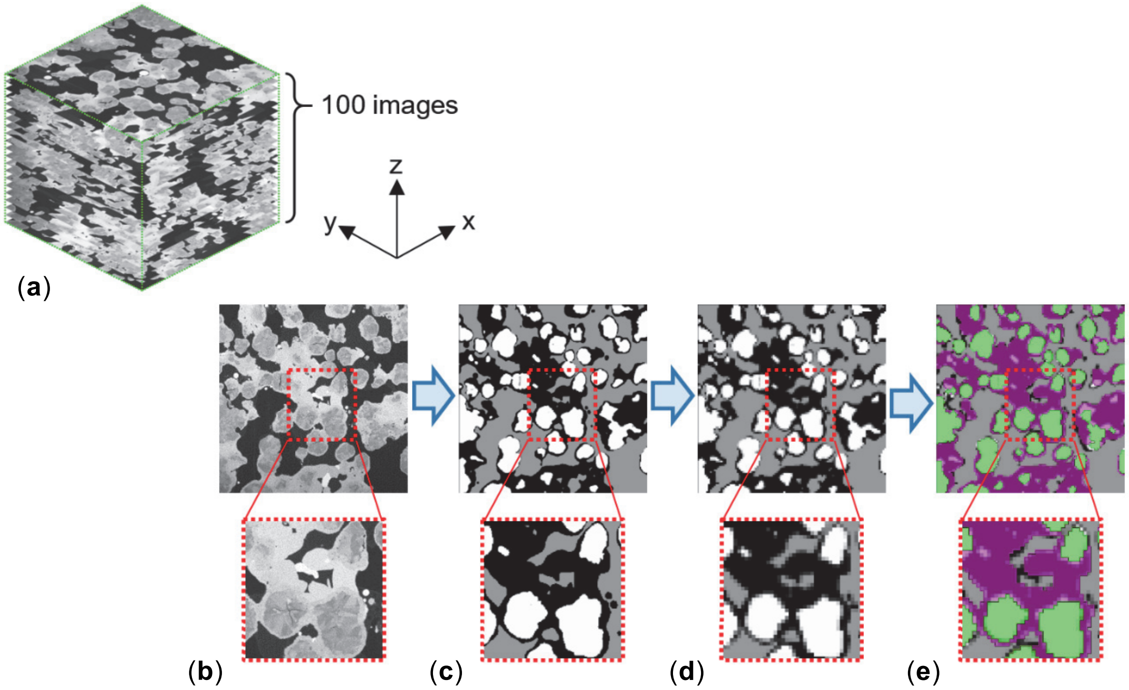

Fig. 5.6. Segmentation flow of the Cu-IMC-resin microstructure composed of Cu, Cu-Sn IMC, and polyimide resin. (a) Illustration of stacked SEM images, (b) preprocessed SEM image, (c) Otsu segmentation of the image, (d) image after Gaussian smoothing, and (e) resegmentated image.

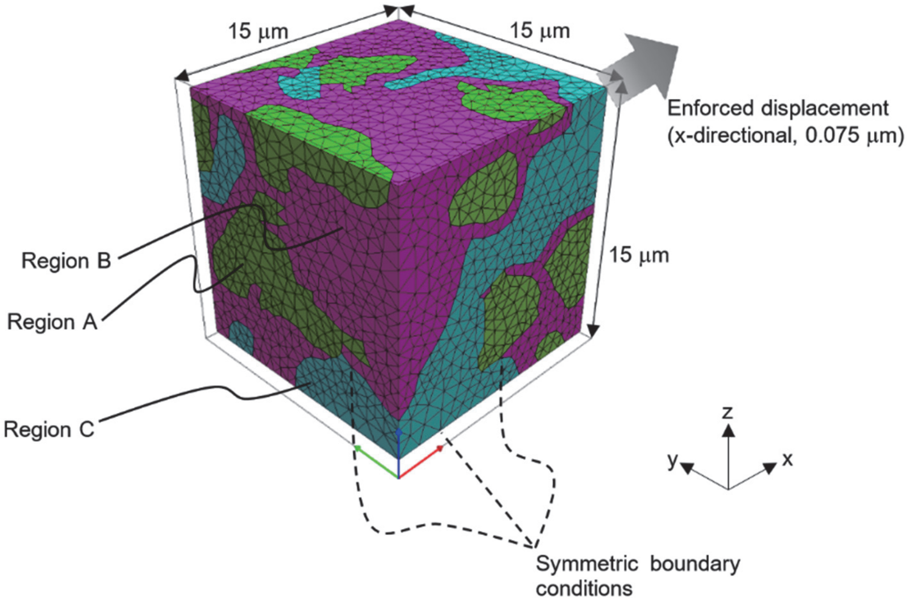

Fig. 5.7. Cu-IMC-resin model of 15-µm-size for FE analysis, which is based on 3D image reconstruction. The model comprises Cu (green), IMC (pink), and resin (light blue).

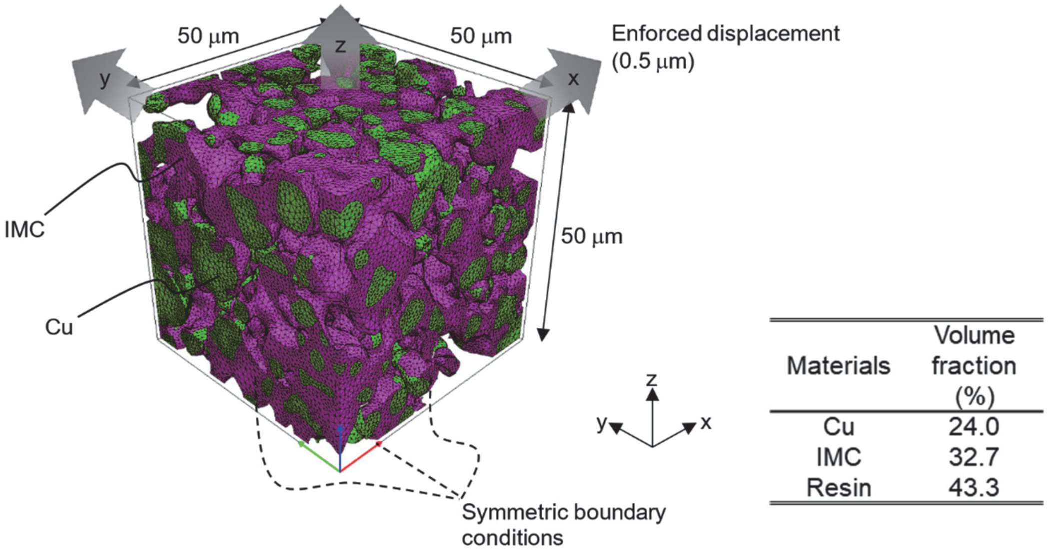

Materials	Volume fraction (%)
Cu	24.0
IMC	32.7
Resin	43.3

Fig. 5.8. Cu-IMC-resin model of 50-µm-size for FE analysis, which is based on 3D image reconstruction. The model comprises Cu (green), IMC (pink), and resin (invisible).

Mechanical FE simulations were performed to estimate the macro- and micro-deformation properties of the microstructure using the commercial software, ANSYS Workbench 18.2 [26]. The 15-µm-sized model (Fig. 5.7) was used to predict the effect of IMC and resin on the homogenized mechanical properties. The model was divided into regions A, B, and C, which represented the presence of Cu, IMC, and resin, respectively. The 1/8 model was used for FE analysis considering the symmetry conditions. Ideal contact was assumed between all the interfaces. An external displacement of 0.075 µm along the x-axis, equivalent to the macroscopic strain of 0.5%, was applied to the yz-surface of the FE model. Ambient temperatures of −55, 22, 100, and 175 °C were considered in the simulations. The homogenized nominal stress-stain curves of the microstructure were calculated at each temperature from the displacement u and the averaged reaction force F on the surface subjected to external displacement, using the following expressions:

$$\sigma = \frac{F}{L^2}, \tag{5.2}$$

$$\varepsilon = \frac{u}{L}, \tag{5.3}$$

where L is the size of the cubic model. The homogenized Young's modulus and the yield strength were obtained from these curves.

A parameter study was performed based on the cases shown in Table 5.2, where the impacts of materials properties in the regions B (IMC) and C (resin) on the microstructure were validated. The properties of polyimide resin were obtained using tensile tests of the cured polyimide resin film, and that of the epoxy resin (reference) were acquired from its commercial specifications. Further, air instead of resins was considered as the region C in the cases for comparison to clarify the impact of the mechanical properties of resins on the homogenized properties. Furthermore, the cases with SAC305 instead of IMC as the region B were also examined to clarify its effect on the homogenized properties. The relevant parameters of the materials are summarized in Tables 5.3 and 5.4 [23]–[25], [27]–[29]. Cu, SAC305, and resins were considered as multi-linear elastoplastic materials with the isotropic hardening described as follows:

$$\sigma = \begin{cases} E\varepsilon & (0 \leq \varepsilon \leq \varepsilon_{\mathrm{Y}}) \\ \dfrac{\sigma_{\mathrm{UTS}} - \sigma_{\mathrm{Y}}}{\varepsilon_{\mathrm{UTS}} - \varepsilon_{\mathrm{Y}}} \cdot (\varepsilon - \varepsilon_{\mathrm{Y}}) + \sigma_{\mathrm{Y}} & (\varepsilon_{\mathrm{Y}} < \varepsilon \leq \varepsilon_{\mathrm{UTS}}) \\ \sigma_{\mathrm{UTS}} & (\varepsilon > \varepsilon_{\mathrm{UTS}}). \end{cases} \tag{5.4}$$

In contrast, all the other materials were modeled as linear elastic. The mechanical properties of Cu, SAC305, and polyimide resin were considered to be temperature dependent.

The utilization of 15-μm-sized model for the analysis provided a quick and efficient prediction of the effect of IMC and resin on the homogenized mechanical properties, whereas that of the 50-μm-sized model provided detailed information about these properties. For the latter, symmetry conditions, ideal contact between all interfaces, and ambient temperature were considered similar to the former method. An external displacement of 0.5 μm along the x, y, and z axes, which is equivalent to the macroscopic strain of 1%, was applied to the yz-, zx-, and xy-surfaces for uniaxial tensile test, respectively. The homogenized properties of the Cu-IMC-resin microstructure, i.e., nominal stress-strain relations, Young's modulus, and yield strength, at each temperature were calculated using the similar approach described above. Moreover, the homogenized Poisson's ratio was calculated from the average displacement of each edge surface of the cubic model against the external load, and the homogenized CTE was calculated from the average displacement while the temperature changed from 22 to 30 °C.

Table 5.2. FE analysis by 15-µm-sized model.

Case	Regions		
	A	B	C
Cu-IMC-resin (PI)	Cu	IMC (Cu_6Sn_5)	Polyimide-resin
Cu-IMC-resin (Epoxy)	Cu	IMC (Cu_6Sn_5)	Epoxy-resin
Cu-IMC-air	Cu	IMC (Cu_6Sn_5)	Air
Cu-SAC-resin (PI)	Cu	SAC305	Polyimide-resin
Cu-SAC-resin (Epoxy)	Cu	SAC305	Epoxy-resin
Cu-SAC-air	Cu	SAC305	Air

Table 5.3. Summary of selected physical properties used in this study; data is from [23]–[25], [27]–[29].

Material	Young's Modulus E (GPa)	Yield Strength σ_Y (MPa)	Ultimate Tensile Strength σ_{UTS} (MPa)	CTE α (10^{-6}/°C)	Poisson's Ratio ν
SiC	410	--	--	3.8	0.33
Si_3N_4	314	--	--	3.0	0.33
Cu	96 (0 °C) 88 (300 °C)	52 (0 °C) 42 (300 °C)	240 (0 °C) 178 (300 °C)	16.7	0.33
IMC (Cu_6Sn_5)	102	--	--	18.3	0.31
SAC305	46 (RT) 35 (100 °C) 4 (200 °C)	45 (RT) 15 (125 °C) 3 (200 °C)	58 (RT) 23 (125 °C) 4 (200 °C)	21.2 (RT) 22.0 (100 °C) 22.5 (200 °C)	0.36

Table 5.4. Physical properties of resin used in FE analysis.

Type of Resin	Young's Modulus E (GPa)	Yield Strength σ_Y (MPa)	Ultimate Tensile Strength σ_{UTS} (MPa)	CTE α (10^{-6}/°C)	Poisson's Ratio ν
Polyimide-resin, used in this study	0.120 (−40 °C)	4.0 (−40 °C)	16.4 (−40 °C)	38.0	0.37
	0.021 (RT)	1.0 (RT)	4.0 (RT °C)		
	0.004 (100 °C)	0.2 (100 °C)	0.7 (100 °C)		
	0.001 (150 °C)	0.1 (150 °C)	0.2 (150 °C)		
Epoxy-resin	2.0	30	70	38.0	0.37

(b) SiC-DBC model based on homogenized properties of Cu-IMC-resin

A 3D FE model was set up using ANSYS Workbench 18.2, which is shown in Fig. 5.9. It consists of a bonding layer sandwiched between a SiC chip and DBC substrate. Homogenized mechanical properties estimated from the Cu-IMC-resin model based on 3D image reconstruction were used. These properties were considered as the average of the calculated results for loading along x-, y-, and z-axis directions. The other material properties are listed in Table 5.3. Dimensions of 8 × 8 × 0.3 mm, 8 × 8 × 0.07 mm, 12 × 12 × 0.3 mm, and 12 × 12 × 0.6 mm were chosen for the SiC chip, bonding layer (Cu-IMC-resin, IMC (Cu_6Sn_5), or SAC305), Cu electrode, and Si_3N_4 substrate, respectively. Here, the 1/4 model was used for FE analysis considering the symmetry conditions. Quadratic hexahedral elements were used, where the number of nodes and elements in the model were 105,299 and 22,300, respectively. Macroscopic strain, which was used for the microscopic simulations to locally identify the crack initiation sites in the model, was calculated for ten steady-state cycles in which the temperature oscillated between −55 and 175 °C. Thermal stress and strain were generated due to the CTE mismatch of the constituent materials during the temperature variation.

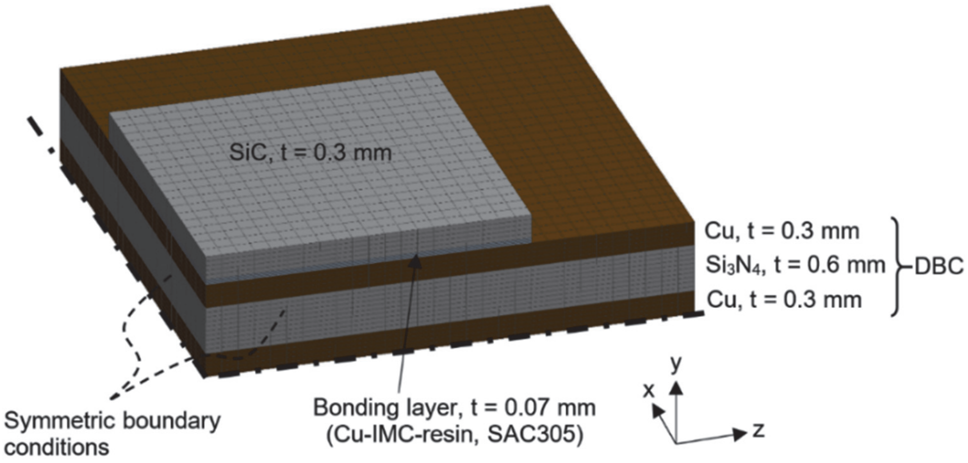

Fig. 5.9. Silicon carbide-direct bonded copper (SiC-DBC) FE model for temperature cycling simulations. The sizes of the SiC chip and DBC substrate are 8 × 8 mm, and 12 × 12 mm, respectively.

5.4. Results

5.4.1. Bonding evaluation

Fig. 5.10 (a) shows an SEM image of the composite paste heated up to 205 °C in an open nitrogen atmosphere. Gray particles represent Cu, while white particles represent the solder. These spherical particles, which are homogeneously independent of each other, were observed at this temperature. The morphology of the paste at 205 °C shows no apparent variation from the unheated state. At the melting point of the solder of 220 °C, the Cu particles are connected through Cu–Sn IMCs, which are light-gray colored in Fig. 5.10 (b). When the composite paste is heated up to 220, 250, and 275 °C, little variation is found according to Figs. 5.10 (b)–(d). The morphology of the heated paste over 220 °C is a homogeneously distributed network-shaped structure. The thermal conductivity analysis showed that the value of the TLPS film sintered at 250 °C is 25.9 W/m·K, as shown in Table 5.5. Fig. 5.11 shows the shear strengths of the SiC-DBC joints bonded at different temperatures. Above the melting point of the solder of 220 °C, the strengths are approximately 12 MPa. The strengths of the samples bonded between 220 and 275 °C vary by just a small amount despite the curing of the polyimide resin at 230–240 °C.

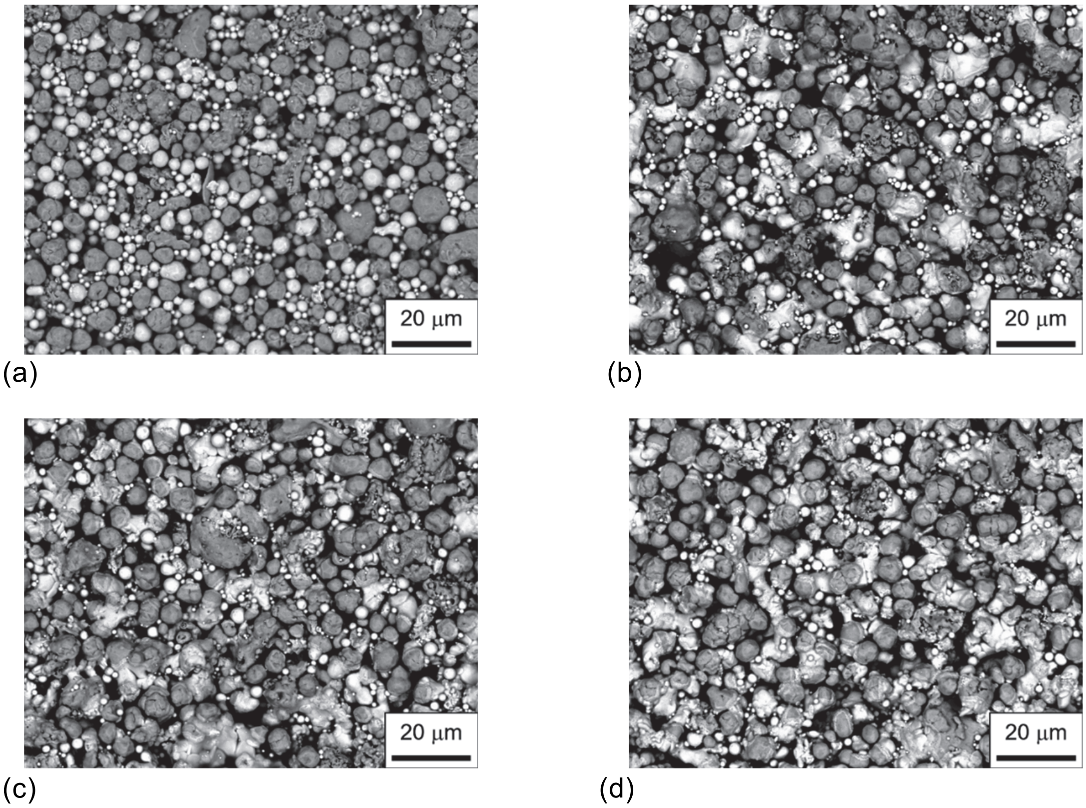

Fig. 5.10. SEM images of Cu-solder-resin composite paste heated up to (a) 205, (b) 220, (c) 250, and (d) 275 °C in nitrogen atmosphere.

Table 5.5. Thermal conductivity of the sintered Cu-solder-resin composite film.

Thermal diffusivity a $[m^2/s]$	Apparent density ρ $[g/mm^3]$	Specific heat c [J/g·K]	Thermal conductivity λ [W/m·K]
13.8×10^{-6}	4.90×10^{-3}	0.383	25.9

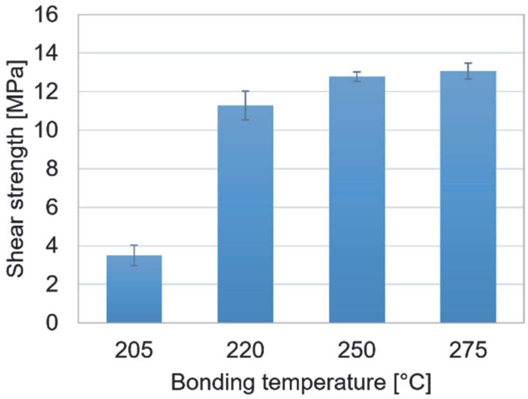

Fig. 5.11. Shear strengths of TLPS joints bonded at different temperatures.

Next, the FE analyses of the 2.5D-simplified model, as shown in Section 5.3.1, were evaluated. The calculated distribution of displacement u in the loading direction is visualized in Fig. 5.12. It can be qualitatively seen that the interconnection density strongly affects the macro- and microscopic deformation behavior of the joints. Similar characteristics are found when the joint consists of only resin in Fig. 5.12 (a) and resin with Cu particles without IMC connections in Fig. 5.12 (b). The deformation in these two cases is governed by the properties of the resin. As a result, stresses higher than 2 MPa could not be applied, because of the severe plastic material flow. Thus, these models do not represent the experimental cases. On the contrary, the connections between the particles and the substrates, as shown in Figs. 5.12 (c) and (d), enabled the application of loads that are in the range of the experimental shear strength.

This effect is further quantified by the three-dimensional plot in Fig. 5.13 where the joint stiffness S was calculated as a function of the number of primary and secondary interconnections per unit length according to

$$S = \frac{F}{A} \cdot u, \tag{5.5}$$

where A is the cross-sectional area of the joint. This result indicates that the joint properties strongly depend on the density of interconnection lines within the resin matrix. Moreover, primary interconnections that link the upper substrate to the lower substrate are more important. Secondary interconnections themselves do not contribute much to the joint stiffness. However, these provide an additional reinforcement effect in combination with the primary ones. The joint stiffness S can vary by up to two orders of magnitude, as can be derived from the logarithmic scale in Fig. 5.13. The simulation also proved that the necks between the particles mainly carry the external load, whereas the experimental observations indicated that these connections result from IMC formation during processing. Thus, it is suggested that the microstructure of the “TLPS-skeleton” structure would strongly affect the joint reliability against thermal cyclic loading. Detailed computational and experimental results are described in the latter Section 5.4.3.

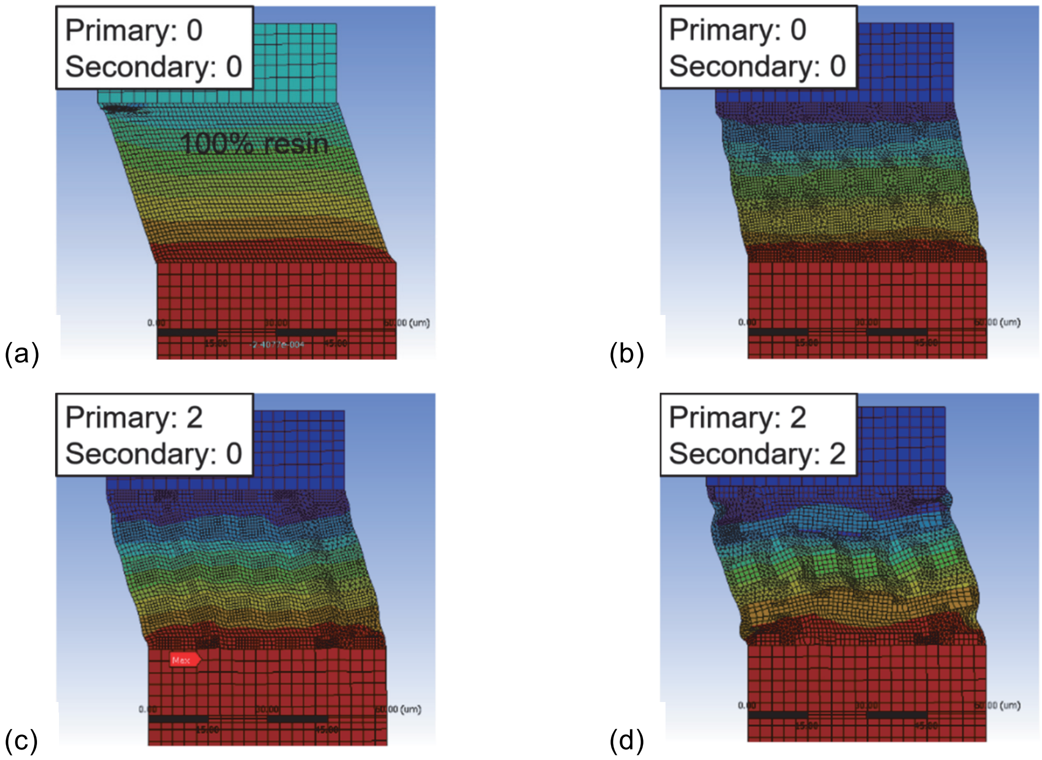

Fig. 5.12. Distribution of displacement *u* (in loading direction) with primary/secondary IMC interconnections: (a) 0/0 (only resin), (b) 0/0 (with Cu particles), (c) 2/0, and (d) 2/2.

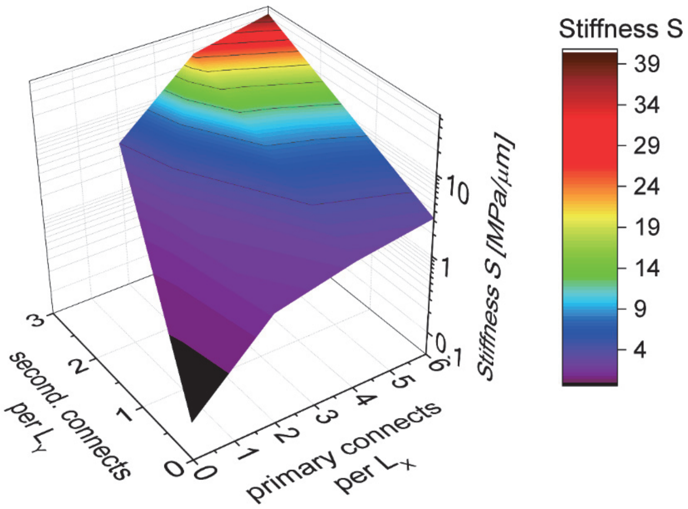

Fig. 5.13. Calculated joint stiffness *S* as a function of primary and secondary IMC interconnections per unit length.

5.4.2. Thermal aging characterization

Fig. 5.14 presents XRD results of the Cu-solder-resin composite paste and a bonding layer in the as-bonded state. Sn, Ag_3Sn, and Cu peaks are detected in the composite paste, while Cu_6Sn_5, Cu_3Sn, Ag_3Sn, and Cu peaks are detected in the as-bonded state. In the as-bonded state, the Sn peaks, which are detected in the composite paste, fully disappear, while the Cu_6Sn_5 and Cu_3Sn peaks appear. The disappearance of Sn and appearance of Cu–Sn IMCs could have occurred through isothermal solidification reactions between the Cu particles and solder particles during bonding. A cross-sectional SEM image of the as-bonded TLPS joint is shown in Fig. 5.15, which indicates that the dark gray Cu particles are connected with the light gray bridges of the Cu–Sn IMCs within a black polyimide resin matrix. This shows the unique microstructure of the TLPS joint, which is a Cu-IMC skeleton shaped microstructure partially filled with polyimide resin. Fig. 5.16 (a) shows the magnified structures of the chip side interface. $(Cu,Ni)_6Sn_5$ is observed on the Ni/Au metalized chip surface, and no intermediate layers are detected between them. An intermediate layer composed of Cu_3Sn IMCs is observed between the Cu particles and $(Cu,Ni)_6Sn_5$ IMCs. Fig. 5.16 (b) shows the substrate side interface, where Cu_6Sn_5 IMCs are observed on the Cu electrode of the substrate with an intermediate layer of Cu_3Sn IMCs. These phases were confirmed by EDX results, as shown in Table 5.6. Additionally, it should be noted that submicron voids are observed in the Cu_3Sn layer, as shown in Fig. 5.16. The submicron voids are observed in the Cu_3Sn layer on the Cu particles but not on the Cu substrate.

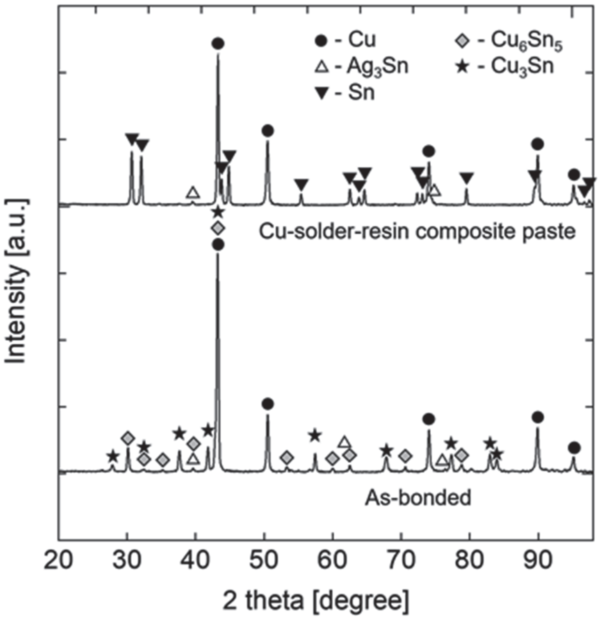

Fig. 5.14. XRD patterns of the Cu-solder-resin composite paste and the as-bonded TLPS bonding layer.

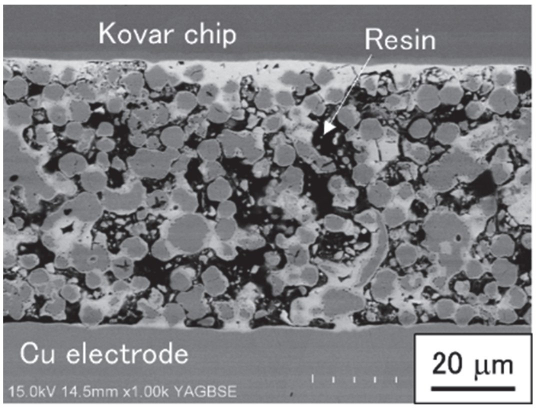

Fig. 5.15. Cross-sectional SEM image of an as-bonded TLPS joint.

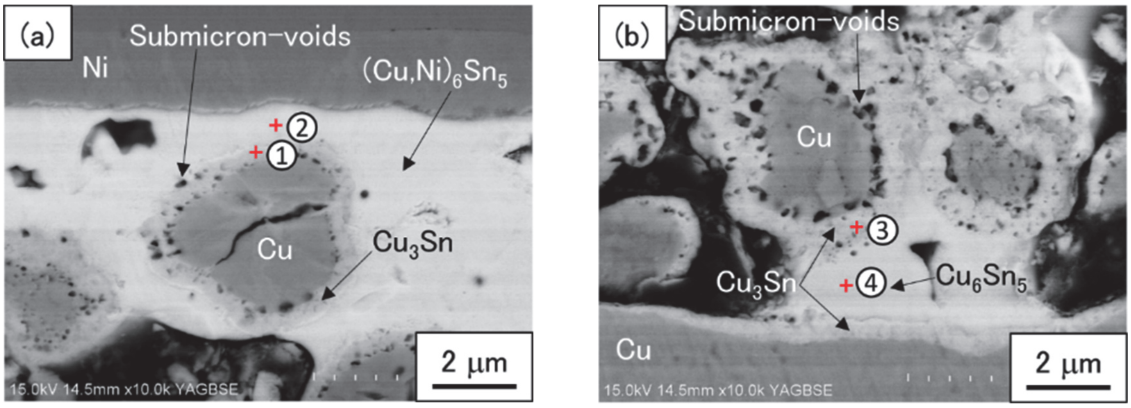

Fig. 5.16. Cross-sectional SEM images of the interfaces between the bonding layer and (a) chip and (b) substrate, as-bonded.

Table 5.6. Chemical composition (at.%) in the marked areas in Fig. 5.16 measured by EDX spectroscopy.

Area	Cu	Sn	Ni	Au	Phase
1	73.8	25.0	--	1.2	Cu_3Sn
2	44.2	44.6	5.3	6.0	$(Cu,Ni)_6Sn_5$ + Au
3	75.6	24.4	--	--	Cu_3Sn
4	56.0	44.0	--	--	Cu_6Sn_5

Cross-sectional SEM images of the TLPS joints aged at 150, 175, and 200 °C for 1000 h, which are shown in Fig. 5.17, show little change compared to the as-bonded state, as shown in Fig. 5.15. The XRD results of the TLPS bonding layer aged at 150, 175, and 200 °C for 1000 h, as shown in Fig. 5.18, show that Cu, Ag_3Sn, and Cu_3Sn peaks—and no Cu_6Sn_5 peaks—are detected in the aged state. This indicates that the Cu_6Sn_5, which are detected only in the as-bonded state, fully transformed into the Cu_3Sn phase during the thermal aging for 1000 h. Focusing on the interfacial microstructure on the chip side (Fig. 5.19 and Table 5.7) surface and substrate side (Fig. 5.20 and Table 5.8) surface, both the Cu_3Sn phase and residual $(Cu,Ni)_6Sn_5$ phase are observed at the chip side interface, whereas only the Cu_3Sn phase is observed at the substrate side interface. Although a small amount of the $(Cu,Ni)_6Sn_5$ phase could remain because of the Ni dissolution from the chip metallization, it can be concluded from these XRD and EDX results that the highest amount of the Cu_6Sn_5 phase, as seen in the as-bonded state, transforms into Cu_3Sn through the thermal aging. In addition, it should be noted that the number of submicron voids at the interface between the Cu_3Sn and Cu particles apparently increases through the thermal aging, as can be seen from a comparison between Fig. 5.16 (as-bonded) and Figs. 5.19 and 5.20 (aged).

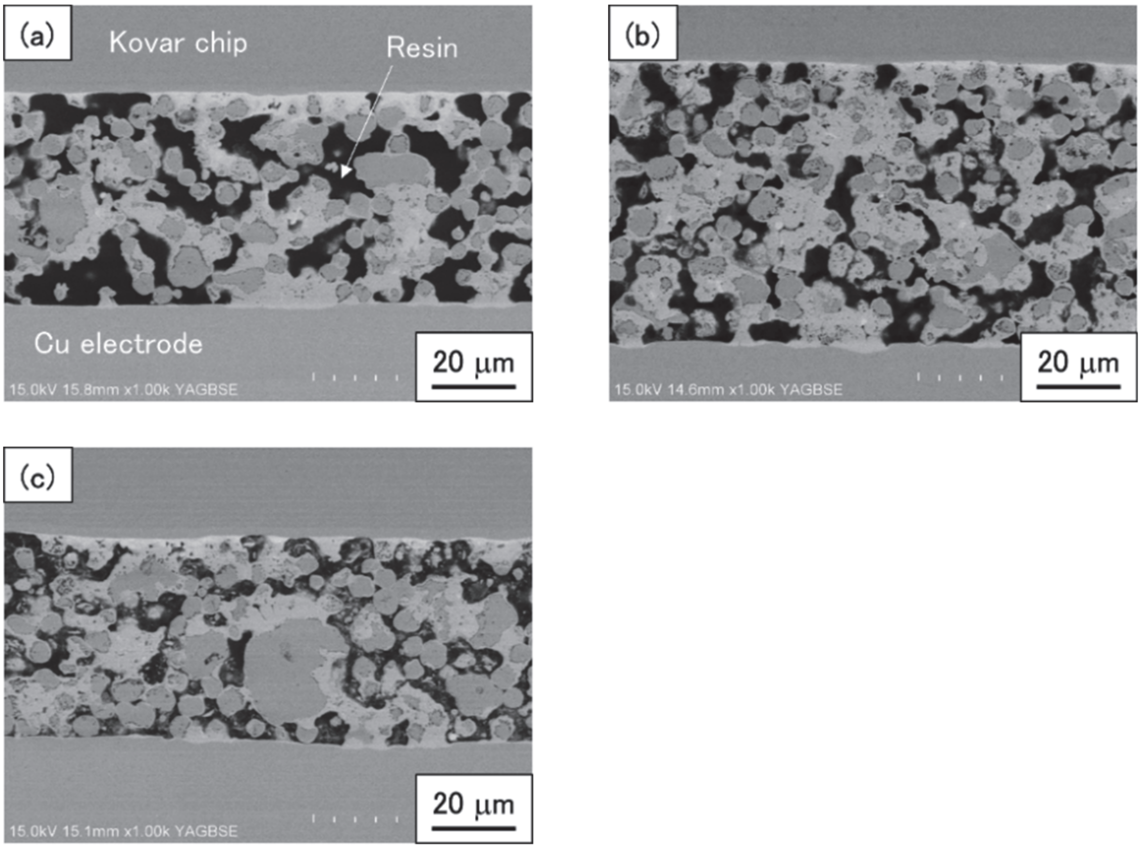

Fig. 5.17. Cross-sectional SEM images of a TLPS joint aged at (a) 150, (b) 175, and (c) 200 °C for 1000 h.

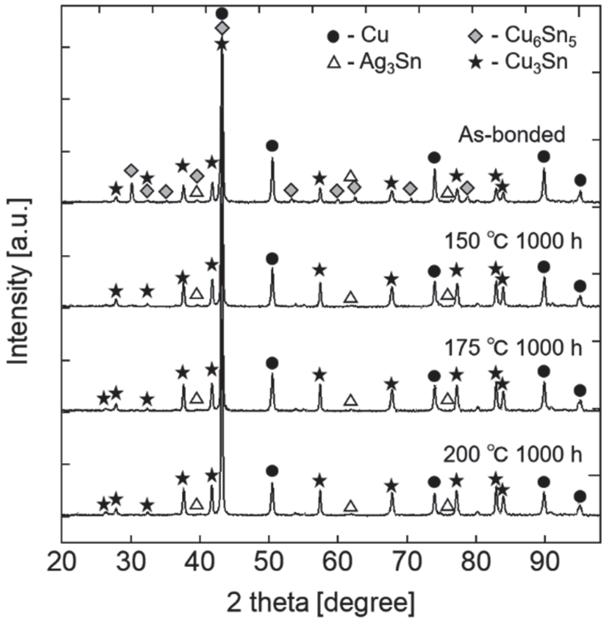

Fig. 5.18. XRD patterns of the TLPS bonding layer as-bonded and aged at 150, 175, and 200 °C for 1000 h.

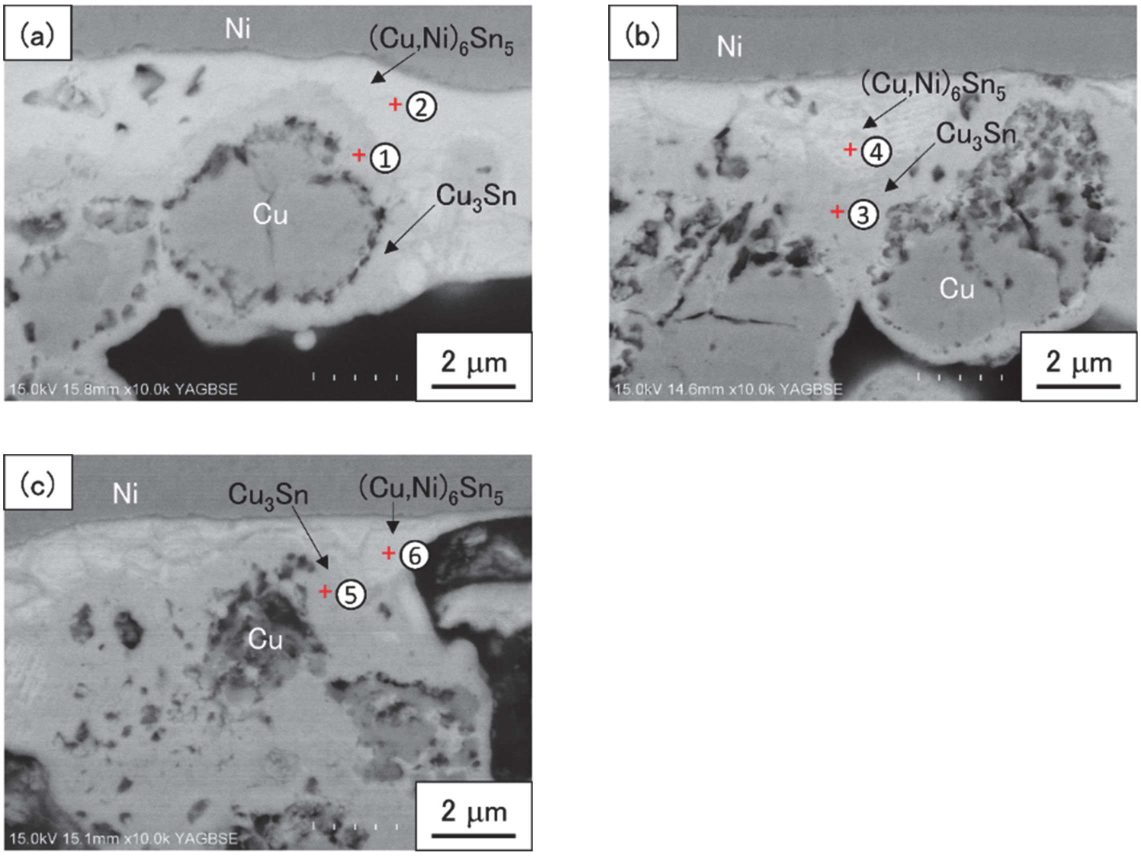

Fig. 5.19. Cross-sectional SEM images of the interfaces between the bonding layer and chip aged at (a) 150, (b) 175, and (c) 200 °C for 1000 h.

Table 5.7. Chemical composition (at.%) in the marked areas in Fig. 5.19 measured by EDX spectroscopy.

Aging Condition	Area	Cu	Sn	Ni	Au	Phase
150 °C 1000 h	1	74.2	24.7	--	1.0	Cu_3Sn
	2	46.9	42.0	4.1	7.1	$(Cu,Ni)_6Sn_5$ + Au
175 °C 1000 h	3	72.8	26.0	--	1.2	Cu_3Sn
	4	47.8	36.3	4.4	11.5	$(Cu,Ni)_6Sn_5$ + Au
200 °C 1000 h	5	71.7	26.6	--	1.7	Cu_3Sn
	6	47.6	38.4	5.8	8.1	$(Cu,Ni)_6Sn_5$ + Au

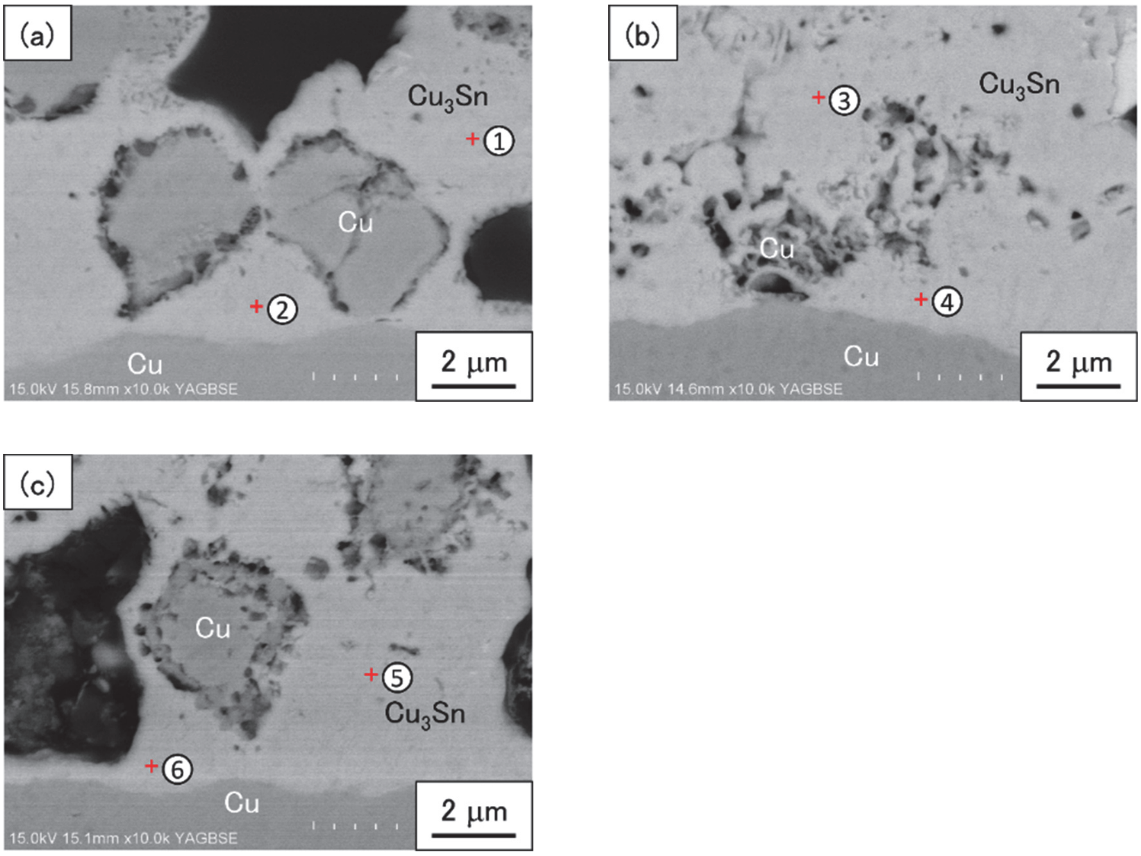

Fig. 5.20. Cross-sectional SEM images of the interfaces between the bonding layer and substrate aged at (a) 150, (b) 175, and (c) 200 °C for 1000 h.

Table 5.8. Chemical composition (at.%) in the marked areas in Figure 5.20 measured by EDX spectroscopy.

Aging Condition	Area	Cu	Sn	Ni	Au	Phase
150 °C 1000 h	1	75.7	24.3	--	--	Cu_3Sn
	2	73.1	26.9	--	--	Cu_3Sn
175 °C 1000 h	3	73.6	26.4	--	--	Cu_3Sn
	4	78.7	21.3	--	--	Cu_3Sn
200 °C 1000 h	5	75.5	24.5	--	--	Cu_3Sn
	6	76.1	23.9	--	--	Cu_3Sn

Fig. 5.21 illustrates the relationship between the shear strengths of the TLPS joints and aging conditions. The shear strength of the as-bonded joints is approximately 22.1 MPa. During the aging process, the shear strengths aged at 150 and 175 °C increase from 22.1 to 24.4 and 27.4 MPa in the first 500 h, respectively; afterward, they decrease to 22.8 and 24.0 MPa, respectively, after 1000 h. In contrast, that aged at 200 °C remains constant in the first 500 h and slightly decreases afterward to 19.0 MPa after 1000 h. The lowest shear strength of all the aged specimens is approximately 19 MPa, which is quite high when compared to the requirement of MIL-STD-883, Method 2019.7 (>0.5 MPa, 7 × 7 mm in die-size). This indicates that the joints could be applied to high-temperature applications with an excellent shear strength stability. The representative fracture surfaces of the as-bonded and aged specimens are shown in Fig. 5.22. The fractography of the as-bonded specimen shows a brittle fracture surface on the Cu_6Sn_5, as shown in Fig. 5.22 (a,b). The fractography of the aged specimens also shows a brittle surface. However, a fracture clearly appears at the interface between Cu and Cu_3Sn, as shown in Fig. 5.22(c)–(h). The morphology of the fractured surface appears similar to a “boiled egg” and “peeled eggshell”, which represents the Cu particle and Cu_3Sn layer covering them. Such unique fracture surfaces are observed only on the aged specimens. Based on the results, the change in the fracture behavior could have occurred by the microstructural variation through thermal aging.

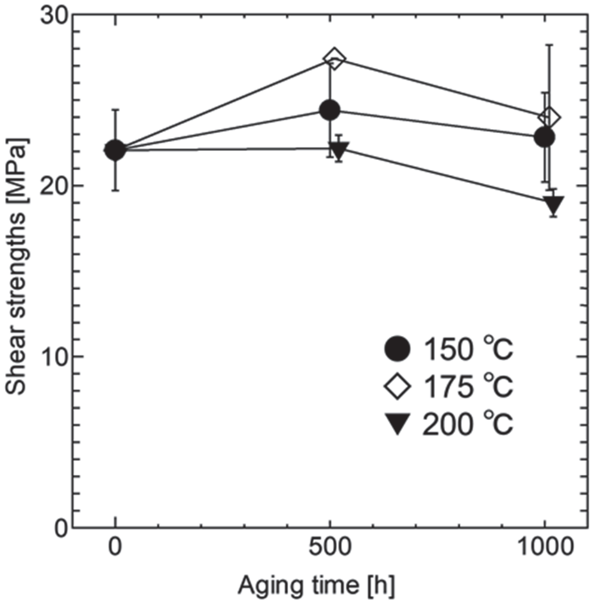

Fig. 5.21. Shear strengths of TLPS joints aged at 150, 175, and 200 °C for 1000 h.

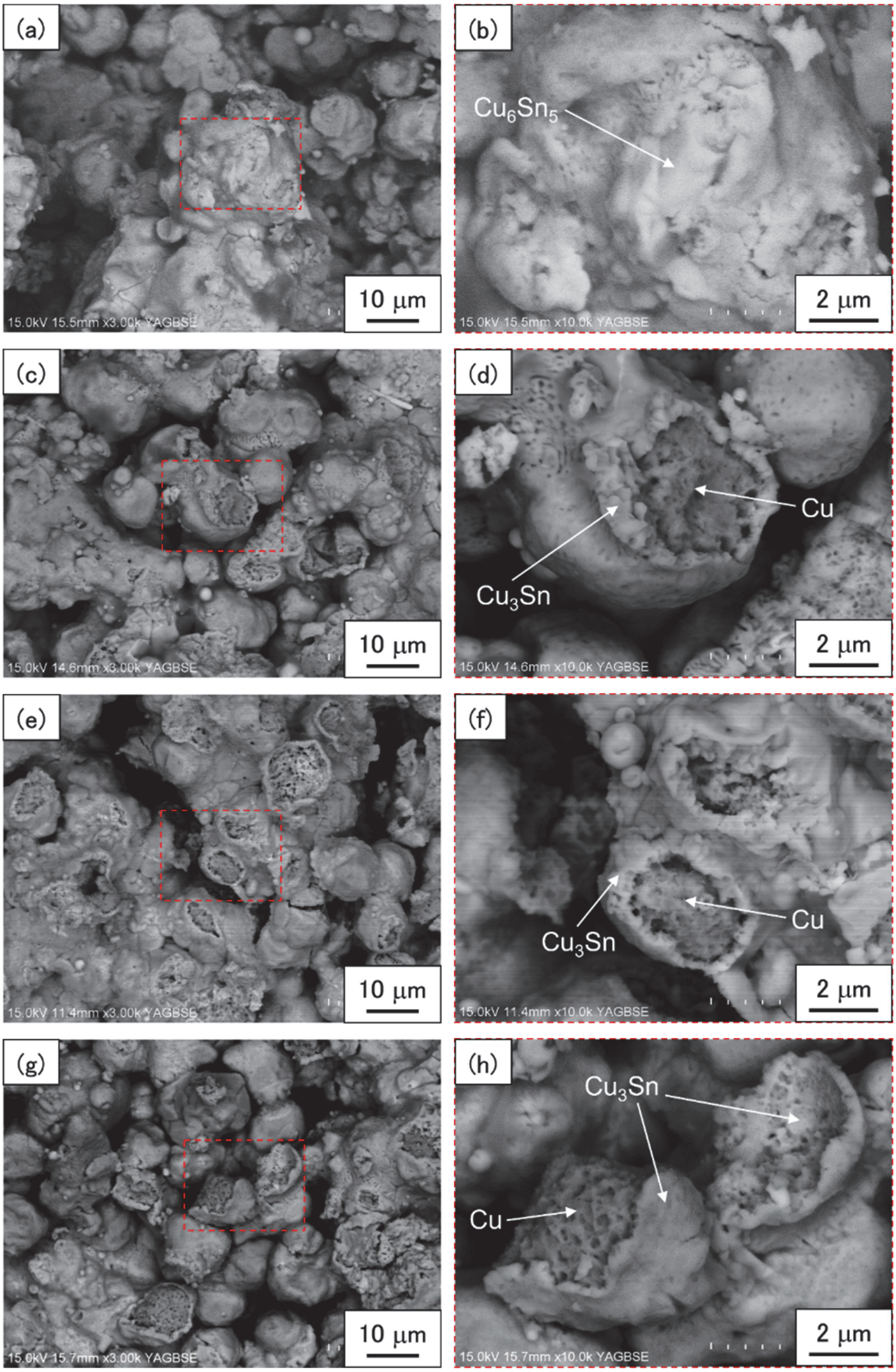

Fig. 5.22. Fracture surfaces of the joints (a,b) as-bonded and aged at (c,d) 150, (e,f) 175, and (g,h) 200 °C for 1000 h.

5.4.3. Macro-deformation behavior

Fig. 5.23 shows the homogenized Young’s modulus and yield strength calculated at each temperature using the 15-μm-sized models of Cu-IMC-resin and Cu-SAC-resin, where the resin region is polyimide, epoxy, or air; the values are normalized with respect to that of the Cu-IMC-resin at 22 °C. The normalized homogenized Young’s modulus of the Cu-IMC-resin is stable against temperature, whereas that of the Cu-SAC-resin decreases with the increase of temperature. The yield strength shows a similar trend (Fig. 5.23 (b)). These trends indicate the stability of properties in Cu and IMC against temperature variations as compared to SAC. In addition, the Young’s modulus and yield strength in the models with polyimide resin and air exhibit a minor difference. Thus, these FE results suggest that the IMC inhibits “softening” at high temperatures accompanied by a reduction in the Young’s modulus and yield strength, which is a significant advantage over SAC solder. Moreover, the load-bearing capacity of polyimide resin is very small due to its softness.

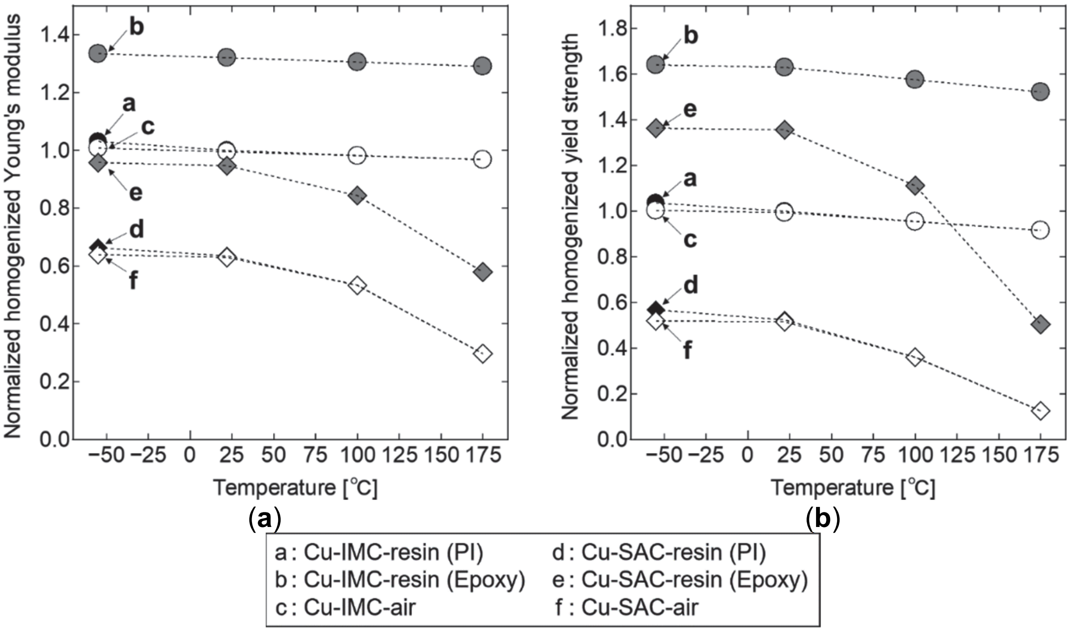

Fig. 5.23 Temperature dependence of the homogenized (a) Young’s modulus and (b) yield strength calculated by the 15-μm-sized models of Cu-IMC-resin and Cu-SAC-resin, where the resin region is polyimide, epoxy, or air. The values are normalized by that of the Cu-IMC-resin (PI) at 22 °C.

Fig. 5.24 shows the homogenized nominal strain–stress curves and mechanical properties calculated with the 50-μm-sized model. Here, the polyimide resin part is neglected for reducing the calculation elements of the model based on the results shown in Fig. 5.23. Although the IMC is considered as a linear elastic material, the curves show a deformation behavior with a yield point. The Cu-IMC-resin microstructure exhibits isotropicity, i.e., there is a negligible difference between the obtained properties along the three load-directions. The Young’s modulus of the Cu-IMC-resin composite (11.3 GPa) is significantly smaller than that of IMC (Cu_6Sn_5, 102 GPa). Moreover, the modulus of the Cu-IMC-resin microstructure is 1/3 times smaller than that of the solder (SAC305, 31 GPa) also. This implies that the Cu-IMC-resin microstructure shows significantly low stiffness compared to the IMC and solder. In addition, CTE is 17.8 × 10^{-6}/°C. The temperature dependence of the homogenized yield strengths was also evaluated using the same method as described before at various ambient temperatures from −55 to 175 °C. The calculated yield strengths at −55, 22, 100, and 175 °C are 17.4 (+0.6%), 17.3 (reference), 17.0 (−1.9%), and 16.7 MPa (−3.7%), respectively. For comparison, those of the SAC305 solder at 22, 100, and 200 °C are 45 (reference), 15 (−66.7%), and 3 MPa (−93.3%), respectively [28], [29]. These results confirm that the Cu-IMC-resin microstructure exhibits remarkably stable mechanical characteristics against temperature variation.

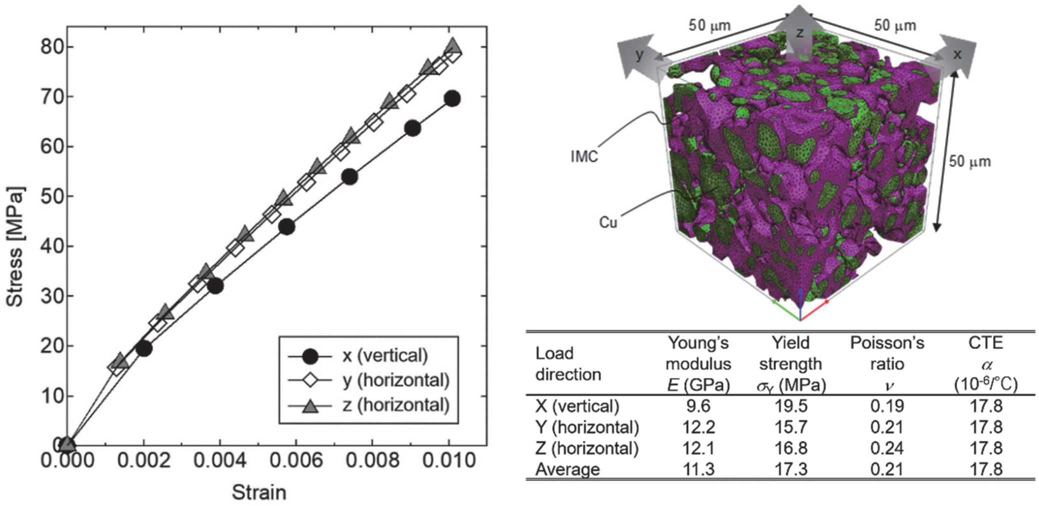

Load direction	Young's modulus E (GPa)	Yield strength σ_Y (MPa)	Poisson's ratio ν	CTE α (10^{-6}/°C)
X (vertical)	9.6	19.5	0.19	17.8
Y (horizontal)	12.2	15.7	0.21	17.8
Z (horizontal)	12.1	16.8	0.24	17.8
Average	11.3	17.3	0.21	17.8

Fig. 5.24. Deformation properties calculated by the 50-μm-sized Cu-IMC-resin microstructure model based on 3D image reconstruction at 22 °C.

5.4.4. Reliability of TLPS joints during thermal cycling

To evaluate the long-term bonding reliability in an accelerated manner, thermal cycling tests were carried out with the TLPS joints and SAC305 solder joints. Fig. 5.25 shows the relationship between the ratio of the unbonded area of these joints and the temperature cycles, where the SAT images of the TLPS joint after 1,200 thermal cycles and the SAC305 joint after 600 thermal cycles are shown. The resolution of the SAT, which is approximately 0.1 mm × 0.1 mm, is insufficient to detect the resin region of the Cu-Sn structure; in other words, we could easily distinguish the unbonded area from the resin region contained within the Cu-Sn structure. The unbonded area of the TLPS joints did not increase during thermal cycling, whereas that of the SAC305 joints increased. Cross-sectional SEM images of the TLPS joint after 1,200 thermal cycles and the solder joint after 600 thermal cycles are presented in Fig. 5.26. The thicknesses of the die-attached layers were not the same: the thicknesses of the TLPS and the SAC305 are approximately 70 μm and 80 μm, respectively. A thinner die-attached layer generally accelerates crack propagation [30]; however, cracks were observed at neither the middle nor the corner of the chip within the die-attached layer of the TLPS, whereas propagated cracks are observed within that of the SAC305 solder joint at both the middle and the corner of the chip. These observations confirm that the TLPS joints are more reliable than the SAC305 solder joints, i.e., the former exhibits fewer crucial delamination or cracks, which are less likely to affect heat dissipation.

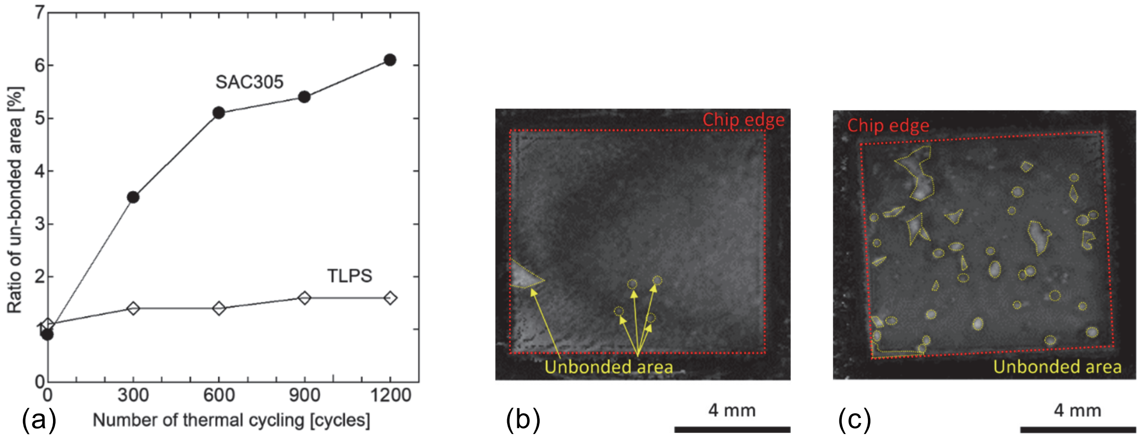

Fig. 5.25. Unbonded area of TLPS and SAC305 solder joints through 1200 thermal cycles in the temperature range of –55 to 175 °C.

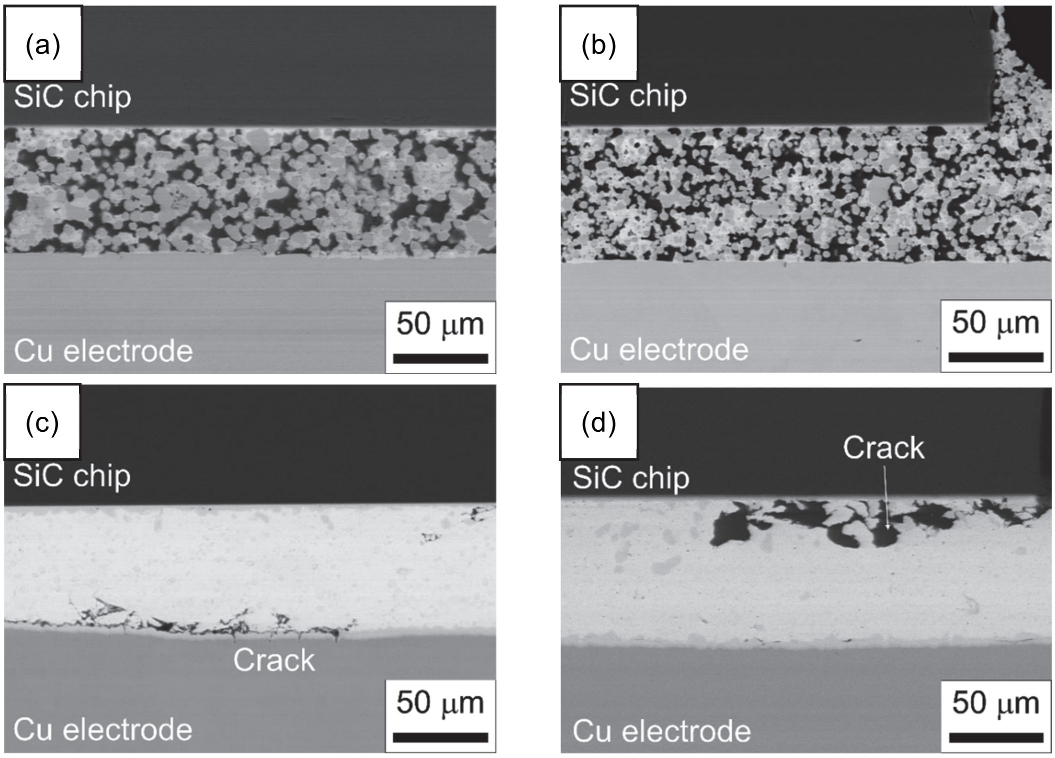

Fig. 5.26. Cross-sectional SEM image of (a, b) a TLPS joint after 1,200 thermal cycles and (c, d) a SAC305 solder joint after 600 thermal cycles in the temperature range from –55 °C to 175 °C. (a, c) and (b, d) show the middle and the corner of the chips, respectively.

Fig. 5.27 shows the FE simulation results of the thermal cycling tests for the SiC-DBC joint bonded by the TLPS layer, where the homogenized properties based on 3D image reconstruction are used. The joints exhibit strain peaks at the edges and corners of the bonding layer, where cracks were expected, as shown in Figs. 5.27 (a) and (b). The homogenized TLPS joint shows the maximum strain ~ 0.4%, which was generated during the thermal cycle with minimum temperature. In contrast, quite low Mises stress was generated in the TLPS layer as compared to that in the DBC substrate. In addition, no stress concentration on the DBC substrate was identified, as shown in Figs. 5.27 (c) and (d). The relationships between the number of thermal cycles and the calculated Mises strain and stress are shown in Figs. 5.28 (a), (b), respectively. Remarkably, the Mises strain of the homogenized TLPS joint, as shown in Fig. 5.28 (a), did not increase through the cycles, while that of the SAC305 joint increased in every cycle. Further, the normalized Mises stress, as shown in Fig. 5.28 (b), of the homogenized TLPS joint (0.08, −92%) is much lower than that of IMC (1.00, reference) and SAC305 (0.11, −89%). These results suggest that the TLPS facilitates the reduction of the both strain and stress macroscopically through thermal cycling.

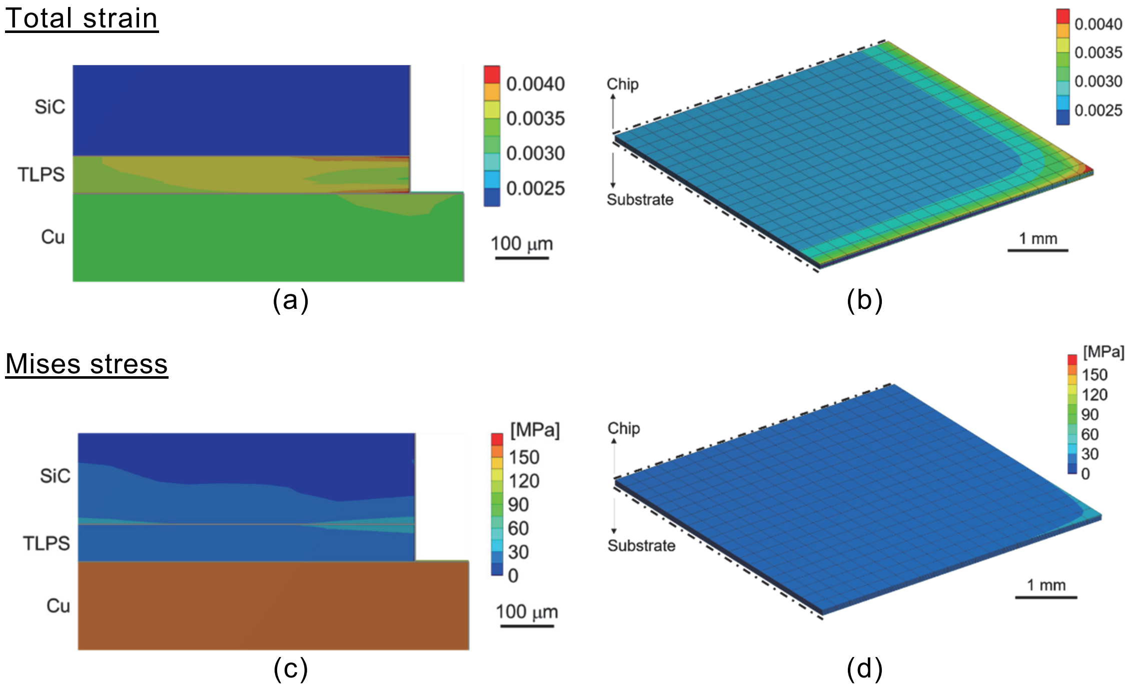

Fig. 5.27. FE simulation results of total strain distribution (a) at cross-sections along the diagonal axis of the joint and (b) in the transient liquid-phase sintering (TLPS) bonding layer. Simulated Mises stress distribution (c) at cross-sections along the diagonal axis of the joint and (d) in the TLPS bonding layer at minimum temperature during the thermal cycling.

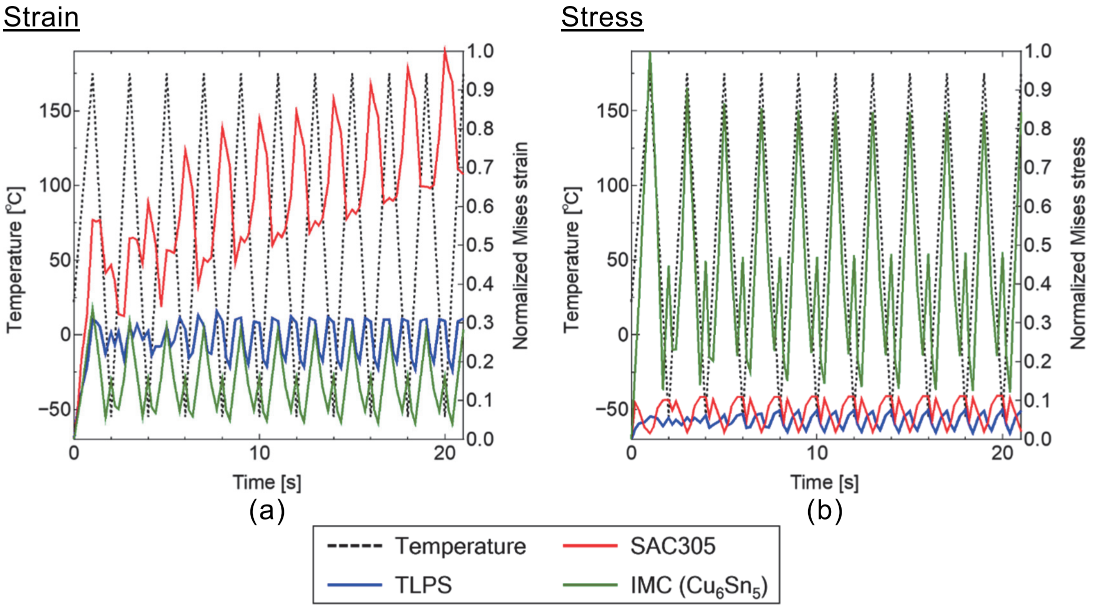

Fig. 5.28. Evolution of calculated (a) normalized Mises strain and (b) Mises stress in TLPS, SAC305, and IMC (Cu_6Sn_5) joints during the ten thermal cycles.

5.5. Discussion

5.5.1 Bonding characteristics

The novel Cu-IMC-resin composite joints were successfully obtained through the pressureless TLPS technique in this study. During processing, the melting of the solder and curing of the resin occurred at 220 and 230–240 °C, respectively. The Cu_6Sn_5 and Cu_3Sn were quickly generated during the bonding process below 250 °C. The morphology of the composite paste heated up from 250 to 275 °C shows little variation in Figs. 5.10 (c) and (d), and the shear tests also show small differences in the joint strengths bonded at these temperatures, as shown in Fig. 5.11 in Section 5.4.1. These results indicate that the molten solder over 220 °C rapidly transformed into Cu-Sn IMCs in this study. However, other studies have reported significant changes in the joint strengths with the increase in the bonding temperature or increase in the duration owing to the growth in IMC thickness [31], [32]. The quick formation of these Cu-Sn IMCs should have occurred because of the large reaction surface area between the micron-sized Cu and solder particles. Fig. 5.29 shows illustrations of the TLPS process using the Cu-solder-resin composite. After heating up to the melting point of the solder, the transient liquid solder spreads over the surface of the Cu particles, the substrate, and the chip. After wetting, the solder rapidly transforms into Cu-Sn IMCs. This isothermal solidification reaction generates a skeleton microstructure, which is composed of Cu cores and IMC bridges. The thermosetting resin is cured in the empty space of the skeleton microstructure at the soldering temperature.

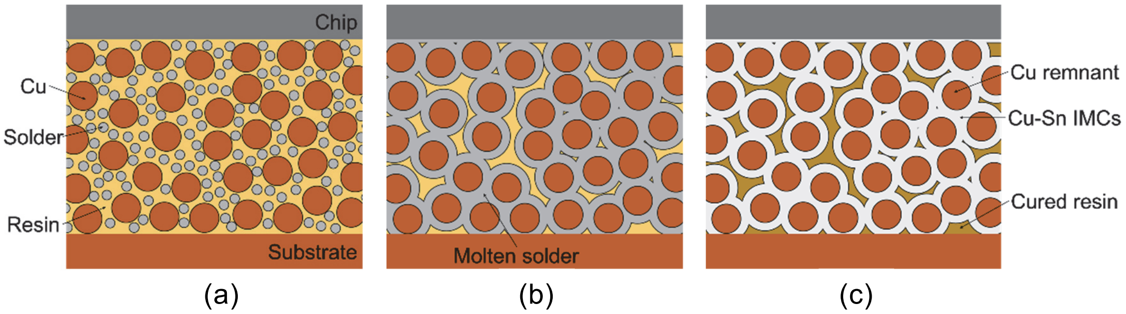

Fig. 5.29. Illustrations of TLPS process using Cu-solder-resin composite (a) before, (b) during, and (c) after process.

The polyimide thermosetting resin with soft mechanical properties, e.g., yield strength of approximately 1 MPa, was utilized in the composite paste in this study. The cured resin filled the network microstructure composed of Cu and IMCs in the joints. The shear test results indicated little variation in the joint strengths bonded at 220 and 250 °C, that is, the variation in the joint strengths was 1–2 MPa before/after the curing temperature of 230–240 °C. These results indicate that the polyimide resin itself had little impact on the mechanical properties of the TLPS joints. This is also supported by the FEM results, where shear stresses higher than 2 MPa could not be applied, because of the severe plastic material flow in the cases of resin-only and resin with Cu particles without IMC connections. In other words, the joint strength over 12 MPa, shown in the experimental section, was mainly acquired by a network of connections composed of Cu and IMCs in the joints. These results suggest that the polyimide resin plays the role of a “spacer” in the composite microstructure, thus enabling the inherent skeleton-shaped microstructure composed of Cu and Cu–Sn IMCs; the reliability of the joints at high temperatures should not be limited by resin deterioration.

The results of FE analysis suggested the stable mechanical properties of the IMC-based composites at high temperature, which is a significant advantage of these composites over the solder-based ones. Furthermore, although the reinforcement of solder-based joint by mold resin is generally effective, the reinforcement of IMC-based joint is not required because of its temperature-stable characteristics. The temperature-stable mechanical properties of the IMC enable the utilization of a soft resin as a part of the composite microstructure; in other words, significant stiffness reduction could be achieved by utilizing the resin with soft material properties and the temperature-stable IMC.

The FEM results also indicate that the joint stiffness S is exponentially affected by the interconnection density of the IMCs between Cu particles, as shown in Fig. 5.13. Although the simplified model does not accurately represent the real microstructure, the results indicate that the morphology of the Cu-IMC skeleton-shaped microstructure dramatically affects the mechanical properties of TLPS joints. Moreover, the joint properties can be tailored to a wide range, and the process control is essential for producing joints with stable interconnection densities and performances. Similar to other (conventional) sintering processes, the effect of bonding temperature, pressure, and time must be clarified. The strong impact of the interconnection density of the IMC on the joint stiffness, and the load-carrying path through the IMC phase against an external load lead to the conclusion that the fracture must predominantly occur within the IMC phase with a brittle fracture mode. The suggestion is also supported by the equivalent stress distribution of the FE simulation, as shown in Fig. 5.30, where high stress values are seen within the IMC bridges. This is in good agreement with the fracture surface analysis in Figs. 5.22 (a) and (b). In addition, the equivalent plastic strain distribution of the FE simulations is illustrated in Fig. 5.31, where high plastic strain values apparently emerge within the Cu particles. This suggests that the Cu particles enhance the joint ductility because they can deform and rotate plastically. The conventional TLP bond line composed of a dense IMC microstructure exhibits a high tensile strength but low toughness against an external load owing to the brittle properties of Cu–Sn IMCs, whereas the addition of Cu enhances the toughness based on existing models of ductile phase toughening [33]. The remaining Cu particles in the skeleton-shaped microstructure in this study can also enhance the toughness against a load based on the models. This can be beneficial to compensate (thermo-)mechanical loadings.

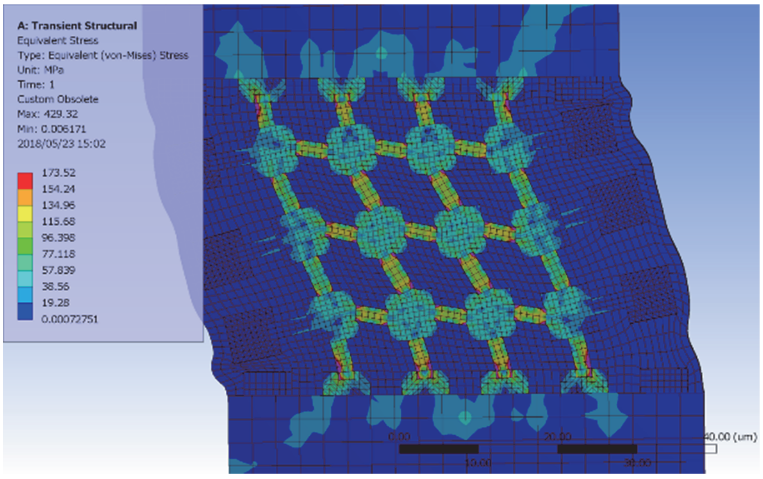

Fig. 5.30. Distribution of equivalent stress with primary/secondary IMC interconnections of 4/3.

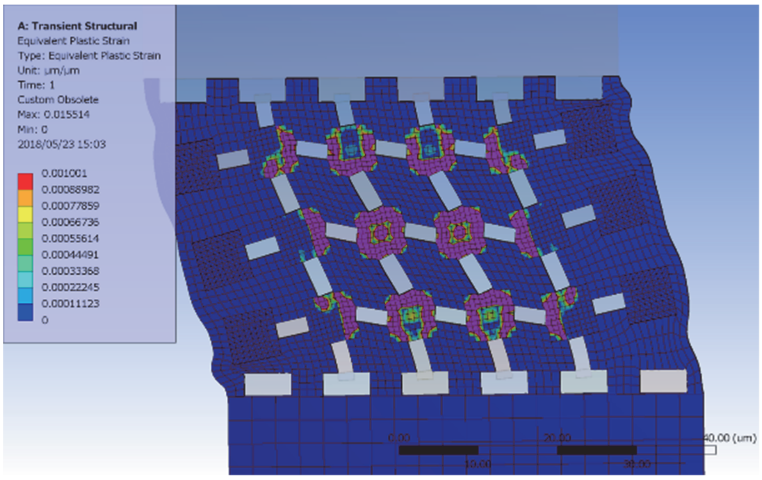

Fig. 5.31. Distribution of equivalent plastic strain with primary/secondary IMC interconnections of 4/3 where SiC and IMC parts, which are modeled as linear-elastic, are invisible.

5.5.2 Microstructural evolution through thermal aging

The microstructural variation of the Cu-IMC skeleton structure through thermal aging at 150, 175, and 200 °C was demonstrated in Section 5.4.2. Cu_6Sn_5 was not detected in the joints aged at 150–200 °C for 1000 h except at the chip side interface, as it was fully transformed to Cu_3Sn. There are two possible reactions for the transformation from Cu_6Sn_5 to Cu_3Sn, as shown in Eqs. 5.6 and 5.7:

$$9\mathrm{Cu} + \mathrm{Cu_6Sn_5} \rightarrow 5\mathrm{Cu_3Sn}, \tag{5.6}$$

$$\mathrm{Cu_6Sn_5} \rightarrow 2\mathrm{Cu_3Sn} + 3\mathrm{Sn}. \tag{5.7}$$

The values of the Gibbs free energy changes of the two reactions calculated by Bao et al. [34] are approximately −89 and 10 kJ/mol (150–200 °C), respectively. Thus, the reaction in Eq. 5.6 was the main pathway for the transformation from Cu_6Sn_5 to Cu_3Sn under the aging conditions in this study. The transformation from Cu_6Sn_5 to Cu_3Sn could affect the joint strengths because of the different mechanical properties of Cu_6Sn_5 and Cu_3Sn. For example, numerical studies estimated the Young's modulus of Cu_6Sn_5 and Cu_3Sn [35], [36]. Some experimental studies evaluated Young's modulus of Cu_6Sn_5 at the macro-scale [37], [38] and micro-scale [24], [39]–[41]. Furthermore, Liu et al. evaluated the mechanical properties of Cu_3Sn and Cu_6Sn_5 through both experimental and modelling techniques of micro-cantilever bending tests of the IMCs [42]. Although there is a wide variability in the values of their mechanical properties, the Cu_3Sn generally exhibits superior properties—including a high strength, high elongation, and low elastic modulus—compared to those of Cu_6Sn_5. For instance, Liu et al. reported the tensile strengths of Cu_3Sn and Cu_6Sn_5 to be 2.15 and 1.13 GPa and the tensile strains of Cu_3Sn and Cu_6Sn_5 to be 0.016 and 0.010, respectively [42]. In addition, Lee et al. reported the bonding strength of TLPS joints composed of Cu_3Sn to be five times higher than that composed of Cu_6Sn_5 [1]. Based on these studies, the transformation from Cu_6Sn_5 to Cu_3Sn could have a positive effect on improving the joint strengths through thermal aging.

Despite the fact that the transformation from Cu_6Sn_5 to Cu_3Sn might have improved the mechanical properties of the joints, the shear strengths of the TLPS joints showed little increase (150 and 175 °C) or a slight decrease (200 °C) through thermal aging in this study, as shown in Fig. 5.21 in Section 5.4.2. The submicron voids observed in the Cu_3Sn, as shown in the SEM images (i.e., Figs. 5.19 and 5.20 in Section 5.4.2), could adversely affect the TLPS joint strengths. Interestingly, the submicron voids were observed in the Cu_3Sn layer on the Cu particles, but not on the Cu substrate, as shown in Figs. 5.16, 5.19, and 5.20 in Section 5.4.2. Some studies demonstrated that submicron voids could be formed because of Kirkendall voids within the TLP layers of Cu–Sn [32], [34], [43], Ni–Sn [44], and Ag–Sn [34] systems. The Kirkendall voids were also observed in joints consisting of Sn-based solders and Cu [14], [45]–[47]. Yu et al. reported that the formation of Kirkendall voids as the diffusion rate of Cu atoms is much higher than that of Sn atoms in the Cu_3Sn layer between the Cu substrate and SAC305 solder [45]. However, previous results on Kirkendall void formation in Cu/Sn systems are not always consistent because of impurity atoms in the joints. Yu et al. [45] demonstrated that S segregation to a Cu/Cu_3Sn interface localized Kirkendall voids at the interface. Laurilla et al. [46] suggested that impurity atoms (not identified) in an electroplated Cu film assisted void formation. Moreover, Yang et al. [47] suggested that excess H in a Cu pad introduced during electroplating condensed into voids in Cu_3Sn. Although further studies are necessary, the submicron voids observed in the Cu_3Sn phase only on the Cu particles in this study might have occurred because of impurity atoms in the Cu particles. Based on the observation results of the cross-section before/after thermal aging, the increase in the amount of the submicron voids could negatively affect the TLPS joint strengths.

The microstructural evolution aged at 150–200 °C can be approximately described as the following evolving model, as shown in Fig.5.32. First, the original metallurgical microstructure of the TLPS layer was mainly composed of Cu_6Sn_5 (or $(Cu,Ni)_6Sn_5$ at the chip side interface), residual Cu particles, and Cu_3Sn layers in between the Cu_6Sn_5 and Cu particles, as shown in Fig. 5.32 (a). Submicron voids formed at the interface between the Cu_3Sn and Cu particles due to the possible mechanisms of the Kirkendall void. Secondly, with the increase in aging time, the transformation of the Cu_6Sn_5 (or $(Cu,Ni)_6Sn_5$ at the chip side interface) into Cu_3Sn through the diffusion of Cu atoms from the residual Cu particles and the formation of submicron voids at the interface between the Cu_3Sn and residual Cu particles occurred simultaneously, as shown in Fig. 5.32 (b). Finally, with the increase in the aging time, the residual Cu_6Sn_5, except for the small amount of $(Cu,Ni)_6Sn_5$ at the chip side interface, fully transformed into Cu_3Sn. Additionally, the number of submicron voids gradually increased, as shown in Fig. 5.32 (c). The analysis of the thermal aging characteristics for the TLPS shows that the joints aged at 150–200 °C for 1000 h maintained a shear strength exceeding 19 MPa on average, as shown in Fig. 5.21 in Section 5.4.2, because of both the positive and negative impacts of thermal aging on the shear strengths, which include the transformation of Cu_6Sn_5 into Cu_3Sn and the formation of submicron voids at the interface between the Cu_3Sn and residual Cu particles, respectively. In other words, the TLPS layer could produce relatively stable strengths for die-attach applications through metallurgical reactions during thermal aging.

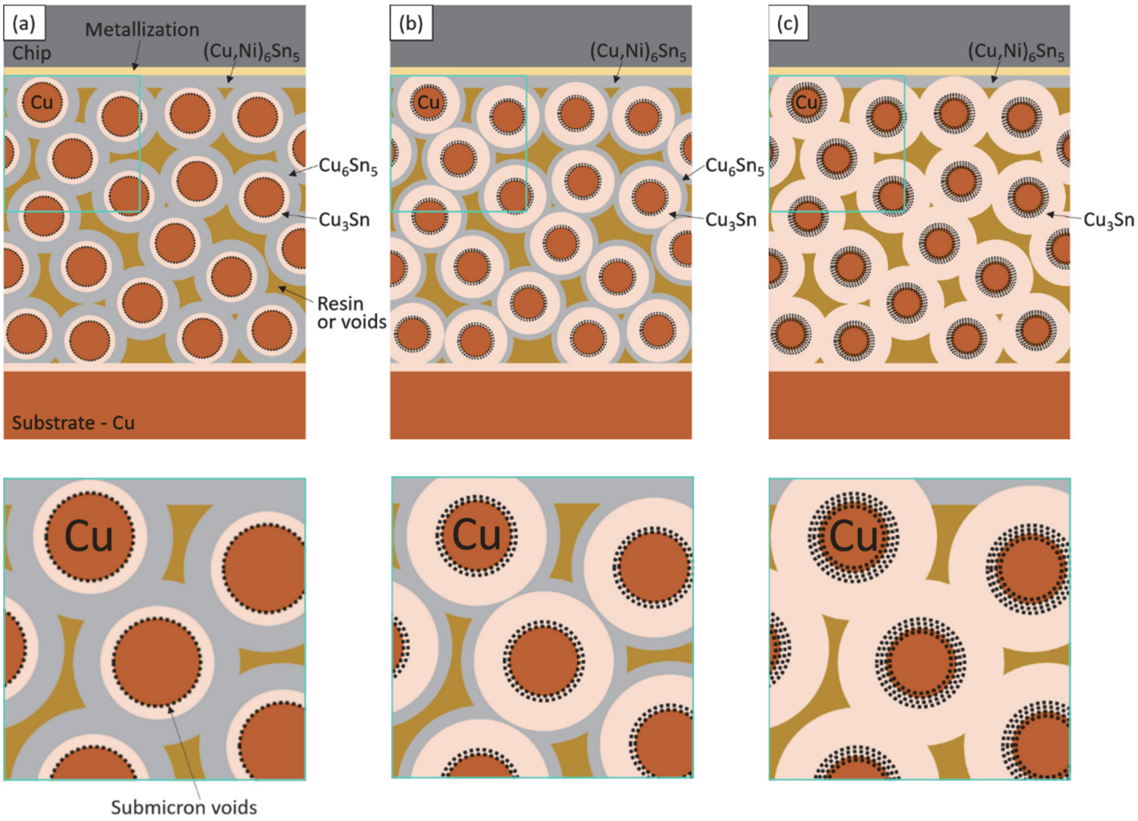

Fig. 5.32. Mechanism model of the microstructural evolution for the TLPS layer aged at 150–200 °C: (a) as-bonded, (b) gradual transformation of Cu_6Sn_5 into Cu_3Sn and formation of submicron voids, and (c) fully-transformed structure with dominated Cu_3Sn.

5.5.3. Impact of the macro- and micro-deformation behavior on the thermal cycling reliability

The macroscopic deformation behavior of the model through thermal cycling is shown in Fig. 5.28, where the strain of the TLPS joint is not increased in each subsequent thermal cycle (Fig. 5.28 (a)). This FE simulation result suggests that the TLPS joint deforms macroscopically during the elastic deformation stage. The joint lifetime of elastoplastic materials can be estimated by the Coffin–Manson equation, as shown in Eq. 4.3 in Section 4.5.2, Chapter 4, where the number of cycles to failure N_f is linearly proportional to the strain increase per cycle $\Delta\varepsilon_{ie}$. The macroscopic strain amplitude of the TLPS joint is shown in Fig. 5.28 (a), where $\Delta\varepsilon_{ie} \sim 0$, which indicates that the thermal-cyclic lifetime might be further improved. Furthermore, thermal stress has to be evaluated against thermal cycling to consider the lifetime of IMC, which is a brittle material. From the macroscopic point of view, the thermal stress of TLPS is much lower than that of the IMC-only joint and SAC305 joint. The thermal stress at the bonding layer can be analytically calculated by considering linear-elastic material properties, as shown in Appendix A. It is clear that the reduction of the Young's modulus of the bonding layer causes the reduction of the thermal stress of the TLPS joint as compared to the IMC-only joint. The above investigations suggest that the addition of resin causes significant stiffness reduction, and the mechanical properties of the IMC-based composite are stable against temperature variations, which facilitates the excellent reliability of the Cu-IMC-resin microstructure against thermal cycling.

To gain further insights, we now discuss the microscopic deformation characteristics, which include distribution of local stress and strain. The shear tests in Section 5.4.2 demonstrated the fracture at the Cu-IMC-resin joints within the IMCs or at the Cu particle-IMC interface with brittle surfaces. In addition, Liu et al. [42] demonstrated (both numerically and experimentally) that Cu_6Sn_5 and Cu_3Sn fractured in brittle mode using the micro-cantilever bending method. Although, the precise fracture behavior of brittle materials should be discussed by considering fracture toughness based on various influence factors; here, we have simply discussed the behavior in terms of Mises stress at potential crack initiation sites. The microscopic distribution of Mises stress of the TLPS microstructure against macroscopic uniaxial load was numerically evaluated, where the ambient temperature was set as −55 °C because the maximum macroscopic strain was generated at the minimum temperature stage during the thermal cycling. The results are shown in Fig. 5.33, where it is evident that the stress concentration sites, which are close to the necks between the connected Cu particles, expand with the increase in macroscopic strain (Fig. 5.33 (b–e)). When the macroscopic strain is 0.4% (which is equivalent to that used in thermal cycling experiment), although the stress concentration sites where the local Mises stress exceeds the tensile strength of Cu_6Sn_5 [42] can be partially identified, it is evident that the stress is broadly distributed (Fig. 5.33 (c)). Further, almost no sites with local Mises stress exceeding the tensile strength of the Cu_6Sn_5 can be found in the low strain (0.1%) condition (Fig. 5.33 (b)); however, many such sites can be found in the high-strain (1.0%) condition (Fig. 5.33 (e)). Considering the poor ductility of the IMCs, the micro-deformation behavior interestingly indicates that the high reliability of the TLPS joint is limited by this specific condition on the macroscopic strain; further evaluation of the durable strain conditions is of particular interest.

It may be noted that some earlier studies have reported the deformation behavior of TLPS joints under temperature variation. Greve et al. [49] experimentally and numerically identified a new failure mechanism, i.e., cooling-induced formation of vertical cracks in Cu-Sn and Ni-Sn TLPS joints based on the stress concentration at the interface of the TLPS layer and DBC substrate. Dudek et al. [21] also numerically investigated Cu-Sn TLPS joint under thermal cycling, where they evaluated the potential failure modes corresponding to the fatigue of chip metallization and brittle fracture of IMC, components, or interfaces. These studies revealed that the brittle fracture modes mainly occurred due to the stiffness and brittleness of the IMCs; therefore, the joint reliability would strongly depend on the stress conditions; e.g., joint dimensions and operation temperature. In contrast, the proposed Cu-IMC-resin TLPS composite exhibited deformation behavior under low-stiffness and broad stress distribution because of its inherent "skeleton-shape", thereby facilitating the excellent thermal cyclic reliability of the joint. From the results as shown in Section 5.4.1, although thermal performance should be investigated further, e.g., interfacial thermal resistance measurements, the thermal conductivity of the TLPS is comparable to that of conventional high-temperature Pb-5Sn solder, which is 23 W/m·K, and less than that of the SAC305 and other Sn-based solders. The thickness of the TLPS die-attached layer could be thinner than that of the conventional solders against a thermal strain during operation because of the low joint stiffness of the TLPS joints. This means that the opposing effects of high thermal conductivity and low stiffness must be compromised to satisfy the requirements of the operating conditions. Therefore, further experimental investigation on optimization of the skeleton microstructure to achieve both high thermal conductivity and low stiffness, and demonstration of the performance for power modules is of particular interest.

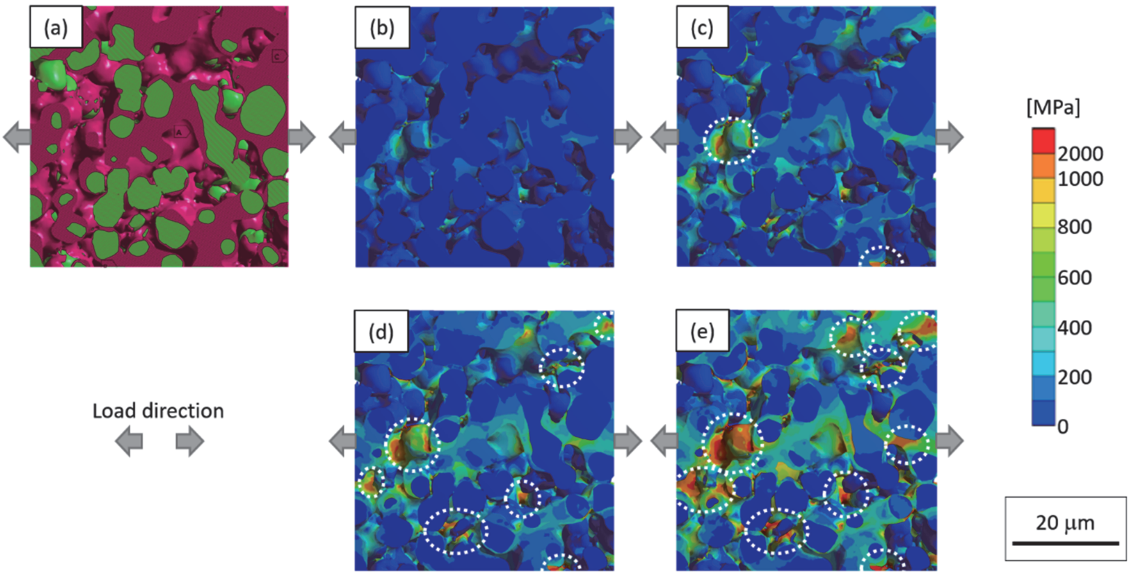

Fig. 5.33. Distribution of Mises stress obtained from the FE analysis of the 50-µm-sized Cu-IMC-resin model against uniaxial displacement at −55 °C. (a) FE model, and the models with uniaxial macroscopic strain of (b) 0.1%, (c) 0.4%, (d) 0.6%, and (e) 1.0%. The areas, whose Mises stress exceeded the tensile strength of Cu_6Sn_5 (approximately 1000 MPa), are shown by white dotted circles.

5.5.4. Advantages and potential issues

The characteristics of the Cu-IMC-embedded polymer composite revealed in this study are described, as follows:

- Young's modulus of 11 GPa,
- thermal conductivity of 26 W/m·K,
- shear strength of 22 MPa, and
- durable temperature of 200 °C.

This composite material showed significantly low stiffness and high durable temperature by utilizing TLPS Cu-Sn IMCs. This stiffness-reduction approach in this study has a great potential to the applications of TLPS techniques for strain-dominated loading conditions. The composite joint showed high temperature-tolerance against thermal aging at 200 °C and also thermal cycling with peak temperature up to 175 °C. Additionally, thermal conductivity and shear strength are satisfactory. Therefore, the advantages and potential issues of this composite material can be described, as follows:

- Advantages;
  - ➢ Good interconnection reliability, and
  - ➢ excellent stress relaxation performance for power chips.

- Potential issues;
    - Moderate heat dissipation performance.

By utilizing the full potential of stiffness-reduced TLPS joint, this composite material would be attractive to thin-chip die-attach applications, such as industry-use or home-appliance-use power modules, because the thermal stress by CTE mismatch is fatal risk for their electrical characteristics. Additionally, the opposing effects of high thermal conductivity and low stiffness must be compromised to satisfy the requirements of the operating conditions. Further experimental investigation on optimization of its morphology to achieve both high thermal conductivity and low stiffness, and demonstration of the performance for power modules is of particular interest.

5.6. Conclusions

This study verifies the good reliability of the pressureless TLPS joints using a Cu-solder-resin composite paste, which is composed of Cu particles, SAC305 solder particles, and polyimide-type thermosetting resin. A unique microstructure composed of the Cu particles connected with Cu–Sn IMC bridges distributed within the polyimide resin matrix was identified as resulting from the TLP reaction and resin curing at 250 °C for 1 min. The thermal conductivity analysis showed that the value of the TLPS film sintered at 250 °C is 25.9 W/m·K.

The averaged shear strengths were found to be 22.1 (reference), 22.8 (+3%), 24.0 (+9%), and 19.0 MPa (−14%) for the as-bonded state and the specimens aged at 150, 175, and 200 °C for 1000 h, respectively. The TLPS joints maintained a shear strength over 19 MPa after the thermal aging at 200 °C for 1000 h because of both the positive and negative impacts of the thermal aging, which are the phase transformation from Cu_6Sn_5 into Cu_3Sn, and the formation of submicron voids at the interface between Cu_3Sn and Cu particles because of the Kirkendall effects. These results indicate an excellent thermal reliability of the TLPS Cu–Sn skeleton microstructure.

FE simulations based on a 3D image reconstruction model to elucidate its macro- and micro-deformation properties. Macroscopically, the Cu-IMC-resin microstructure showed temperature-stable and low-stiffness mechanical characteristics because the Cu and IMC primarily acted as the load-carrying phases, and the embedded easily-deformable resin acted as the spacer. The homogenized Young’s modulus of the TLPS Cu-IMC-resin microstructure (11 GPa, −89%) was significantly lower than that of Cu_6Sn_5 (102 GPa, reference). Microscopically, the local stresses were broadly distributed on the IMC parts under uniaxial tensile simulation. This micro-deformation behavior indicated that the TLPS microstructure can exhibit highly reliable performance under a specific macroscopic strain condition in spite of the poor ductility of the IMCs. SiC-DBC die-attached numerical model using the homogenized mechanical properties of the Cu-IMC-resin predicted its excellent reliability during thermal cycling, as the deformation behavior showed both quite low strain and stress from the macroscopic view, and lower local-stress than the tensile strength of Cu_6Sn_5 from the microscopic view. This prediction was supported by the experimental results.

References in Chapter 5

[1] B. S. Lee and J. W. Yoon, “Cu-Sn Intermetallic Compound Joints for High-Temperature Power Electronics Applications,” *J. Electron. Mater.*, vol. 47, no. 1, pp. 430–435, 2018.

[2] J. Cho, R. Sheikhi, S. Mallampati, L. Yin, and D. Shaddock, “Bismuth-Based Transient Liquid Phase (TLP) Bonding as High-Temperature Lead-Free Solder Alternatives,” in *2017 IEEE 67th Electronic Components and Technology Conference (ECTC)*, 2017, pp. 1553–1559.

[3] S. W. Yoon, M. D. Glover, and K. Shiozaki, “Nickel-tin transient liquid phase bonding toward high-temperature operational power electronics in electrified vehicles,” *IEEE Trans. Power Electron.*, vol. 28, no. 5, pp. 2448–2456, 2013.

[4] J. F. Li, P. A. Agyakwa, and C. M. Johnson, “Suitable thicknesses of base metal and interlayer, and evolution of phases for Ag/Sn/Ag transient liquid-phase joints used for power die attachment,” *J. Electron. Mater.*, vol. 43, no. 4, pp. 983–995, 2014.

[5] H. A. Mustain, W. D. Brown, and S. S. Ang, “Transient liquid phase die attach for high-temperature silicon carbide power devices,” *IEEE Trans. Components Packag. Technol.*, vol. 33, no. 3, pp. 563–570, 2010.

[6] A. A. Bajwa, Y. Qin, R. Reiner, R. Quay, and J. Wilde, “Assembly and Packaging Technologies for Higherature and High-Power GaN Devices,” *IEEE Trans. Components, Packag. Manuf. Technol.*, vol. 5, no. 10, pp. 1402–1416, 2015.

[7] C. Shearer, B. Shearer, G. Matijasevic, and P. Gandhi, “Transient liquid phase sintering composites: Polymer adhesives with metallurgical bonds,” *J. Electron. Mater.*, vol. 28, no. 11, pp. 1319–1326, 1999.

[8] H. Feng, J. Huang, J. Yang, S. Zhou, R. Zhang, and S. Chen, “A Transient Liquid Phase Sintering Bonding Process Using Nickel-Tin Mixed Powder for the New Generation of High-Temperature Power Devices,” *J. Electron. Mater.*, vol. 46, no. 7, pp. 4152–4159, 2017.

[9] T. Hu, H. Chen, M. Li, and Z. Zhao, “Cu@Sn Core – Shell Structure Powder Preform for High-Temperature Applications Based on Transient Liquid Phase Bonding,” *IEEE Trans. Power Electron.*, vol. 32, no. 1, pp. 441–451, 2016.

[10] Y. Yamada *et al.*, “Pb-Free High Temperature Solder Joints for Power Semiconductor Devices,”

Trans. Japan Inst. Electron. Packag., vol. 2, no. 1, pp. 79–84, 2009.

[11] T. Y. Lee *et al.*, “Morphology, kinetics, and thermodynamics of solid-state aging of eutectic SnPb and Pb-free solders (Sn-3.5Ag, Sn-3.8Ag-0.7Cu and Sn-0.7Cu) on Cu,” *J. Mater. Res.*, vol. 17, no. 2, pp. 291–301, 2002.

[12] K. N. Tu and R. D. Thompson, “Kinetics of interfacial reaction in bimetallic CuSn thin films,” *Acta Metall.*, vol. 30, no. 5, pp. 947–952, 1982.

[13] D. Mu, H. Huang, S. D. McDonald, and K. Nogita, “Creep and mechanical properties of Cu_6Sn_5 and (Cu,Ni)6Sn5 at elevated temperatures,” *J. Electron. Mater.*, vol. 42, no. 2, pp. 304–311, 2013.

[14] C. Li, X. Hu, X. Jiang, and Y. Li, “Interfacial reaction and microstructure between the Sn3Ag0.5Cu solder and Cu–Co dual-phase substrate,” *Appl. Phys. A Mater. Sci. Process.*, vol. 124, no. 7, pp. 1–13, 2018.

[15] Y. Takaku, X. J. Liu, I. Ohnuma, R. Kainuma, and K. Ishida, “Interfacial Reaction and Morphology Between Molten Sn Base Solders and Cu Substrate,” *Mater. Trans.*, vol. 45, no. 3, pp. 646–651, 2004.

[16] A. Haque, Y. S. Won, and B. H. Lim, “Effect of Ni Metallization on Interfacial Reactions and Die Attach Properties of Zn-AI-Mg-Ga High Temperature Lead-Free Solders,” *Electron. Manuf. Technol. Symp.*, pp. 1–6, 2010.

[17] P. L. Tu, Y. C. Chan, and J. K. L. Lai, “Effect of intermetallic compounds on the thermal fatigue of surface mount solder joints,” *IEEE Trans. Components Packag. Manuf. Technol. Part B*, vol. 20, no. 1, pp. 87–93, 1997.

[18] T. An and F. Qin, “Effects of the intermetallic compound microstructure on the tensile behavior of Sn3.0Ag0.5Cu/Cu solder joint under various strain rates,” *Microelectron. Reliab.*, vol. 54, no. 5, pp. 932–938, 2014.

[19] K. Guth, N. Heuck, C. Stahlhut, A. Ciliox, N. Oeschler, and I. T. Ag, “End-of-life investigation on the . XT interconnect technology,” in *PCIM Europe 2015*, 2015, pp. 72–79.

[20] K. Guth *et al.*, “New assembly and interconnect technologies for power modules,” in *Integrated Power Electronics Systems (CIPS) 2012 7th InternationalConference*, 2012, pp. 1–5.

[21] R. Dudek, P. Sommer, A. Fix, S. Rzepka, and B. Michel, “Reliability issues for high temperature interconnections based on transient liquid phase soldering,” in *14th International Conference on Thermal, Mechanical and Multi-Physics Simulation and Experiments in Microelectronics and Microsystems (EuroSimE)*, 2013, pp. 1–8.

[22] B. S. Lee, S. K. Hyun, and J. W. Yoon, “Cu–Sn and Ni–Sn transient liquid phase bonding for die-attach technology applications in high-temperature power electronics packaging,” *J. Mater. Sci. Mater. Electron.*, vol. 28, no. 11, pp. 7827–7833, 2017.

[23] W. D. Jenkins, T. G. Digges, and C. R. Johnson, “Tensile properties of copper, nickel, and 70%copper30%nickel and 30%copper70%nickel alloys at high temperatures,” *J. Res. Natl. Bur. Stand.*, vol. 58, no. April, pp. 201–211, 1957.

[24] X. Deng, N. Chawla, K. K. Chawla, and M. Koopman, “Deformation behavior of (Cu, Ag)-Sn intermetallics by nanoindentation,” *Acta Mater.*, vol. 52, no. 14, pp. 4291–4303, 2004.

[25] P. Forquin, C. Denoual, C. E. Cottenot, and F. Hild, “Experiments and modelling of the compressive behaviour of two SiC ceramics,” *Mech. Mater.*, vol. 35, no. 10, pp. 987–1002, 2003.

[26] ANSYS Inc., *ANSYS 18.2 Workbench User's Guide*. Canonsburg, PA, USA: ANSYS Inc., 2017.

[27] C. Chen, C. Choe, Z. Zhang, D. Kim, and K. Suganuma, “Low-stress design of bonding structure and its thermal shock performance (− 50 to 250 °C) in SiC/DBC power die-attached modules,” *J. Mater. Sci. Mater. Electron.*, vol. 29, no. 16, pp. 14335–14346, 2018.

[28] I. Shohji, T. Yoshida, T. Takahashi, and S. Hioki, “Tensile Properties of Sn-3.5Ag-0.75Cu Lead-free Solders,” *Mater. Trans.*, vol. 43, no. 8, pp. 1854–1857, 2002.

[29] P. Lall, S. Shantaram, J. Suhling, and D. Locker, “Effect of aging on the high strain rate mechanical properties of SAC105 and SAC305 leadfree alloys,” in *2013 IEEE 63rd Electronic Components and Technology Conference (ECTC)*, 2013, pp. 1277–1293.

[30] H. Lu, C. Bailey, and L. Mills, “Impact of uneven solder thickness on IGBT substrate reliability,” in *2015 IEEE 65th Electronic Components and Technology Conference (ECTC)*, 2015, pp. 1888–1893.

[31] M. Fujino *et al.*, “Transient liquid-phase sintering using silver and tin powder mixture for die bonding,” *Jpn. J. Appl. Phys.*, vol. 55, no. 4, 2016.

[32] X. Liu, S. He, and H. Nishikawa, “Low temperature solid-state bonding using Sn-coated Cu particles for high temperature die attach,” *J. Alloys Compd.*, vol. 695, pp. 2165–2172, 2017.

[33] N. S. Bosco and F. W. Zok, “Strength of joints produced by transient liquid phase bonding in the Cu-Sn system,” *Acta Mater.*, vol. 53, no. 7, pp. 2019–2027, 2005.

[34] Y. Bao, A. Wu, H. Shao, Y. Zhao, L. Liu, and G. Zou, “Microstructural evolution and mechanical reliability of transient liquid phase sintered joint during thermal aging,” *J. Mater. Sci.*, vol. 54, no. 1, pp. 765–776, 2018.

[35] W. H. Chen, C. F. Yu, H. C. Cheng, and S. T. Lu, “Crystal size and direction dependence of the elastic properties of Cu_3Sn through molecular dynamics simulation and nanoindentation testing,” *Microelectron. Reliab.*, vol. 52, no. 8, pp. 1699–1710, 2012.

[36] T. Shen *et al.*, “First-principles calculations of structural and mechanical properties of Cu_6Sn_5,” *Optoelectron. Adv. Mater. Rapid Commun.*, vol. 10, no. 3–4, pp. 268–272, 2016.

[37] B. Subrahmanvan, “Elastic Moduli of some complicated binary alloys systems,” *Mater. Trans.*,

vol. 13, no. 2, pp. 93–95, 1971.

[38] H. Rhee, J. P. Lucas, and K. N. Subramanian, “Micromechanical characterization of thermomechanically fatigued lead-free solder joints,” *J. Mater. Sci. Mater. Electron.*, vol. 13, no. 8, pp. 477–484, 2002.

[39] F. X. Che and J. H. L. Pang, “Characterization of IMC layer and its effect on thermomechanical fatigue life of Sn-3.8Ag-0.7Cu solder joints,” *J. Alloys Compd.*, vol. 541, pp. 6–13, 2012.

[40] L. Xu and J. H. L. Pang, “Nanoindentation on SnAgCu lead-free solder joints and analysis,” *J. Electron. Mater.*, vol. 35, no. 12, pp. 2107–2115, 2006.

[41] P.-F. Yang, Y.-S. Lai, S.-R. Jian, J. Chen, and R.-S. Chen, “Nanoindentation identifications of mechanical properties of Cu_6Sn_5, Cu_3Sn, and Ni3Sn4 intermetallic compounds derived by diffusion couples,” *Mater. Sci. Eng. A*, vol. 485, no. 1–2, pp. 305–310, 2008.

[42] L. Liu, Z. Chen, C. Liu, Y. Wu, and B. An, “Micro-mechanical and fracture characteristics of $Cu_6Sn_5$and Cu_3Sn intermetallic compounds under micro-cantilever bending,” *Intermetallics*, vol. 76, pp. 10–17, 2016.

[43] L. Mo, Z. Chen, F. Wu, and C. Liu, “Microstructural and mechanical analysis on Cu-Sn intermetallic micro-joints under isothermal condition,” *Intermetallics*, vol. 66, pp. 13–21, 2015.

[44] H. Feng *et al.*, “Microstructural Evolution of Ni-Sn Transient Liquid Phase Sintering Bond during High-Temperature Aging,” *J. Electron. Mater.*, vol. 47, no. 8, pp. 1–11, 2018.

[45] J. Yu and J. Y. Kim, “Effects of residual S on Kirkendall void formation at Cu/Sn-3.5Ag solder joints,” *Acta Mater.*, vol. 56, no. 19, pp. 5514–5523, 2008.

[46] T. Laurila, V. Vuorinen, and J. K. Kivilahti, “Interfacial reactions between lead-free solders and common base materials,” *Mater. Sci. Eng. R Reports*, vol. 49, no. 1–2, pp. 1–60, 2005.

[47] W. Yang and R. W. J. Messler, “Microstructure Evolution of Eutectic Sn-Ag Solder Joints,” *J. Electron. Mater.*, vol. 23, no. 8, 1994.

[48] A. Lis, S. Kicin, F. Brem, and C. Leinenbach, “Thermal Stress Assessment for Transient Liquid-Phase Bonded Si Chips in High-Power Modules Using Experimental and Numerical Methods,” *J. Electron. Mater.*, vol. 46, no. 2, pp. 729–741, 2017.

[49] H. Greve, S. A. Moeini, P. McCluskey, and S. Joshi, “Prediction and Mitigation of Vertical Cracking in High-Temperature Transient Liquid Phase Sintered Joints by Thermo-Mechanical Simulation,” *J. Electron. Packag.*, vol. 140, pp. 020903-1-020903–9, 2018.

Chapter 6. Conclusions

In this study, NC and MC materials are applied to power electronics interconnections. The NC and MC materials have a potential to meet the various requirements for state-of-the-art power electronics applications, including higher complexity, system integration, product miniaturization, higher power density, and reliability enhancement. A comprehensive discussion of the NC and MC materials by computational calculation method to predict their equivalent characteristics was introduced by utilizing an idealized RVE model. This macroscopic evaluation suggested promising material combinations. Subsequently, specific materials and bonding processes were studied and successfully demonstrated as valid for power module implementation of these promising NC and MC materials, as follows: Sintered closed-porous Ag material (Chapter 3), metallic mesh-embedded solder composite (Chapter 4), and Cu-IMC-embedded polymer composite (Chapter 5). The results achieved in this dissertation are summarized as follows:

In Chapter 1, the fundamentals of interconnections and assembly in power electronics were described. Furthermore, a wide variety of NC and MC interconnection materials were reviewed based on our morphological classification (i.e., matrix-dilute inclusion composites and bicontinuous composites).

In Chapter 2, equivalent Young's modulus and thermal conductivity were estimated by FE simulations using simplified RVE models representing the matrix-dilute inclusion and bicontinuous composites. The impacts of the properties and the volume fraction of inclusions on the equivalent properties were predicted from a macroscopic perspective. The FE simulations revealed that the bicontinuous morphology further enhances the equivalent properties of NC and MC materials. Based on the FE simulations, three distinctive NC and MC candidates, promising the favorable material properties—low Young's modulus, high thermal conductivity and strength, and high-temperature tolerance—were proposed, as follows:

(a) Porous Ag material: High thermal conductivity and strength, and highly durable temperature,
(b) Cu-embedded solder composite: Moderately high strength and thermal conductivity,
(c) Cu (and/or Cu_6Sn_5)-embedded polymer composite: Significantly low stiffness and high temperature durability.

Chapter 3 describes an approach utilizing the sintered closed-porous Ag material for high-temperature SiC die-attachment applications. The closed-porous Ag microstructure is successfully realized by a pressure-assisted sintering process at 260 °C in air by utilizing a Ag nanoparticle paste. Metallurgical observations of the sintered Ag material showed that the nanocrystalline closed-porous structure in the as-sintered state. Tensile tests revealed that the as-sintered Ag materials macroscopically showed low ductility compared with the annealed specimen at RT. Additionally, lower stiffness than that estimated from the porosity was found. The as-sintered Ag material shows a significant temperature-dependent mechanical property. The as-sintered Ag material was suggested showing the inherent mechanical properties of nanocrystalline metals. The porous material was verified a high-temperature operation at a maximum temperature of 250 °C, which suggests the applicability of the material to high-temperature uses.

Chapter 4 describes an approach utilizing the metallic mesh-embedded solder composites for Si die-attachment application. The combination of SAC305 solder paste and Cu or Ni thin metallic mesh successfully provides bicontinuous composite microstructure by a pressureless reflow process. Metallurgical observations and shear tests demonstrated their unique microstructural and mechanical properties by comparing to monolithic SAC305 solder joint. Long-term stability against a constant elevated temperature of 150 °C and temperature cycling reliability with a peak temperature of 200 °C demonstrated superior performance over the monolithic SAC305. Furthermore, the thermal and mechanical FE simulations demonstrated their mechanically and thermally reinforced characteristics. This research has proven that the metallic mesh-embedded solder composite joint, especially Cu mesh-embedded solder composite, is an attractive joining solution for power modules below 200 °C.

Chapter 5 describes an approach utilizing the Cu-IMC-embedded polymer composite. A unique bicontinuous microstructure composed of the Cu particles connected with Cu–Sn IMC bridges embedded within the polyimide resin matrix was successfully fabricated by a pressureless TLPS process using a Cu-solder-resin composite paste at 250 °C for 60 s in nitrogen atmosphere. The shear strength and thermal conductivity of this composite interconnection are compatible with the conventional Pb-5Sn solder. This composite material showed significantly low stiffness and high durable temperature by utilizing TLPS Cu-Sn IMCs, the result of which was supported by the FE simulation of the real 3D microstructure model. Furthermore, the Cu-IMC-embedded polymer composite interconnection shows excellent reliability during thermal aging at 200 °C and thermal cycling between -55 and 175 °C despite their brittle characteristic. This stiffness-reduction approach in this study has a great potential to be applied in TLPS techniques under strain-dominated loading conditions.

In summary, the three promising composites have been demonstrated to be attractive joining solutions, which have their unique properties. These materials have great potential to achieve multiple required properties at a level superior to conventional monolithic solders. However, it is also clear that each material has its potential challenges. Based on these expected advantages and potential issues, the following combinations of “materials: favorable applications” were derived, as follows:

- Sintered closed-porous Ag material: Performance-driven high-temperature interconnections, such as state-of-the-art SiC power module die-attachments,
- Cu mesh-embedded solder composite: Interconnections that require cost-effective superior interconnection reliability and heat dissipation over conventional solders, such as next-generation interconnections to replace conventional solder in automotive power modules,
- Cu-IMC-embedded polymer composite: Thin-chip die-attach solutions, where thermal stress by CTE mismatch is fatal risk for their electrical characteristics, such as industry- or home-appliance-use power modules.

As described above, the concept of NC and MC materilas tailored to various requirements for power electronics interconnections was comprehensively verified by the prediction of equivalent characteristics, and the evaluations of three specific materials. A further comprehensive study, including a prediction method based on microscopic perspective, would provide additional insights in future work. This concept can still have tremendous potential by choosing various constituents and morphology; therefore, exploring other tailored combinations in future research can facilitate the attainment of additional state-of-the-art electronics interconnections.

Appendix A. Analytical calculation of thermal stress within three-layered structure

Thermal stress within multi-layered structure against ambient temperature change ΔT (= T - T_0) can be analytically given by considering force and moment balance equations, based on the 2-dimensional model, as shown in Fig. A.1, by assuming that thermal strain and stress within each parts are "zero" at T_0. In the three-layered structure assuming linear-elastic material properties, thermal stress within layer 1 $\sigma_{x,1}$, layer 2 $\sigma_{x,2}$, and layer 3 $\sigma_{x,3}$, are assumed as follows:

$$\begin{cases} \sigma_{x,1} = E_1 \cdot (\varepsilon_{\mathrm{F},1} + \varepsilon_{\mathrm{M},x}) & (-t_0 \le x \le -t_0 + t_1) \\ \sigma_{x,2} = E_2 \cdot (\varepsilon_{\mathrm{F},2} + \varepsilon_{\mathrm{M},x}) & (-t_0 + t_1 \le x \le -t_0 + t_1 + t_2) \\ \sigma_{x,3} = E_3 \cdot (\varepsilon_{\mathrm{F},3} + \varepsilon_{\mathrm{M},x}) & (-t_0 + t_1 + t_2 \le x \le -t_0 + t_1 + t_2 + t_3) \end{cases} \tag{A.1}$$

where Young's modulus, layer thickness, and coefficient of thermal expansion (CTE) of each layer are E_n, t_n, and α_n (n = 1, 2, or 3), respectively. Neutral axis of the model t_0 passes through the point x=0, described as follows:

$$t_0 = \frac{\int_0^{t_1+t_2+t_3} Exdx}{\int_0^{t_1+t_2+t_3} Edx} = \frac{E_1 t_1{}^2 + E_2 t_2{}^2 + E_3 t_3{}^2 + 2E_2 t_1 t_2 + 2E_3 t_3 t_1 + 2E_3 t_2 t_3}{2(E_1 t_1 + E_2 t_2 + E_3 t_3)} \tag{A.2}$$

$\varepsilon_{\mathrm{F,n}}$ is the term of uniaxial strain caused by constraints between laminated layers assumed in the both-ends-fixed model against temperature change ΔT, as shown in Fig. A.2 (a), as follows:

$$\varepsilon_{\mathrm{F,n}} = \varepsilon_{\mathrm{y}} - \alpha_n \cdot \Delta T \tag{A.3}$$

where ε_{y} is the average strain of the fixed-end. On the other hands, $\varepsilon_{\mathrm{M},x}$ is the term of strain caused by bending moment of each layer, as shown in Fig. A.2 (b), as follows:

$$\varepsilon_{\mathrm{M},x} = ax = \frac{x}{\rho} \tag{A.4}$$

where ρ is curvature radius of the model ($\rho > 0$: convex downward, $\rho < 0$: convex upward).
The force balance equation between each layer is described, as follows:

$$\int_{-t_0}^{-t_0+t_1} \sigma_1\, dx + \int_{-t_0+t_1}^{-t_0+t_1+t_2} \sigma_2\, dx + \int_{-t_0+t_1+t_2}^{-t_0+t_1+t_2+t_3} \sigma_3\, dx = 0 \tag{A.5}$$

which leads to

$$A_1 \cdot a + B_1 \cdot \varepsilon_{\mathrm{y}} + C_1 \cdot \Delta T = 0 \tag{A.6}$$

where,

$$\begin{aligned}&A_1 = 0\\&B_1 = E_1t_1 + E_2t_2 + E_3t_3\\&C_1 = -(E_1\alpha_1t_1 + E_2\alpha_2t_2 + E_3\alpha_3t_3)\end{aligned} \tag{A.7}$$

Next, the moment balance equation between each layer is described, as follows:

$$\int_{-t_0}^{-t_0+t_1} \sigma_1 x\,dx + \int_{-t_0+t_1}^{-t_0+t_1+t_2} \sigma_2 x\,dx + \int_{-t_0+t_1+t_2}^{-t_0+t_1+t_2+t_3} \sigma_3 x\,dx = 0 \tag{A.8}$$

which leads to

$$A_2 \cdot a + B_2 \cdot \varepsilon_\mathrm{C} + C_2 \cdot \Delta T = 0 \tag{A.9}$$

where,

$$\begin{aligned}A_2 = {}&\frac{E_1}{3}\{(t_1 - t_0)^3 - (-t_0)^3\} + \frac{E_2}{3}\{(t_1 + t_2 - t_0)^3 - (t_1 - t_0)^3\}\\&+\frac{E_3}{3}\{(t_1 + t_2 + t_3 - t_0)^3 - (t_1 + t_2 - t_0)^3\}\\B_2 = {}&0\\C_2 = {}&-\frac{E_1}{2}\alpha_1t_1(t_1 - 2t_0) - \frac{E_2}{2}\alpha_2t_2(t_2 + 2t_1 - 2t_0) - \frac{E_3}{2}\alpha_3t_3(t_3 + 2t_2 + 2t_1 - 2t_0)\end{aligned} \tag{A.10}$$

ε_F and ε_B are obtained from the Eqs. from A.5 to A.10, as follows:

$$\begin{aligned}\varepsilon_{\mathrm{F,n}} &= \left(\frac{E_1t_1\alpha_1 + E_2t_2\alpha_2 + E_3t_3\alpha_3}{E_1t_1 + E_2t_2 + E_3t_3} - \alpha_n\right) \cdot \Delta T\\\varepsilon_{\mathrm{M},x} &= 3/2 \cdot \{E_1\alpha_1t_1(t_1 - 2t_0) + E_2\alpha_2t_2(t_2 + 2t_1 - 2t_0)\\&\quad + E_3\alpha_3t_3(t_3 + 2t_2 + 2t_1 - 2t_0)\}\\&\quad /[E_1\{(t_1 - t_0)^3 - (-t_0)^3\} + E_2\{(t_1 + t_2 - t_0)^3 - (t_1 - t_0)^3\}\\&\quad + E_3\{(t_1 + t_2 + t_3 - t_0)^3 - (t_1 + t_2 - t_0)^3\}] \cdot x\end{aligned} \tag{A.11}$$

Consequently, the thermal stress gradient along the thickness of the three-multi-layered model is obtained by inserting Eq. A.11 into Eq. A.1, as follows:

$$\begin{cases} \sigma_{\mathrm{x},1} = E_1 \cdot \{k_{\mathrm{I}} x + (k_{\mathrm{II}} - \alpha_1) \cdot \Delta T\} & (-t_0 \le x \le -t_0 + t_1) \\ \sigma_{\mathrm{x},2} = E_2 \cdot \{k_{\mathrm{I}} x + (k_{\mathrm{II}} - \alpha_2) \cdot \Delta T\} & (-t_0 + t_1 \le x \le -t_0 + t_1 + t_2) \\ \sigma_{\mathrm{x},3} = E_3 \cdot \{k_{\mathrm{I}} x + (k_{\mathrm{II}} - \alpha_3) \cdot \Delta T\} & (-t_0 + t_1 + t_2 \le x \le -t_0 + t_1 + t_2 + t_3) \end{cases}$$

where, $k_{\mathrm{I}} = 3/2 \cdot \{E_1\alpha_1 t_1(t_1 - 2t_0) + E_2\alpha_2 t_2(t_2 + 2t_1 - 2t_0)$
$+ E_3\alpha_3 t_3(t_3 + 2t_2 + 2t_1 - 2t_0)\}$
$/[E_1\{(t_1 - t_0)^3 - (-t_0)^3\} + E_2\{(t_1 + t_2 - t_0)^3 - (t_1 - t_0)^3\}$
$+ E_3\{(t_1 + t_2 + t_3 - t_0)^3 - (t_1 + t_2 - t_0)^3\}]$

$$k_{\mathrm{II}} = \frac{E_1 t_1 \alpha_1 + E_2 t_2 \alpha_2 + E_3 t_3 \alpha_3}{E_1 t_1 + E_2 t_2 + E_3 t_3} \tag{A.12}$$

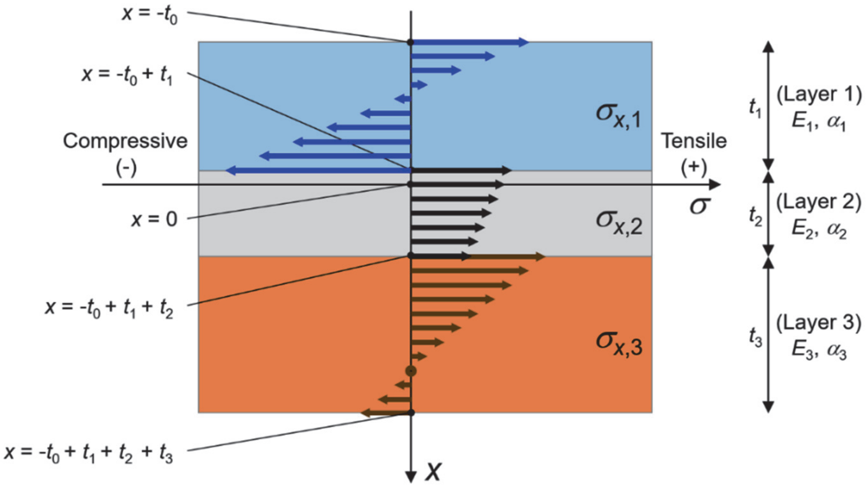

Fig. A.1. Schematic illustration of thermal-stress distribution within three-layered structure against ambient temperature change.

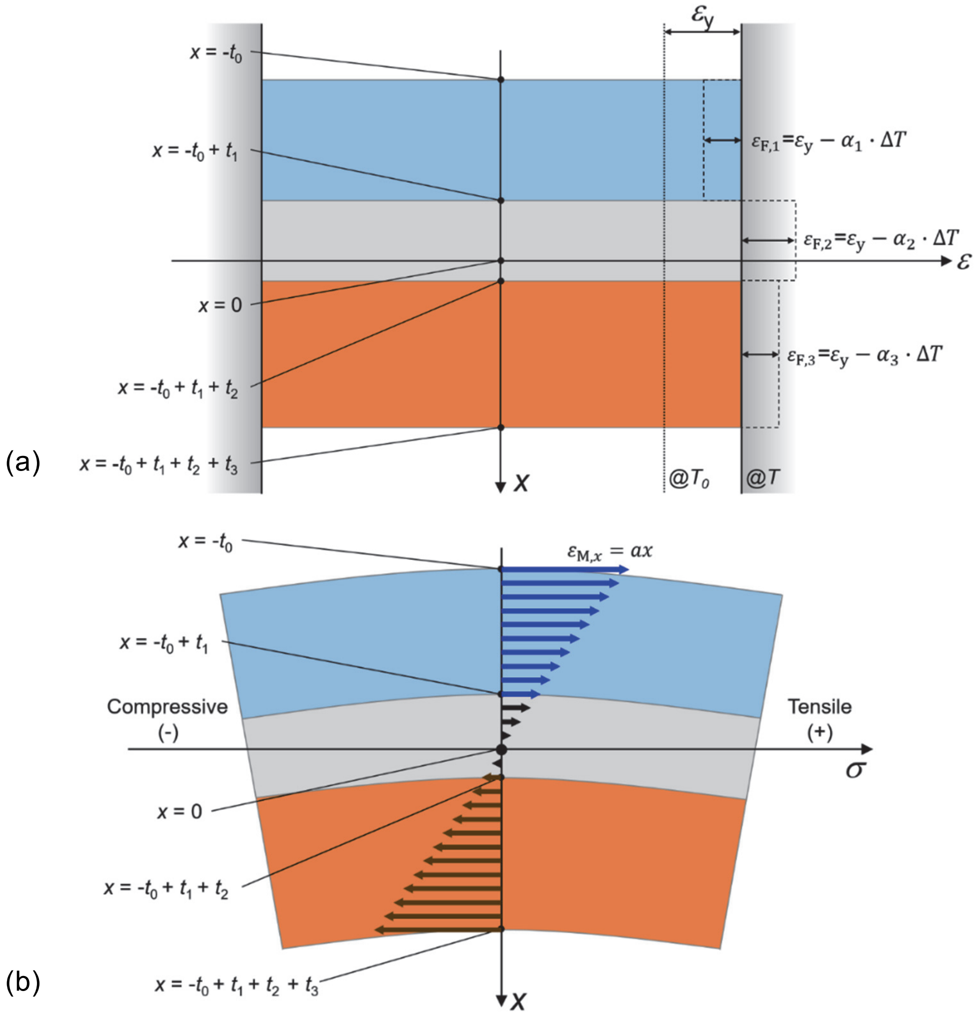

Fig. A.2. Schematic illustration of (a) uniaxial thermal strain caused by constraints between each layer assumed in the both-ends-fixed model against temperature change ΔT, and (b) bending stress caused by bending moment.

Appendix B. Favorable mechanical properties for power electronics interconnection material

Power electronics interconnection material is desired to provide heat dissipation performance, interconnection reliability, and stress-relaxation for power chips, as mentioned in Section 1.2.2. In this section, desirable mechanical properties for power interconnection, especially about interconnection reliability and stress-relaxation for power chips, were discussed based on the analytical calculation of thermal stresses.

The thermal stress within a three-layered structure against ambient temperature change ΔT (= T - T_0) can be analytically derived by considering force and moment balance equations, based on the 2-dimensional model, as shown in Appendix A. The material and geometrical parameters used in this study are shown in Table B.1. Layers 1, 2, and 3 present a chip, a bonding layer, and a substrate, respectively. The Layer 1 parameters are chosen as the SiC properties [1] with varying the thickness from 0.05 to 0.30 mm. The Layer 2 parameters are selected as the common thickness and CTE of solders, and varying Young's modulus from 1 to 100 GPa to evaluate its effect on thermal stress. The Layer 3 parameters are selected by roughly assuming the effective properties of DBC substrate. Ambient temperature change is assumed to be from T_0 = 200 °C to T = 22 °C, assuming the cooling process after the bonding process.

Table B.1. Parameters in the analytical calculations [1].

		Thickness, t [mm]	Young's modulus, E [GPa]	CTE, α [$\times 10^{-6}$/K]
Layer 1:	Chip	0.05–0.30	430	4.1
Layer 2:	Bonding layer	0.1	1–100	20
Layer 3:	Substrate	1.0	100	10

Fig. B.1 (a) shows analytically-calculated thermal stresses within the chip (Layer 1), the bonding layer (Layer 2), and the substrate (Layer 3), where the thickness of Layer 1 (chip) was 0.15 mm. Positive and negative stress values, which are in the y-axis, show tensile and compressive stresses, respectively. Fig. B.1 (b) shows the schematic illustration of the thermal stresses, where the $\sigma_{\mathrm{top},n}$ and $\sigma_{\mathrm{btm},n}$ are shown at the top and bottom edge of each layer n, respectively. Compressive stresses occurred in the chip (Layer 1), which increased with increasing Young's modulus of the bonding layer. Conversely, tensile stresses occurred in the bonding layer (Layer 2), which increased with increasing Young's modulus of the bonding layer. Finally, the stresses in the substrate (Layer 3) were relatively low, which were barely affected by Young's modulus of the bonding layer. These results showed that the reduction of Young’s modulus of the bonding layer reduced the compressive and tensile stresses at the chip and the bonding layer, respectively.

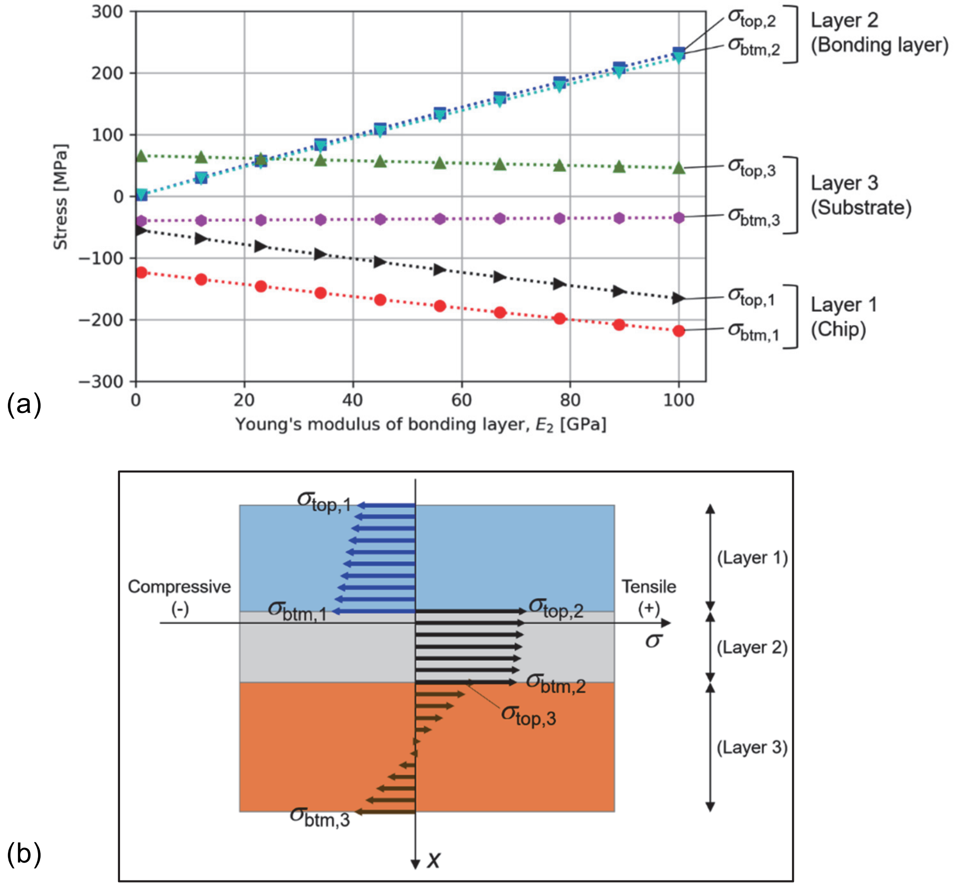

Fig. B.1. (a) Analytically-calculated thermal stresses of a three-layered model consisting of a chip (Layer 1, t_1 = 0.15 mm), a bonding layer (Layer 2), and a substrate (Layer 3), where positive and negative stress values show tensile and compressive stress, respectively. (b) Schematic illustration of the thermal stresses, where the $\sigma_{top,n}$ and $\sigma_{btm,n}$ are shown at the top and bottom edge of each layer n, respectively. Ambient temperature change is assumed to be from T_0 = 200 °C to T = 22 °C.

The relationship between the chip thermal stress $\sigma_{top,1}$, Young’s modulus of the bonding layer E_2, and the chip thickness t_1 was calculated, as shown in Fig. B.2 (a). This result indicated that either the reduction of E_2 or the increase in t_1 significantly reduced the thermal compressive stress at the chip layer $\sigma_{top,1}$. Recent leading-edge power modules require thinner chip for power-loss reduction; therefore, Young’s modulus reduction and lower bonding temperature are suggested to be helpful for power chip stress-relaxation.

Next, the relationship between the bonding layer thermal stress $\sigma_{\mathrm{top},2}$, Young's modulus of the bonding layer E_2, and the chip thickness t_1 was calculated, as shown in Fig. B.2 (b). The result indicated that the reduction of Young's modulus of the bonding layer E_2 significantly reduced the bonding layer thermal tensile stress $\sigma_{\mathrm{top},2}$. In contrast, the chip thickness reduction t_1 only slightly did so.

From a macroscopic point of view, the fracture criterion of a bonding layer can be qualitatively described from the balance between the thermal stress and the bonding layer strength. There are two simple approaches for joint reliability enhancement: Thermal stress reduction or joint strengthening. For the former approach, these analytical calculations suggest the effectiveness of Young's modulus reduction. For the latter approach, reinforced composite materials are evaluated in this study. Additionally, high-temperature-tolerant properties would contribute to strengthening at high temperatures. A high-strength and high-temperature-tolerant constituent material can be expected by strengthening a monolithic material.

Although an actual deformation behavior has to be discussed by considering both the elastoplastic and creep properties of each layer and also repetitive temperature profiles during service, these analytical calculations provided helpful insight in determining favorable mechanical characteristics of power electronics interconnections, summarized as shown in Table B.2.

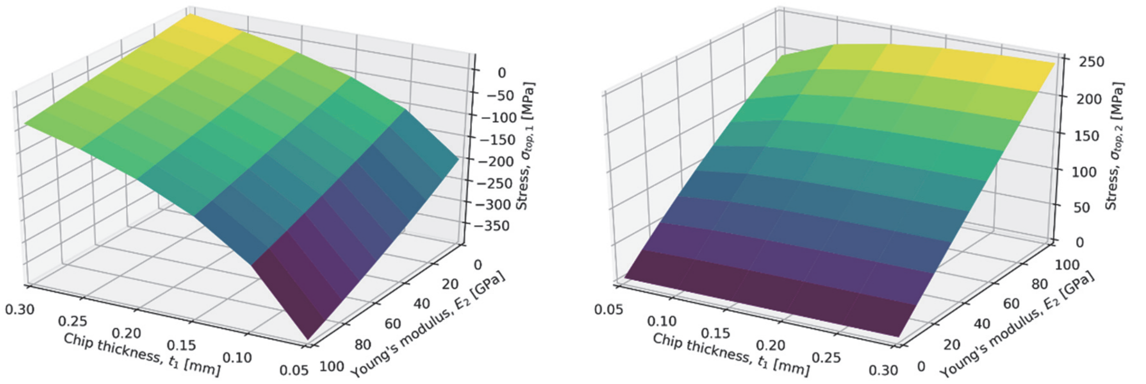

(a) Stress at chip, $\sigma_{\mathrm{top},1}$

(b) Stress at bonding layer, $\sigma_{\mathrm{top},2}$

Fig. B.2. Relationship between the chip thickness t_1, Young's modulus of the bonding layer E_2, and the thermal stress of (a) the chip $\sigma_{\mathrm{top},1}$ and (b) the bonding layer $\sigma_{\mathrm{top},2}$. Ambient temperature change is assumed to be from T_0 = 200 °C to T = 22 °C.

Table B.2. Favorable mechanical properties for interconnection materials, corresponding to the requirements for power electronics interconnections.

Mechanical requirements for power electronics interconnections	Favorable mechanical properties
Interconnection reliability	• Low Young’s modulus • High strength • High-temperature tolerance
Stress-relaxation for power chips	• Low Young’s modulus

References in Appendix B

[1] C. Chen, C. Choe, Z. Zhang, D. Kim, and K. Suganuma, “Low-stress design of bonding structure and its thermal shock performance (−50 to 250 °C) in SiC/DBC power die-attached modules,” *J. Mater. Sci. Mater. Electron.*, vol. 29, no. 16, pp. 14335–14346, 2018.

Acknowledgments

This research has been carried out during my doctoral course at Division of Materials and Manufacturing Science, Graduate School of Engineering, Osaka University, under the guidance of Professor Akio Hirose. This dissertation would not have been possible without the noble help from many people. I would like to have an opportunity to express my sincere gratitude and appreciate to all the people who have helped me during the doctoral course at Osaka University.

I would like to express my deep gratitude to my supervisor, Prof. Akio Hirose in Division of Materials and Manufacturing Science, Graduate School of Engineering, Osaka University, for giving me the opportunity and his trust for this dissertation. I highly appreciated his interest and support of my work during many scientific discussions.

I would like to extend my sincere gratitude to Professor Shinji Fukumoto and Professor Tomokazu Sano in Division of Materials and Manufacturing Science, Graduate School of Engineering, Osaka University, and Professor Hiroshi Nishikawa in Joining and Welding Research Institute, Osaka University, for their careful review on this dissertation and valuable comments.

I would like to thank Guest Professor Yoshihiro Kashiba in Mitsubishi Electric Research Laboratory of Manufacturing Converging Technologies, Graduate School of Engineering, Osaka University, for his kindness, encouragement and valuable advices for my studies and this dissertation throughout the PhD program and other industrial works.

I would like to express my appreciation to Hiroshi Yamaguchi, Section manager of Welding and Joining Section, Manufacturing Engineering Center, Mitsubishi Electric Corporation, for his continuous support and encouragement. He offered me a chance for my PhD work and very pleasant working atmosphere.

I am grateful to Dr. Adrian Lis, who was Assistant Professor in Mitsubishi Electric Research Laboratory of Manufacturing Converging Technologies, Graduate School of Engineering, Osaka University, for his great insight in scientific discussions, technical support for experimental and computational analyses, and all the effort on the publications we authored together.

I would like to thank Associate Professor Tomo Ogura, and Assistant Professor Tomoki Matsuda in Division of Materials and Manufacturing Science, Graduate School of Engineering, Osaka University, for their constructive suggestions and continuous support.

I would like to thank Toshiyuki Yoneda, Department manager of Structural Engineering Department, Manufacturing Engineering Center, Mitsubishi Electric Corporation, for his continuous support and encouragement.

I would like to thank Dr. Shinji Nakashima, Manufacturing Engineering Center, Mitsubishi Electric Corporation, for his valuable advices for my studies with the analytical calculations.

I want to express my thanks to Sho Kumada and Dr. Atsuhi Fukuda for providing useful experimental inputs to my research. I want to thank Shingo Kasaki and Keisuke Nishimoto for their great support with finite element analyses. I want to thank Kohei Nakanishi, Hajime Ashida, and Daiki Yamagiwa for their support with the simulations and experiments in Hirose group. I want to thank Dr. Soichi Sakamoto for his support of die-shear tests.

I would like to extend my gratitude to all members in Welding and Joining Section, Manufacturing Engineering Center, Mitsubishi Electric Corporation, for their support and helps. I also want to express thanks to all members of Hirose group for their friendly supports and helps during the PhD course.

Finally, I would like to thank my parents, my wife, and my sons, for their encouragement to accomplish the present work.

List of Publications

Publications related to dissertation

1. H. Tatsumi, S. Kumada, A. Fukuda, H. Yamaguchi and Y. Kashiba, “Impact of Metallurgical and Mechanical Properties of Sintered Silver Joints on Die-Attach Reliability of High-Temperature Power Modules”, Journal of Microelectronics and Electronic Packaging, vol. 13, pp. 121–127 (2016).
2. A. Lis, H. Tatsumi, T. Matsuda, T. Sano, Y. Kashiba and A. Hirose, “Bonding through novel solder-metallic mesh composite design”, Materials & Design, vol. 160, pp. 475–485 (2018).
3. H. Tatsumi, A. Lis, H. Yamaguchi, T. Matsuda, T. Sano, Y. Kashiba and A. Hirose, “Evolution of Transient Liquid-Phase Sintered Cu-Sn Skeleton Microstructure During Thermal Aging,” Applied Sciences, vol. 9, no. 1, pp. 157–168 (2019).
4. A. Lis, H. Tatsumi, T. Matsuda, T. Sano, Y. Kashiba and A. Hirose, “Reliability and Temperature Resistance of Solder–Metallic Mesh Composite Joints”, Journal of Electronic Materials, vol. 48, no. 6, pp. 3699–3712 (2019).
5. H. Tatsumi, H. Yamaguchi, T. Matsuda, T. Sano, Y. Kashiba and A. Hirose, “Deformation Behavior of Transient Liquid-Phase Sintered Cu-Solder-Resin Microstructure for Die-Attach,” Applied Sciences, vol. 9, no. 17, pp. 3476–3490 (2019).
6. H. Tatsumi, A. Lis, H. Yamaguchi, Y. Kashiba and A. Hirose, “Evaluation of Stiffness-Reduced Joints by Transient Liquid-Phase Sintering of Copper-Solder-Resin Composite for SiC Die-Attach Applications”, IEEE Transactions on Components, Packaging and Manufacturing Technology, vol. 9, no. 10, pp. 2111-2121 (2019).

Conference contributions

1. H. Tatsumi, S. Kumada, A. Fukuda, H. Yamaguchi and Y. Kashiba, “Impact of Metallurgical and Mechanical Properties of Sintered Silver Nanoparticles on Die-attach Reliability of High-temperature Power Modules”, In 48th International Symposium on Microelectronics (IMAPS2015), 842-847 (2015).
2. H. Tatsumi, S. Kumada, A. Fukuda, H. Yamaguchi and Y. Kashiba, “Reliability of Silver Sinter Joint for High-Temperature Power Modules”, In 3rd International Conference on Nanojoining and Microjoining 2016 (NMJ2016), University of Waterloo, et al., Crowne Plaza, Niagara Falls,

Canada, September 25-28 (2016).

3. A. Lis, H. Tatsumi, T. Matsuda, T. Sano, Y. Kashiba, and A. Hirose, in Proceedings of the International Conference and Exhibition on High Temperature Electronics (HiTEC), pp. 57–62 (2018).
4. H. Tatsumi, A. Lis, T. Monodane, H. Yamaguchi, Y. Kashiba, and A. Hirose, "Transient Liquid Phase Sintering Using Copper-Solder-Resin Composite for High- temperature Power Modules," in 2018 IEEE 68th Electronic Components and Technology Conference (ECTC), pp. 564–567 (2018).
5. H. Tatsumi, A. Lis, T. Monodane, H. Yamaguchi, Y. Kashiba, and A. Hirose, "High-Temperature Reliability of Transient Liquid Phase Sintering Joints Using Copper-Solder-Resin Composite", In 4th International Conference on Nanojoining and Microjoining 2018 (NMJ2018), Micro Joining Committee of Japan Welding Society, Todaiji Culture Center, Nara, Japan, December 2-5, (2018).
6. H. Tatsumi, S. Kumada, A. Fukuda, H. Yamaguchi, and Y. Kashiba, "Effects of Mechanical Properties of Sintered Silver Nanoparticles on Bonding Reliability", The 21st Symposium on "Microjoining and Assembly Technology in Electronics (Mate 2015)", pp.75-80 (2015). (in Japanese)
7. H. Tatsumi, A. Lis, T. Monodane, H. Yamaguchi, Y. Kashiba, and A. Hirose, "Die-attach Technologies of Power Modules by Transient Liquid Phase Sintering Using Copper-Solder-Resin Composite", The 28th Microelectronics Symposium (MES2018), pp.237-240 (2018). (in Japanese)

Other publications on Ag sintering technology

1. H. Tatsumi, Y. Akada, T. Yamaguchi, A. Hirose, "Sintering Mechanism of Composite Ag Nanoparticles and its Application to Bonding Process", Advanced Materials Research, vol. 26-28, pp. 499-502 (2007).
2. Y. Akada, H. Tatsumi, T. Yamaguchi, A. Hirose, T. Morita, E. Ide, "Interfacial Bonding Mechanism Using Silver Metallo-Organic Nanoparticles to Bulk Metals and Observation of Sintering Behavior", Materials Transaction, vol. 49, No.7, pp.1537-1545 (2008).
3. A. Hirose H. Tatsumi, N. Takeda, Y. Akada, T. Ogura, E. Ide and T. Morita, "A Novel Metal-to-Metal Bonding Process through In-situ Formation of Ag Nanoparticles Using Ag2O Microparticles", Journal of Physics: Conference Series (JPCS), vol. 165, pp. 012074-1-6 (2009).
4. T. Ogura, M. Nishimura, H. Tatsumi, N. Takeda, W. Takahara, A. Hirose, "Evaluation of

Interfacial Bonding Utilizing Ag2O-Derived Silver Nanoparticles using TEM Observation and Molecular Dynamics Simulation", The Open Surface Science Journal, vol. 3, pp. 55-59 (2011).

5. A. Hirose, N. Takeda, H. Tatsumi, Y. Akada, T. Ogura, E. Ide, T. Morita, "Low Temperature Sintering Bonding Process Using Ag Nanoparticles Derived from Ag2O for Packaging of High-temperature Electronics", Materials Science Forum, vol. 706-709, pp. 2962-2967 (2012).
6. T. Ogura, M. Nishimura, H. Tatsumi, W. Takahara, A. Hirose, "Interfacial Bonding Behavior between Silver Nanoparticles and Gold Substrate Using Molecular Dynamics Simulation", Materials transactions, vol. 53, pp. 2085-2090 (2012).

Award

- 48th International Symposium on Microelectronics (IMAPS2015) "Best of Track" Outstanding Paper Award (2015/10)

  H. Tatsumi, S. Kumada, A. Fukuda, H. Yamaguchi and Y. Kashiba, "Impact of Metallurgical and Mechanical Properties of Sintered Silver Nanoparticles on Die-attach Reliability of High-temperature Power Modules", International Microelectronics Assembly and Packaging Society